Internal Cooling for HP Turbine Blades

Robert Pearce

Worcester College

University of Oxford

A thesis submitted for the degree of

Doctor of Philosophy

Michaelmas Term 2016

Internal Cooling for HP Turbine Blades

Robert Pearce, Worcester College, University of Oxford

A thesis submitted for the degree of Doctor of Philosophy, Michaelmas Term 2016

Abstract

Modern gas turbine engines run at extremely high temperatures which require the high pressure turbine blades to be extensively cooled in order to reach life requirements. This must be done using the minimum amount of coolant in order to reduce the negative impacts on the cycle efficiency. In the design process the cooling configuration and stress distribution must be carefully considered before verification of the design is conducted. Improvements to all three of these blade design areas are presented in this thesis which investigates internal cooling systems in the form of ribbed, radial passages and leading edge impingement systems.

The effect of rotation on the heat transfer distribution in ribbed radial passages is investigated. An engine representative triple-pass serpentine passage, typical of a gas turbine mid-chord HP blade passage, is simulated using common industrial RANS CFD methodology with the results compared to those from the RHTR, a rotating experimental facility. The simulations are found to perform well under stationary conditions with the rotational cases proving more challenging.

Further study and simulations of radial passages are undertaken in order to understand the salient flow and heat transfer features found, namely the inlet velocity profile and rib orientation relative to the mainstream flow. A consistent rib direction gives improved heat transfer characteristics whilst careful design of inlet conditions could give an optimised heat transfer distribution.

The effect of rotation on the heat transfer distribution in leading edge impingement systems is investigated. As for the radial passages, RANS CFD simulations are compared and validated against experimental data from a rotating heat transfer rig. The simulations provide accurate average heat transfer levels under stationary and rotating conditions.

The full target surface heat transfer in an engine realistic leading edge impingement system is investigated. Experimental data is compared to RANS CFD simulations. Experimental results are in line with previous studies and the simulations provide reasonable heat transfer predictions.

A new method of combined thermal and mechanical analysis is presented and validated for a leading edge impingement system. Conjugate CFD simulations are used to provide a metal temperature distribution for a mechanical analysis. The effect of changes to the geometry and temperature profile on stress levels are studied and methods to improve blade stress levels are presented.

The thermal FEA model is used to quantify the effect of HTC alterations on different surfaces within a leading edge impingement system, in terms of both temperature and stress distributions. These are then used to provide improved target HTC distributions in order to increase blade life.

A new method using Gaussian process regression for thermal matching is presented and validated for a leading edge impingement case. A simplified model is matched to a full conjugate CFD solution to test the method's quality and reliability. It is then applied to two real engine blades and matched to data from thermal paint tests. The matches obtained are very close, well within experimental accuracy levels, and offer consistency and speed improvements over current methodologies.

Acknowledgements

I would like to thank everyone who has offered me support and encouragement throughout my DPhil, I am very grateful to all of you.

Firstly I'd like to thank my supervisor, Professor Peter Ireland, for all the advice and direction for my work. Your knowledge and enthusiasm has been invaluable.

I would like to thank Rolls-Royce, the EPSRC and the EU FP7 ERICKA project for funding this work. Thanks to Ed Romero, Janendra Telisinghe and Ed Dane at Rolls-Royce for their advice and support for the industrial aspects of the work, to Professor Matthew McGilvray in the Osney Lab for his help with the initial computational work, and to the many others in the Osney Lab who have offered advice over the past years.

Thank you to all in the workshop and maintainence at the Osney lab for offering practical help and aiding in the construction of my experimental rig, particularly Gerald Walker, Dave O'Dell, Dave Mountain and Jason McCluskey.

Finally, thank you to all my family and friends who've given such great support to me over the past few years.

Contents

Nomenclature

Abbreviations

ACARE	Advisory Council for Aviation Research and Innovation in Europe
ADJ	Adjusted simulation
AR	Aspect ratio
B.C.	Boundary conditions
CCD	Central composite design
CCD	Charged-coupled device
CFD	Computational fluid dynamics
DNS	Direct numerical simulation
ERICKA	Engine Realistic Internal Cooling Knowledge and Application
Ext.	External
FEA	Finite element analysis
FFT	Fast Fourier transform
GPR	Gaussian process regression
HP	High pressure
HTC	Heat transfer coefficient
Int.	Internal
IP	Intermediate pressure
IR	Infra-red
LE	Leading edge
LED	Light emitting diode
LES	Large eddy simulation
NGV	Nozzle guide vane
PS	Pressure surface
RANS	Reynolds-averaged Navier-Stokes
RHTR	Rotating heat transfer rig
RR	Rolls-Royce
RTDF	Radial temperature distribution factor
SS	Suction surface
SST	Shear stress transport

TBC	Thermal barrier coating
TE	Trailing edge
TET	Turbine entry temperature
THTAC	Transient heat transfer analysis code
TLC	Thermochromic liquid crystal
TP	Test point

Dimensionless no.

Bo	Buoyancy no.
Nu	Nusselt no.
Re	Reynolds no.
Ro	Rotation no.

Parameters

Cycle analysis

$\dot{m}$	Mass flow rate	$[kgs^{-1}]$
Q_{in}	Heat in	$[W]$
W_c	Compressor work	$[J]$
W_{net}	Net work	$[J]$
W_t	Turbine work	$[J]$
γ	Ratio of specific heats	
η_c	Compressor isentropic efficiency	
η_t	Turbine isentropic efficiency	
η_{cycle}	Cycle efficiency	
$\eta_{overall}$	Overall efficiency	
$\eta_{propulsive}$	Propulsive efficiency	

Geometric

A	Area	$[m^2]$
d	Inner diameter	$[m]$
D	Diameter	$[m]$
D_H	Hydraulic diameter	$[m]$
e	Rib height	$[m]$
L	Length	$[m]$
p	Pitch	$[m]$
R	Radius of rotation	$[m]$
t	Time	$[s]$
z	Length down radial passage	$[m]$
z	Jet to target distance - impingement	$[m]$
x, y, z	Spatial location	
ω	Rotation speed	$[rpm]$

Fluid

c_p	Specific heat	$[Jkg^{-1}K^{-1}]$
C_d	Discharge coefficient	
C^*	Critical flow function	
M	Molar mass	$[kgkmol^{-1}]$
p	Pressure	$[Pa]$
p_0	Total pressure	$[Pa]$
s	Specific entropy	$[Jkg^{-1}K^{-1}]$
R	Gas Constant	$[Jkmol^{-1}K^{-1}]$
T	Temperature	$[K]$
T_0	Total temperature	$[K]$
u,v,w	Velocity components	$[ms^{-1}]$
U,V,W	Ensemble average velocity	$[ms^{-1}]$
u',v',w'	Fluctuating velocity components	$[ms^{-1}]$
u_b	Bulk fluid velocity	$[ms^{-2}]$
$\mathbf{u}$	Vector velocity	$[ms^{-1}]$
y^+	Dimensionless wall distance	
μ	Dynamic viscosity	$[Nsm^{-2}]$
ν	Kinematic viscosity	$[m^2s^{-1}]$
ρ	Density	$[kgm^{-3}]$
τ_w	Wall shear stress	$[Pa]$

Thermal

c	Solid specific heat	$[Jkg^{-1}K^{-1}]$
k	Thermal conductivity	$[Wm^{-1}K^{-1}]$
h	Heat transfer coefficient	$[Wm^{-2}K^{-1}]$
q	Heat flux	$[Wm^{-2}]$
T_{gas}	Gas temperature	$[K]$
$T_{initial}$	Initial temperature	$[K]$
$T_{surface}$	Surface temperature	$[K]$

Solid Mechanics

E	Youngs modulus	$[MPa]$
F_x	Force in x direction	$[N]$
G	Shear modulus	$[MPa]$
K_C	Fracture toughness	
K_I, K_{II}, K_{III}	Stress intensity factor (Mode *I, II, III*)	
K_t	Stress concentration factor	
$S-N$	Stress - Number of cycles	
UTS	Ultimate tensile strength	$[MPa]$
ΔT	Temperature change	$[K]$
T_m	Melting temperature	$[K]$
α	Coefficient of thermal expansion	$[K^{-1}]$
γ_{xy}	Shear strain	
ε_{xx}	Strain	
$\varepsilon_{thermal}$	Thermal strain	
ν	Poisson's ratio	
σxx	Stress	$[Pa]$
τxy	Shear stress	$[Pa]$

Machine Learning

Δh	HTC multiplier
f	Fitting function
GP	Gaussian process
h	Basis function
k	Covariance function
x	Input parameters
x'	Training data parameters
y	Outputs
I	Identity matrix
β	Basis function coefficients
θ	Kernel parameters
σ_f	Covariance function standard deviation
σ_l	Covariance function charactistic length scale
σ	Model noise standard deviation

Chapter 1

Introduction

Gas turbine engines are widely used in the modern aviation industry and have evolved greatly since their inception, around 1940, in both Germany and Britain. Modern engines are considerably more intricate than the initial designs as they have been developed for an increase in power output and efficiency, which has a great bearing on running costs. More recently environmental concerns have driven engine manufacturers to reduce emissions, and therefore improve engine efficiency. An example of these is the ACARE vision 2020 target of reducing fuel consumption and carbon dioxide emissions by 50 %, of which 15-20 % is expected to be achieved through more efficient engines [1].

New airframes require bespoke engines from the manufacturers, who compete to sell their engines to the airlines purchasing the planes. The commercial case for an engine relies heavily on its efficiency and running costs, which therefore must be constantly improved for the engine manufacturer to remain competitive.

Over time these factors have driven engine manufacturers to increase specific power output and cycle efficiency, partly through an increased turbine entry temperature, as illustrated in figure 1.1.

This increase led to the initial requirement for cooled blades, and subsequently the increased complexity of these systems as the cooling requirement has become higher. This is due to a combination of the increase in the turbine entry temperature and the desire for increased blade life.

Figure 1.1: Increase in turbine entry temperature with time for Rolls Royce civil gas turbine engines [2]

1.1 Gas Turbine Theory

A key consideration for a gas turbine engine is its efficiency as a more efficient engine is more cost-effective to run. Therefore this is a vital component in the commercial case for any new engine. The efficiency of a gas turbine engine can be described in the form given in equation 1.1.

$$\eta_{overall} = \eta_{cycle} * \eta_{propulsive} \tag{1.1}$$

$$\eta_{cycle} = \frac{Mechanical\ Power\ Out}{Power\ In} \qquad \eta_{propulsive} = \frac{Propulsive\ Power}{Mechanical\ Power}$$

The overall efficiency is a product of the cycle and propulsive efficiencies. The propulsive efficiency results from mechanical losses in the gas turbine and aerodynamic losses in the fan. The cycle efficiency can be illustrated by a simple analysis of the Joule cycle, which represents the gas turbine. This is shown schematically in figure 1.2, and on a T-s plot in figure 1.3.

The simplest analysis of the cycle consists of approximating the three processes as follows:

1. Isentropic compression - *Work in*
2. Heat addition at constant pressure - *Heat in*
3. Isentropic expansion - *Work out*

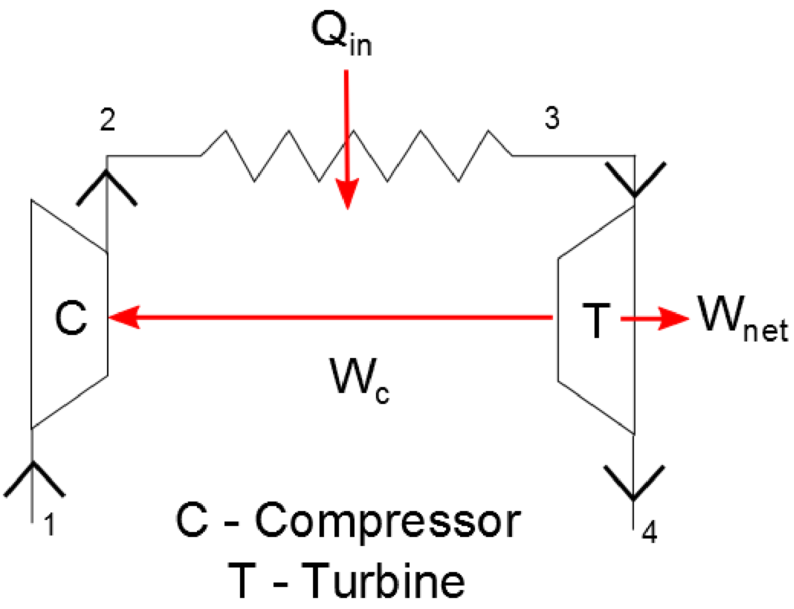

Figure 1.2: Schematic of Joule cycle

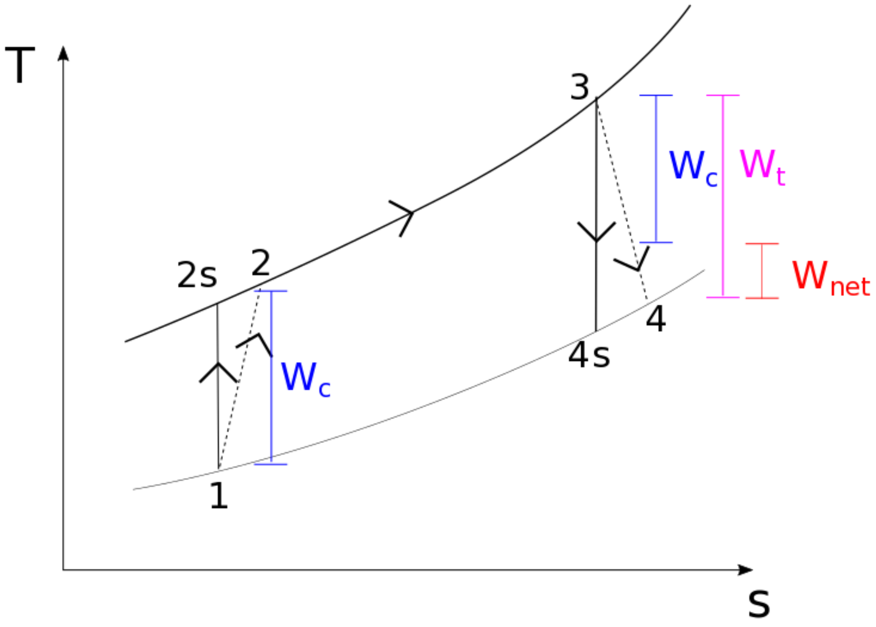

Figure 1.3: T-s diagram of ideal and non-ideal Joule cycle

The net work produced by the cycle is given by equation 1.2. This is as a large proportion of the turbine work produced is required to drive the compressor. In a turbofan engine most of the net work is used to drive the fan at the front of the engine which provides the propulsion.

$$W_{net} = W_t - W_c \tag{1.2}$$

With the isentropic compression and expansion assumptions, the the cycle efficiency can be calculated by equation 1.3.

$$\eta_{cycle} = \frac{W_{net}}{Q_{in}} = \frac{c_p(T_3 - T_{4s}) - c_p(T_{2s} - T_1)}{c_p(T_3 - T_{2s})} = 1 - \frac{T_1}{T_2} = 1 - (\frac{p_1}{p_2})^{\frac{\gamma-1}{\gamma}}) \tag{1.3}$$

In the case of the ideal cycle, the efficiency is dependent purely on the pressure ratio of the compressor and turbine, however when non-idealities are accounted for the efficiency equation contains other terms, seen in equation 1.4.

$$\eta_{cycle} = \frac{W_{net}}{Q_{in}} = \frac{\eta_t \frac{T_3}{T_1}(1 - (\frac{p_1}{p_2})^{\frac{\gamma-1}{\gamma}}) - \frac{1}{\eta_c}((\frac{p_2}{p_1})^{\frac{\gamma-1}{\gamma}}) - 1)}{\frac{T_3}{T_1} - \frac{1}{\eta_c}((\frac{p_2}{p_1})^{\frac{\gamma-1}{\gamma}} - 1) - 1} \tag{1.4}$$

The efficiency is a key metric for a gas turbine, however in civil aircraft the net work output is of equal importance as it governs the size (and therefore weight) of the engine. The net work is given by equation 1.5.

$$W_{net} = \dot{m} c_p T_1 (\eta_t \frac{T_3}{T_1}(1 - (\frac{p_1}{p_2})^{\frac{\gamma-1}{\gamma}}) - \frac{1}{\eta_c}((\frac{p_2}{p_1})^{\frac{\gamma-1}{\gamma}}) - 1)) \tag{1.5}$$

This shows a dependence on the ratio of $\frac{T_3}{T_1}$, the turbine entry temperature (TET) to engine inlet temperature ratio. The engine inlet temperature, T_1 is fixed at the atmospheric temperature and therefore improvements in net engine work can be directly achieved by raising the TET, T_3. The efficiency also increases significantly with a higher TET.

The variation of the efficiency and net work with different pressure and temperature ratios is given in figure 1.4.

An increase in T_3 leads to an additional cooling requirement in the HP turbine stage, which necessitates improvements in blade cooling methods.

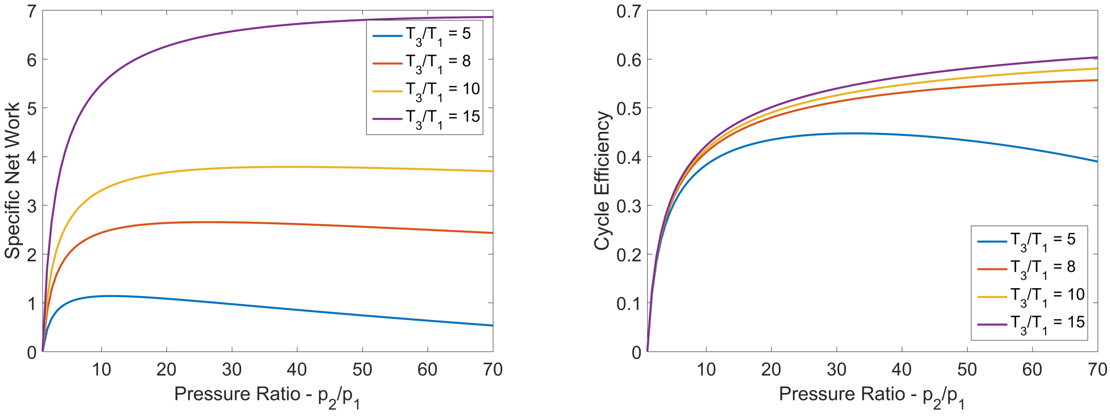

(a) Specific net work at different conditions (b) Cycle efficiency at different conditions

Figure 1.4: Variation of net work and efficiency with pressure and temperature ratio

1.2 Turbine Blade Cooling

With an increased TET the mainstream gas temperature at the HP turbine is also increased. This leads to an increase in the required level of cooling needed to keep the blade metal temperature within acceptable limits for life and fatigue. To remain competitive an engine manufacturer must provide an efficient engine to customers and therefore coolant flow rate must be minimised, as increased coolant usage reduces the work that can be extracted from a given quantity of air that passes through the compressor.

Multiple factors must be considered when designing a turbine blade internal cooling system, which include:

- Maintain sufficient cooling of the metal
- Minimise coolant requirement
- Keep stresses within allowable limits
- Ability to manufacture and inspect blade

This leads to a complex problem in which many different cooling configurations may be feasible and to achieve this, multiple sophisticated cooling methods are required for an HP turbine blade [3].

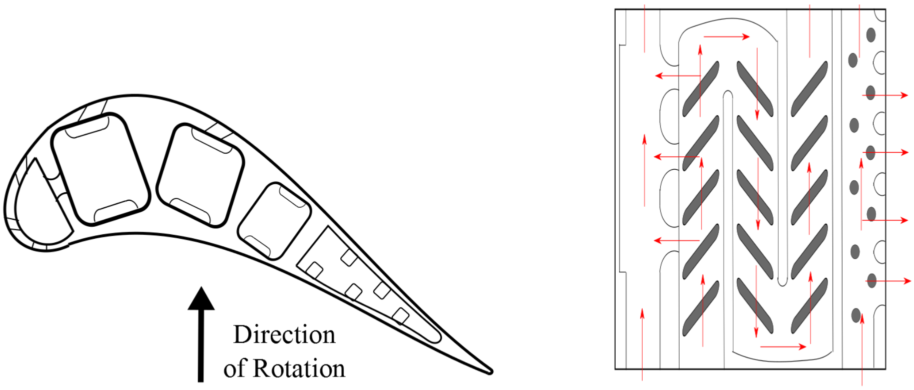

Figure 1.5: Internal cooling types and locations within turbine blade

1.2.1 Internal Cooling

Internal cooling covers multiple methods by which the metal is cooled from relatively cold air bled from the compressor upstream in the engine using passages and other features contained inside the blade. In modern shroudless blades these are fed exclusively from the blade root with the coolant ejected through film holes, trailing edge slots and dust holes. Different internal cooling methods are utilised depending on the location within the blade and include ribbed radial passages and impingement cooling, figure 1.5.

Radial passages are often used in the mid-section of blades where sufficient cooling can be applied to moderate heat loads and they provide this with a low pressure penalty. Impingement cooling is increasingly used in a leading edge configuration where exceptionally high heat loading is found and therefore the greater pressure loss associated with such systems can be tolerated.

1.2.2 Film Cooling

Film cooling utilises cold air from inside the blade, often having been previously used for internal cooling and ejects it through arrays of small holes through the surface of the blade. The design is for coolant to be expelled at such a rate as to not detach from the blade surface and therefore create a thin film of cool air close to the surface of the blade, which acts as a barrier to the hot mainstream flow and maintains the metal at a lower temperature, figure 1.6. A secondary cooling effect is also present as the film cooling channels within the blade shell act as small internal cooling passages, reducing the metal temperature local to them.

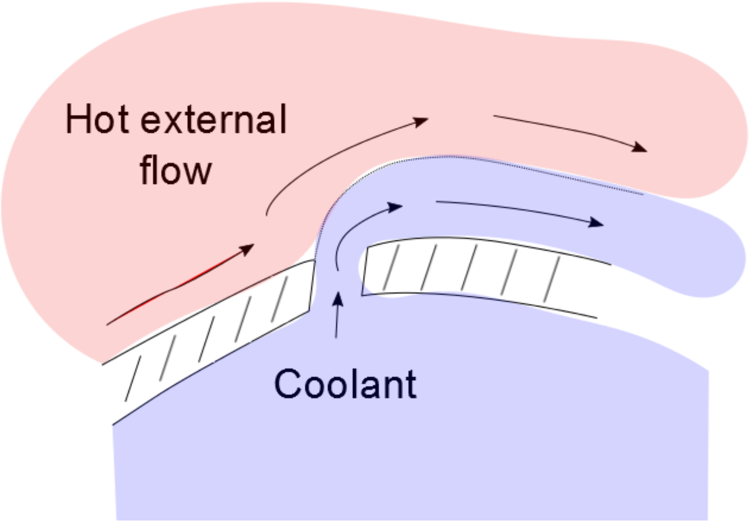

Figure 1.6: Diagram of film cooling

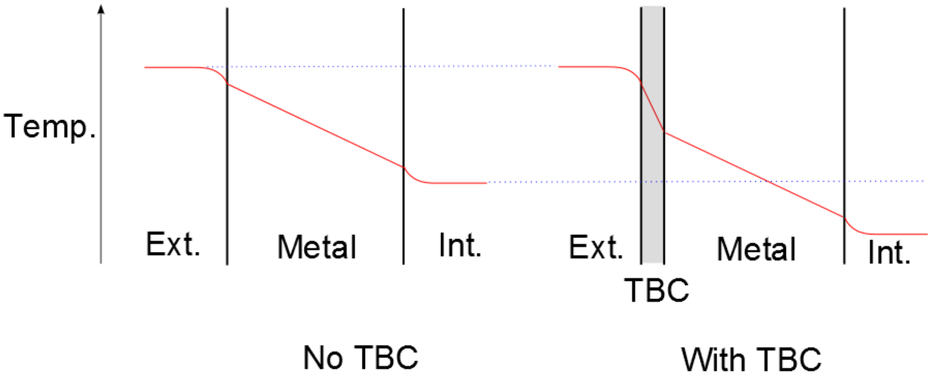

Figure 1.7: Thermal barrier coating and thermal resistance diagram

Many different hole shapes have been investigated in order to improve film effectiveness across a range of blowing ratios, such as fans and conical holes [4,5]. The blowing and pressure ratios across film holes must be carefully maintained in order to avoid both film detachment, if the coolant momentum is too high, or film ingestion where the external flow pressure is too high and hot mainstream air is forced inside the blade, likely causing blade failure.

1.2.3 Thermal Barrier Coatings

Thermal barrier coatings are ceramic coatings that are bonded to the external blade surfaces. These aid blade thermal management by providing an additional thermal resistance against the hot mainstream gas. The process by which this reduces metal temperature is illustrated in figure 1.7.

The coating has a low thermal conductivity and therefore causes a drop in temperature across it, due to the additional thermal resistance. This then reduces the metal temperature in the layer below it, which consequently improves the blade lifespan.

A combination of these different cooling methods are implemented in a modern turbine blade in order to give a manageable metal temperature and therefore acceptable blade life. This thesis focuses on internal cooling within HP turbine blades.

1.3 Turbine Blade Design Process

There are a number of distinct processes in designing a current HP turbine blade, the most critical of which are outlined below:

- Aerodynamic - The external turbine blade shape is fixed by maximising the aerodynamic efficiency of the turbine.
- Cooling - Internal and external cooling designs are added, which must provide adequate cooling whilst fitting inside the previously defined blade shape.
- Mechanical - Stress distributions are then found, based on the output from thermal models, in order to determine whether adequate blade life will be achieved.
- Verification - Thermal paint tests are conducted and the thermal models matched to these to ensure blade life predictions are correct.

There are likely to be a significant number of iterations between the cooling and mechanical processes to reach a satisfactory design. The work undertaken in this thesis researches and offers improved methods for the cooling, mechanical and verification processes required for turbine blade design.

1.4 Thesis Aims

The main aims of this thesis are detailed below.

1. Assess the performance of RANS CFD using common industrial methodologies for the prediction of heat transfer levels in engine realistic ribbed radial passages and leading edge impingement systems under rotating conditions.

2. Perform experimental tests to give full heat transfer distributions on the target surface for a leading edge impingement system, and use these to further validate CFD methodologies.
3. Provide a method by which the effect of heat transfer changes on the stress distributions within a leading edge impingement system can be found, and use this method to offer mechanical improvements to a leading edge impingement system.
4. Improve the current methods by which a thermal match is obtained in the verifcation stage of a turbine blade design through automation of the process.

1.5 Thesis Outline

This thesis investigates internal cooling systems in the form of ribbed, radial passages and leading edge impingement systems. The effects of rotation are closely studied with particular focus on the modelling capabilities of current industrial CFD methodology. This is then extended to conjugate CFD and mechanical analyses to directly assess the effect of heat transfer distributions on blade life. Finally an automated method for thermal matching is developed. The work discussed in this thesis is arranged as follows.

- The effect of rotation on the heat transfer distribution in ribbed radial passages is investigated. An engine representative triple-pass serpentine passage, typical of a gas turbine mid-chord HP blade passage, is simulated using common industrial RANS CFD methodology with the results compared to those from the RHTR, a rotating experimental facility.
- Further study and simulations of radial passages are undertaken in order to understand the salient flow and heat transfer features found, namely the inlet velocity profile and rib orientation relative to the mainstream flow.
- The effect of rotation on the heat transfer distribution in leading edge impingement systems is investigated. As for the radial passages, RANS CFD simulations are compared and validated against experimental data from a rotating heat transfer rig.
- The heat transfer distribution in a leading edge impingement system derived directly from a real engine turbine blade is investigated experimentally under stationary conditions to

provide detailed distributions on the target surface, which are then used for further CFD validation.

- A new method of combined thermal and mechanical analysis is presented and validated for a leading edge impingement system. Conjugate CFD simulations are used to provide a metal temperature distribution for a mechanical analysis. The effect of changes to the geometry and temperature profile to stress levels are investigated.
- The thermal FEA model is used to quantify the effect of HTC alterations on different surfaces within a leading edge impingement system, in terms of both temperature and stress distributions.
- A new method using Gaussian process regression for thermal matching is presented and validated for a leading edge impingement case. A simplified model is matched to a full conjugate CFD solution to test the method's quality and reliability.
- The new thermal matching procedure is applied to a real engine blade and matched to data from a thermal paint test providing real world validation of the methodology.

The work conducted offers improvements to turbine blade cooling methods, mechanical modelling and thermal verification processes. An overall summary of the work presented and the conclusions drawn from it are then given.

Chapter 2

Review of Internal Cooling - Techniques and Methods

Internal cooling is vital in order to keep gas turbine blades within operational temperature limits. In this study two types of internal cooling are investigated, ribbed radial passages and impingement cooling. Ribbed radial passages are used throughout the mid-section of the turbine blade, with varying aspect ratios dependent on their chordal location, while impingement cooling is used in the leading edge of the blade where very high heat loads are present. An overview of these types of cooling and the parameters which affect their performance are given in this chapter. Multiple methods that are, or could be, used in the turbine blade internal cooling design process are then introduced.

2.1 Radial Passages

Radially aligned cooling passages are the most common method for cooling turbine blades in the high pressure (HP) stage of the engine. Initial radial passages were smooth however they have evolved and now contain ribs, and feed film and impingement cooling systems. Ribs and other features, such as dimples and pin fins, are often placed on passage walls closest to the pressure and suction surfaces of the external blade in order to enhance heat transfer when the coolant flow has sufficient pressure margin. Ribs enhance heat transfer in a radial passage by:

- Causing the boundary layer to be disrupted and restarted

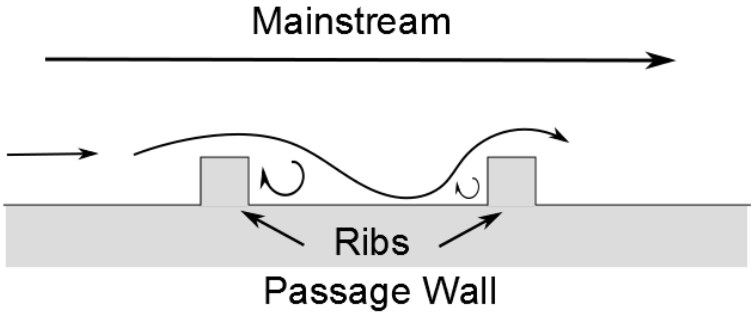

Figure 2.1: Schematic of flow structure around rib - 90^o to mainstream flow

- Increasing fluid mixing, which maintains a high temperature gradient at the passage wall
- Increasing the surface area over which heat transfer can take place

However, there are penalties which come with the increased heat transfer obtained by including ribs. These include:

- Additional pressure loss
- Localised peaks in heat transfer, which can lead to a non-uniform temperature distribution and increased stresses

Therefore ribbed passages must be designed not exclusively to maximise heat transfer levels, but to do so with acceptable pressure losses and without introducing unwanted stress concentrations caused by high metal temperature gradients.

In previous studies many different rib configurations have been investigated, particularly under stationary conditions, to optimise radial passage performance. It has been found that there are many parameters that can greatly influence passage performance, which are detailed in section 2.1.3.

2.1.1 Flow Structure in Ribbed Passages

Early ribbed passages used ribs aligned at 90^o to the mainstream flow. These were positioned on the pressure and suction surfaces of the passages, which are adjacent to the external surfaces of the blade and therefore experienced higher heat loads. The ribs enhanced heat transfer through the disruption of the boundary layer, as illustrated in figure 2.1.

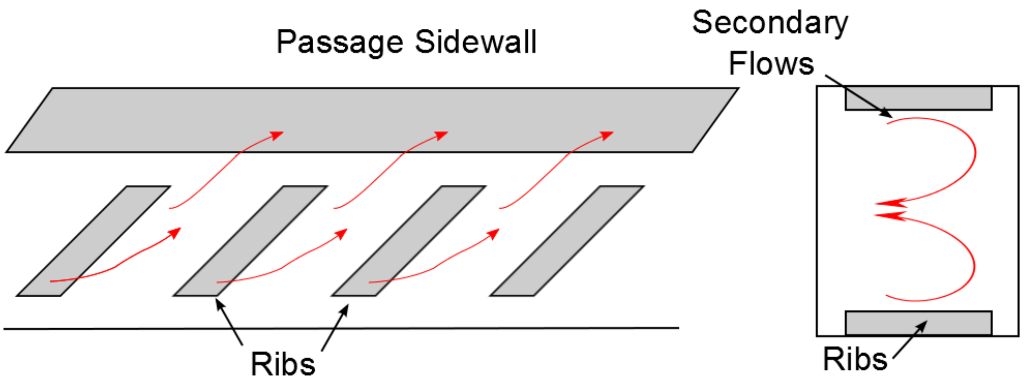

Figure 2.2: Schematic of flow structure around rib - inclined to mainstream flow

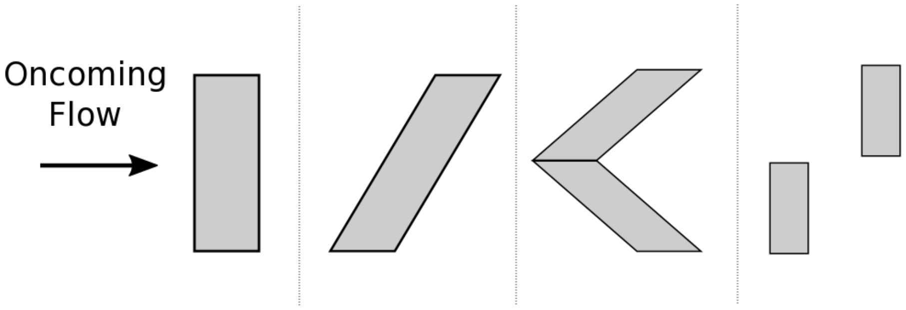

Figure 2.3: Schematic of different rib designs

Further development of ribbed passages led to the use of inclined ribs. The inclined ribs generate a secondary flow structure, which consists of twin pairs of vortices, which promote mixing of the coolant and lead to increased heat transfer performance. Ribs also help to disrupt the unhelpful temperature profile of hotter coolant near to the passage surface. This flow structure is given in figure 2.2.

Further attempts to increase heat transfer performance, and minimise pressure drop, led to more complex rib configurations. Some of these are given by figure 2.3, however are difficult to manufacture in a real engine blade, and often offer little improvement in heat transfer performance.

Other designs include the ’wrapping’ of ribs around the fillets and onto the leading or trailing edge surface of the passage. These have been found to increase heat transfer levels further on certain blade surfaces at the cost of increased pressure losses [6]. They have also proven difficult to model accurately using RANS CFD methodologies under stationary conditions.

Ribs in actual turbine blades are rounded, figure 2.4. This is due to the casting process

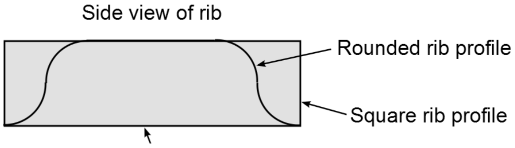

Figure 2.4: Rounded rib illustration

used to manufacture the blades. The small scale (approximately 0.5 mm rib height) leads to the inability to cast sharp edges on this scale, and therefore ribs are invariably rounded.

Modern gas turbine blades therefore often used rounded ribs angled at 45^o to the mainstream flow on the pressure and suction surfaces of the passage. These have been found to offer good heat transfer enhancement at a relatively low pressure drop [6].

2.1.2 Effect of Rotation

Under rotating conditions two additional forces become significant in the Navier Stokes equations, specifically the Coriolis and Buoyancy forces. These have a significant impact on flow structure, and therefore heat transfer, in radial passages with different effects depending on the flow direction within the passage [4,5]. A discussion of the relevant dimensionless groups that must be considered in an experimental simulation is included in [7].

Coriolis forces arise directly from rotation and shift the core flow within the passage. When travelling radially outwards the higher velocity flow away from the walls is pushed towards the pressure surface, while for a radially inward passage the core flow shifts towards the suction surface [8]. Heat transfer is enhanced on the surface towards which the core flow is shifted, with the secondary flows induced by the ribs on that surface strengthened. The pressure and suction surfaces referred to are illustrated in figure. 2.5.

Buoyancy forces are caused by the temperature difference between the core flow and passage walls in the presence of a centrifugal force. In an engine, and in this thesis, the passage walls are at a higher temperature than the coolant within them. Buoyancy forces accelerate the cold, more dense fluid at the passage core away from the centre of rotation, while the hotter, lighter fluid by the passage walls travels relatively towards the centre of rotation. In a radially outward passage the hot fluid at the walls is accelerated in the opposite direction to the core flow, while in a radially inward passage the mainstream flow and heated wall flow are aligned. The buoyancy induced flows interact with those induced by the Coriolis force, leading to a more

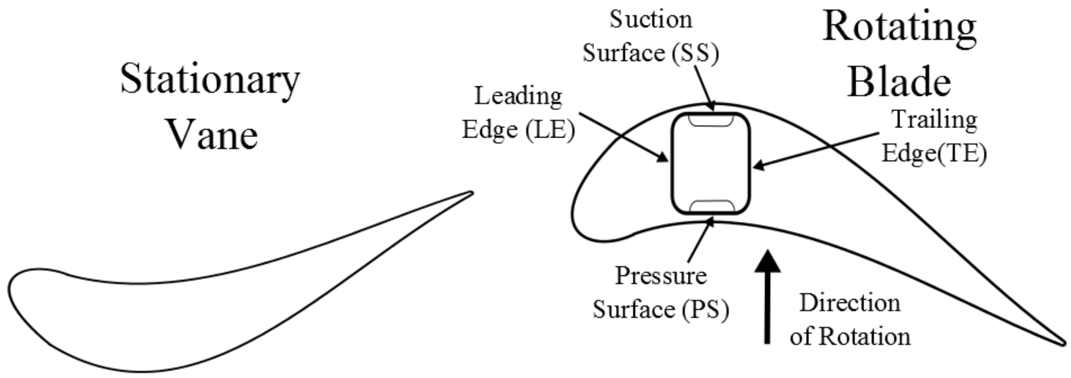

Figure 2.5: Schematic of radial passage within turbine blade

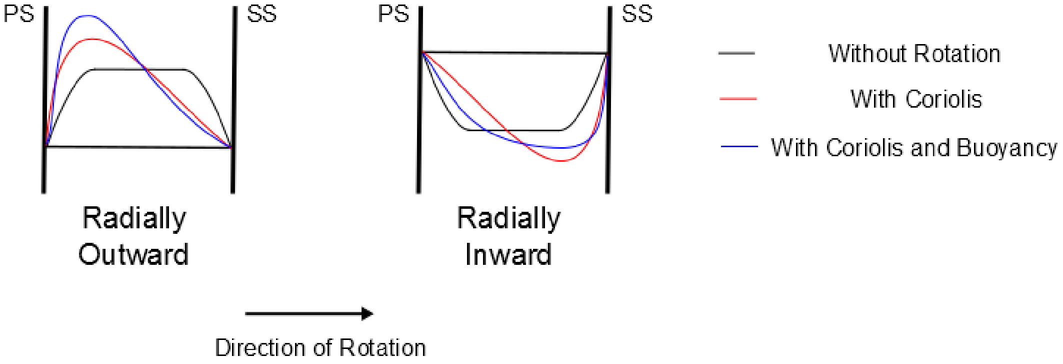

Figure 2.6: Changes in velocity profile with Coriolis and Buoyancy forces (based on figure from [8])

complex heat transfer distribution than for the stationary case.

Studies in the literature which incorporate rotation were initially for smooth radial passages with ribs added in later studies. Often these included sharp edge passages and could only provide results of coarse spatial resolution due to the method used to measure heat transfer. Overall trends for the effects of rotation on heat transfer in radial passages were quantified. The rotating studies were also of shorter passages, with few ribs ($<$10) in each pass for most investigations. In radially outward passages, enhancement was found on the pressure surface, and a reduction on the suction surface, with increasing rotation number. For radially inward passages the converse effect is observed with respect to the pressure and suction surfaces [9–20]. For the studies involving serpentine passages rotation leads to more complex trends, which are attributed to bend and buoyancy effects.

CFD studies have been undertaken for a range of geometries and conditions however they have only been validated against relatively coarsely averaged data, due to the unavailability of high resolution heat transfer data for radial passages [21–23].

2.1.3 Effect of Passage Parameters

There are a number of different parameters of ribbed passages that have an effect of heat transfer, which have been characterised by previous studies. These parameters, and their effects, are detailed below.

Passage Reynolds No.

Heat transfer in radial passages is heavily dependent on Reynolds number. An increase in Reynolds number results from a greater coolant flow which leads to a greater capacity for heat removal. Therefore Nusselt number increases with Reynolds number. Multiple correlations illustrate this with Nusselt number proportional to approximately $Re^{0.6}$ [24, 25].

Aspect Ratio

Aspect ratio is defined as the ratio of passage width to height. A wide range of aspect ratios are present in a blade, from tall aspect ratios in the mid-span to much wider aspect ratios in the trailing edge. [6] gives experimental data for three commonly found aspect ratios of 1:2, 1:3 and

1:4. It is found that the heat transfer performance is best for the 1:2 and 1:3 passages, with the 1:4 passage significantly worse. More extreme ratios than these are found to have much poorer heat transfer characteristics. Narrower channels have been found to give better heat transfer perfomance [26].

Rib Height

An increase in rib height increases the blockage within the passage. This contributes to a much increased pressure loss however also an increase in heat transfer enhancement and therefore can be used for locations with demanding heat transfer conditions where the pressure drop is of less concern [27].

Rib Pitch

If the rib pitch is increased, or decreased reduced heat transfer enhancement is found however with a reduced pressure drop penalty. A short rib pitch increases pressure drop but does not allow the boundary layer to reattach, a region where high heat transfer is found. With a long rib pitch the boundary layer is not disturbed frequently enough and therefore heat transfer levels are reduced compared to the optimum pitch. [28–30] found this to be for $p/e = 10$ for sharp ribs based on total channel area.

Rib Shape

Multiple ribs shapes have been investigated with some improvements found using delta, or v-shaped, ribs. These induce different secondary flow vortices which can offer enhanced heat transfer at a set pressure drop [31–33], however are difficult to manufacture in practice.

Channel Orientation

Channel orientation can influence the heat transfer distribution in rotating radial passages. Studies have shown that if passages are not orientated at 0^o to the axis of rotation but are angled to it then rotational effects are reduced [10, 12].

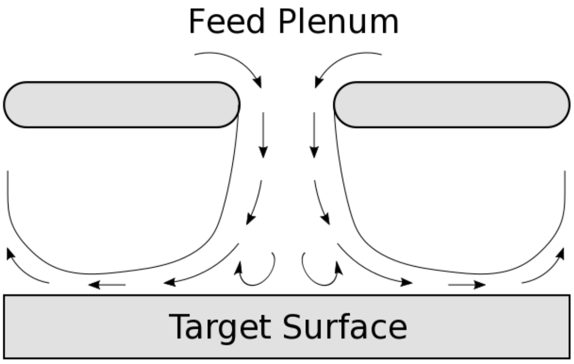

Figure 2.7: Impingement jet flow structure

Serpentine/Multi-Pass Passages

Serpentine, or multi-pass, passages are often used in the mid-section of blades to maximise heat removal into a given coolant flow. The individual passes act as a single pass would, however with an increasing coolant temperature and reduced coolant flow with distance along the passage as film cooling flows are bled off. Inlet conditions and bend effects can also have an influence on the downstream passage heat transfer. Serpentine passes may also be connected in order to improve heat transfer characteristics which incorporate some impingement cooling [34–38].

2.2 Impingement Cooling

Impingement cooling involves the use of jets of coolant that impinge onto a hot surface in order to cool it. It is used in many areas of the gas turbine, such as combustor casings and nozzle guide vanes (NGVs), however in this study it will be considered for the application of the leading edge of a turbine blade where there is a high thermal load and a thick enough blade cross section to accommodate such a system. These systems have also only recently been incorporated into blade designs due to stress considerations that are reduced with the recent introduction of shroudless blades.

2.2.1 Flow Structure in Impingement Systems

There are many distinct regions to the flow structure of a submerged impinging jet which are illustrated in figure 2.7. The jet exits the nozzle with a velocity and temperature profile which are dependent on the upstream conditions and geometry. Initially there is a free jet region, where it is sufficiently far from the target surface to be unaffected by it. In this region the velocity gradient between the jet and surrounding fluid creates shear forces at the edge of the jet which transfer momentum laterally outwards, whilst also increasing the jet mass flow slightly by pulling in additional fluid. The jet loses energy in this process, resulting in a widened velocity profile. In the centre of the jet there remains a core region which is unaffected by processes at the edge of the jet [39–42].

If the jet-target distance is sufficiently long the core region may disappear with a reduced, wider profile velocity distribution across the jet. As the flow approaches the target surface a stagnation region is formed. The axial velocity of the jet is decreased, and the flow is turned and enters a wall jet region. The stagnation region is where the highest heat transfer is found. The wall jet region consists of jet flow that has been turned parallel to the wall, where it runs with a developing boundary layer along the wall. This will develop until it interacts with wall flows formed from adjacent impingement jets, or other flow structures developed by a particular geometry.

2.2.2 Heat Transfer in Impingement Systems

Impingement systems are generally used in situations that require high heat transfer rates. Very high heat transfer coefficients are found under the impinging jets due to the highly turbulent flow and therefore very thin boundary layer. In theory there would be very low heat transfer at the stagnation point, as the fluid would be stationary, however in practice this region is very unstable and the stagnation point is constantly shifting so high heat transfer is found. Moving away from the stagnation region the thin laminar boundary layer leads to high levels of heat transfer, decreasing with distance away from the stagnation point. Depending on jet characteristics there may be a secondary peak where the wall jet transitions to a turbulent boundary layer. The overall high levels of turbulence lead to good fluid mixing which further aids heat transfer [40–43].

2.2.3 Effect of Rotation

Rotation can have a significant effect on impingement heat transfer. Depending on the jet orientation the jet can be deflected from its initial axial direction. This can result in a greater effective jet-target spacing, leading to reduced heat transfer [44]. The jet deflection can also lead to a bias on the heat transfer on one side of a concave target surface. Higher heat transfer would be expected on the pressure surface of such as system in a blade setting under rotation [45–47]. There may also be rotational effects within the feed channel, which can alter entry conditions into the impinging jets.

2.2.4 Effect of Different Parameters

A number of different parameters influence the flow structure and heat transfer in impingement systems, some of which are discussed in this section.

Jet Reynolds Number

Impingement heat transfer is heavily dependent on jet Reynolds number. An increase in Reynolds number for a given geometry will result in increased coolant flow, and therefore heat removal capacity. The increased jet velocity will lead to a thinner boundary layer on the target surface, enhancing the heat transfer. This enhancement is at the cost of an increased coolant and pressure requirement, however [48–56].

Jet to Target Distance

Jet to target distance, normalised to z/D_H, has a significant effect on the flow structure in impingement cooling systems. Low z/D_H jets are highly constrained and are likely to have significant interaction with neighbouring jets. This interaction can cause a reduction in jet momentum and consequently a reduction in heat transfer levels. For high z/D_H the jet velocity is often significantly lessened and therefore lower heat transfer is found. There is therefore an optimum jet height in terms of heat transfer found for each geometry, usually in the range $2 < z/D_H < 8$ [48,49,57–61].

Jet Spacing

When jet spacing is sparse, with fewer jets for a given surface area, heat transfer rates are relatively low as the high heat transfer regions under the impinging jets cover only a small proportion of the target surface. Increased heat transfer is therefore observed as jet density is increased, until the impingement holes become very tightly packed and jet to jet interactions increase in importance. If the jet shear layers for adjacent jets interact the velocity gradients are reduced, lowering turbulence production and therefore heat transfer rates. Adjacent wall jets can also interact leading to the formation of 'fountains', where the wall flows collide and are pushed away from the target surface. This can cause another location stagnation point on the target surface. There is an optimum jet spacing for given flow conditions when jet-jet interactions are minimal however the jet spacing is dense enough to provide high average heat transfer levels [51, 62–64].

Jet Geometry

Many different jet geometries can be used for impingement cooling, with round jets most common, and the upstream geometry also can alter cooling performance. A relatively large upstream plenum can be used to dampen out upstream oscillations and lead to a smooth jet formation, whilst smaller feed geometries can lead to non-uniform feed conditions, and therefore non-uniformity between jets and in jet velocity profiles. Arrays of smaller jets, or slots, can be used to increase the uniformity of the heat transfer distribution where this is desired [65–67]. Inclined jets produce lower heat transfer due to the increased z/D_H [68].

Target Surface Geometry

The target surface geometry has a large influence on the flow structure and heat transfer. Concave target surfaces, such as those in leading edge impingement systems, often inhibit the boundary layer growth in comparison to a flat surface and therefore increase heat transfer away from the stagnation point. Roughness features, such as ribs and pins, may also be used on the target surface. These disturb the wall jet, increase turbulence and provide a larger area over which heat transfer can take place which increases heat transfer rates outside the stagnation region. However in the stagnation region heat transfer rates are decreased due to deceleration of the wall jet [67, 69–73].

Crossflow

Crossflow generally decreases the heat transfer on the target surface on an impingement system. This is because the jets are disturbed and wall boundary layers are thickened. They are also deflected with the stagnation region pushed further downstream and the jet to target distance increased. Extremely high crossflows can cause the jets not to impact on the target surface at all which greatly reduces the heat transfer on this surface and leads to the system behaving much like a film cooling system on the reverse surface and a simple radial passage on the target surface [52, 55, 56, 70, 74–77].

2.3 CFD Modelling for Internal Cooling

CFD (Computational Fluid Dynamics) is very important in turbine blade design as accurate modelling is required in order to understand how a component will operate. Experimental setups can be used for general cases and to provide correlations, however they are too time consuming and expensive to be conducted on all possible geometries. Therefore CFD can be used, in conjuction with validation experiments, to provide full fluid modelling of cooling systems.

Multiple different CFD formulations are now available. The most commonly used in industry is the Reynolds-Averaged Navier Stokes (RANS) methodology due to the relatively accurate solutions that can be obtained for lower computational cost than other modelling techniques. This and alternative formulations are discussed in the following section.

2.3.1 RANS Formulation

In order to solve three dimensional fluid flow six dependent variables must be found for each location in the fluid, for each point in time.

These variables are $p, \rho, T, u, v, w,$ at (x, y, z, t). Therefore six equations are required to solve for these variables. The first three are provided from mass conservation (continuity), energy conservation and an equation of state relating the fluid density to its pressure and temperature, often the ideal gas equation. The final three arise from the conservation of momentum in three dimensions, and for viscous fluids are given by the Navier-Stokes equations [78].

For an incompressible fluid, and in the absence of any external body forces, these are given in vector form as equation 2.1

$$\rho(\frac{\partial \mathbf{u}}{\partial t}) + \rho(\mathbf{u}\nabla)\mathbf{u} = -\nabla p + \mu \nabla^2 \mathbf{u} \tag{2.1}$$

The terms on the left side are the inertia terms, given by the unsteady and convective acceleration, and those on the right represent the pressure gradient and viscous diffusion. These partial differential equations are non-linear, due to the convective acceleration term, and are therefore very difficult to solve with a limited number of exact solutions.

The Reynolds averaging procedure decomposes these equations for a turbulent flow into the ensemble average and fluctuating parts, U and u' and can be written as follows in equation 2.2, for the x direction, with similar equations for the y and z directions.

$$\begin{aligned}\rho(\frac{\partial U}{\partial T} + \frac{\partial (UU)}{\partial x} + \frac{\partial (UV)}{\partial y} + \frac{\partial (UW)}{\partial z} = -\frac{\partial p}{\partial x} + \mu(\frac{\partial^2 U}{\partial x^2} + \frac{\partial^2 U}{\partial y^2} + \frac{\partial^2 U}{\partial z^2})\\ -\frac{\partial}{\partial x}\rho\overline{u'^2} - \frac{\partial}{\partial y}\rho\overline{u'v'} - \frac{\partial}{\partial z}\rho\overline{u'w'}\end{aligned} \tag{2.2}$$

It can be seen that new terms have been created, the Reynolds stresses $\overline{u_i u_j}$, however the equations apart from these now are the same as those for a laminar flow.

The addition of these new terms requires additional equations in order for the fluid flow to be found, the turbulence closure problem. Therefore turbulence modelling is required - which usually relate the Reynolds stresses to the mean flow - in order for the solution to be obtained.

2.3.2 Turbulence Modelling

Multiple different models of varying complexity have been proposed and used for predicting flows in different situations. These can be purely empirical or have a physical basis with a number of empirical constants obtained from particular experimental setups. Higher-order models can provide improved results in certain situations, however these are at the expense of additional computational cost.

One Equation Models

The Spalart-Allmaras model is a simple one-equation model which solves a transport equation for a turbulent eddy viscosity variable. These equation and constants were determined empirically from an experimental setup [79].

Two Equation Models

Two-equation models are all based on the Boussinesq approximation, that the Reynolds stress tensor is proportional to the mean strain rate tensor. These are related by a scalar property, the eddy viscosity. This eddy viscosity is computed from two transport variables, hence why these are categorised as two equation models. The transport variables used are k, the turbulent kinetic energy and either ε, the turbulent dissipation or ω, the specific dissipation. k determines the energy in the turbulence while the second variable controls the length scale of the turbulence.

The k-ε model separately models the turbulent kinetic energy and dissipation through equations that are direct functions of the velocity gradients and are based on expected trends, with experimentally determined constants used to fully close the equations [80].

The k-ε realizable model is an extension of this where ‘realizable’ limits have been placed on the Reynolds stresses, to prevent non-physical negative normal, and excessively high shear, Reynolds stresses.

The k-ω model solves for the turbulent kinetic energy and specific dissipation rate. Unlike the previous models the dissipation is calculated from an experimentally determined conservation equation rather than directly from the velocity field [81].

k-ω SST is a combination of the k-ε and k-ω models, where the k-ω formulation is used in the boundary regions while in free stream regions it switches to a k-ε formulation [82].

Two equation models all assume isotropic Reynolds stresses which can impact on their accuracy in some flow regimes.

Higher Order Models

Reynolds stress models are significantly more complex as the Reynolds stresses are directly computed, and there are no eddy viscosity assumptions. The Reynolds stresses are computed individually from a number of transport equations before being used directly to close the RANS equations. The $v^2 - f$ model is based on the k-ε model however with two additional equations that are used to incorporate a level of turbulence anisotropy into the model.

2.3.3 LES and other Methods

With the increase in available processing power, more complex methods which require greater computational time have become more feasible. These include LES (Large Eddy Simulation) and DNS (Direct Numerical Simulation).

LES involves the direct simulation of the large eddies present in flows whilst modelling those at smaller scales. The full equations are solved down to the given grid spacing, with sub-grid models used to formulate turbulent activity at scales below this. In some situations this methodology has given very promising results. However in order to be accurate a high resolution grid is required, as well as small time steps when turbulent flows are involved. Therefore it still demands a high computational cost and is yet to be of significant practical application to internal cooling design despite advances in a pure research environment.

DNS is the direct numerical simulation of the Navier-Stokes equations, and is the most physically exact of the computational methods. The full Navier-Stokes, continuity and energy equation are solved for discrete units of time and space. As these are fully solved an extremely fine grid is required to resolve the very small turbulent flow properties as they have very small length scales. Therefore the DNS calculations have a very high computational cost, and are currently limited to simplified academic situations and as yet have no practical use in turbine internal cooling.

2.3.4 CFD for Heat Transfer

CFD methodologies were intially developed for aerodynamic calculations, and for these they obtain very good results. However they are in general less accurate when used for heat transfer predictions. This is because of the difficulty in accurately modelling the boundary layer flows on which convective heat transfer is highly dependent. In order to model the boundary layer effectively, a fine mesh resolution near to the wall is required. This is characterised by the y^+ value, equation 2.3. As a rule of thumb $y^+ < 1$ should be ensured for calculations involving heat transfer.

$$y^+ = \frac{\sqrt{\frac{\tau_w}{\rho}}y}{\nu} \tag{2.3}$$

RANS Turbulence Modelling for Internal Flows

A number of the turbulence models available for RANS modelling, as introduced in section 2.3.2, have been used for modelling of internal cooling flows. These include both radial passages and impingement geometries. The realizable k-ε and k-ω models are most widely used, however the Spalart-Allmaras and Reynolds stress models have also been utilised [21–23, 50, 83–85]. The Spalart Allmaras model is found not to perform satisfactorily for heat transfer predictions. The two equation models perform reasonably well, matching overall levels within 20% of experimental data, and are capable of predicting the main features in the heat transfer distributions. In cases where the two-equation models do not accurately predict heat transfer levels, such as in [84], the Reynolds stress models are found to offer no improvement over the two equation models.

2.3.5 This Research

This research uses RANS simulations with a variety of different turbulence models. This is due to the current high computational cost of the more complex CFD methods being prohibitive to gas turbine internal cooling design, due to the highly complex geometries and large domains that must be simulated.

2.4 Experimental Methods

Despite the advances in numerical methods, experimental data is still required to validate the modelling of new cooling systems and conditions.

Many different experimental methods are available to obtain heat transfer measurements in an experimental setting. These provide different levels of spatial resolution and accuracy however are of varying levels of complexity to implement. They are also each suited to different applications due the varying material and target surface viewing requirements.

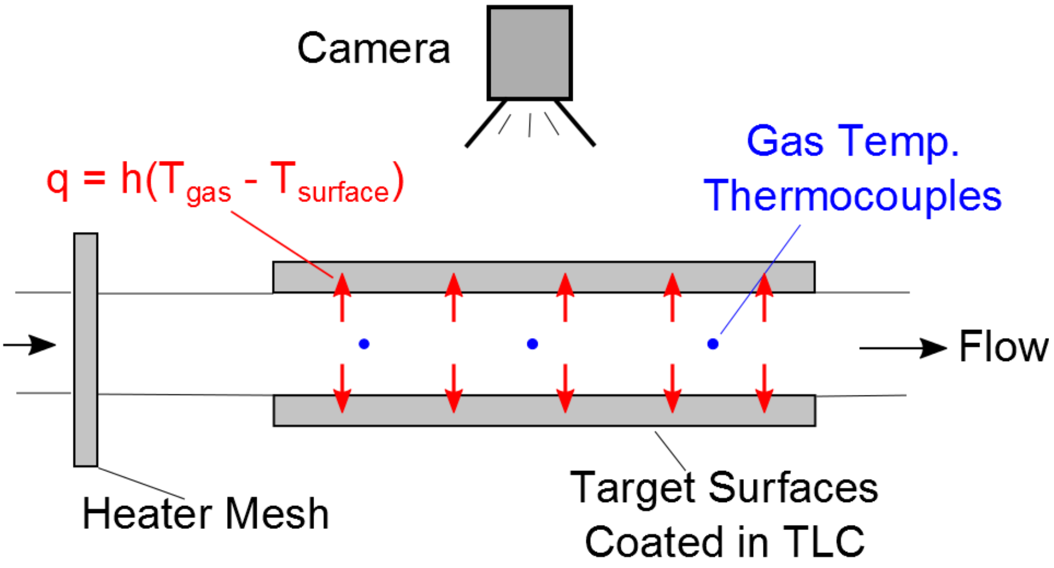

Figure 2.8: Schematic diagram of transient heat transfer experiment

2.4.1 Transient Liquid Crystal Method

The transient liquid crystal method has been used in a multitude of different experiments to provide fully spatially resolved heat transfer data [86, 87]. A schematic diagram of the experimental setup is given in figure 2.8. The experimental setup requires a heat (or cooling) source in order to provide a difference in the gas and surface temperatures, and optical access for a video camera to view the colour change of the crystals during the test [88]. Thermocouples are needed to provide a gas reference temperature and a surface temperature for calibration.

The method relies on a solution of the one-dimensional conduction equation to a step change in external gas temperature, illustrated in figure 2.9. The one dimensional heat equation has an analytical solution to this, equation 2.4, from which a heat transfer coefficient can be calculated. This is done for each pixel to give a fully-resolved heat transfer map.

$$\frac{T_{surface}-T_{initial}}{T_{gas}-T_{inital}} = 1 - e^{(\frac{h\sqrt{t}}{\sqrt{\rho ck}})^2} erfc(\frac{h\sqrt{t}}{\sqrt{\rho ck}}) \tag{2.4}$$

Thermochromic Liquid Crystals

Thermochromic liquid crystals change colour in reaction to a change in temperature. This response is due to the twisting of the crystals in their optically active phase which changes the wavelength of the reflected light.

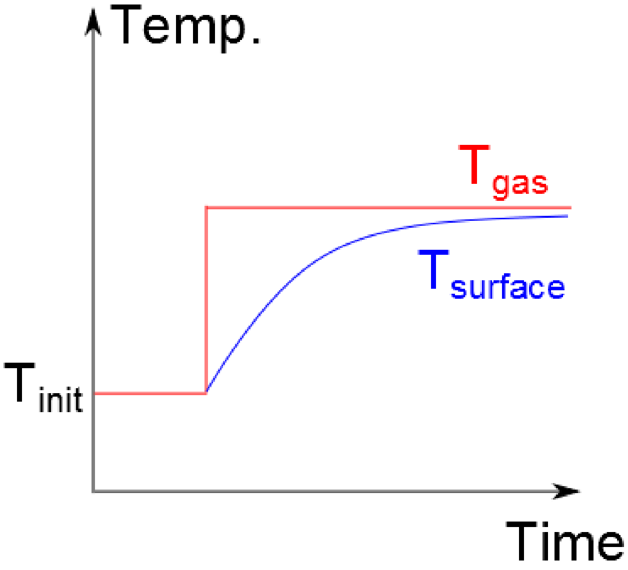

Figure 2.9: Gas and surface temperature response in TLC experiment

The crystals used are encapsulated in gelatine and mixed with a binder to be applied to the relevant surface to form a thin 20-30μm coating. A black coating is then applied to eliminate any transmitted light and provide a contrasting background. The crystals have a very weak pressure dependency and a slight viewing angle dependency which are easily made insignificant. Narrow band crystals are used in transient experiments to give sharp peaks for data processing.

Multiple crystals, where each is active at a different temperature range, can often be used to improve experimental results. The different crystals will have varying activation times and therefore decrease errors where a large range of HTC values are present, and can also improve the fitting procedure in the data post-processing.

Experimental Setup Requirements

There are multiple aspects which must be considered when setting up a transient liquid crystal experiment.

Scaling: Rigs must be scaled so that the required Reynolds numbers can be achieved at near atmospheric pressure and density, which leads to large scale rigs. This has the advantages of easier instrumentation and camera setup, however with increased flow and heater power requirement costs are generally increased.

Test Duration: Tests must be run for long enough to ensure enough crystals are activated to obtain sufficient information on the thermal transient in all locations to keep HTC uncertainty levels low. However the test duration must be below the maximum permitted given the model wall thickness and short enough in order that lateral conductions errors will remain small.

Wall Thickness: The wall thickness must be sufficiently thick for the thermal semi-infinite assumption used in the post-processing to be valid. This gives a maximum test time of $t_{max} = \frac{\rho c_p}{k}(\frac{x}{4})^2$, which must be halved if the wall is heated from both sides [88].

Lateral Conduction: If there are high lateral gradients in HTC, or the surface is highly three-dimensional, there is likely to be lateral conduction within the wall. These must therefore be corrected using a method such as [89].

Material Choice: Perspex is often used to construct the test section of transient liquid crystal experiments as it is transparent and thermally insulating with known thermal properties. Other materials such as polycarbonate and stereo lithography resins may also be used.

Mesh Heater: A step change in temperature must be applied to start the test. This is generally achieved using a mesh heater, described in detail in [90].

Instrumentation: The main instrumentation requirements consist of a video camera to view the relevant surfaces, and thermocouples. The thermocouples must provide surface temperature data for calibration, as well as gas temperatures to be used for the driving gas temperature in HTC calculation.

Calibration: There is a key requirement to calibrate the colour behaviour of the liquid crystals to a particular temperature. This is often done in-situ through the use of a surface thermocouple that is visible from the camera. This allows the exact crystal mix on the experiment to be calibrated and removes any viewing angle issues.

Data Processing

The data processing is undertaken by comparing temperature data from the transient tests to analytical solutions of the Fourier equation.

The simplest method is done by relating the peak value for the green intensity for a given pixel in time to the calibration temperature. This gives an activation time and surface temperature which can be used in the the relevant analytical solution to calculate an HTC value. The analytical solution is determined from the gas temperature thermocouple measurements.

The gas temperature can often be closely approximated as a series of arbitrary steps, equation 2.5, for which the solution may be written as in equation 2.6.

$$T_{gas} = T_{initial} + \sum_{1}^{n} (T_i - T_{i-1}) u(t - t_i), \quad T_0 = T_{initial} \tag{2.5}$$

$$T_{surface} = T_{initial} + \sum_{1}^{n} (T_i - T_{i-1}) (1 - e^{\frac{h^2 (t-t_i)}{\rho c k}} erfc(\frac{h\sqrt{t - t_i}}{\sqrt{\rho c k}})) \tag{2.6}$$

With a given calibration temperature and crystal activation time the solution is a function of heat transfer coefficient only. Therefore a minimisation technique can be employed to obtain an HTC for each pixel location.

An alternative to peak finding can be used where the full intensity signal from the entire test time is used to obtain a best fit of the temperature events from the different crystals. This requires the crystal intensity with temperature calibration, the driving gas temperature history and a digitised version of each pixel intensity history. A look up table is generated containing ideal intensity histories for the gas temperature history for the range of possible HTC values. This is then compared to the actual intensity data with an HTC value for each pixel selected in order to minimise error. This method provides more robust and reliable outcomes than the individual peak finding method.

2.4.2 Energy Balance Techniques

Energy balance techniques are relatively simple to implement however only provide coarse spatial resolution of data in heat transfer tests. These have been employed in multiple situations for the determination of heat transfer in radial and impingement systems. In their simplest form, a uniform heat flux is applied to the surface of interest, often using a resistive heating element. Then thermocouple readings of the surface and gas temperature, combined with knowledge of the thermal losses, can be used to extract a heat transfer coefficient.

This technique can be easy to implement and provide accurate heat transfer measurements, however is only able to give coarsely averaged data. This creates difficulties when trying to investigate detailed features of a heat transfer distribution or comprehensively validate CFD simulations.

2.4.3 IR Thermography

Infra-red (IR) thermography is increasing in use as the cost of high resolution IR cameras has decreased. These can provide a full temperature distribution on a surface, and therefore fully spatially resolved heat transfer. With knowledge of the gas temperature and the surface heat flux, often applied using resistive heating, the full IR camera temperature distribution can be used to calculate an HTC distribution [91, 92]. Care must be taken to account for reflections and the emissivity of the material however the process is well established for external surfaces. For internal surfaces, however, the process is much more complex. A viewing window, which is delicate and expensive, is needed for internal flow and it can be very difficult to set up the camera positioning for complex geometries.

2.4.4 This Research

The experimental data used in this thesis has all been gained using the transient liquid crystal technique. Fully-spatially resolved heat transfer distributions are required for full understanding of a cooling system and for complete CFD validation. Therefore only the TLC method or IR thermography would be suitable. However, IR thermography is far better suited to external surfaces as there are significant complications when it is used for internal surfaces, such as the requirement for a viewing window. As this thesis concentrates on internal cooling the transient liquid crystal method is far more suitable and therefore was used to obtain all experimental heat transfer data in this thesis.

2.5 Stress Analysis and FEA

Finite element analysis is a crucial part of turbine blade design as it provides an estimate of the stresses, and therefore expected life, of the blade. This section details the basics of stress analysis and the finite element method, and the main mechanisms that can cause blade failure - fatigue, creep and fracture.

2.5.1 Solid Mechanics Theory

The following section describes basic linear elastic stress analysis, which forms the basis of a finite element analysis [93, 94].

Stress-Strain Relations

In order to solve for the stress distribution within a mechanical system three sets of equations are required. These are equilibrium, compatibility of strains and stress-strain relation equations.

The equilibrium equations are found simply from the equilibrium of stresses on a material element, and in cartesian co-ordinates are given by equations 2.7 for the x-direction, and similarly for y, z.

$$\frac{\partial \sigma_{xx}}{\partial x} + \frac{\partial \tau_{xy}}{\partial y} + \frac{\partial \tau_{xz}}{\partial z} + F_x = 0 \tag{2.7}$$

The different strains on an element all arise from the same displacements, and therefore it is possible to express these in terms of each other in the compatibility of strains equations. These are given for the x-direction in cartesian co-ordinates in equation 2.8 and 2.9, with similar equations also for y, z giving 6 compatibility equations in total.

$$\frac{\partial^2 \varepsilon_{xx}}{\partial y^2} + \frac{\partial^2 \varepsilon_{yy}}{\partial x^2} = \frac{\partial^2 \gamma_{xy}}{\partial x \partial y} \tag{2.8}$$

$$2\frac{\partial^2 \varepsilon_{xx}}{\partial y \partial z} = \frac{\partial}{\partial x}(-\frac{\partial \gamma_{xy}}{\partial x} + \frac{\partial \gamma_{xy}}{\partial y} + \frac{\partial \gamma_{xy}}{\partial z}) \tag{2.9}$$

The final equations relate the stress to strains, and for linear elasticity these are Hooke's law, as shown in equation 2.10

$$\varepsilon_{xx} = \frac{1}{E}(\sigma_{xx} - \nu(\sigma_{yy} + \sigma zz)) \quad etc. \qquad\qquad \tau_{xy} = G\gamma_{xy} \quad etc. \tag{2.10}$$

These equations in conjunction with appropriate boundary conditions can be solved together to give the full stress and strain distribution in a material.

Thermal strains are also presented when there are temperature differences within the material which cause non-uniform expansion. These thermal strains have to be added into the above equations, and the relationship for uniaxial strain is given in equation 2.11.

$$\varepsilon_{thermal} = \alpha \Delta T \tag{2.11}$$

These equations can be directly solved for simple situations, however for more complex arrangements other methods such as finite element analysis are far more appropriate.

In components where there are geometric discontinuities, such as holes in the web of an impingement system, local stress levels can be increased significantly. These are characterised by the stress concentration factor in equation 2.12.

$$K_t = \frac{max.\ boundary\ stress\ at\ discontinuity}{average\ stress\ through\ body\ cross\ section} \tag{2.12}$$

Stress concentration factors vary in the region 2-3 for circular holes in an axially loaded strip.

2.5.2 Finite Element Method

The finite element method is an effective method for the analysis of stress in a solid continuum. The solid is split into a mesh of three-dimensional elements which are connected at their nodes. For a given element's shape there is a stiffness matrix which relates the forces on that element to its nodal displacements. The external loads on the system are replaced by an equivalent set of loads at element nodes and the resulting matrix equations is then solved to obtain the nodal displacements throughout the solid domain. These nodal displacements are then used to calculate the strain, and subsequently stress, giving full distributions for the entire material. In order for successful modelling a suitably high mesh density is required in order for sufficient fidelity in the solution and for minimal stress discontinuities between elements.

2.5.3 Factors in Blade Life

There are multiple different potential factors that must be considered when calculating blade life, the three most crucial of which are fracture, creep and fatigue. The basic theory behind these and the features that they are dependent on are introduced in this section.

Fracture

Fracture is the process of the initiation and propagation of cracks within a material until the extent of the crack leads to the component being unable to sustain the applied loading [93].

In linear elastic fracture mechanics there are three modes of cracking - opening, shearing and tearing which are labelled with subscripts I, II and III respectively. Each of these modes has a corresponding stress intensity factor, K_I, K_{II} or K_{III}, which represents the elastic stress distribution near the crack tip and is dependent on the applied stress, crack size and geometry. Unstable crack growth, which would lead to blade failure, occurs when these factors reach a critical value, K_C, which can be determined by material tests.

In practice there is a region of plastic deformation at the tip of the crack which must be accounted for, which can be done using an equivalent crack length which also includes the plastic zone radius.

Fatigue

Fatigue can cause failure in a mechanical component despite nominal stresses well below the material strength and originates from cyclical loading of a component. Fatigue failure is due to microscopic cracks or material defects which gradually grow due to the stress fluctuations until complete fracture. Fatigue is charactised by the number of cycles until failure and applied cyclic stress, which are often represented on an $S-N$ curve. Fatigue can be broadly split into high and low cycle fatigue, the former relating to a low-stress, high number of cycle failure and the latter a high-stress, low number of cycle failure. Fatigue is also statistical in nature due to the random distribution of internal defects within a material, which leads to varying life spans for different specimens to which the same loading is applied, and therefore multiple $S-N$ curves can be required each with a different probability of failure.

Creep

Creep occurs in loaded components operating at high temperatures, nominally at $T > 0.3T_m$, such as gas turbine blades. It is where increasing strain is observed with time under constant applied load. Over a long period of time even with low creep rates the creep strains can become quite large and therefore cause failures, such as the impact of a blade tip on the turbine casing.

2.5.4 This Research

Current blade design has segregated thermal and mechanical design processes where several iterations of a cooling design are required in order to obtain satisfactory blade life. In this thesis these will be integrated, with the effects of alterations in thermal models on the stress distribution directly assessed.

2.6 Machine Learning

Machine learning is a field of computer science that studies induction and other algorithms that are said to 'learn'. This is meant as the ability for it to model and make predictions from data without being explicitly programmed with the model.

Tasks performed in machine learning can be roughly characterised into the three following categories

- Supervised learning - A computer is given a set of training data containing multiple inputs and their desired outputs. Its goal is then to create a model to map the inputs to their outputs and hence provide predictions for new inputs.
- Unsupervised learning - In the unsupervised the computer is supplied training data with no designated output, or label. The goal is then to either find hidden patterns or features within the data
- Reinforcement learning - The computer program can dynamically interact with an environment, and must try to achieve a certain goal without explicitly being told whether it is close to the target goal.

In this setting only supervised learning will be considered as there will be no dynamic interaction with the environment and there is always a particular desired output to be obtained from the created model.

2.6.1 Methods for Supervised Learning

There are multiple approaches that can be used in order to undertake supervised learning. Some of those that are commonly used are described briefly below however many other methods can also be used, these are detailed in [95].

In supervised learning there are two main categories of machine learning tasks. These are classification, where inputs are divided into two or more classes and the model must predict the discrete class in which to place a new input, and regression where the output of the model is continuous.

Support Vector Machines

The support vector method is a simple technique of classification in which the inputs are divided into two categories by a linear boundary. This technique has since been extended to be used for regression problems where the goal is to find a function that fits the data with a maximum error whilst remaining as flat as possible.

Decision Tree Learning

Decision tree learning is a widely used method for classification. An input is classified from the root to the leaf node, which provides the classification of the input. Each node tests an attribute with each branch providing a possible value for it. These methods are robust and simple and can also be extended to be used for regression if required.

Random Forests

Random forests are an extension of decision trees. In this random forest case there are many different decision trees which are each fitted to a subset of the training data. The output for a given new input is then taken as the mode (for classification) or mean (for regression) of the outputs of each decision tree.

Artificial Neural Networks

Artificial neural networks are loosely based on biological learning systems, in that they consist of a large number of interconnected nodes. In a neural network these nodes each output a given value based on a weighted sum of their inputs, with the top layer providing the actual outputs for the task prediction. These can be trained by a number of algorithms and exhibit many structures, more details of which are given in [95].

Gaussian Process Regression

Gaussian Process Regression is a machine learning process that forms a model through two functions of the inputs - a basis function and covariance functions which represent a Gaussian process [96]. The model is formed using a weighted sum of the covariance functions evaluated at each training data location. These can provide very detailed modelling of an output for many different input parameters.

These models are each applicable to difference machine learning problems, and vary in their success in modelling different situations and therefore the method of machine learning used for a given task must be carefully chosen. For this application in turbine blade cooling the method must be able to accurately model the data and also maintain a representation to the underlying physical processes in order to be satisfactory to be used in the design process.

2.6.2 Applications

Machine learning is currently used for a large and expanding number of applications. These include computer vision and image recognition, fraud detection, marketing, finance and many biomedical applications. The expanded used of the techniques is largely down to an increase in computing power which allows for the processing (and in some cases generation) of the training data that is required for the programs to operate. With this increase in computing power there has been a significant reduction in the time taken for analyses for turbine blades to be run. Therefore training data can be obtained at a reasonable cost, which allows for machine learning methods to be used in this field.

The two cooling configurations and multiple modelling methodologies introduced in this chapter were investigated throughout the work conducted for this thesis.

Chapter 3

Radial Passages

This chapter investigates the effects of rotation on the heat transfer in a triple-pass ribbed serpentine passage and the ability of commonly used industrial RANS CFD methodology to predict these.

Experimental data obtained from a rotating heat transfer facility under the ERICKA programme is used to validate industrial CFD methodology, with the effect of rotation and specific geometry also evaluated. The experimental data used in this chapter was collected by researchers at Rolls Royce, another partner in the ERICKA programme. The full experimental data is presented by them in [97].

3.1 Experimental Facility

The Rotating Heat Transfer Rig (RHTR) is capable of matching Reynolds, Rotation and Buoyancy numbers found within internal cooling geometries in HP turbine blades and is described in full in [7]. A photo of the rig is given in figure 3.1, and a schematic diagram is shown in figure 3.2.

Two perspex test sections are contained within titanium cylinders at the end of each arm. The transient liquid crystal method is used to provide spatially resolved heat transfer maps of a section of both the PS and SS of each passage. Details of this method are given in section 2.4.1. Each side is viewed using separate CCD cameras which are embedded within the model along with LED lighting. Cold air (at approximately 210K) is fed along the arms into the models, which are initially at room temperature, to provide the temperature difference required for the

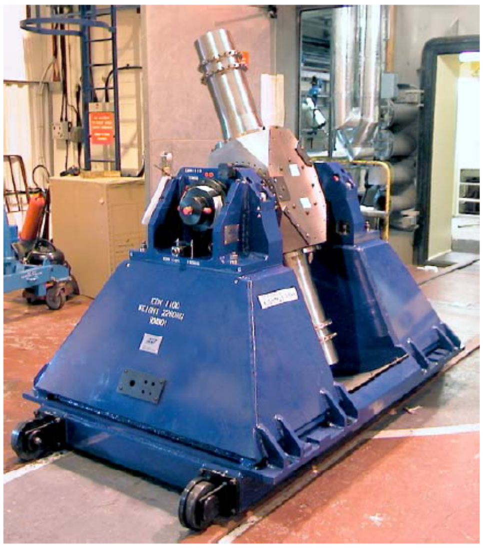

Figure 3.1: Photo of the Rolls-Royce rotating heat transfer rig [97]

measurements. The cold air is produced by a heat exchanger linked to a liquid nitrogen supply.

The temperature of the air fed into the rig is less than ambient in order to obtain a temperature ratio which gives an engine realistic buoyancy number. The air temperature change is not an instantaneous drop and therefore average values taken over the test time were used in the simulations.

Instrumentation within the rig consists of a number of pressure taps and thermocouples, figure 3.3. These provide details as to the flow structure within the rig, and temperature data from which to calculate heat transfer coefficients, and Nusselt numbers. Thermocouple readings are taken on the centreline at two locations within each pass of the serpentine passage. This data is then interpolated to provide a gas temperature from which to calculate heat transfer coefficients.

The data is fed out through the test section arm and across a slip ring assembly, and then collected for post-processing on a computer in the control room.

Results are processed using a bespoke in-house code to convert each pixel activation time into an HTC value, based on centreline temperature measurements obtained from thermocouples, which are later converted to Nusselt number using equation 3.2. Gas properties for this calculation are evaluated using temperature and pressure measurements made at relevant locations for each pass.

These were then fed into a Matlab script to remove distortion from the camera lens and present the data in a manner which was directly comparable to the CFD results. Example initial

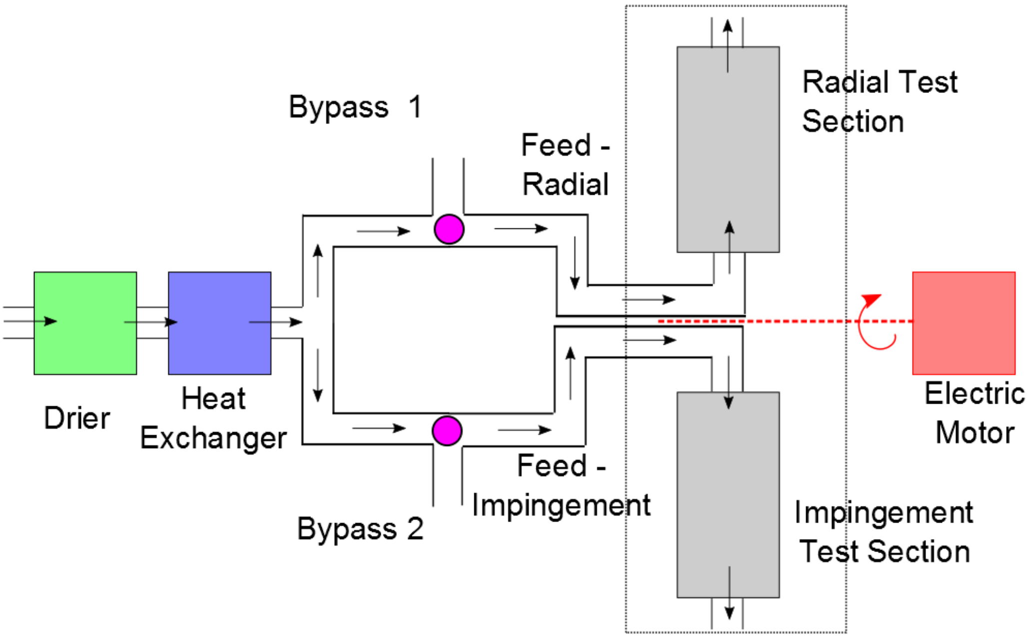

Figure 3.2: RHTR schematic layout

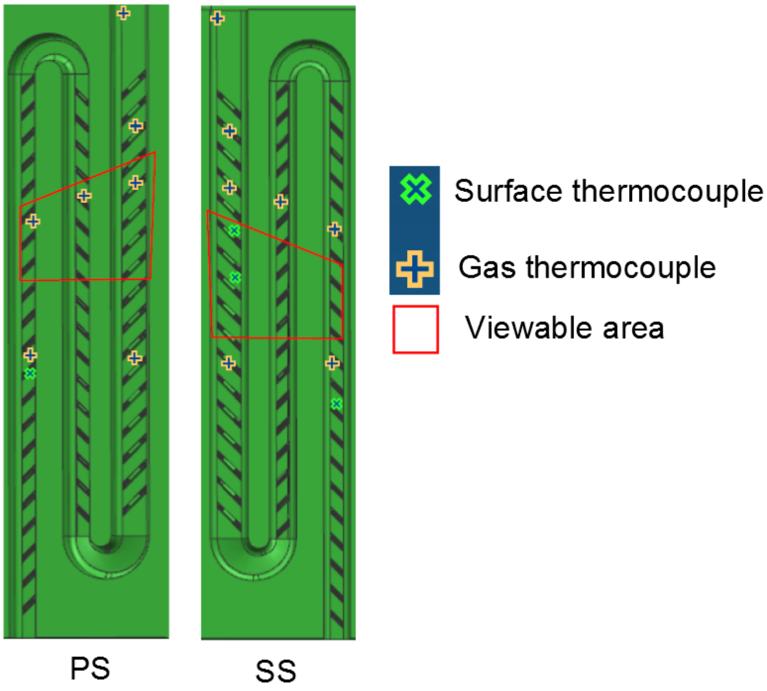

Figure 3.3: RHTR instrumentation layout [97]

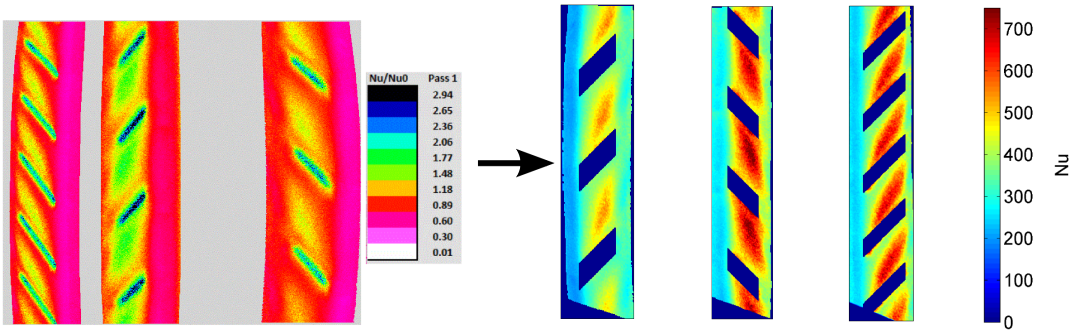

Figure 3.4: Manipulation of experimental heat transfer distributions

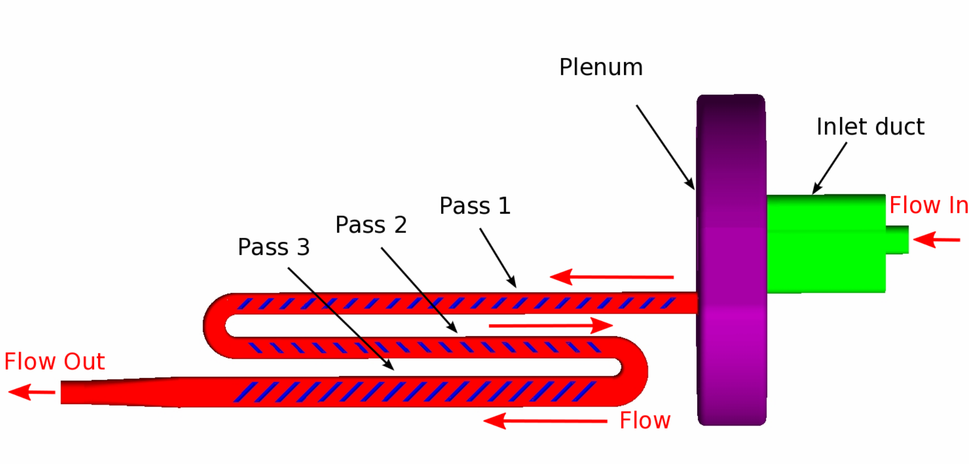

Figure 3.5: CFD geometry

and final images of experimental heat transfer distributions are shown in figure 3.4. The ribs have been blanked out in these views due to the high curvature on these surfaces, which leads to inaccurate HTC values in the experimental setup.

3.2 Simulation Setup

3.2.1 Geometry

The CFD geometry is shown in figure 3.5. The HP blade serpentine passage, shown in red, has three passes with aspect ratios defined as 1:4, 1:4 and 1:2 connected by 180^o bends, with all passes having the same cross-sectional area. Rounded rib-turbulators angled at 45^o are present in each pass with the mean radius of rotation 0.7 m. Further geometric details and flow conditions are given in table 3.1. The Rotation number is slightly lower in pass 2, compared to pass 1, due to the increasing fluid temperature, and therefore density, which results in a higher flow velocity. The plenum that precedes the passages is asymmetrical and narrow, while the

Table 3.1: Geometric details and flow numbers from CFD (Ro and Bo defined by equations 3.3 and 3.4.)

	Pass 1		Pass 2		Pass 3	
AR	1:4		1:4		1:2	
Ribs	21		17		17	
e/D_h	0.058		0.058		0.049	
e/p	0.1		0.1		0.1	
	Stat.	Rot.	Stat.	Rot.	Stat.	Rot.
Re	98400	96700	95300	93600	110500	108000
Ro	0	0.081	0	0.077	0	0.088
Bo	0	0.052	0	0.039	0	0.035

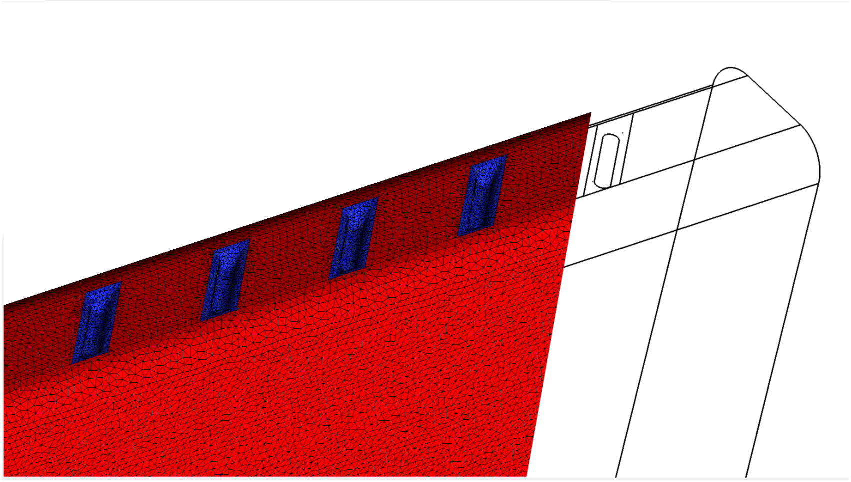

Figure 3.6: Typical meshing of passage and ribs

feed pipe entering it is also small with a diameter of 12 mm. This is due to space constraints within the rotor assembly as the passages and instrumentation must all be contained within the rotating arm.

3.2.2 Meshing

Meshing was undertaken using the ICEM 14.0 software. An unstructured tetrahedral mesh was used with 15 prismatic layers used to capture the boundary layer. The total mesh consisted of 25.6 million cells with an area-averaged y^+ value of 1.1 and a maximum $y^+ < 6$. An example of the mesh resolution is given in figure 3.6.

3.2.3 Solver Setup

Fluent 14.0 was used for all CFD simulations. A stepped solution procedure was followed with the complexity of the calculations built up gradually. The working fluid was air, modelled as an ideal gas with temperature dependent specific heat, viscosity and thermal conductivity. The SIMPLE pressure-based solver was utilised with second order discretisation for energy, momentum and turbulence properties. The realizable k-ε turbulence model was used for these calculations due to high quality predictions produced for very similar geometries under stationary conditions [83]. The k-ω SST turbulence model was also used. Pressure outlets and mass flow inlets were specified to match experimental conditions.

3.2.4 Post-processing

Heat transfer coefficients were calculated for the CFD setup using equation 3.1 where T_{gas} is an interpolated centreline value which allows for direct comparisons to the experimental results. The effect of choosing centreline or mixed bulk temperature in a stationary multi-pass cooling system is discussed in detail in [85,98,99].

$$h = \frac{q}{T_{gas} - T_{wall}} \tag{3.1}$$

$$Nu = \frac{hD_H}{k} \tag{3.2}$$

Following the calculation of HTC values these were converted to Nusselt number, equation 3.2, using a temperature dependent thermal conductivity based on the centreline gas temperature. These maps were then overlayed onto the geometry, as shown in figure 3.7 to form a three-dimensional, spatially resolved map of the heat transfer distribution within the passage. Rotation and Buoyancy Numbers were calculated using equations 3.3 and 3.4.

$$Ro = \frac{\omega D_H}{u_b} \tag{3.3}$$

$$Bo = (\frac{T_{wall} - T_{gas}}{T_{wall}})(Ro)^2(\frac{R}{D_H}) \tag{3.4}$$

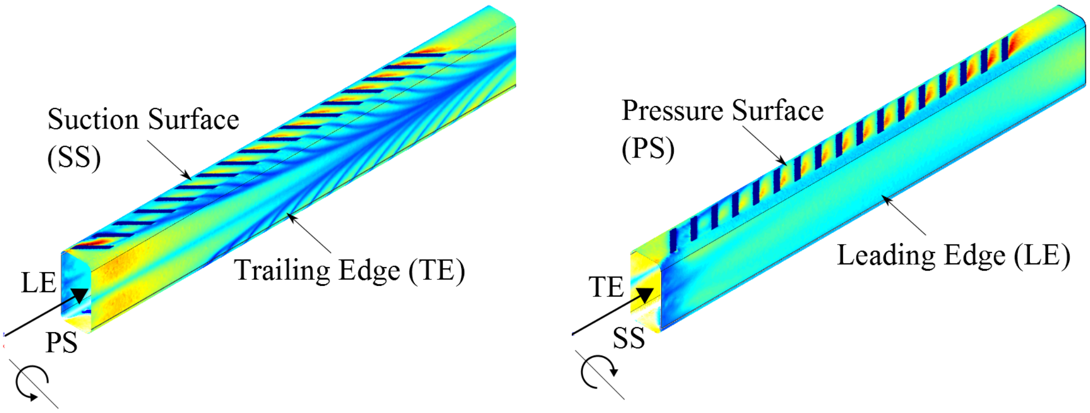

(a) SS/TE (b) PS/LE

Figure 3.7: Presentation method used for the CFD heat transfer distribution

3.3 Results

The results of the RANS simulations are presented first to enable the effect of rotation on the flow and heat transfer distribution to be discussed. This comparison is done with simulations that use the realizable k-ε turbulence model. The heat transfer predictions from the CFD simulations are then compared to the experimental data.

3.3.1 Flow Structure

The flow structure is investigated by considering velocity contours from CFD simulations of a static rig, with a smooth inlet, and the RHTR under both stationary and rotating conditions. The static rig is used as a base line for flow conditions without inlet or bend effects for the same rib and passage geometry [83, 100].

Inlet Effects/Plenum

The flow structure within the plenum has a significant impact on both the flow structure and heat transfer within the first pass of the cooling passage. Due to the combination of a relatively small diameter inlet pipe and narrow plenum the inlet flow impinges onto the downstream wall of the plenum, as observed from the velocity contours on a plane through the plenum, in figure 3.8. This in turn creates a wall jet near to this surface, on which the entrance to the cooling passage is located. Therefore a significant cross-flow is found at the entrance to the passage.

Under rotating conditions the flow structure is altered as the impinging inlet jet is deflected

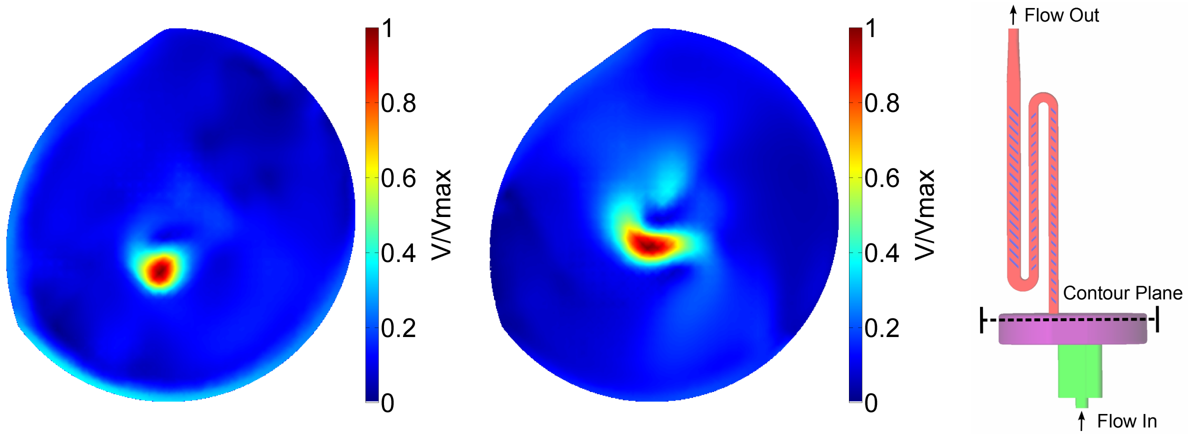

(a) Stationary (b) Rotating

Figure 3.8: Velocity contours on plane through the plenum

towards the effective pressure surface of the geometry. This results in different inlet conditions for the first pass of the serpentine passage under rotating conditions, increasing the complexity of the flow structure within the first pass.

Pass 1

Figure 3.9 clearly illustrates the development of the flow structure after 0, 5, 10 and 15 ribs for the static rig, and rotating rig under stationary and rotating conditions. The inlet velocity profile for the static rig is uniform in the centre of the passage with lower velocities near the walls, as expected, before rib-induced secondary flows are introduced. The secondary flow then progressively develops symmetrically with two clear rib-induced vortices near the pressure and suction surfaces. This development has been seen many times before, eg. [101].

Some differences to this structure are seen for the RHTR geometry, even under stationary conditions figure 3.9 (b). The first contour shows the inlet velocity has significant non-uniformities, with higher values towards the suction surface of the passage, due to the cross-flow introduced by the upstream geometry. The non-uniformity at the flow inlet causes the flow structure to develop more slowly than in the case with a smooth inlet, figure 3.9 (a), delaying the formation of the secondary flows. However the figure shows that the difference in inlet velocity profile only delays the formation of the developed flow structure, with asymmetries washed out after only 5 ribs.

Under rotating conditions the inlet effect is again clearly visible with much higher velocities near the suction surface. Further along the passage from the inlet the secondary flows form, but

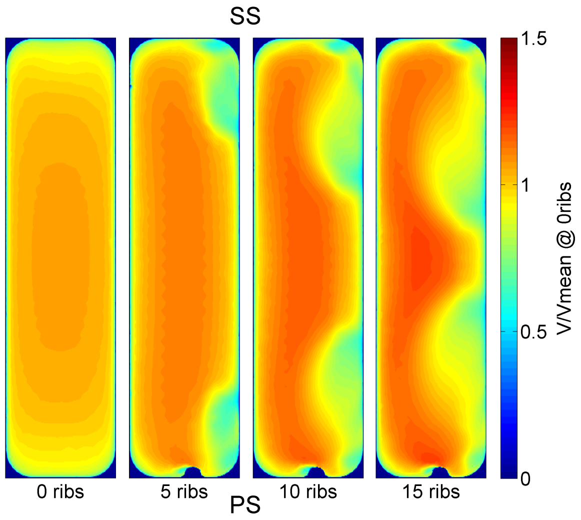

(a) Static Rig AR 1:4

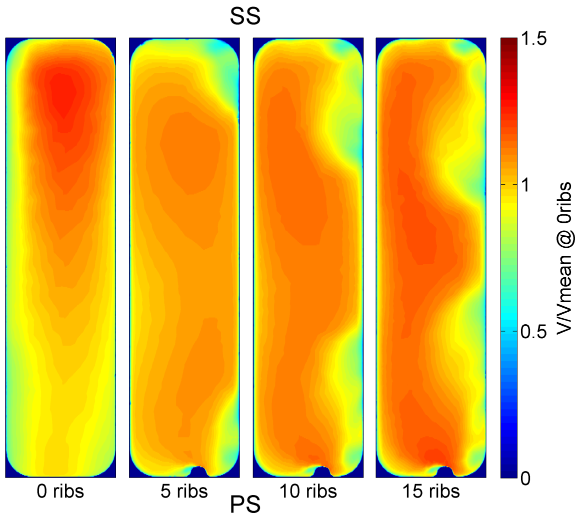

(b) RHTR Pass 1 - Static

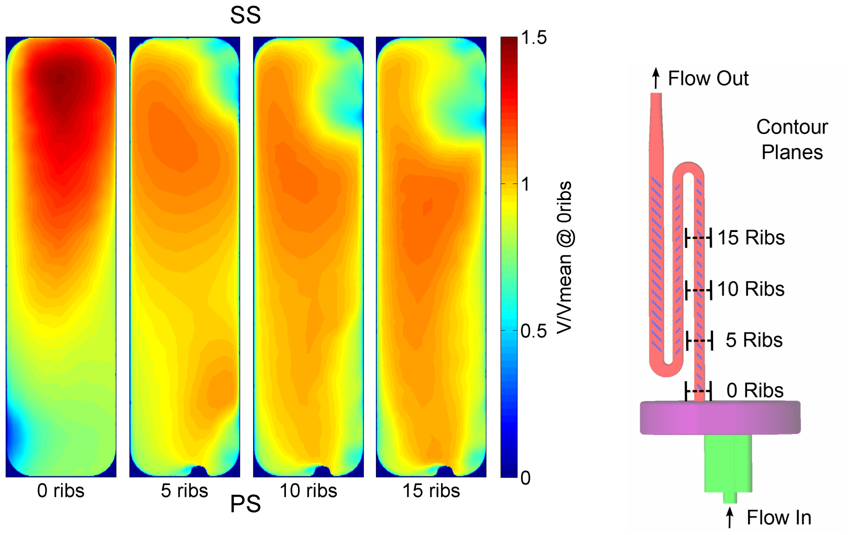

(c) RHTR Pass 1 - Ro = 0.081

Figure 3.9: CFD predictions of flow structure for 1st pass - velocity contours after 0, 5, 10 and 15 ribs - flow is radially outward for (b) and (c)

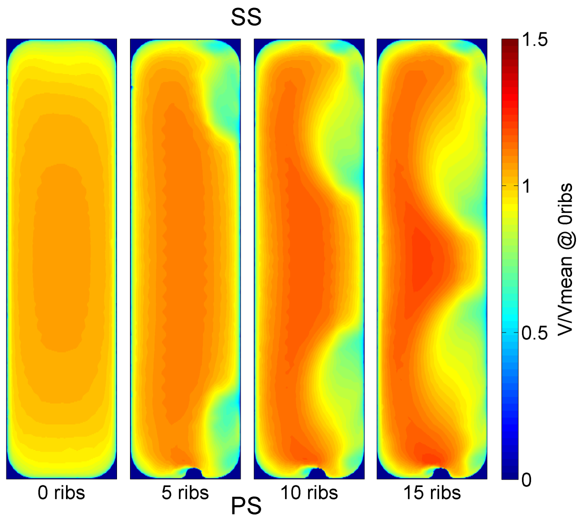

(a) Static Rig AR 1:4

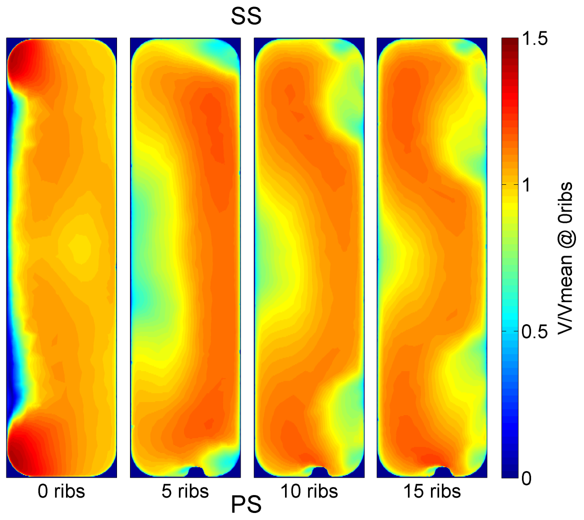

(b) RHTR Pass 2 - Static

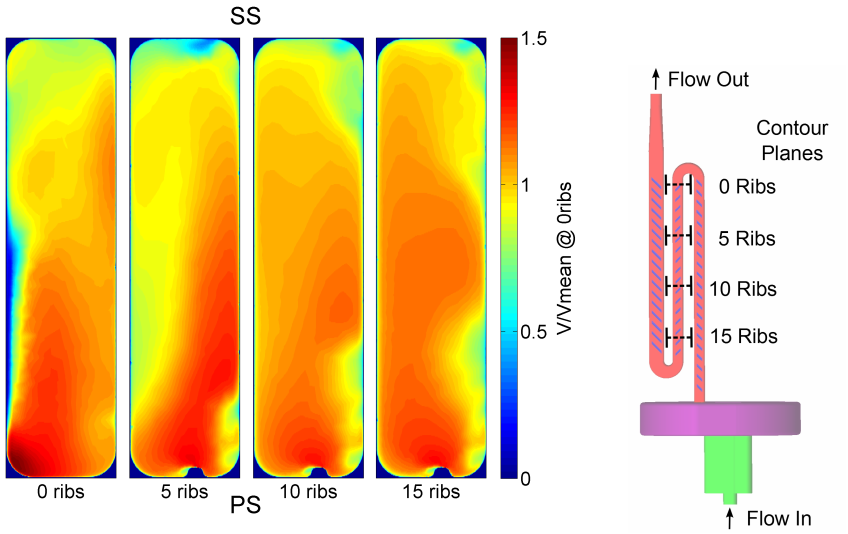

(c) RHTR Pass 2 - Ro = 0.077

Figure 3.10: CFD predictions of flow structure for 2nd pass - velocity contours after 0, 5, 10 and 15 ribs - flow is radially inward for (b) and (c)

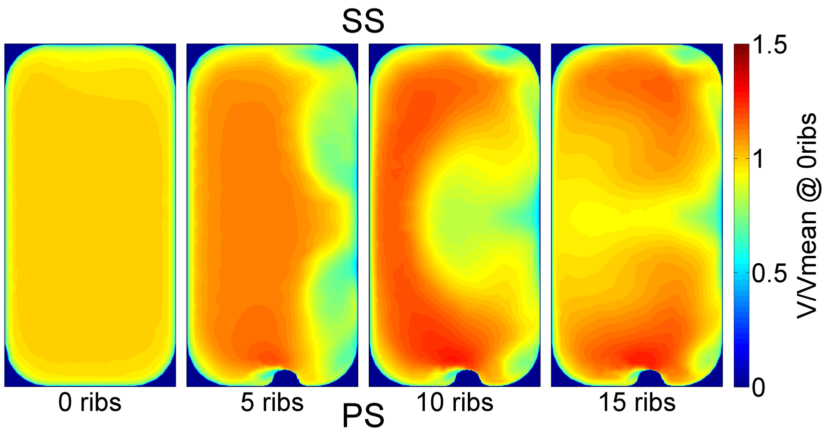

(a) Static Rig AR 1:2

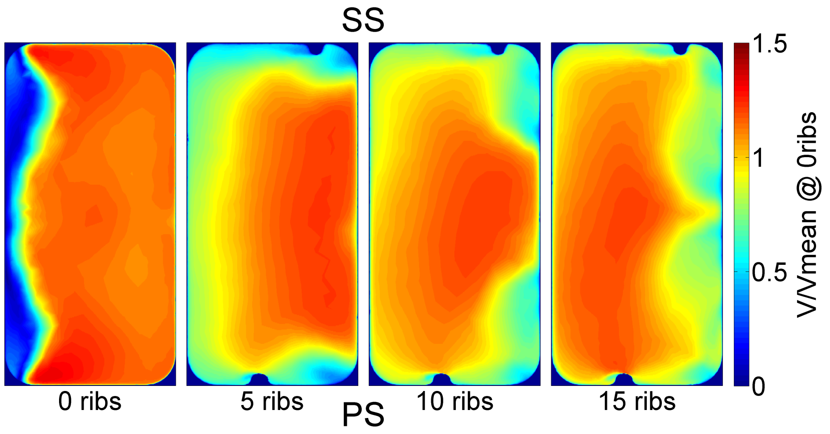

(b) RHTR Pass 3 - Static

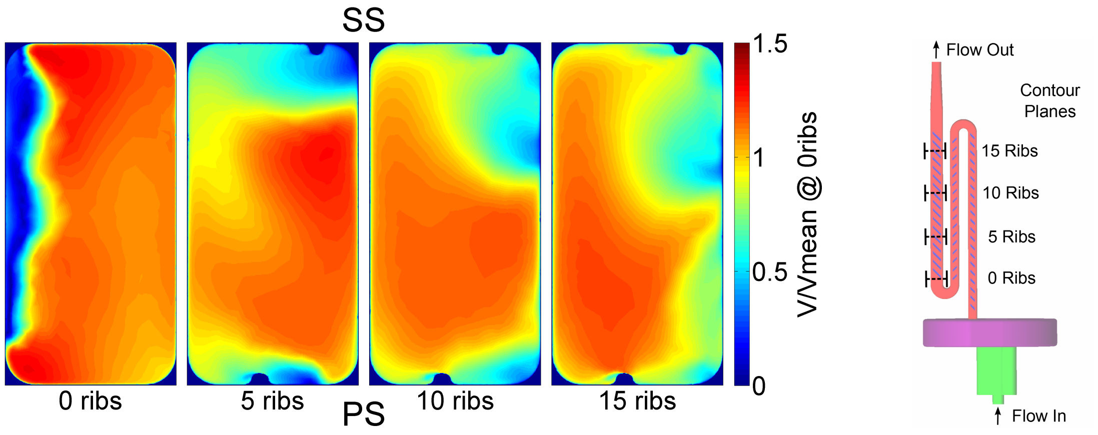

(c) RHTR Pass 3 - Ro = 0.088

Figure 3.11: CFD predictions of flow structure for 3rd pass - velocity contours after 0, 5, 10 and 15 ribs - flow is radially outward for (b) and (c)

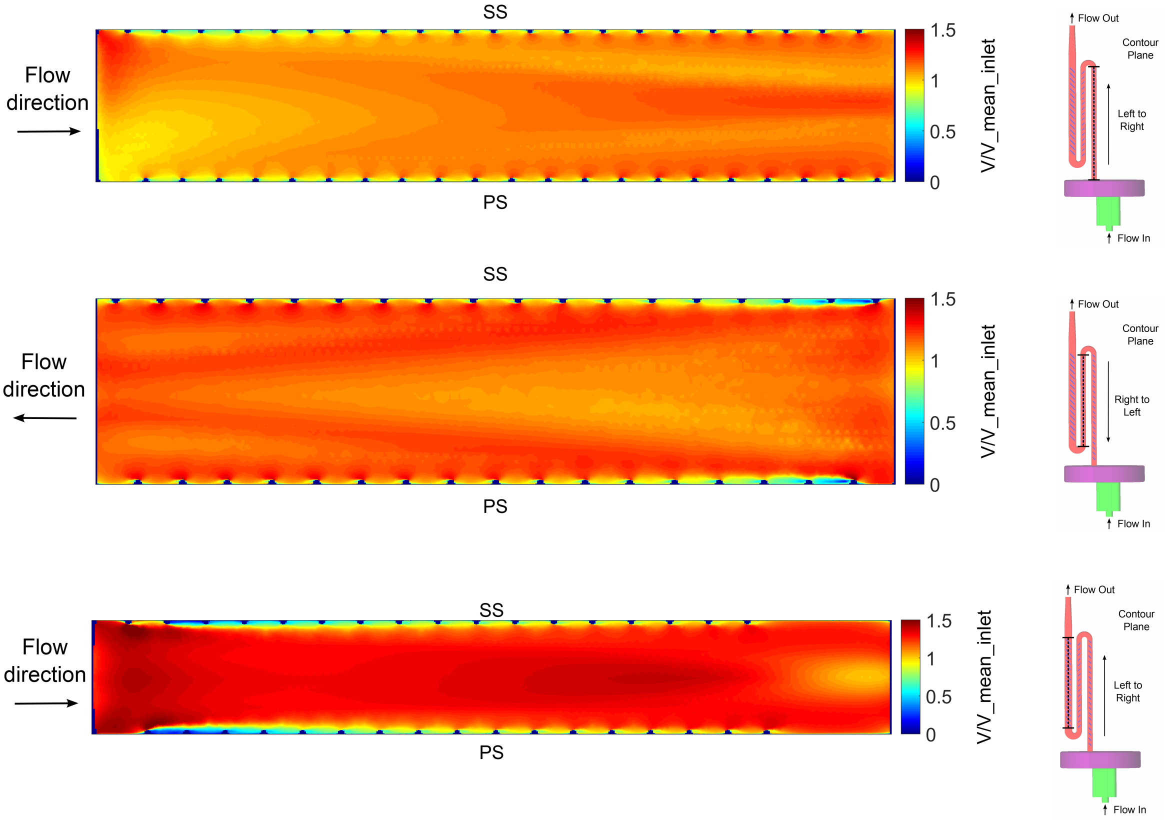

Figure 3.12: CFD predictions of flow structure - velocity contours on mid-passage slice - static

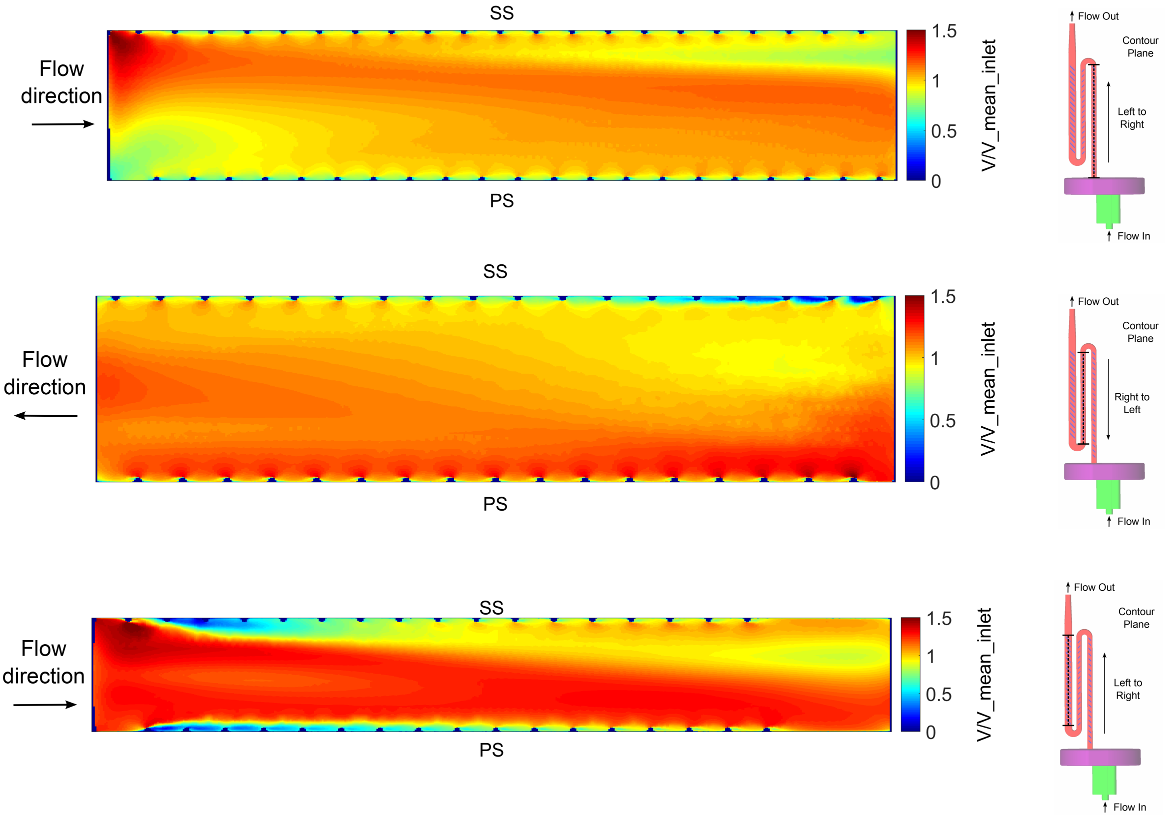

Figure 3.13: CFD predictions of flow structure - velocity contours on mid-passage slice - rotating

they are no longer symmetrical, with larger flows seen towards the pressure surface. This is due to a shift in core flow towards this surface which enhances the rib-induced flows as described in [8].

Pass 2

Figure 3.10 shows the same contours for the static rig, and the equivalent contours for the 2nd pass of the serpentine passage in the RHTR. The effect of the bend can be seen clearly in the first contour with regions of very high velocity at the fillets on the inside of the bend, which are remnants of the rib-induced secondary flows in the first pass.

The flow structure in this pass develops very differently to that in the static setup, and the first pass, due to the reversal in rib direction between these two passes. This reversal causes the secondary flows induced by ribs in the second pass to be in the opposite direction to those developed by the ribs in the first pass. Consequently there are four secondary flow vortices in this pass, those initially created in the first pass are pushed towards the centre of the passage and those induced by the ribs in the second pass remain near to the pressure and suction surfaces. Under stationary conditions the flow structure remains symmetrical.

However with rotation the structure is further complicated. The region of high velocity in the vicinity of the bend's inner radius is restricted to the PS as the core flow has been shifted towards this surface, with far lower velocities towards the opposing side of the passage, figure 3.10 (c).

Pass 3

The third pass has an aspect ratio of 1:2, and consequently some differences are observed between this and the previous passes. In the static setup the inlet profile is quickly altered by the rib-induced secondary flows, with two counter-rotating vortices in the passage. The flow continues to develop with these vortices detaching from the leading edge after the 15th rib. This occurs in the examined length of the AR 1:2 passage due to its wider cross-section, figure 3.11 (a).

The static RHTR simulation is significantly different to the flow structure for the AR 1:2 pass, figure 3.11 (b), due to the bend effects and reversal in rib direction. The velocity profile upstream of the ribs in the RHTR is already largely non-uniform with significant secondary flows from the previous passes and bends. With distance downstream, and therefore additional ribs, the secondary flows induced by the ribs in this pass begin to take effect. The flow structure after 15 ribs is approximately the same as that after 5 ribs with the smooth inlet geometry, indicating the bend and rib reversal effects cause a delay in the setup of the flow structure of approximately 10 rib pitches.

With rotation introduced the flow structure is complicated further. The velocity distribution now shows very strong secondary flows carried from the ribs in the previous passage towards the pressure surface of the passage. Therefore, despite the shift in core flow towards this surface, the newly induced secondary flows are established relatively slowly. Consequently the larger secondary flows towards the pressure surface that would be expected, are not observed.

Figures 3.12 and 3.13 show the normalised velocity contours on the mid-slice plane for each of the passes under static and rotating conditions.

Under stationary conditions the velocity distribution is initially biased to the SS due to the upstream geometry, however for the second and third passes a symmetric distribution is found, as expected for a symmetric passage geometry with no rotation. For the rotating case the Coriolis forces cause a clear migration of flow to the pressure surface for the radially outward first and third passes, with the opposing effect found for the radially inward second pass. This effect is likely to causes an increase in heat transfer on the surface towards which the core flow migrates.

3.3.2 Heat Transfer

Spatially resolved Nusselt number maps are presented in figures 3.14-3.16 for each pass under stationary and rotating conditions to allow the effect of rotation on the heat transfer distribution predicted by the CFD simulations to be reviewed.

Pass 1

A large inlet effect is seen at the start of the first pass in the form of a region of very high heat transfer, which is particularly prominent on the leading edge. This is caused by cross-flow at the inlet, the wall jet from the impinging inlet flow. Under rotating conditions the inlet effect is slightly enhanced due to the change of flow structure within the plenum. This inlet effect causes a slight delay in the establishment of the heat transfer distribution for developed flow.

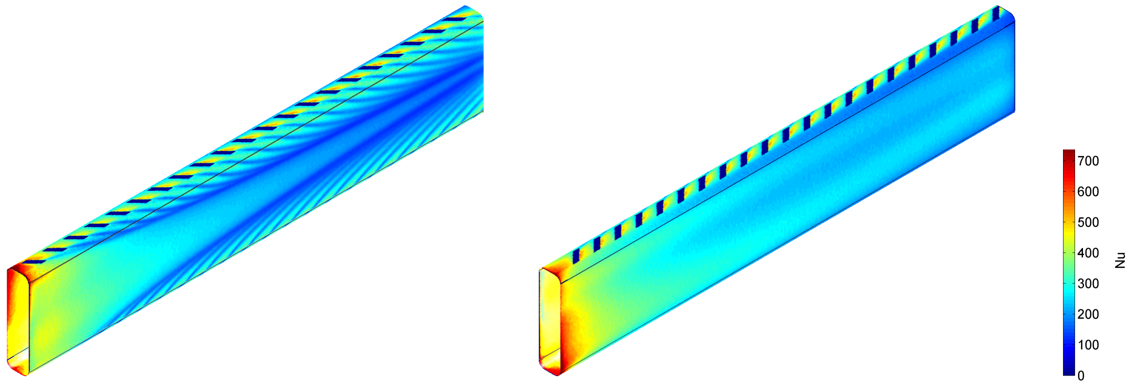

(a) Static - SS/TE (b) Static - PS/LE

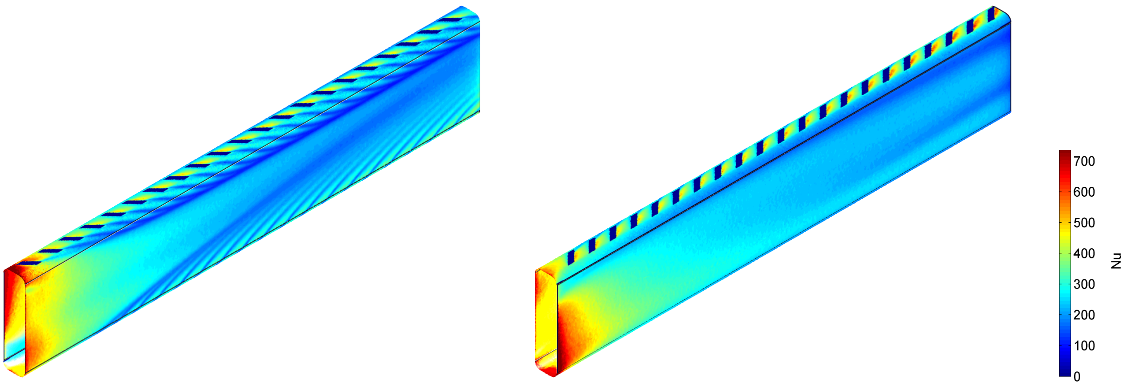

(d) Ro = 0.081 - SS/TE (e) Ro = 0.081 - PS/LE

Figure 3.14: CFD Heat transfer comparison for 1st Pass - flow radially outward

In both cases regions of high heat transfer are observed immediately downstream of each rib, as the flow reattaches. Streaks of high heat transfer are found on the trailing edge due to the upwash from each rib, which grow with streamwise direction as the flow develops.

The stationary case shows a symmetric heat transfer distribution after the initial inlet effect, indicating the impacts of the latter are washed out. With rotation introduced the core flow shifts towards the pressure surface which increases the heat transfer on this surface. A reduction in heat transfer is observed on the suction surface. These trends are in line with results from previous studies [8].

Pass 2

In this pass the upstream passage, and therefore flow structure, has a large influence on the heat transfer. Significantly higher heat transfer is found on the trailing edge, at the outside of the bend, than the leading edge at the start of the passage as the core flow migrates to the outside of the bend. Multiple peaks are found in this region as the secondary flows impinge onto this surface, and all surfaces show a symmetric distribution. With rotation introduced the flow

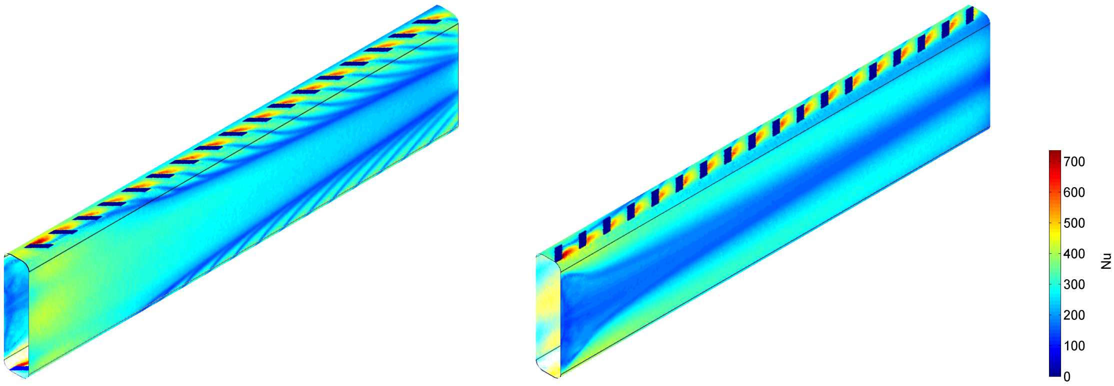

(a) Static - PS/TE (b) Static - SS/LE

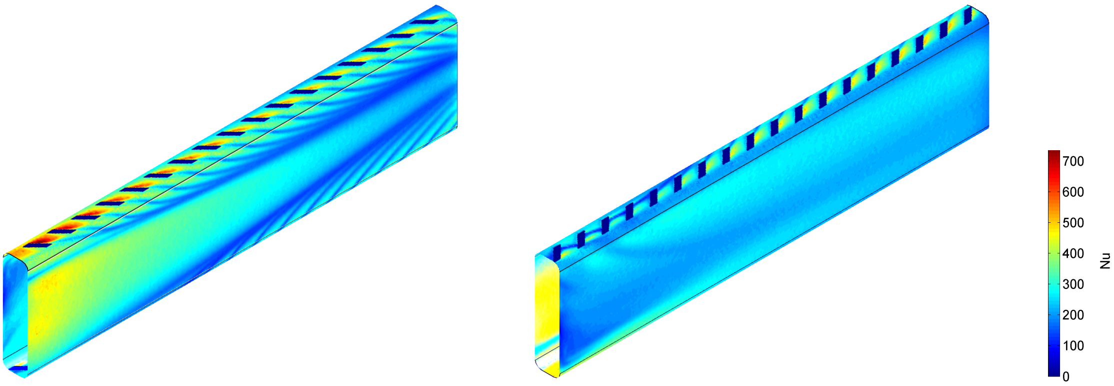

(d) Ro = 0.077 - PS/TE (e) Ro = 0.077 - SS/LE

Figure 3.15: CFD Heat transfer comparison for 2nd Pass - flow radially inward

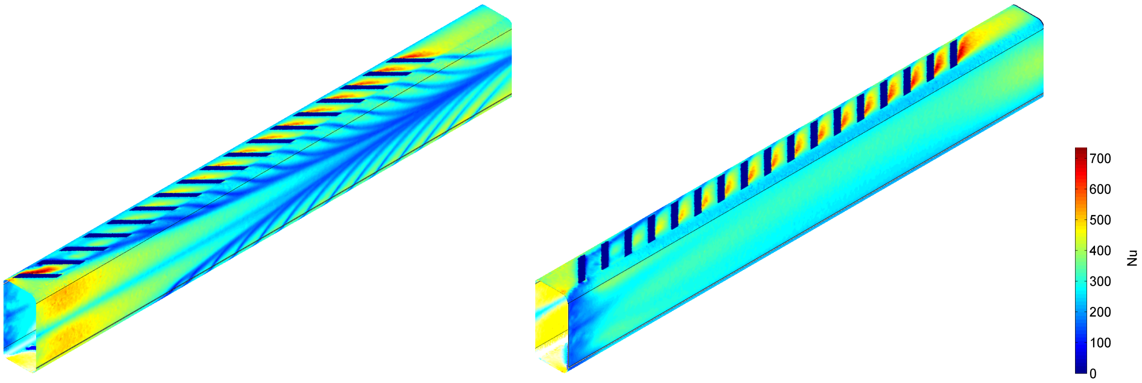

(a) Static - SS/TE (b) Static - PS/LE

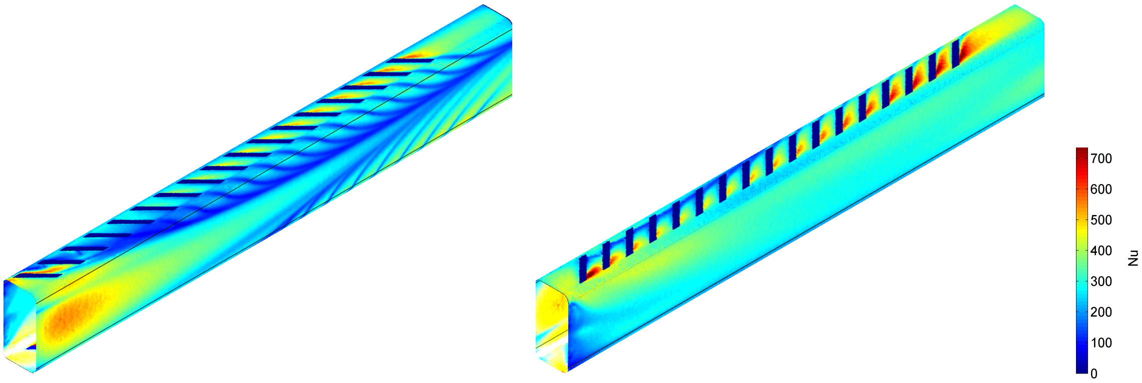

(d) Ro = 0.088 - SS/TE (e) Ro = 0.088 - PS/LE

Figure 3.16: CFD Heat transfer comparison for 3rd Pass - flow radially outward

through the bend is far more disrupted with only a single peak on the trailing edge observed, although this exhibits higher values than the stationary case.

The rest of the passage has a similar distribution to that of the first pass with locally enhanced heat transfer in rib reattachment and upwash regions. However due to the presence of secondary flows from the first pass the upwash regions are far more restricted, extending less far up the trailing edge walls, and a strip of low heat transfer is found on the leading edge wall.

The rotating simulation shows significant differences with heat transfer around the suction surface ribs initially much lower than that on the pressure surface. This then increases throughout the pass, while pressure surface heat transfer decreases with streamwise distance. Theory and previous studies suggest that the enhancement of heat transfer on the suction surface of radially inward passes under rotation is expected, and this would be seen without the presence of the bend and rib reversal effects at the start of this pass.

Pass 3

The bend and reversal in rib direction have a significant impact on heat transfer in the 3rd pass, however to a lesser extent to that seen in the 2nd pass. This is due to the wider 1:2 aspect ratio of this pass. Two clear peaks are seen in the stationary simulation as the two vortices from upstream are forced to the outer edge of the bend and subsequently impinge onto the trailing edge. The first rib on the suction surface causes a very large reattachment region which could be caused by the high velocities through the bend near to this surface. When rotation is introduced the peak towards the pressure surface immediately downstream of the bend is enhanced greatly in size in comparison to that near the suction surface, with reattachment regions for the initial pressure surface ribs also enhanced, due to the shift in core flow towards the pressure surfaces within the bend.

The heat transfer distribution for the rest of the passage is seen to be reasonably symmetric. The secondary flows from previous passages are eliminated before the end of the passage with those induced by the ribs in the 3rd pass becoming dominant.

When rotation is introduced the setup of the rib-induced flows is delayed on both surfaces, due to the increased complexity of the flow structure through the bend. However towards the end of the pass the pressure surface exhibits enhanced heat transfer, with the opposing effect on

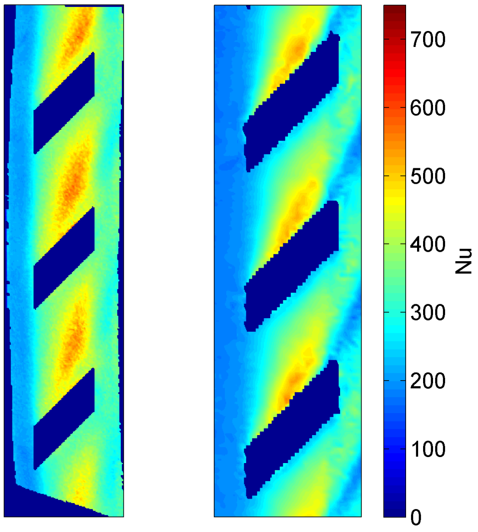

(a) PS Exp Stat. (b) PS CFD Stat. (c) PS Exp Rot. (d) PS CFD Rot.

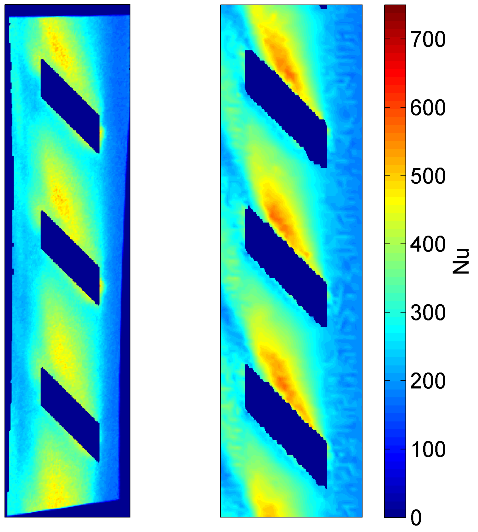

(e) SS Exp Stat. (f) SS CFD Stat. (g) SS Exp Rot. (h) SS CFD Rot.

Figure 3.17: CFD and experimental comparison for 1st pass - flow radially outward - Nusselt Number - Static and Ro = 0.081

the suction surface, as expected in a radially outward passage.

3.3.3 Comparison with Experiments

Results from the CFD simulations are compared to those from the experiment in the form of Nusselt number maps of the section of each pass visible within the experimental setup [97], figures 3.17-3.19.

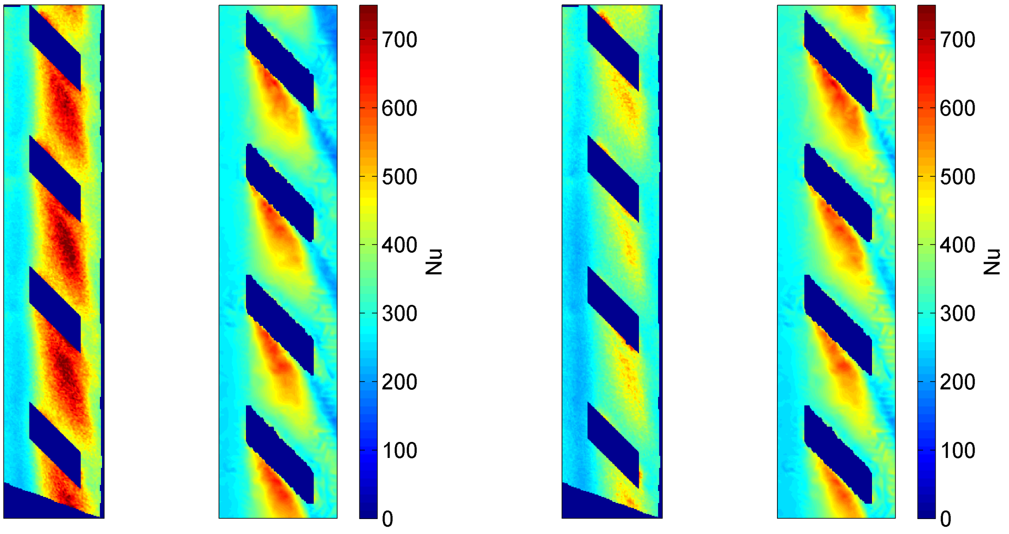

(a) PS Exp Stat. (b) PS CFD Stat. (c) PS Exp Rot. (d) PS CFD Rot.

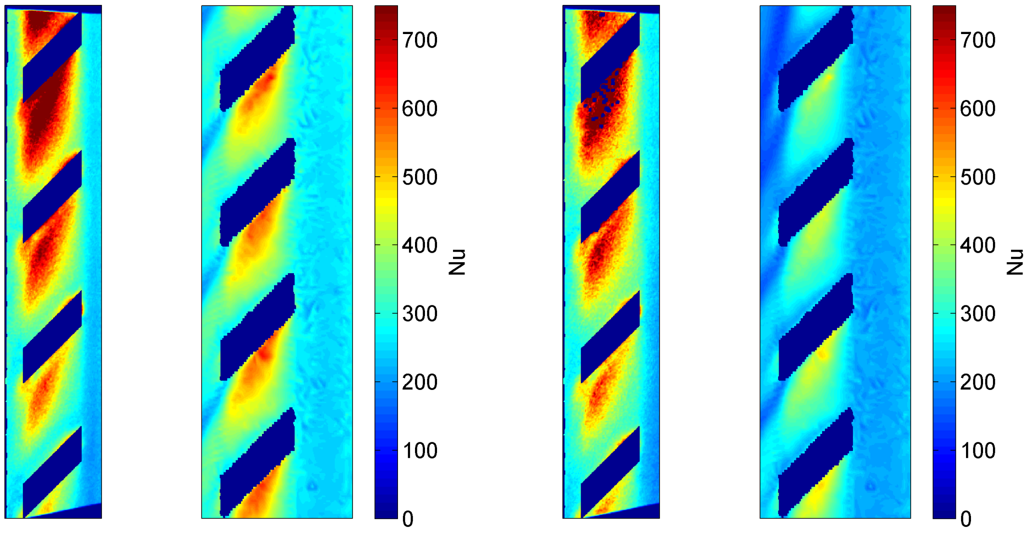

(e) SS Exp Stat. (f) SS CFD Stat. (g) SS Exp Rot. (h) SS CFD Rot.

Figure 3.18: CFD and experimental comparison for 2nd pass - flow radially inward - Nusselt Number - Static and Ro = 0.077

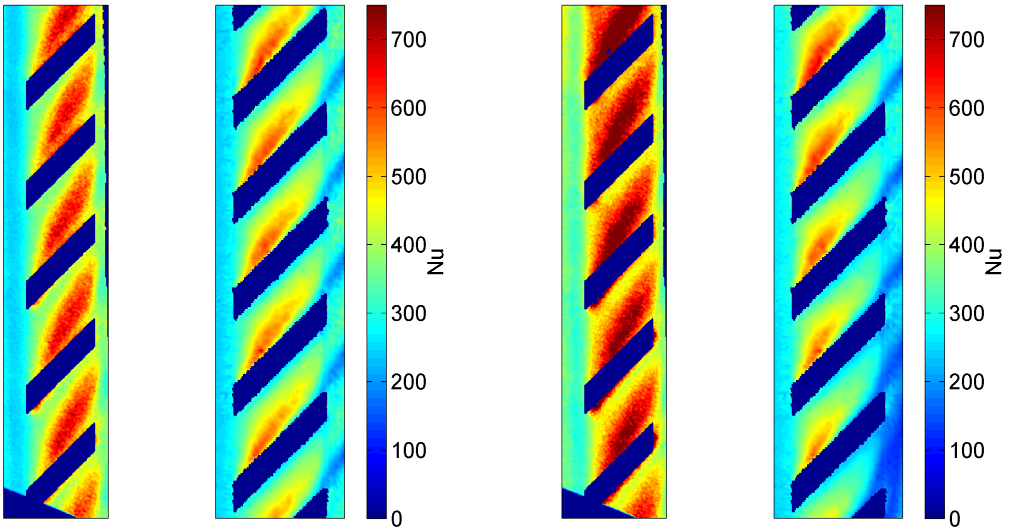

(a) PS Exp Stat. (b) PS CFD Stat. (c) PS Exp Rot. (d) PS CFD Rot.

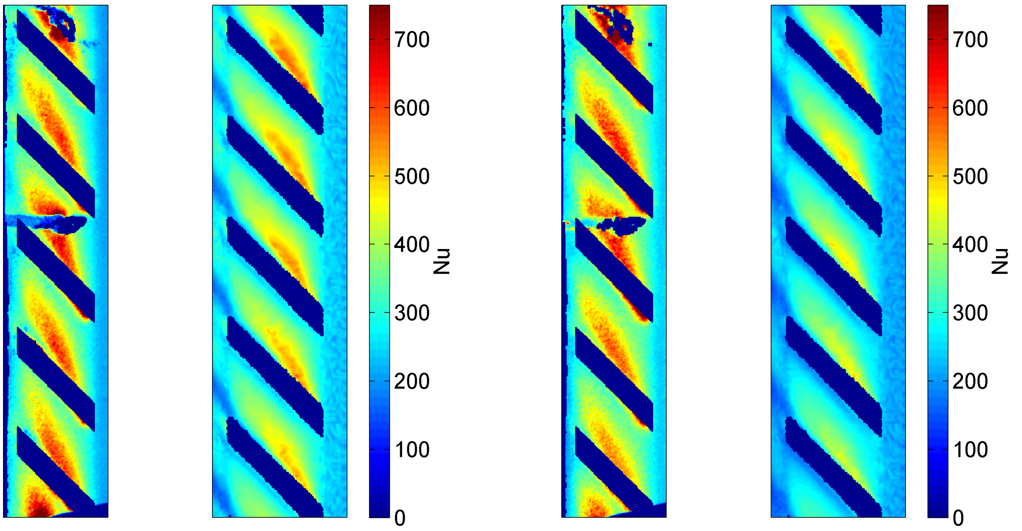

(e) SS Exp Stat. (f) SS CFD Stat. (g) SS Exp Rot. (h) SS CFD Rot.

Figure 3.19: CFD and experimental comparison for 3rd pass - flow radially outward - Nusselt Number - Static and Ro = 0.088

Pass 1

Under stationary conditions the Nusselt number distribution for the first pass pressure surface predicted by CFD is very close to the experimental data, both in terms of levels and distribution. When rotation is introduced large discrepancies are observed, with experimental values much higher than those predicted by the CFD.

For the suction surface the stationary results are reasonably matched however large differences are found under rotating conditions. The same trends of decreasing heat transfer under rotation for this surface are seen for both CFD and experiment.

The differences between experimental and CFD results found under rotating conditions are most likely due to differences in driving gas temperature. The flow structure at the start of the passage is very complex, and the gas temperature thermocouple is located on the centreline of the duct within this complex region. Small differences in this position between CFD and experiment could lead to large changes in driving gas temperature, and hence calculated HTC values.

Pass 2

The heat transfer levels for the pressure surface of this pass are slightly higher in the experimental setup than CFD with similar distributions downstream of each rib. Rotation produces a large decrease in Nusselt number relative to the stationary case for the experimental data, while there is very little change in the CFD values.

The suction surface exhibits similar levels in the heat transfer to the stationary simulation however a significantly different distribution. There is little change in Nusselt number with streamwise direction in the CFD, while the experimental values decrease significantly. With rotation introduced the levels for the CFD are significantly lower for the experiment with the differences in distribution still seen.

The differences observed between the experimental data and CFD predictions for this pass are attributed to the reversal in rib direction in this pass which greatly complicates the flow structure and therefore heat transfer distribution. These effects are particularly prominent due to the location of the camera view being very close to the upstream bend for this pass.

Pass 3

In the third pass under stationary conditions both levels and distribution for the experiments and CFD are very similar for the pressure surface. Under rotating conditions a clear increase is seen in the experimental results which is not found in the CFD, where a slight decrease is observed.

As with the pressure surface, suction surface results for the stationary test point are reasonably well matched with CFD values slightly lower. With rotation introduced there is very little change in the experimental values, while in the CFD a significant decrease in Nusselt number is observed.

The discrepancies observed between CFD and experimental values and trends are attributed to the effects of reversing the direction of the ribs in this pass, as for the second pass. The differences found are smaller for this pass due to its wider aspect ratio and the positioning of the camera a greater distance from the upstream bend.

There are some significant differences found between the CFD and experimental heat transfer results, particularly under rotating conditions. These discrepancies were found for many simulations that are not presented in this thesis including meshes with higher cell counts, different specified inlet conditions and other turbulence models, one of which is presented in section 3.3.4. The higher cell count meshes had no effect on heat transfer results, as mesh independence had been reached with the results presented, and all solutions were converged. DIfferent inlet conditions, particularly turbulence levels, were also investigated at the inlet, however any effect of these was washed out by the impinging jet within the feed plenum and therefore had no effect on the heat transfer in the radial passages. Therefore the large discrepancy in heat transfer results is attributed to the inability of the CFD simulations to accurately model the complex inlet flow into the radial passage.

3.3.4 Turbulence Modelling

Other commonly used turbulence models were also applied to investigate their accuracy when predicting heat transfer in radial cooling passages. Figure 3.20 shows the unwrapped heat transfer distributions for the stationary test point using the k-ε realizable and k-ω SST turbulence models.

Under stationary conditions the simulations with the k-ω SST model show the same main

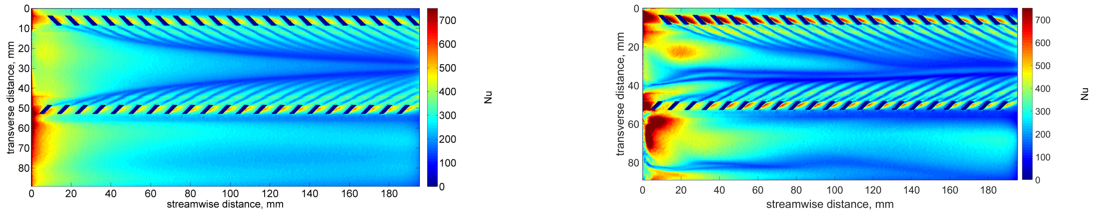

(a) Pass 1 - k-ε realizable (b) Pass 1 - k-ω SST

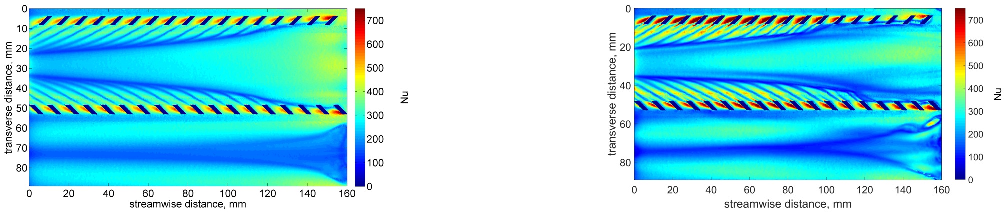

(c) Pass 2 - k-ε realizable (d) Pass 2 - k-ω SST

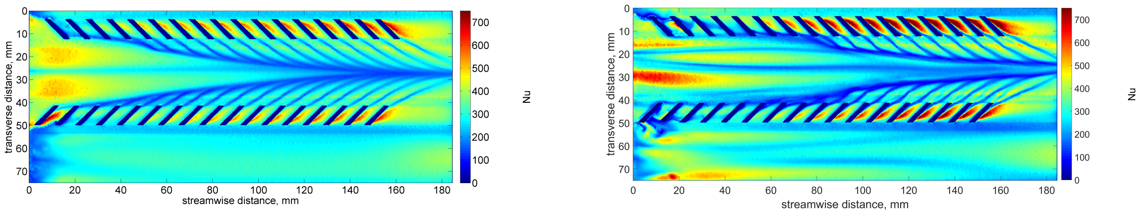

(e) Pass 3 - k-ε realizable (f) Pass 3 - k-ω SST

Figure 3.20: Turbulence model heat transfer comparison - unwrapped - static

features as those using the k-ε realizable model. These are the area of high heat transfer at the inlet to the first pass and downstream of each bend. The inlet effect is slightly more pronounced, however, leading to a small asymmetry in the first pass. The other passes both give symmetric distributions. The rib induced secondary flows are stronger when using the k-ω SST model with larger upwash regions and regions of high heat transfer downstream of each rib.

When rotation is included in the simulation both turbulence models again offer very similar results, which are given in figure 3.21. There are minor differences in the inlet effect and regions of high heat transfer downstream of each bend. Again the rib-induced flows are stronger with the k-ω SST model.

These simulations indicate little difference between using these two turbulence models for heat transfer predictions, and also suggest that the major differences found in the experimental comparison are not due to poor turbulence modelling but difficulties in modelling the highly complex flow region near to the passage inlet.

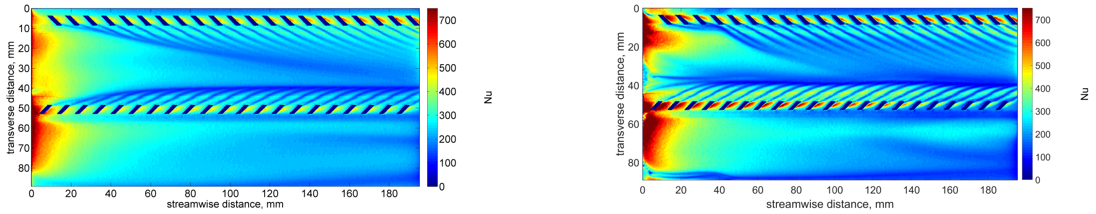

(a) Pass 1 - k-ε realizable (b) Pass 1 - k-ω SST

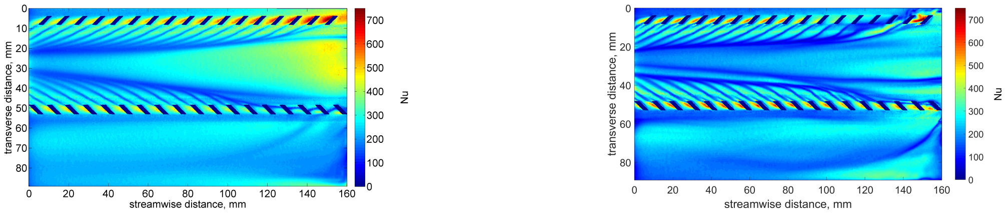

(c) Pass 2 - k-ε realizable (d) Pass 2 - k-ω SST

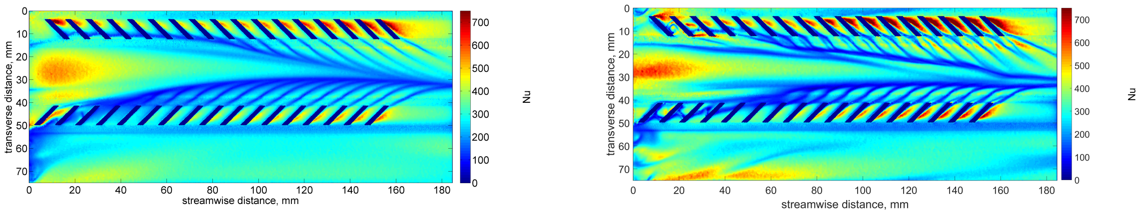

(e) Pass 3 - k-ε realizable (f) Pass 3 - k-ω SST

Figure 3.21: Turbulence model heat transfer comparison - unwrapped - rotating

3.3.5 Average Values

Figures 3.22-3.24 show average Nusselt number values for the area visible in the experiment plotted against Rotation number. The figure shows data from the experiments and simulations using the realizable k-ε and k-ω SST turbulence models. For the first pass clear trends are observed in the experimental data, with an increase on the pressure surface and decrease on the suction surface, with increasing rotation number. The computational results show the same trends however these are far less pronounced.

In the second pass smaller differences are observed in the experimental data, however the suction surface data shows consistently higher heat transfer at high rotation numbers. The CFD results are not in agreement with higher values on the pressure surface.

In the third pass, pressure surface heat transfer is higher than that on the suction surface for high rotation numbers, however the trends are far less clear than for the first pass.

The lack of clear trends is due to the reversal of rib direction in the 2nd and 3rd passes, leading to the new secondary flows being created, which oppose those from the upstream pass. This means the expected flow structure, and therefore heat transfer distribution, cannot develop

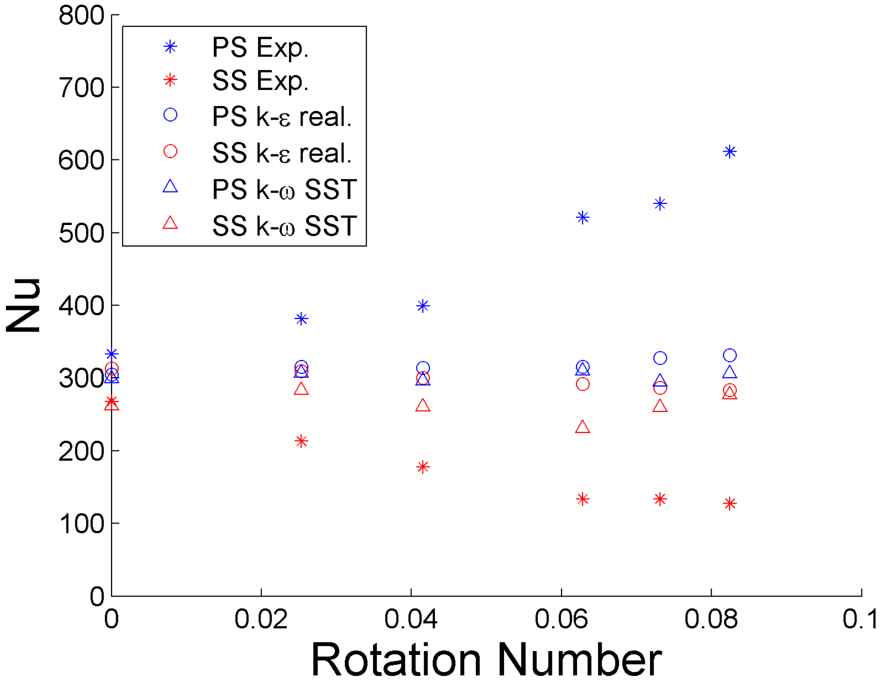

Figure 3.22: Average Nusselt number with Rotation number - comparison of CFD with experiment - Pass 1

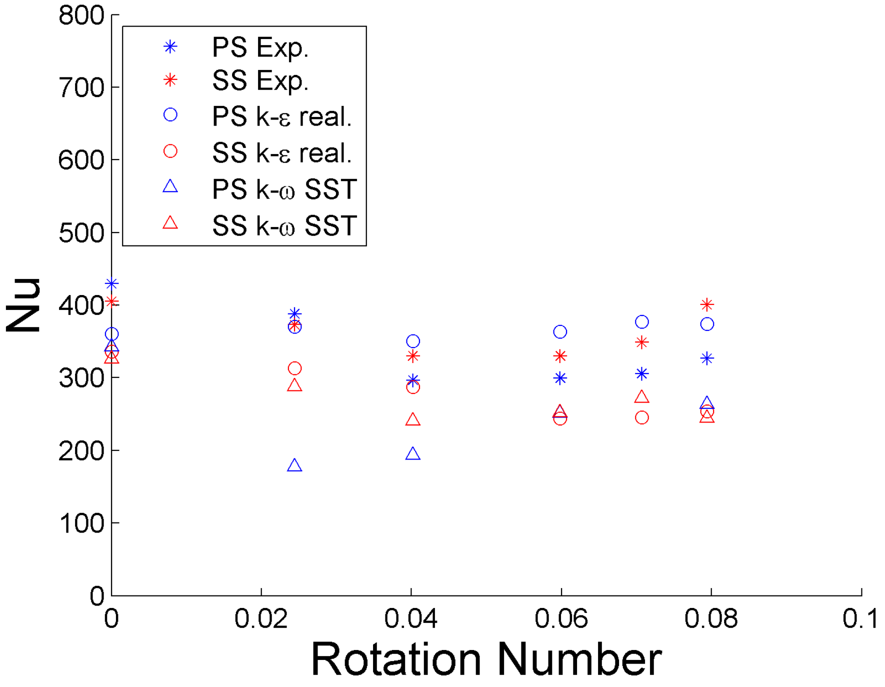

Figure 3.23: Average Nusselt number with Rotation number - comparison of CFD with experiment - Pass 2

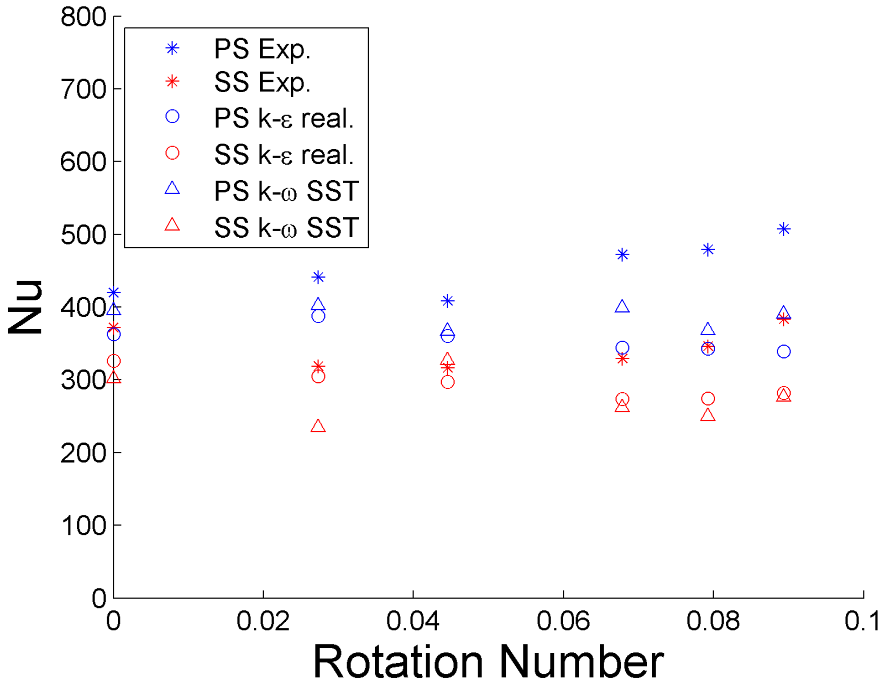

Figure 3.24: Average Nusselt number with Rotation number - comparison of CFD with experiment - Pass 3

in these passes. The computational simulations also have great difficulty in simulating the complex interaction of secondary flows, resulting in predictions that are not well matched to the experimental data.

3.4 Summary and Conclusions

CFD simulations of a triple-pass, ribbed, radial serpentine passage have been run using methodology commonly used in industry under stationary and rotating conditions. Heat transfer results from these have been compared with high resolution data obtained in the RHTR at Rolls-Royce Bristol. The following conclusions have been drawn from this research.

1. Rotation introduces additional forces which impact greatly on the flow structure and heat transfer within ribbed, radial cooling passages.

2. The CFD methodology presented provides good predictions under stationary conditions, with the error between the CFD and experiments less than 20 % for all passes and both turbulence models.

3. With rotation introduced, CFD simulations show significant differences to the experimental data, with overall levels and trends with rotation poorly predicted.
4. Upstream geometry can have a very large impact on flow structure and heat transfer within a passage, which increases the complexity of simulations and therefore creates difficultites in obtaining accurate CFD predictions.
5. The poor predictions of the heat transfer under rotating conditions is attributed to the CFD being unable to accurately model the complex inlet conditions to the radial passages that are found due to the specific upstream geometry in the experimental setup.

Chapter 4

Radial Passages - Inlet Velocity Profile and Rib Direction

This chapter investigates the effect of different inlet flow conditions on the heat transfer performance of a typical ribbed, radial cooling passage and examines the effect of rib direction reversal between passes using RANS CFD with common industrial methodology. This follows on from chapter 3 where these were found to be the features which influence the flow and heat transfer most in the CFD simulations, experiments and the comparison between these.

4.1 Simulation Setup

Two geometries are considered in this chapter. The initial geometry is that given in figure 3.6, the same as in the previous chapter. This geometry has rib orientations that are reversed relative to the oncoming mainstream flow from the 1st to 2nd, and 2nd to 3rd passes. This results in the upwash from the ribs being directed towards the same surface in each pass relative to the blade in which it is contained. The second geometry is identical to this however with the ribs in the second passage orientated in the opposite direction, resulting in no rib-reversal between passes. These rib configurations are illustrated in figure 4.1.

Meshing was undertaken using the ICEM 14.0 software. An unstructured tetrahedral mesh was used, with 15 prismatic layers to capture the boundary layer and the same sizing settings as in the previous chapter. The total mesh consisted of 6.81 million cells with an area-averaged y^+ value of 1.01 and a maximum $y^+ < 5.5$. An example of the mesh resolution is given in

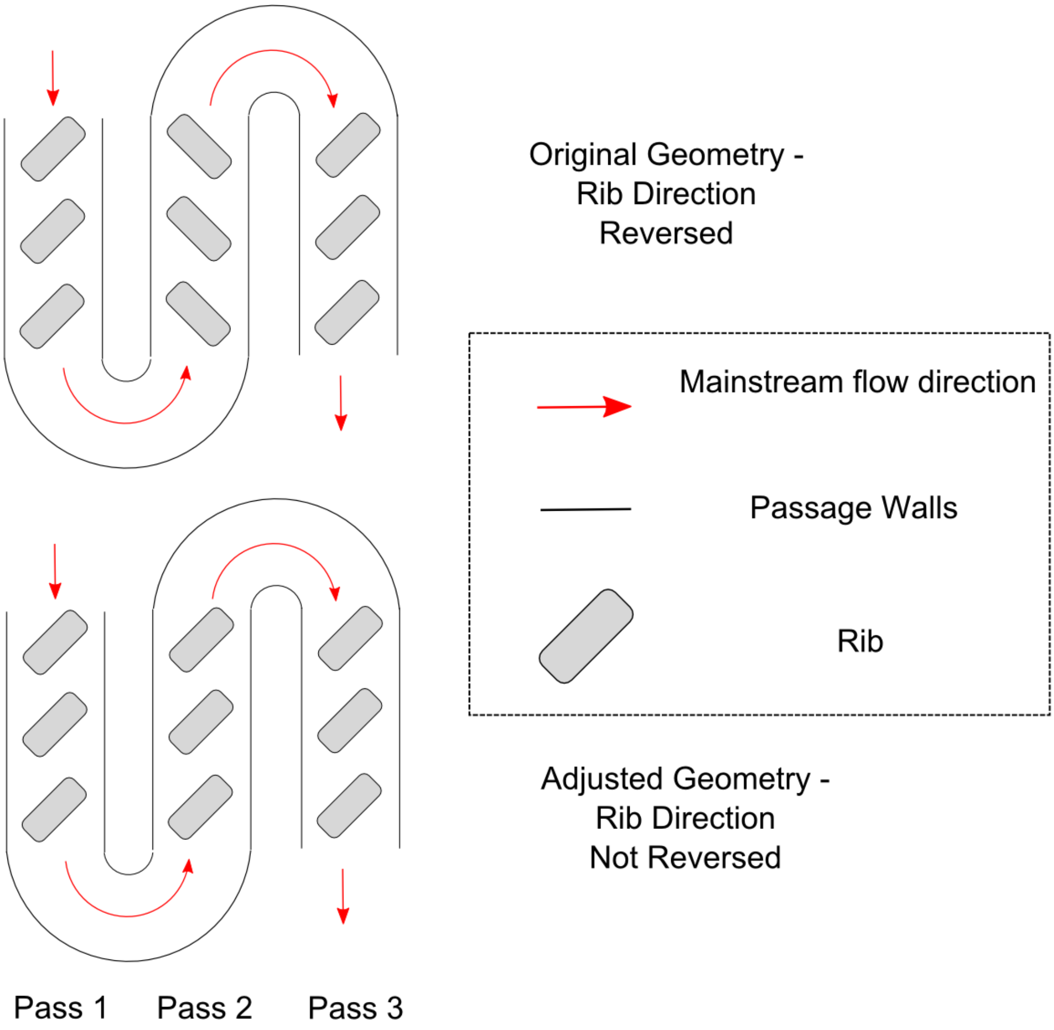

Figure 4.1: Schematic rib reversal diagram

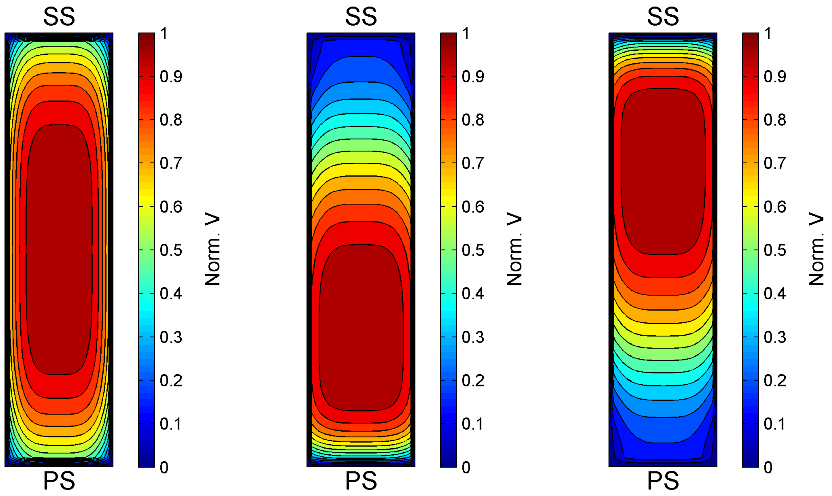

(a) Symmetric (b) PS Bias (c) SS Bias

Figure 4.2: Velocity profiles

figure 3.6.

The simulations were run using the procedure detailed in section 3.2.

4.1.1 Velocity Profiles

Three different inlet velocity profiles are considered in this chapter, illustrated in figure 4.2. The first is a symmetric profile, designed to be representative of a smooth inlet and will be used as a baseline. The remaining two have a significant pressure or suction surface bias whilst remaining physically realistic. These were selected to compare a typical profile to those with a fairly extreme bias.

4.2 Results

Simulations were initially run under stationary conditions for all inlet velocity profiles and following these, simulations were run at rotating conditions as detailed in table 3.1. This was to assess the influence of the inlet conditions on the serpentine passage without the added complexity of rotation before observing if the inlet effects were maintained under rotating conditions. This was also due to the good performance of the commonly used industrial methodology under stationary conditions, [83], however its poorer performance under rotating conditions in chapter 3, which is thought to be mainly due to poor modelling of the inlet effects.

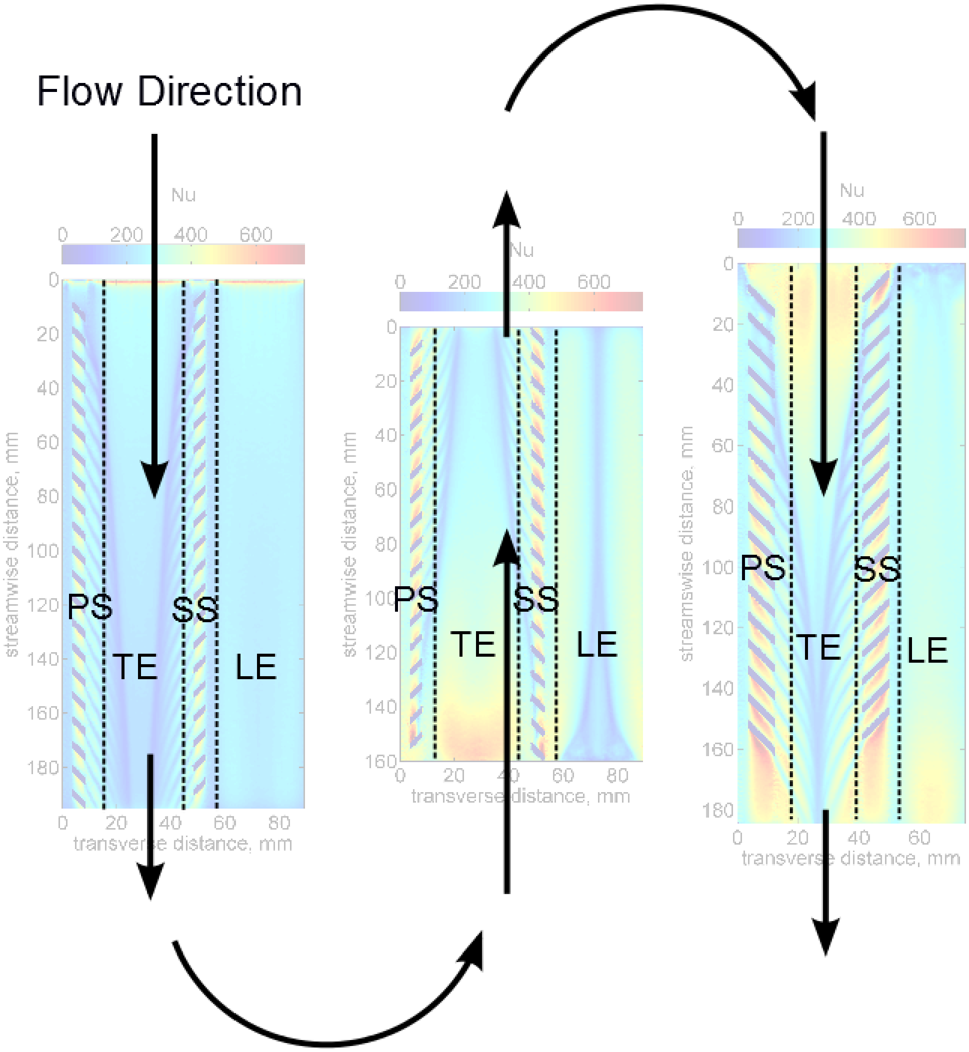

Figure 4.3: Presentation method for heat transfer figures

After the influence of the inlet profiles was determined the results were compared to experimental results with complex inlet conditions to assess whether difficulties in modelling the upstream inlet conditions present in the RHTR caused the discrepancies found between the CFD and experimental results in chapter 3.

Flow structure results are presented in the form of velocity magnitude contours at 0, 5, 10 and 15 ribs from the start of each pass normalised to the mean inlet velocity. Heat transfer results are presented in ‘unwrapped’ Nusselt number contours as illustrated in figure 4.3, with the plots orientated as to represent the serpentine nature of the passage.

4.2.1 Stationary Simulations

Simulations under stationary conditions were run for all velocity profiles, at conditions detailed in table 3.1, however detailed flow structure and heat transfer results are not presented.

This is because all stationary simulations exhibited similar and consistent features which are also found in the rotational simulations, however under rotation additional effects are observed.

4.2.2 Original Geometry - Rotating - Flow Structure

The inlet profiles illustrated in figure 4.2 were applied in the relative frame to a rotating simulation of the passage at the conditions given in table 3.1. Figures 4.4, 4.6, 4.8 show the velocity contours after 0, 5, 10 and 15 ribs for the three passes, for the initial geometry with reversed rib directions.

For the first pass of the simulation with a symmetric inlet velocity profile there is a clear effect of rotation in the first pass. The rib-induced secondary flows on the pressure surface are far larger than those on the suction surface due to the shift in core flow. This shift in core flow leads to a bias towards the pressure surface at the start of the second pass, which is reduced throughout the length of this pass as it shifts back towards the suction surface. However, due to the inlet conditions the secondary flows are larger on the pressure surface of this pass, despite weakening with distance down the pass. The flow at the inlet to the third pass is slightly biased towards the suction surface however the secondary flows on the pressure surface are soon stronger than those on the suction surface due to the rotational effects.

The second simulation has a bias of flow towards the pressure surface at the inlet to the first pass. This is maintained throughout the first pass as the Coriolis force pushes the flow towards this surface leading to much stronger secondary flows on this surface, with very little flow on the suction side of the passage. Leading into the second pass much of the flow is again towards the pressure surface of the passage, which is then pushed to the suction surface with distance along the pass due to the Coriolis effect within a radially inward pass. By the third pass the flow is almost indistinguishable from that in the simulation of a symmetric inlet, indicating that inlet effects do not propagate this far down the passage for this geometry.

The third rotating simulation has the inlet flow biased towards the suction surface. In this case the flow clearly spreads towards the pressure surface due to the rotation, however the secondary flows on the suction surface are far stronger throughout the pass due to the initial flow conditions. When the flow reaches the start of the second pass it is more evenly spread than in the two previous cases, whilst retaining a bias towards the pressure surface. This leads to the flow spreading towards the suction surface a little faster than in the other cases, however the secondary flows remain stronger on the pressure surface. By the third pass the flow structure is very similar to the two previous cases indicating all inlet effects are well washed out by this point.

The velocity profiles for the different simulations indicate that there are likely to be significant differences in heat transfer levels for the first pass with different inlet velocity profiles. In the second pass small differences may be expected with very similar heat transfer levels by the time the third pass is reached.

4.2.3 Original Geometry - Rotating - Heat Transfer

Figures 4.10, 4.12, 4.14 show the unwrapped heat transfer distribution for the three different inlet velocity profiles for the initial geometry with rib reversal.

The largest differences in heat transfer distribution are found in the first pass, closest to the inlet, whilst the distribution in the later passes is found to be less sensitive to the inlet conditions.

In the first pass with a symmetric inlet profile, the streaks of high heat transfer from the rib upwash are far greater from the pressure surface ribs than those on the suction surface, with the heat transfer distribution far from symmetric. The heat transfer on the ribbed pressure surface is also significantly higher than that on the suction surface. In the second pass the pressure surface heat transfer is initially higher due to the flow being biased towards this surface from the first pass. It then decreases with distance down the passage, while the suction surface heat transfer increases, as the flow shifts across towards the suction side of the passage. There is an area of high heat transfer on the trailing edge immediately downstream of the bend as the flow impinges onto this surface as it exits the bend. The region of high heat transfer directly downstream of the bend is also observed at the beginning of the third pass. In this third pass the heat transfer, and rib induced secondary flows, are far greater on the pressure surface due to the Coriolis forces in a radially outward pass.

When the inlet flow is biased towards the pressure surface the heat transfer on this surface

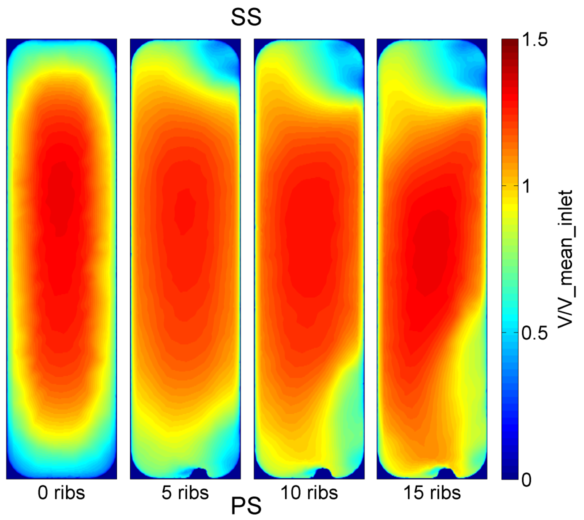

(a) Reversed - Symmetric

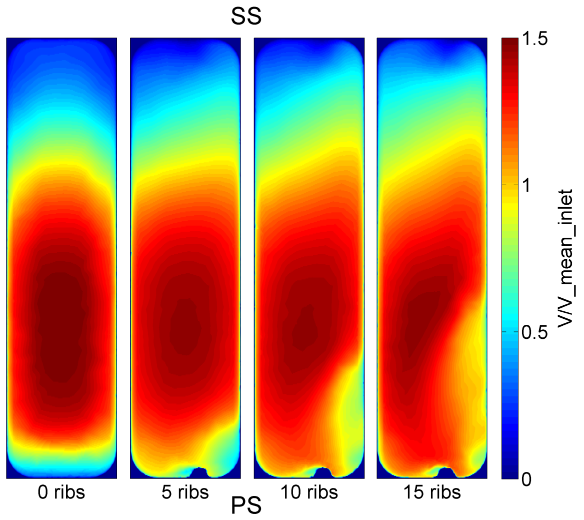

(b) Reversed - PS Bias

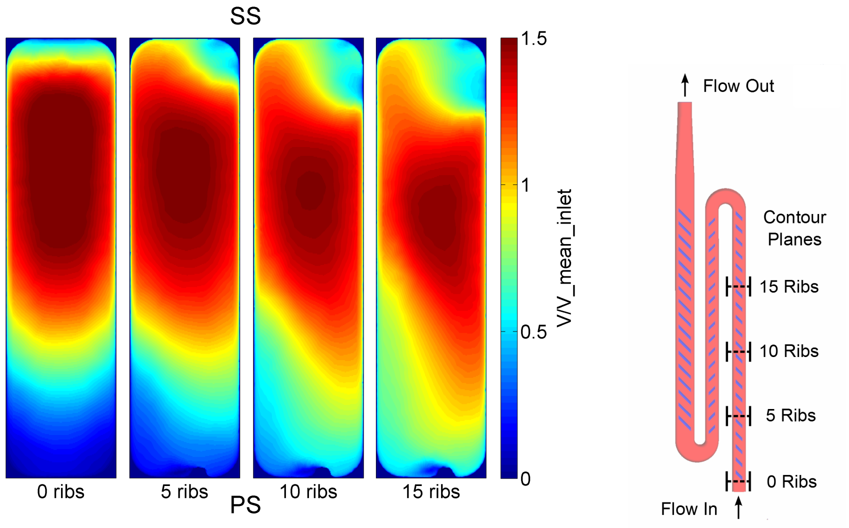

(c) Reversed - SS Bias

Figure 4.4: Velocity contours after 0, 5, 10 and 15 ribs with inlet velocity profiles - Ro = 0.092 - pass 1 - reversed

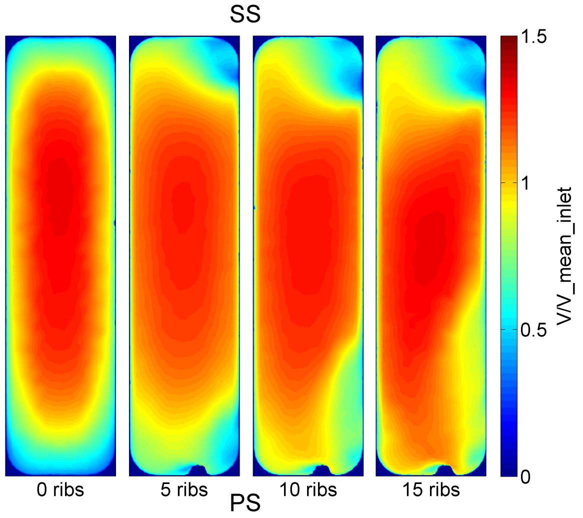

(a) Non-reversed - Symmetric

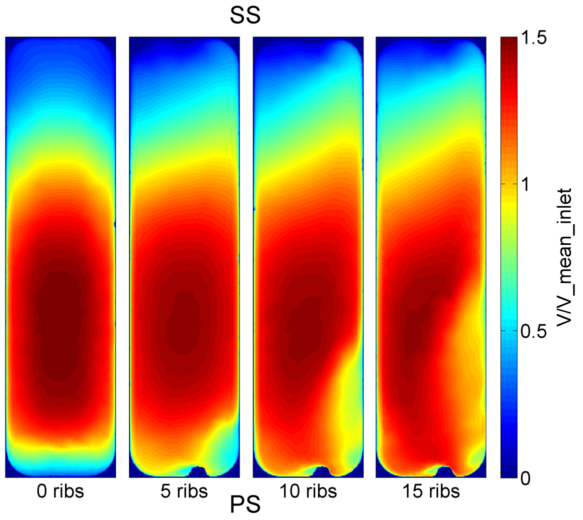

(b) Non-reversed - PS Bias

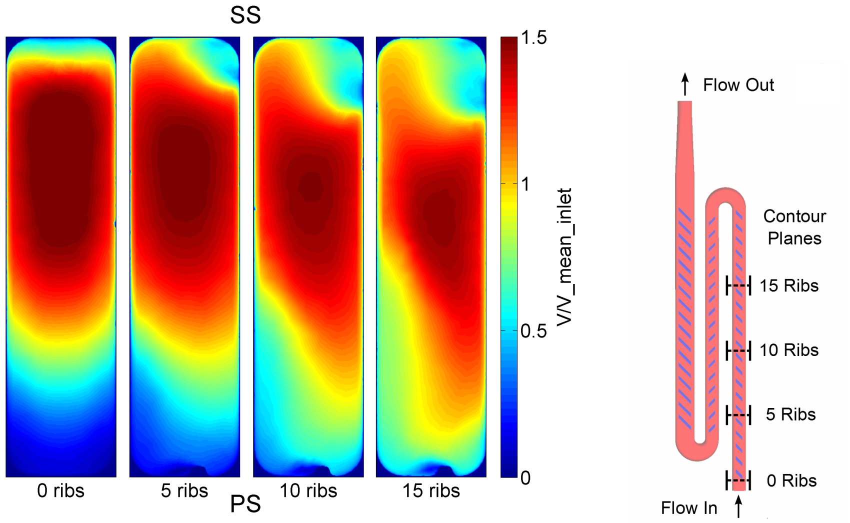

(c) Non-reversed - SS Bias

Figure 4.5: Velocity contours after 0, 5, 10 and 15 ribs with inlet velocity profiles - Ro = 0.092 - pass 1 - non-reversed

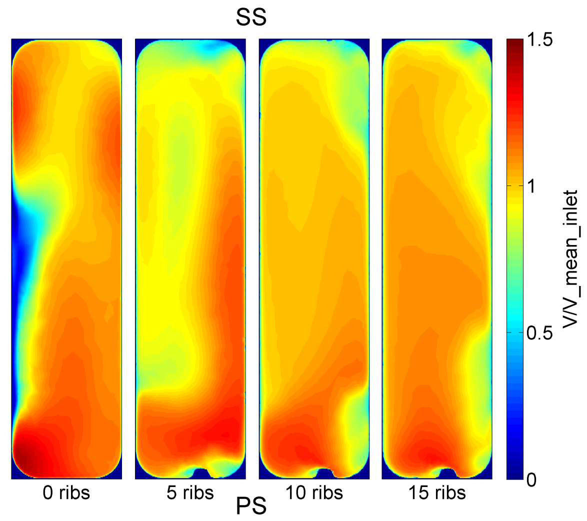

(a) Reversed - Symmetric

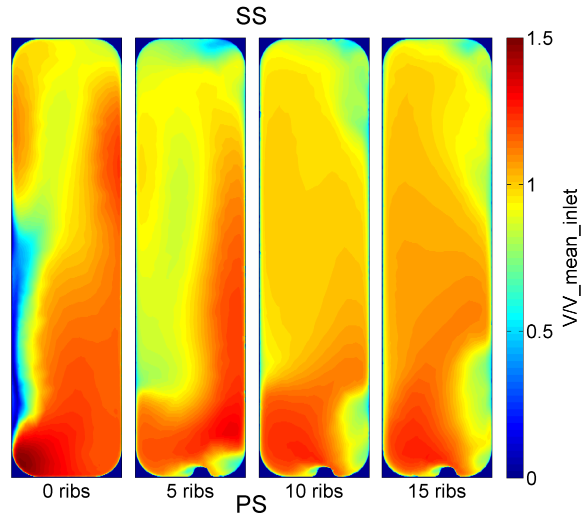

(b) Reversed - PS Bias

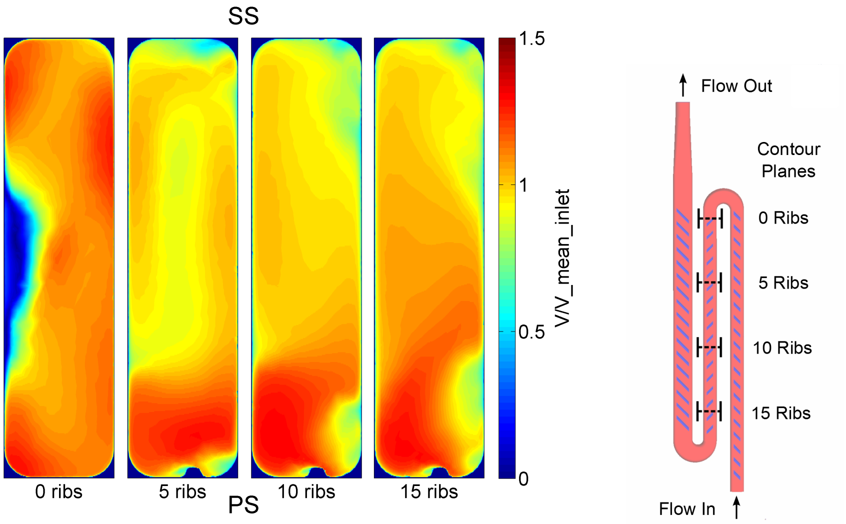

(c) Reversed - SS Bias

Figure 4.6: Velocity contours after 0, 5, 10 and 15 ribs with inlet velocity profiles - Ro = 0.084 - pass 2 - reversed

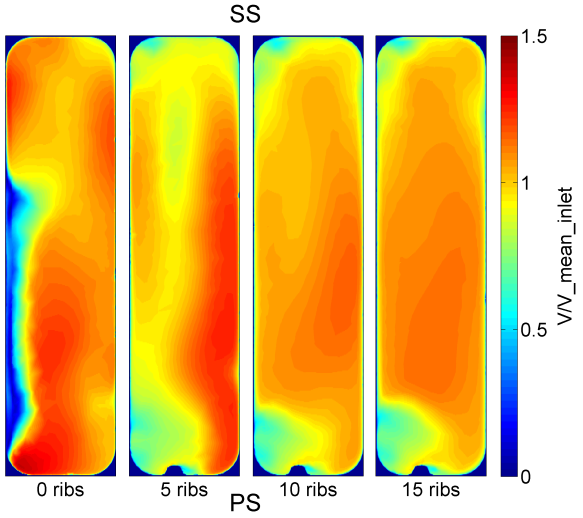

(a) Non-reversed - Symmetric

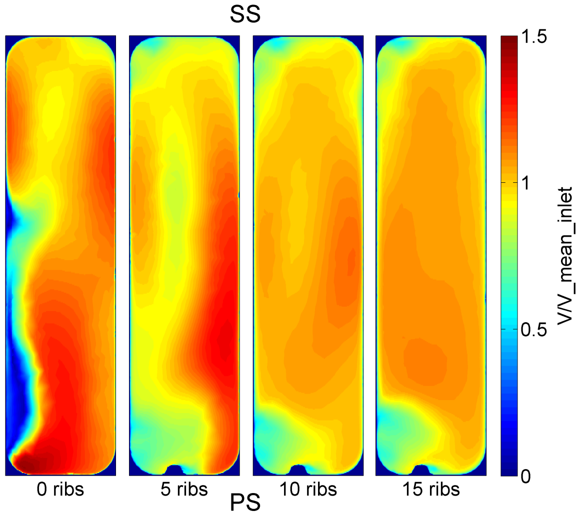

(b) Non-reversed - PS Bias

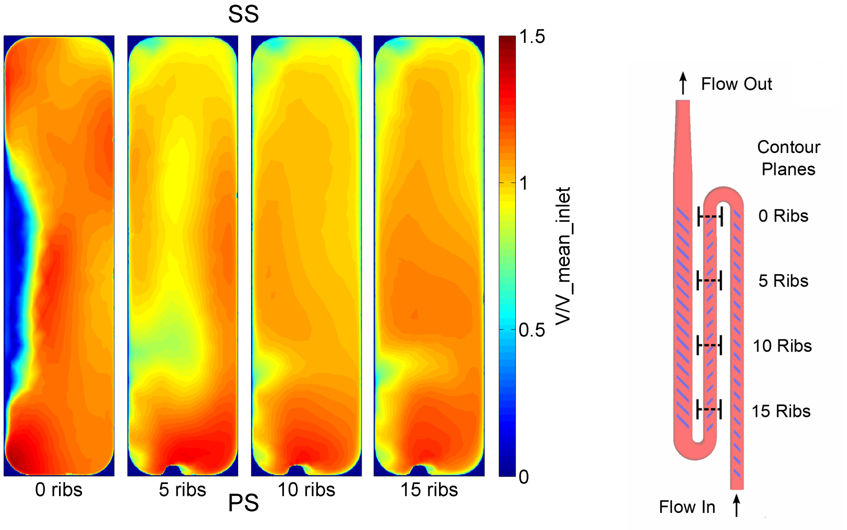

(c) Non-reversed - SS Bias

Figure 4.7: Velocity contours after 0, 5, 10 and 15 ribs with inlet velocity profiles - Ro = 0.084 - pass 2 - non-reversed

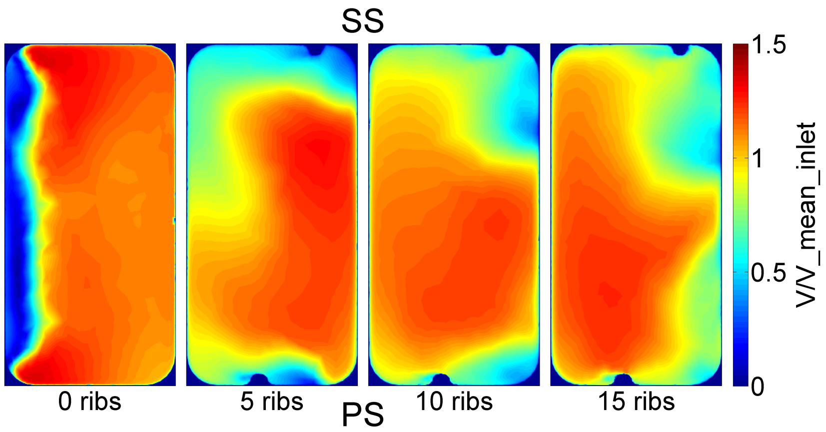

(a) Reversed - Symmetric

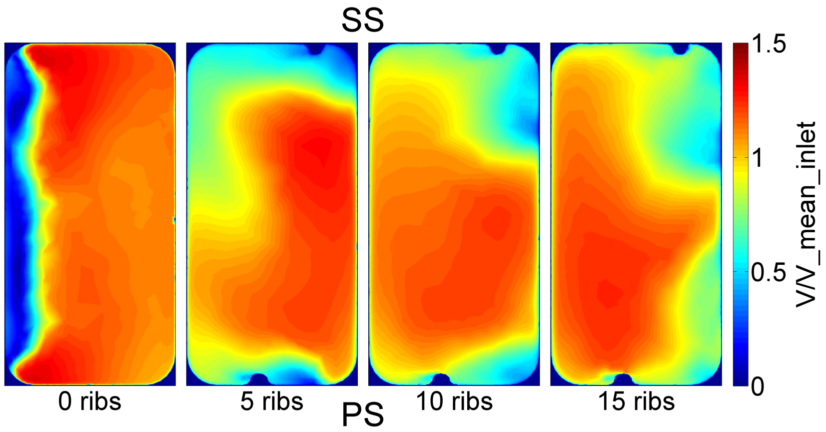

(b) Reversed - PS Bias

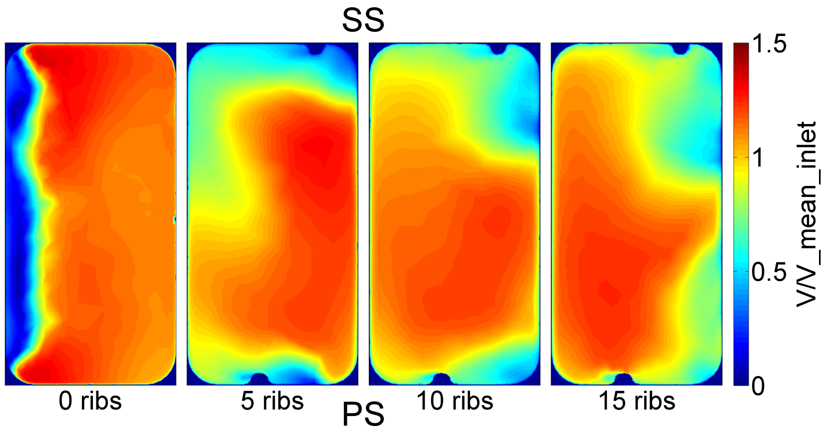

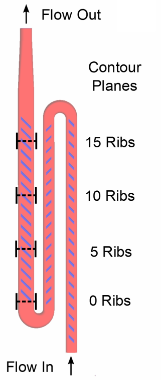

(c) Reversed - SS Bias

Figure 4.8: Velocity contours after 0, 5, 10 and 15 ribs with inlet velocity profiles - Ro = 0.094 - pass 3 - reversed

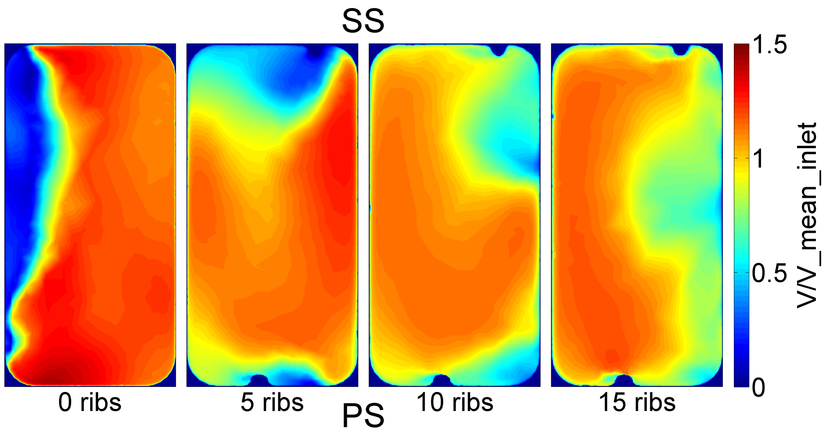

(a) Non-reversed - Symmetric

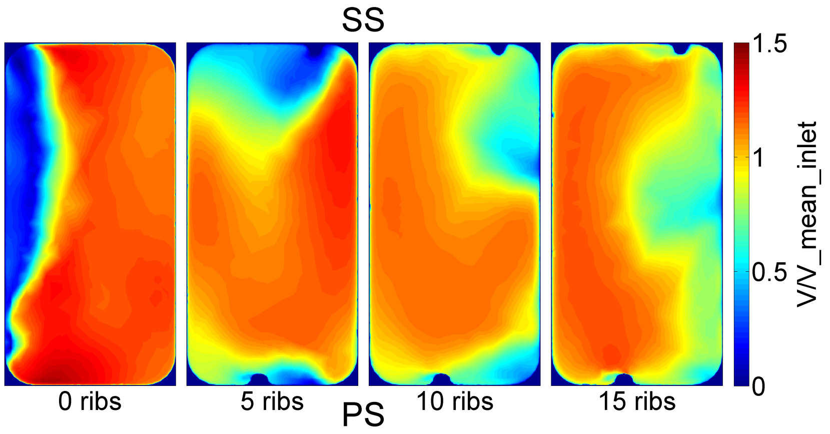

(b) Non-reversed - PS Bias

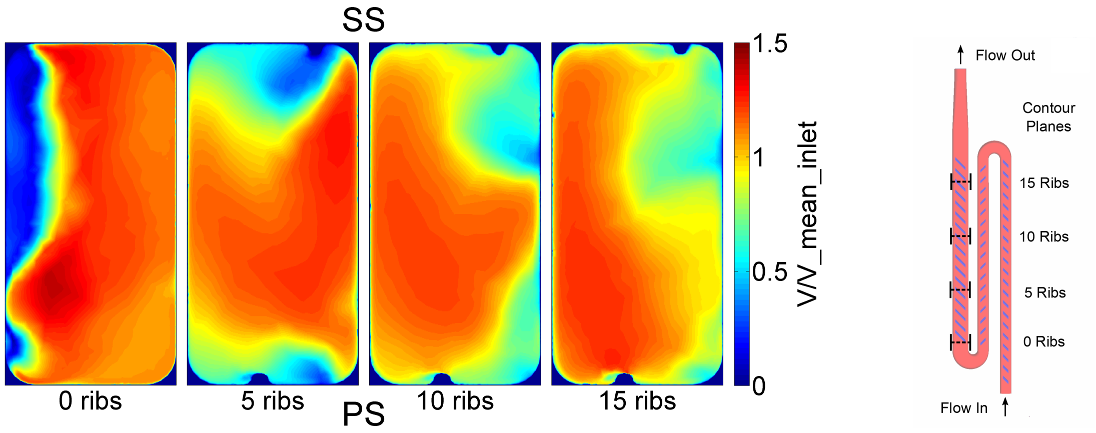

(c) Non-reversed - SS Bias

Figure 4.9: Velocity contours after 0, 5, 10 and 15 ribs with inlet velocity profiles - Ro = 0.094 - pass 3 - non-reversed

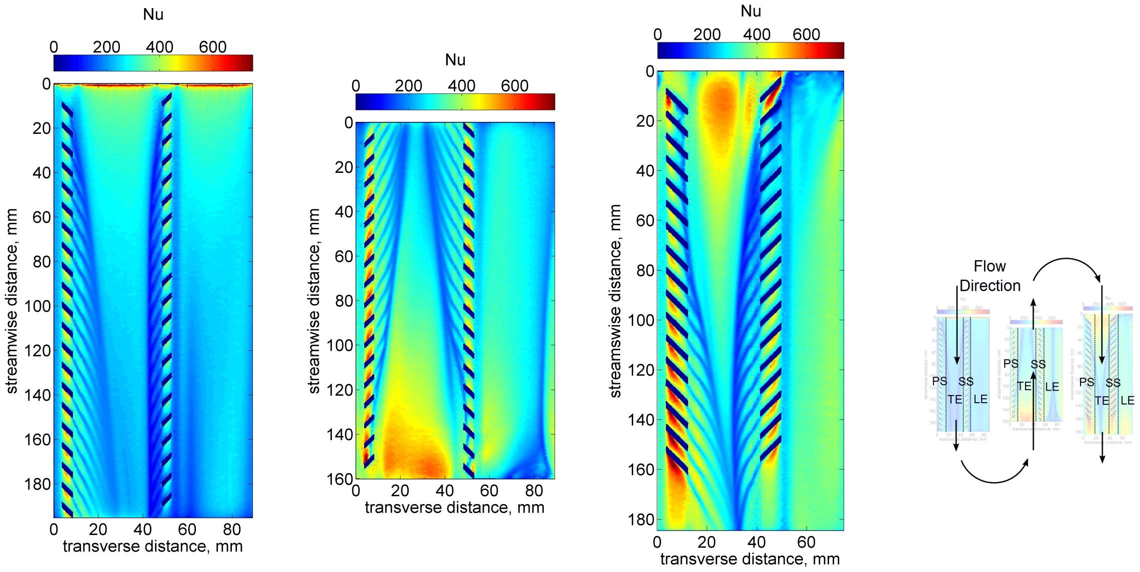

(a) Rev. - Pass 1 (b) Rev. - Pass 2 (c) Rev. - Pass 3

Figure 4.10: Heat transfer with symmetric inlet velocity profile - rotating - reversed

is very high, with strong rib-induced secondary flows, whilst the suction surface heat transfer is extremely low with very little effect of ribs seen. This is due to the initial bias and then containment of the flow towards the pressure surface. The second pass heat transfer is similar to that with the symmetric inlet condition, however with slightly higher heat transfer initially on the pressure surface and a stronger impingement downstream of the bend. There are no visible differences in heat transfer for the third pass, indicating the inlet conditions have no effect on it.

With the inlet flow biased towards the suction surface the heat transfer on this surface in the first pass is higher than that on the pressure surface. However the regions of high heat transfer immediately downstream of each rib decrease in size and strength with distance down the passage as the core flow shifts towards the pressure surface. This is also clear with the start of rib induced, increased heat transfer for the final pressure surface ribs in this pass. In the second pass the heat transfer is largely similar to the two previous simulations however with initally lower heat transfer on the pressure surface, as the flow is less biased towards this side. The third pass heat transfer is indistinguishable from the other simulations, confirming that the inlet profile has no influence on the third pass heat transfer.

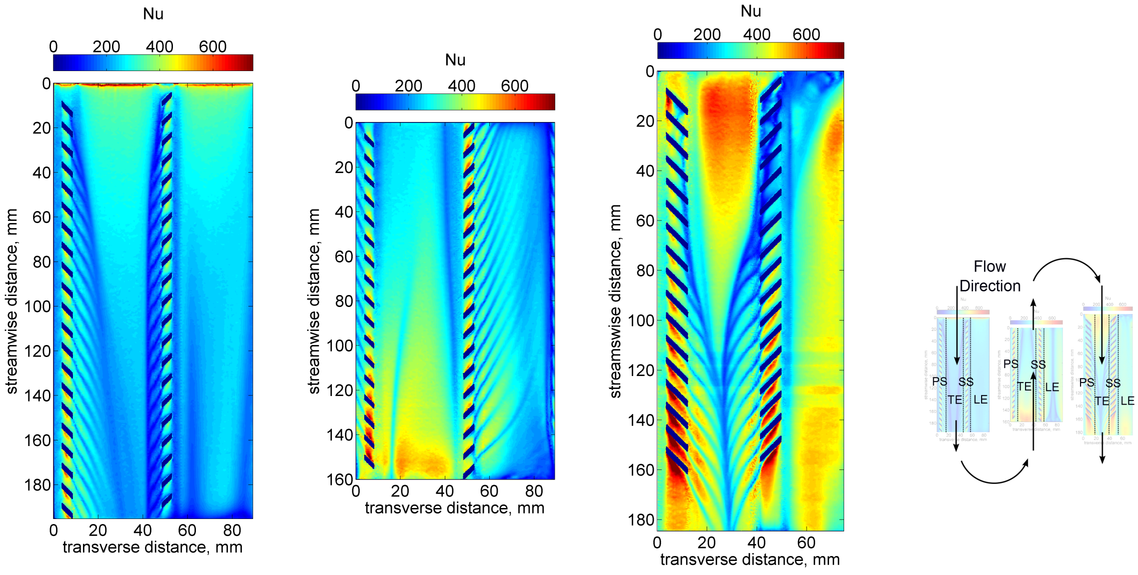

(a) Non-rev. - Pass 1 (b) Non-rev. - Pass 2 (c) Non-rev. - Pass 3

Figure 4.11: Heat transfer with symmetric inlet velocity profile - rotating - non-reversed

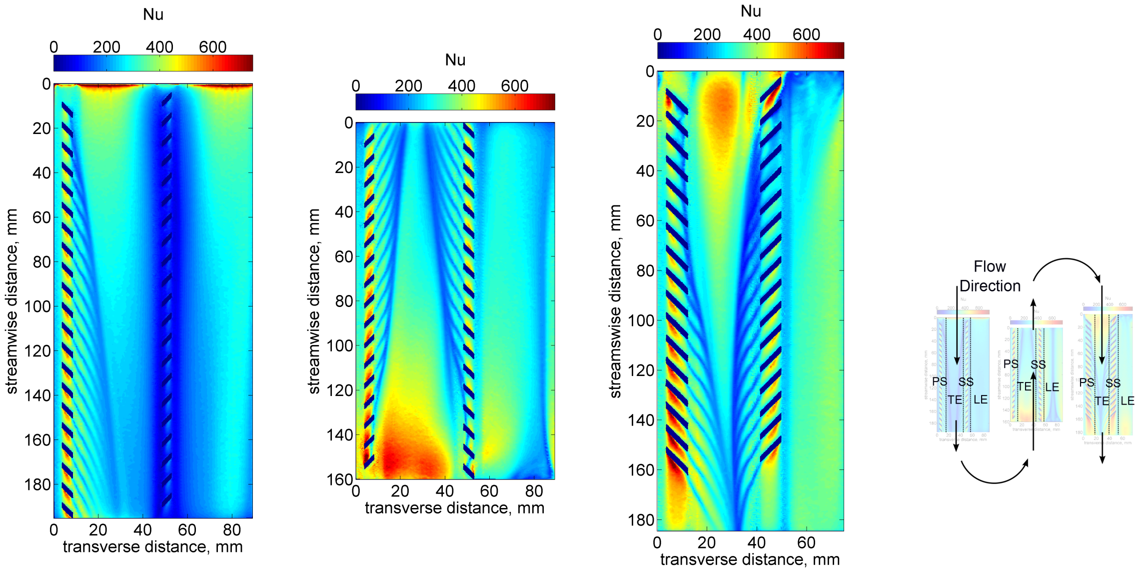

(a) Rev. - Pass 1 (b) Rev. - Pass 2 (c) Rev. - Pass 3

Figure 4.12: Heat transfer with PS bias inlet velocity profile - rotating - reversed

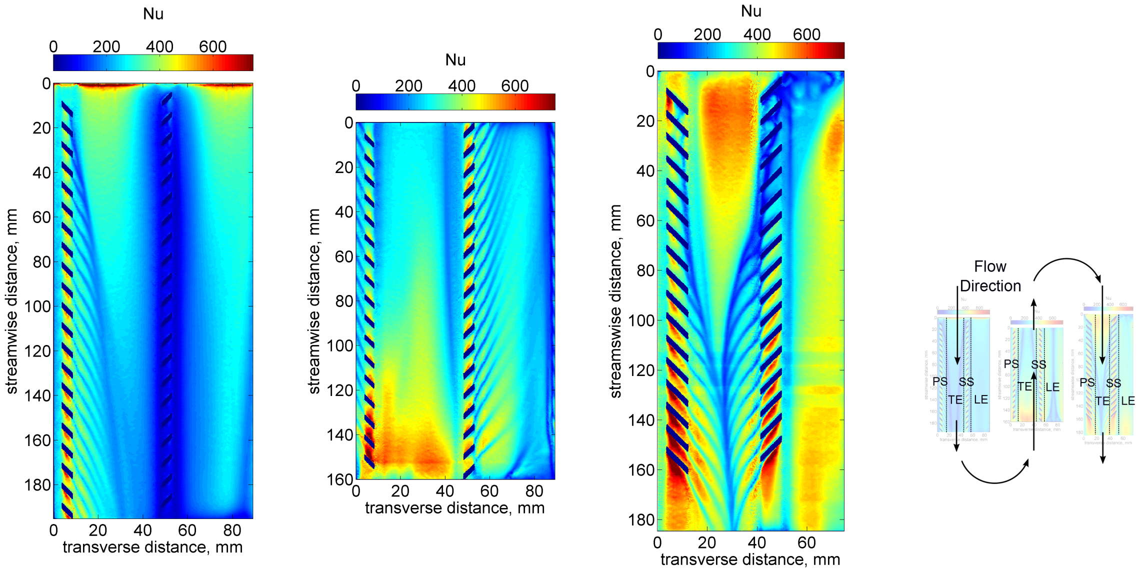

(a) Non-rev. - Pass 1 (b) Non-rev. - Pass 2 (c) Non-rev. - Pass 3

Figure 4.13: Heat transfer with PS bias inlet velocity profile - rotating - non-reversed

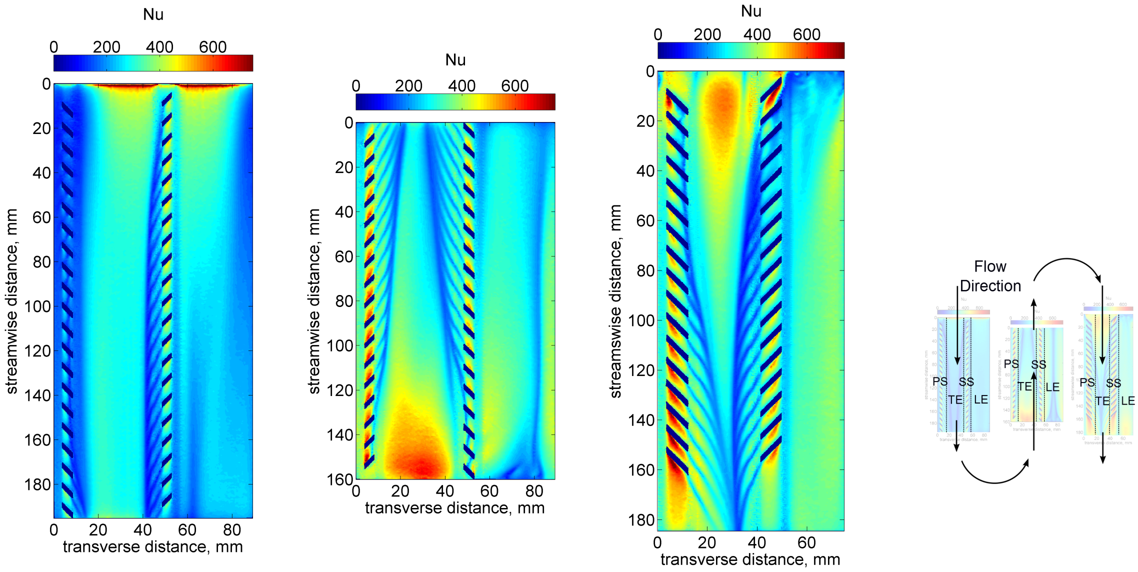

(a) Rev. - Pass 1 (b) Rev. - Pass 2 (c) Rev. - Pass 3

Figure 4.14: Heat transfer with SS bias inlet velocity profile - rotating - reversed

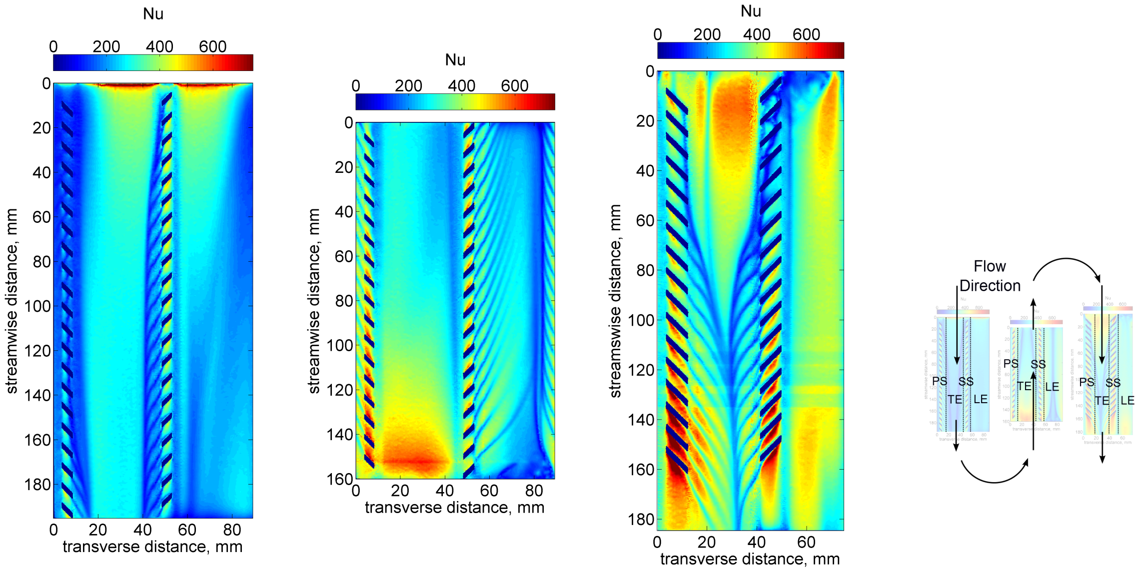

(a) Non-rev. - Pass 1 (b) Non-rev. - Pass 2 (c) Non-rev. - Pass 3

Figure 4.15: Heat transfer with SS bias inlet velocity profile - rotating - non-reversed

4.2.4 No Rib Reversal - Rotating - Flow Structure

This section compares simulations with no rib direction reversal between the 1st-2nd and 2nd-3rd passes to the previous where the ribs in each pass have a reversed orientation with respect to the mainstream flow between consecutive passes. These configurations are illustrated in figure 4.1.

Figures 4.5, 4.7, 4.9 show the velocity contours after 0, 5, 10 and 15 ribs for the three passes, with no rib reversal between passes. These will be compared against the previously described simulations with rib reversal.

For the first pass with all velocity profiles the contours are very similar, as is expected with the first pass geometry being identical.

In the second pass the simulation with no rib reversal shows two clear counter-rotating vortices, the larger being from the suction surface ribs, whilst the original geometry gives very complex flow conditions due to the rib reversal with all inlet profiles. The non-reversed case shows some sensitivity to the inlet profile, unlike the original geometry, particularly for the SS bias.

In the third pass a smoother, and slightly faster development of secondary flows is again seen for the non-reversed case, however there are less pronounced differences due to the wider aspect ratio of the passage. There is little effect on flow structure of the inlet velocity profile with any effects largely washed out by this point.

4.2.5 No Rib Reversal - Rotating - Heat Transfer

Figures 4.11, 4.13, 4.15 show the heat transfer distribution for the simulations with no rib reversal. As with the flow structure these will be compared against the previously described simulations with rib reversal.

As for the stationary simulation, the heat transfer distribution in the first pass is very similar for the two cases as the geometry is identical.

In the second pass there are some significant differences between the reversed and non-reversed simulations. With no rib reversal the flow is able to shift from the pressure to suction surfaces more easily and therefore the secondary flows on the suction surface are much stronger. This leads to higher heat transfer on the suction surface for this radially inward passage. The distribution on the non-ribbed surfaces is also far smoother in the case with no rib direction change, resulting from the simpler flow structure.

The effect of the rib-reversal in the third pass is less pronounced, as the rotation combined with the wider passage aspect ratio help to wash out the effect of the upstream pass ribs. However, there is still slightly higher heat transfer observed throughout this pass with no reversal in rib direction, as the flow development is not reset at the start of this passage.

These simulations indicate that the reversal in rib direction causes additional complexity to the flow structure but does not increase heat transfer levels. The simulations with no change in rib orientation between the three passes appear to give better heat transfer performance for the second and third passes with higher overall heat transfer levels and a more even distribution. However the passage with no rib reversal is more sensitive to the inlet velocity profile with effects visible in both the first and second passes.

4.2.6 Average Heat Transfer

Figures 4.16-4.18 show the PS and SS heat transfer values for each pass and inlet velocity profile under stationary and rotating conditions.

For the first pass it is found that both geometries give very similar results and show the expected effects of rotation for the no inlet bias case with the PS exhibiting higher heat transfer

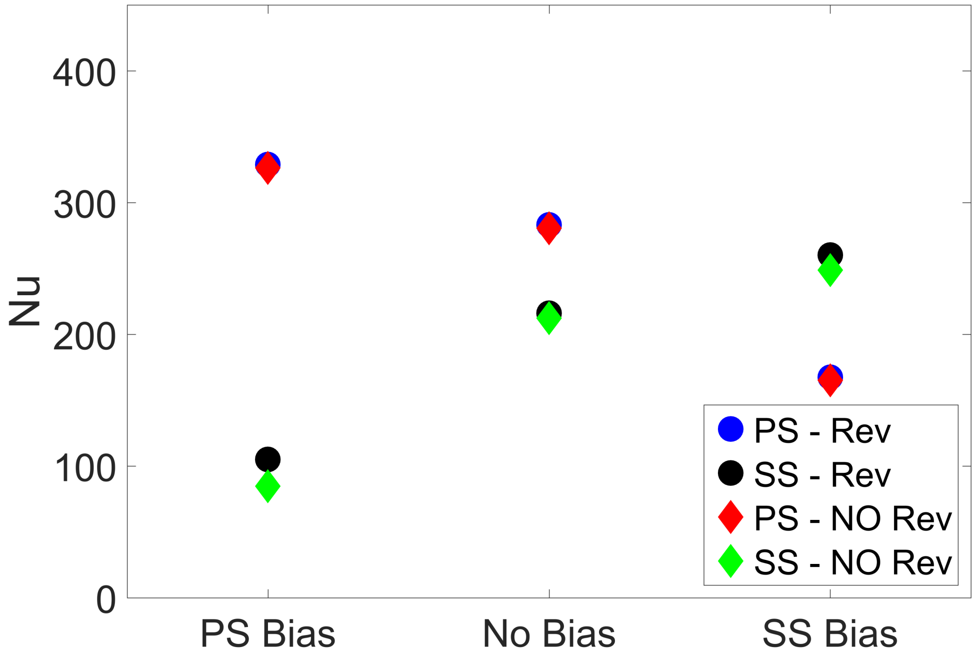

Figure 4.16: Average Nusselt number with different inlet profiles - pressure and suction surfaces - rotating - pass 1

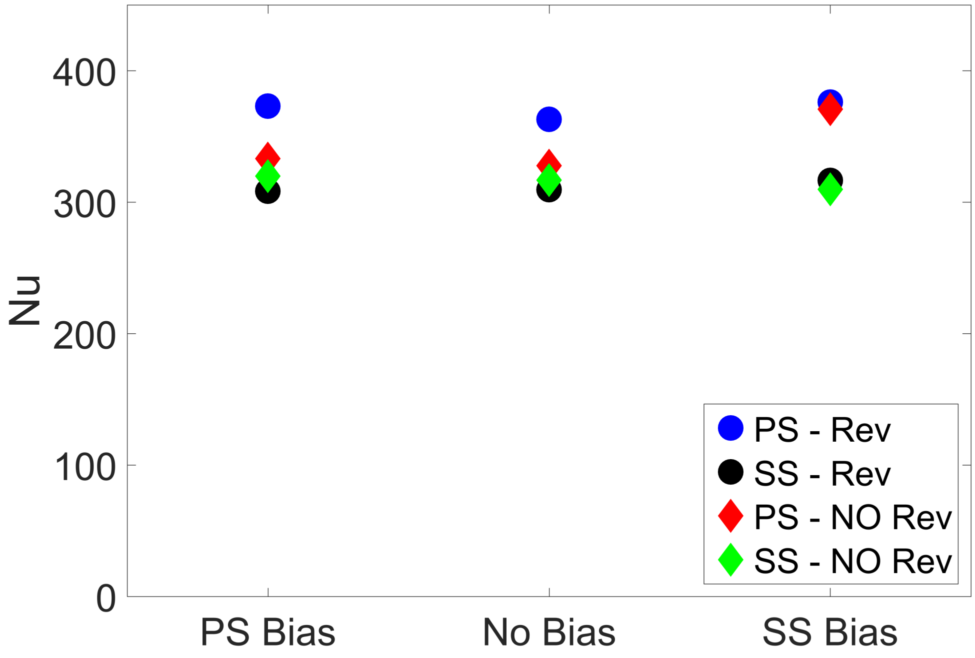

Figure 4.17: Average Nusselt number with different inlet profiles - pressure and suction surfaces - rotating - pass 2

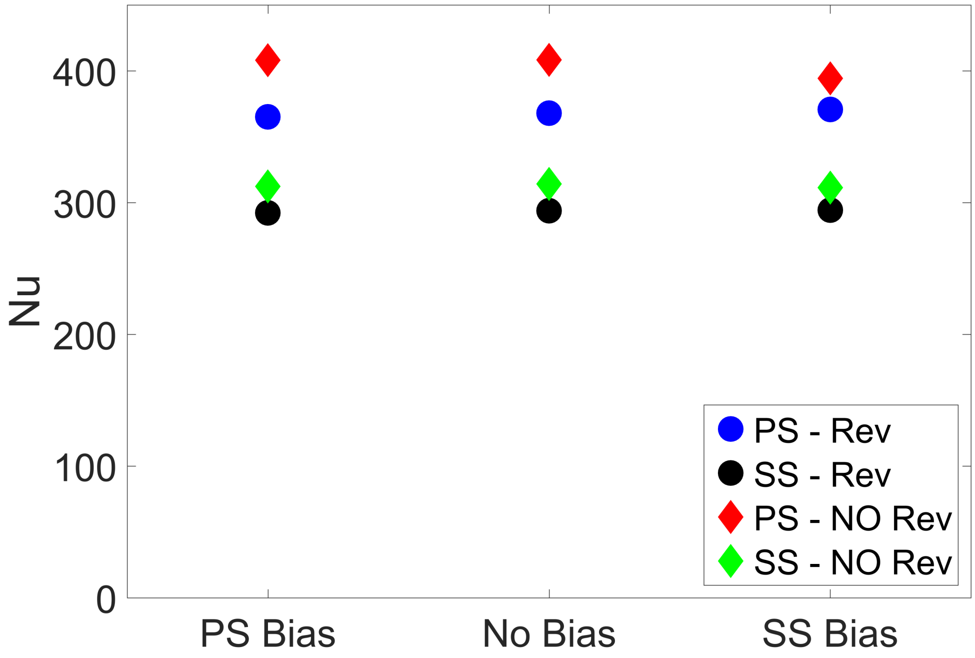

Figure 4.18: Average Nusselt number with different inlet profiles - pressure and suction surfaces - rotating - pass 3

than the SS. With a PS bias this effect is enhanced, while for a SS bias this is reversed with the initial shift in core flow causing higher heat transfer on the suction surface.

Some differences are observed in the second pass. With rib reversal there is higher heat transfer on the pressure surface as the shifted core flow from the first pass is ‘trapped’ near to this side of the passage, enhancing the heat transfer on it. Where there is no rib reversal the flow is able to migrate back towards the suction surface during the second pass and therefore the heat transfer levels are much more closely matched.

In the third pass the results are consistent across the inlet profiles for both geometries, indicating that any effect of the inlet profile is washed out by this point. The non-reversed rib geometry shows higher heat transfer than the geometry with reversed ribs. This is due to the secondary flows being set up faster and their direction is not reversed, resulting in more developed, stronger secondary flows and consequently higher heat transfer levels.

4.2.7 Comparison of Inlet Profiles with Experimental Results - First Pass

In this section the heat transfer results from the rib reversed simulations are compared to experimental and CFD results presented in the previous chapter. The complex upstream geometry

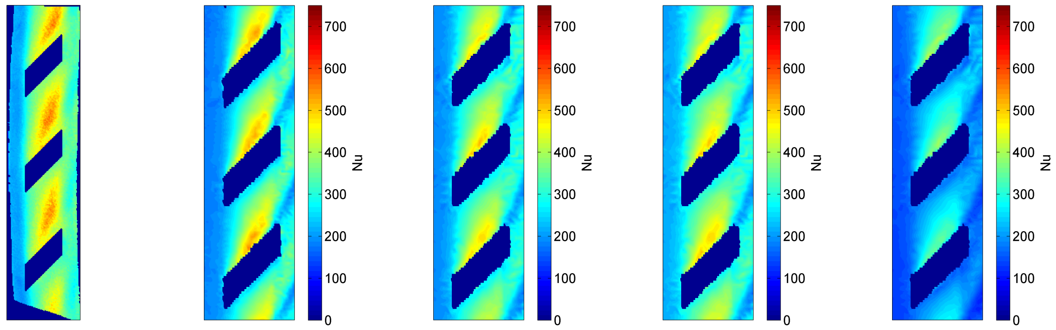

(a) Exp. (b) CFD (c) Sym (d) PS (e) SS

Figure 4.19: PS1 comparisons of experiment, CFD and inlet velocity profiles - stationary

in the experimental setup with an impinging jet into a narrow plenum led to modelling difficulties, particularly under rotating conditions. The rotational simulations gave heat transfer distributions that were very different from the experimental results, thought to be due to incorrect modelling of the upstream flow resulting in an incorrect velocity profile into the serpentine passage. The simulations with varied inlet profiles offer a chance to test this. If results with a particular profile are close to the experimental results it is possible that the upstream modelling led to these errors, rather than the modelling of the passage themselves, which was reasonably accurate for the second and third passes under both stationary and rotating conditions.

Figure 4.19 gives the first pass pressure surface results under stationary conditions, with figure 4.20 giving the suction surface results.

Under stationary conditions the full CFD gives results very close to those from the experiment, as does the symmetric profile. However the biased profiles are very different. This indicates that under stationary conditions the inlet profile is largely symmetric and also well modelled in the simulations incorporating the full inlet geometry.

Figure 4.21 gives the first pass pressure surface results under rotating conditions, with figure 4.22 giving the suction surface results.

With rotation it was found that the full CFD showed very poor agreement with the experiment, which is thought to be due to incorrect modelling of the upstream geometry. The symmetric inlet profile gives similar results to the full simulation, whilst the simulations with biased inlet profiles have very different heat transfer results. The suction surface biased profile gives even greater discrepancies however the pressure surface bias offers much closer levels to the experimental data. This indicates that the large discrepancies found in the previous chapter

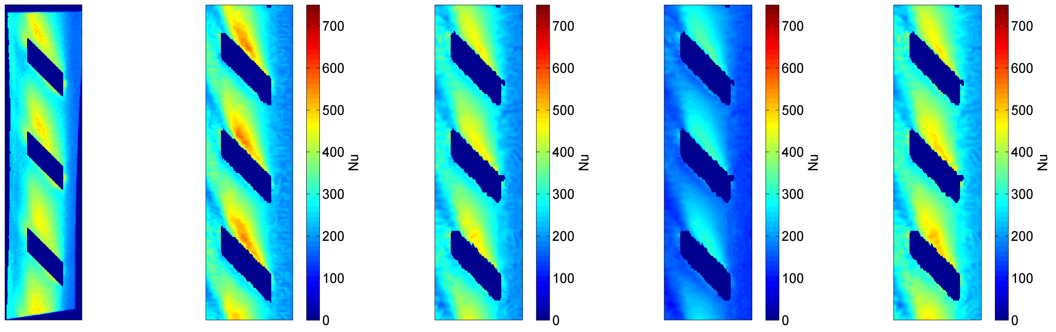

(a) Exp. (b) CFD (c) Sym (d) PS (e) SS

Figure 4.20: SS1 comparisons of experiment, CFD and inlet velocity profiles - stationary

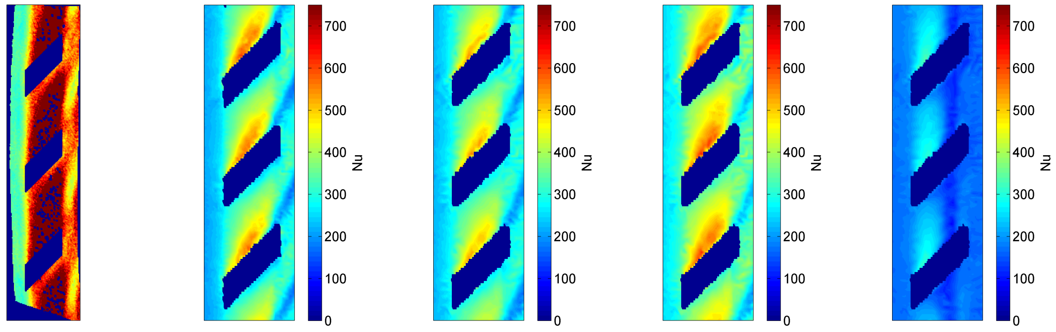

(a) Exp. (b) CFD (c) Sym (d) PS (e) SS

Figure 4.21: PS1 comparisons of experiment, CFD and inlet velocity profiles - rotating

are likely to be due to incorrect upstream modelling, as far closer results for the first pass can be obtained by imposing an alternative inlet profile, in this case a PS bias. The inlet profile is also shown earlier to have a minimal effect on the heat transfer in the later passes which previously had more positive results with regards to the experimental data.

Therefore the large discrepancies found in the previous chapter are most likely due to incorrect modelling of the upstream conditions.

4.3 Summary and Conclusions

In summary two aspects of ribbed radial serpentine cooling passages have been investigated. Three different inlet velocity profiles have been simulated with the flow structure and heat transfer distribution investigated. The effect of reversing the rib direction relative to the mainstream flow between passages has also been investigated. Results were then compared to previous

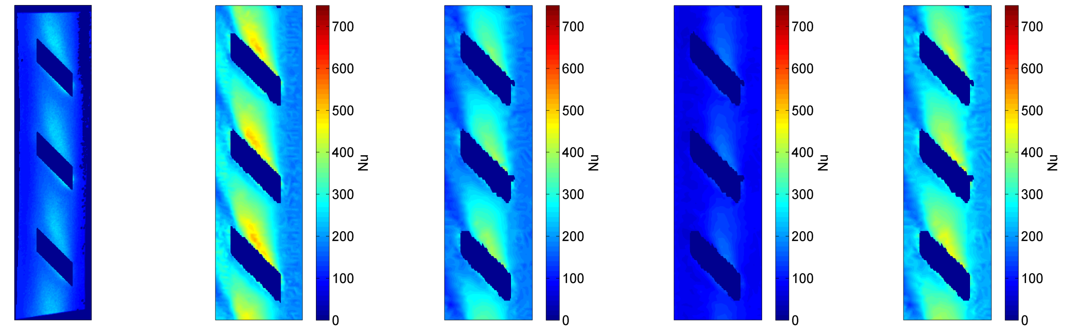

(a) Exp. (b) CFD (c) Sym (d) PS (e) SS

Figure 4.22: SS1 comparisons of experiment, CFD and inlet velocity profiles - rotating

experimental and CFD results from chapter 3.

The following conclusions have been drawn from this investigation.

1. The inlet velocity profile can have a dominant effect on the flow structure and heat transfer in the first pass of a serpentine passage under stationary and rotating conditions, with a far lesser effect on subsequent passes.

2. The inlet conditions must therefore be well modelled in order to obtain accurate heat transfer predictions for ribbed radial passages, with very large errors possible if they are not accounted for.

3. There is potential for a reduction in coolant flow requirement by using upstream conditions to 'design' an inlet profile to positively influence the heat transfer distribution, particularly in locations near to the first pass of a radial cooling passage or where an asymmetric heat transfer distribution, with respect to the pressure and suction surfaces, is desirable.

4. A coolant passage with no reversal in rib orientation greatly changes the flow structure and gives a higher level of heat transfer in the third pass.

5. Incorrect modelling of inlet conditions have been shown as the most likely cause of the discrepancies found between experimental and computational results in chapter 3.

6. Experimental setups must take inlet effects into account, with more easily modelled inlet geometries, in order to provide good validation data for CFD methodologies.

Chapter 5

Leading Edge Impingement - Rotating

Impingement cooling is increasingly being used in the leading edge of turbine blades where very high heat loads are found. This is possible due to advances in materials and changes in mechanical design from shrouded to shroudless blades. This has resulted in a reduction in web stress levels which allows the use of impingement holes through the web despite the stress concentrations that they introduce.

This chapter looks to validate commonly used industrial CFD methods under rotating conditions for leading edge impingement systems using experimental results from the RHTR. As for the radial passages, the experimental data used in this chapter was collected by researchers at Rolls Royce, another partner in the ERICKA programme. The full experimental data is presented by them in [102].

5.1 Simulation Setup

5.1.1 Geometry

In the opposing arm of the RHTR to the radial passages leading edge impingement geometries were tested. This chapter investigates the heat transfer characteristics and CFD performance for an Avio 'box section' geometry [103].

The geometry consists of a trapezoidal channel which feeds five impingement jets, figure 5.1. These jets have a converging cross-section with a sharp edged outlet and a racetrack cross section. They impinge onto the walls of a leading edge passage with a triangular cross sec-

Table 5.1: Geometry details for leading edge impingement configuration

No. of Jets	5
D_H	5.08 mm
z/D_H	2.3
p/D_H	3.5
Target surface open angle	41.42^o

tion that has an angle of 41.42^o between the target surfaces. The five jets are partially confined by fins that extend across approximately two-thirds of the passage height from the leading edge of the channel at the midpoint between jets. There are three rows of holes that bleed off flow, these simulate a showerhead hole and a film cooling row on each of the pressure and suction sides and feed into separate plenums. There is an outlet at the end of the feed channel to allow cross-flow in this passage. Geometric details are given in table 5.1.

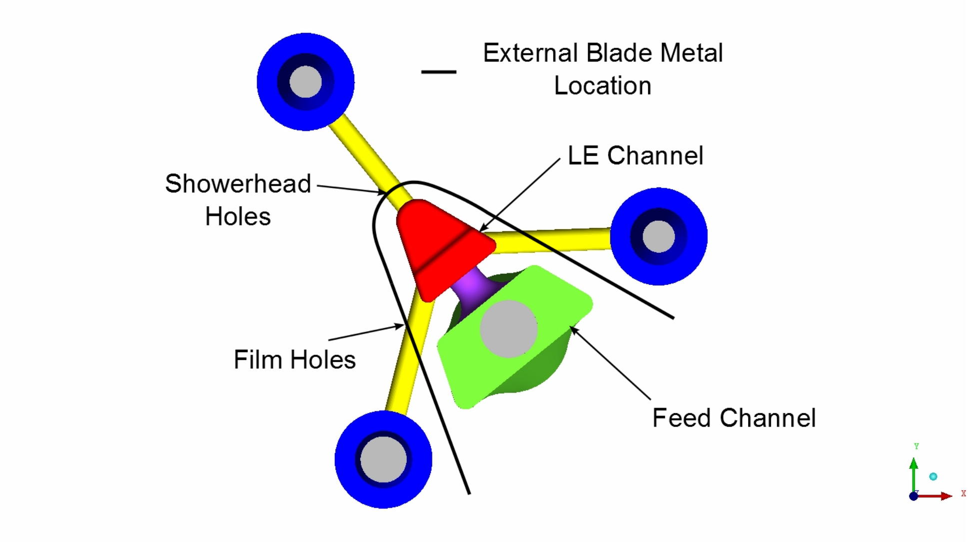

Figure 5.1: Geometry for CFD simulations

5.1.2 Mesh Setup

The meshing process used for the impingement geometries was the same as that for the radial cooling passages, with an unstructured tetrahedral with a number of prismatic layers to adequately capture the boundary layer. The meshing was undertaken using the ICEM 14.0 software. The mesh details are shown in table 5.2 with an image of representative mesh sizing of the impingement channel given in figure 5.2.

Table 5.2: Mesh details for impingement geometry

No. of Cells	10.9 million
No. of Prism Layers	15
Max y^+	1.879
Area-averaged y^+	0.516

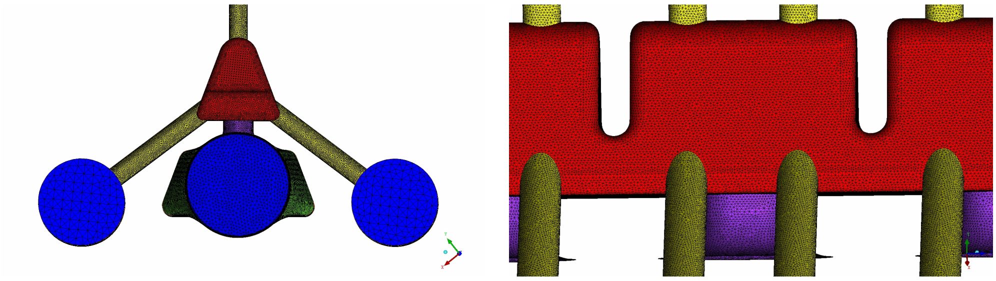

Figure 5.2: Mesh detail for impingement geometry

5.1.3 Solver Setup and Turbulence Modelling

The solver setup used the same methodology as for the radial passages in chapter 3. The turbulence modelling was slightly different however, with initial work utilising the k-ω SST turbulence model for its better performance for previous configurations tested in the ERICKA programme [52], under stationary conditions. This research gives the chance for the methodologies to be tested under rotating conditions.

5.1.4 Post-Processing

CFD

Post-processing for the computational simulations was done in the same way as for the radial passages, with heat flux and temperature data extracted in the form of ASCII files before being read into a bespoke Matlab code. The heat transfer coefficient on the impingement target surface was calculated using equation 5.1.

$$h = \frac{q}{T_{feed} - T_{wall}} \tag{5.1}$$

The gas temperature (represented by T_{feed}) used to calculated the HTC at each data point

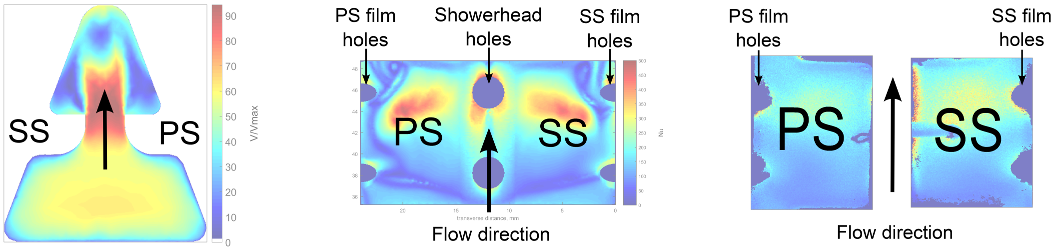

(a) Flow Structure - CFD (b) Heat Transfer - CFD (c) Heat Transfer - Exp.

Figure 5.3: Results presentation for impingement geometry

is the interpolated centreline temperature in the feed channel at the corresponding streamwise location.

Experimental

Experimental heat transfer results were also calculated using a centreline gas temperature. Multiple thermocouples were present on the centreline of the feed channel for each geometry, and the readings for these were interpolated to be used to calculate a heat transfer coefficient using the transient liquid crystal method.

Some distortion of the image is found due to the 'fish-eye' camera lens and therefore a bespoke Matlab script was used to remove this from the images and allow them to be directly compared to the CFD simulations. The experimental HTC maps were only of a small section of the target surface for the impingement geometries due to the constraints on the camera position in the rotating rig. For this geometry the available data was on the pressure and suction surfaces of the central jet.

As the target surface is flat there is little distortion in the images and therefore comparisons can be made fairly simply and accurately, both in terms of spatial distributions and streamwise or circumferential averages.

Results Presentation

Results will be presented as normalised velocity magnitude contour plots through a cross section of the central (third) impingement jet, and Nusselt number maps for the pressure and suction surfaces for this central jet. These are illustrated in figure 5.3.

Table 5.3: Impingement simulation details

Test Point	Re. No.	Rot. Speed (rpm)	Ro. No.	Bo. No.
3	57180	0	0	0
7	55330	600	0.0049	0.0010
5	49020	800	0.0073	0.0022
6	50940	1000	0.0088	0.0032
8	50410	1550	0.0138	0.0078
16	49720	1850	0.0167	0.0115
17	49000	2050	0.0187	0.0145

5.2 Results

Results are presented for multiple test points each with a similar Reynolds number, but with increasing rotation numbers to assess the effect of rotation and CFD performance over a range of conditions. Details of the test points are given in table 5.3.

5.2.1 Flow Results

Figure 5.4 shows normalised velocity magnitude contours on the plane through the centre of the central (third) impingement jet for each test point.

The contours for the stationary simulation show that the flow in the feed passage is symmetrical, as expected due to the symmetrical geometry, with the flow smoothly accelerating into the impingement jet. The jet itself is therefore symmetrical as it enters the leading edge passage and has a relatively flat velocity profile. The jet velocity is quickly reduced when it enters the target surface chamber due to the confined nature of the jet. In the leading edge passage itself, the jet impinges on the centre of the leading edge target surface before recirculating back along the pressure and suction surfaces. Some flow exits through the central showerhead holes under the jet however a significant portion recirculates and exits through the pressure and suction surface film holes.

When rotation is introduced there are large changes in the flow structure, particularly in the feed channel. There is significant asymmetry in the velocity distribution in the feed channel which in turn results in a non-uniform velocity profile in the impingement jet itself. The Coriolis

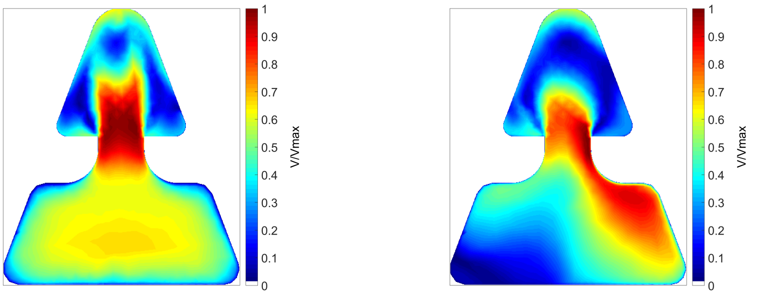

(a) TP3 - Stat (b) TP7 - Ro = 0.0049

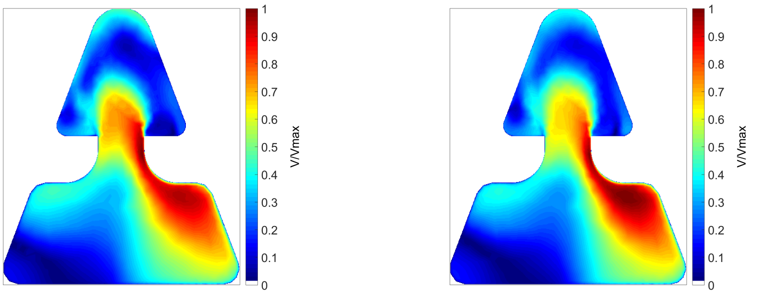

(c) TP5 - Ro = 0.0073 (d) TP6 - Ro = 0.0088

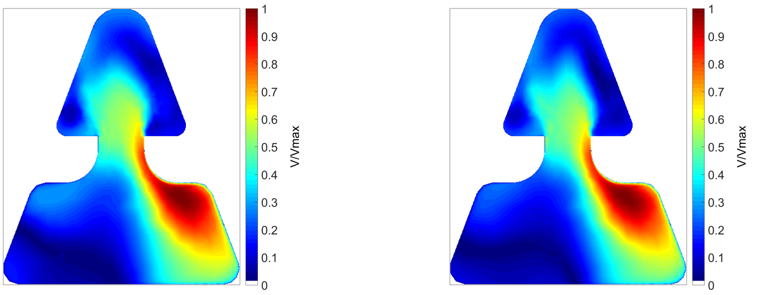

(e) TP8 - Ro = 0.0138 (f) TP16 - Ro = 0.0167

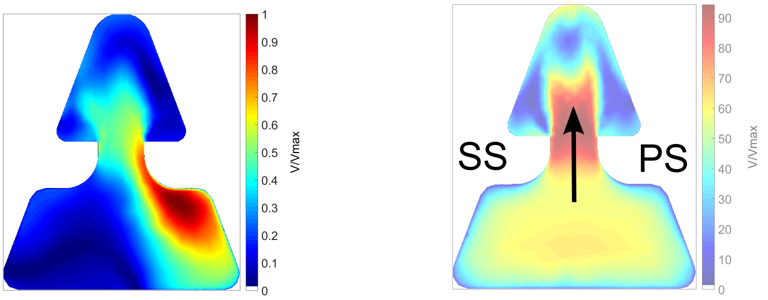

(g) TP17 - Ro = 0.0187

Figure 5.4: Flow structure - CFD

force induced by rotation caused a shift in the flow to the pressure surface of the feed chamber, as it is a radially outward passage. This shift in the inlet flow condition directs the impingement jets towards the suction surface of the leading edge passage, giving an asymmetric flow structure with this region. The shift of flow in the feed channel is seen clearly for all test points, with a larger effect observed with increasing rotational speed. The jet itself is not deflected by the rotation due to the high velocity flow that is present, but the changes in jet structure are heavily dependent on the changes in flow distribution with the feed channel.

Due to the very large change in flow structure with rotation a significantly different heat transfer distribution is present when rotation is increased, however it is likely to be driven by the effects in the feed channel rather than those in the leading edge channel, or jet deflection.

5.2.2 Heat Transfer Results

Figure 5.5 shows the heat transfer for the third (central) jet of the geometry for each of the test points given in table 5.3.

The heat transfer distribution under stationary conditions is largely symmetrical as expected from the flow structure. There are two main regions of high heat transfer on the PS and SS as the jet impinges on these inclined surfaces. These are angled in the streamwise direction due to the crossflow in the feed passage, which also causes the peak to be offset towards the downstream side of the chamber, despite the jet being positioned centrally. This is made possible by the contoured nature of the jet geometry. Very high heat transfer is also seen at the central film hole as it is located under the impingement jet, and also has a large mass flow rate entering it, while some areas of enhancement are present on the shoulder film holes.

There are regions of low heat transfer towards the lower side (upstream) of the target surface where the jet does not impinge and the flow is recirculating. The small regions of enhanced heat transfer adjacent to each of the film holes are due to the acceleration of the flow as it enters the holes; these have been previously explained in [104, 105].

Under rotating conditions there are significant changes to the heat transfer distribution. The velocity profile of the jet is no longer uniform and subsequently the heat transfer is significantly enhanced on the suction side of the target surface, both in terms of size and magnitude. The peak is also shifted a little further upstream on the target surface. The pressure side heat transfer is similar to the stationary case however is shifted towards the centre, near to the central film hole, which has significantly higher heat transfer around it. The peak value on this surface is reduced with the jet spread over a larger area. There are still some areas where there is recirculation of the flow, particularly on the pressure surface, where the heat transfer levels are

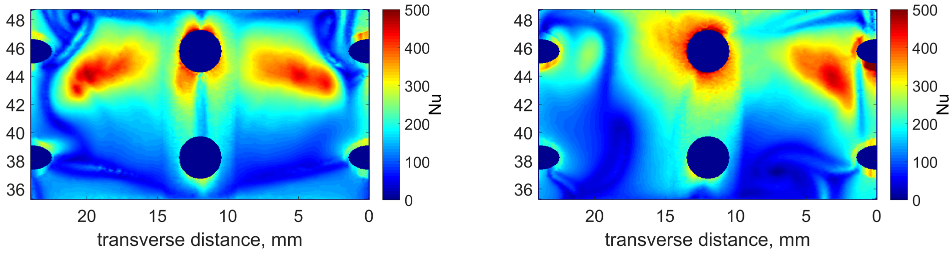

(a) TP3 - Stat (b) TP7 - Ro = 0.0049

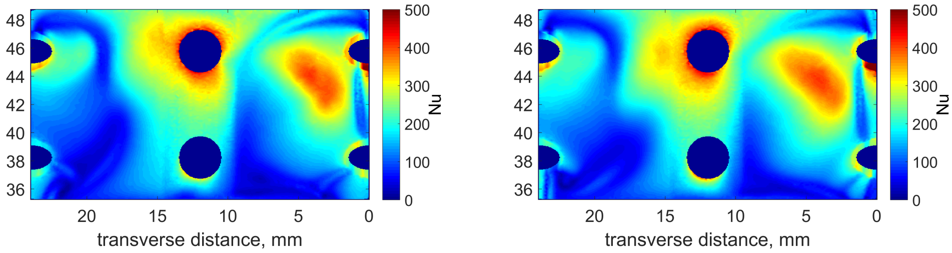

(c) TP5 - Ro = 0.0073 (d) TP6 - Ro = 0.0088

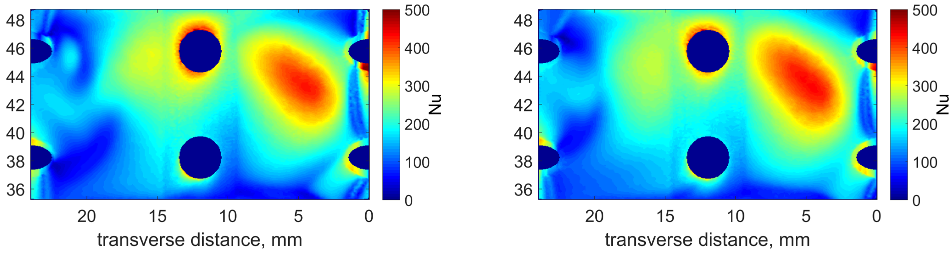

(e) TP8 - Ro = 0.0138 (f) TP16 - Ro = 0.0167

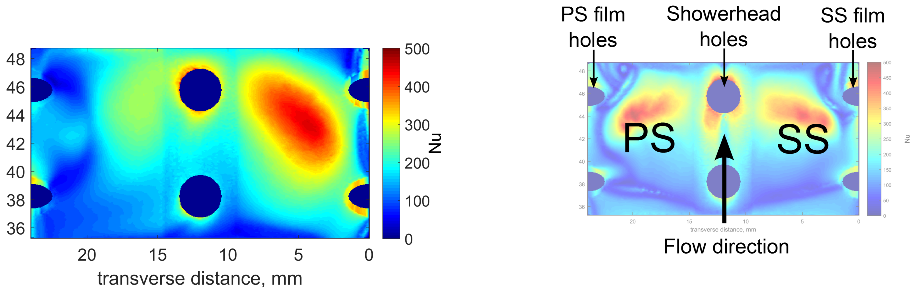

(g) TP17 - Ro = 0.0187

Figure 5.5: Heat transfer - CFD

reduced. However the jets are in general more spread for the rotating simulations and therefore fewer low heat transfer regions are observed.

The effects in heat transfer distribution are consistent with increasing rotational speed, with an increased region of high heat transfer, both in size and magnitude, on the suction surface and a corresponding reduction on the pressure surface.

These effects are primarily caused by flow structure changes in the feed channel. The shift in flow towards the pressure surface of the feed alters the jet velocity profile, resulting in more jet spreading and a directed jet towards the suction surface. The heat transfer changes are dominated by this effect, with very little influence of rotation found on the jet and target chamber due to the higher velocities and confined nature of the flow in this region.

5.2.3 Comparison to Experiments

The heat transfer results obtained from the CFD simulations will now be compared to those from the experimental setup [102]. The same test points will be used as in the previous section.

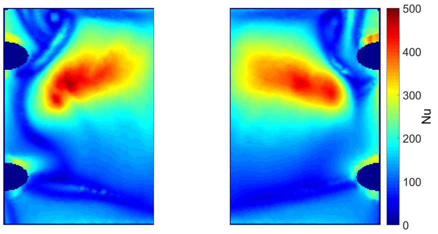

(a) Experimental

(b) CFD

Figure 5.6: HTC map comparison - TP3

Figure 5.6 shows the comparison between the CFD simulation and experimental results under quasi-stationary conditions.

The CFD predictions perform well in some areas however there are still significant differences, even under stationary conditions. Overall heat transfer levels are predicted reasonably well, however peak values are found to be significantly higher in the CFD simulations than the experiments. Both figures show regions of high heat transfer in a similar location, under the impinging jet, with much lower heat transfer in the recirculation regions away from this jet. Despite over-predicted levels by the CFD in the peak regions, similar levels are found in the areas with low Nusselt numbers. The experimental data also shows some asymmetry between the pressure and suction surfaces, which is not present for the stationary CFD simulations. The peaks in the experimental data are less sharp than predicted by the CFD, likely due to noise in the data output, and potentially some lateral conduction occurring during the test time.

Figures 5.7-5.12 give the comparison between the experimental and CFD results with increasing rotation.

Under rotating conditions there are changes observed for both the CFD predictions and experimental data. Significant enhancement is found on the suction surfaces, with greater jet

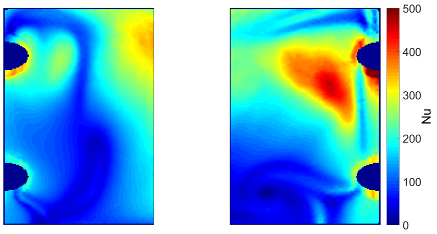

(a) Experimental (b) CFD

Figure 5.7: Nu map comparison - TP7 - Ro = 0.049

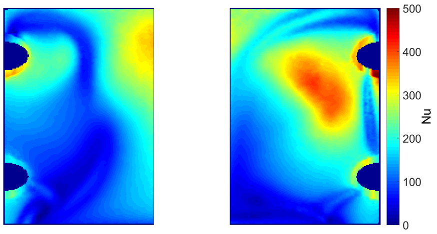

(a) Experimental (b) CFD

Figure 5.8: Nu map comparison - TP5 - Ro = 0.0073

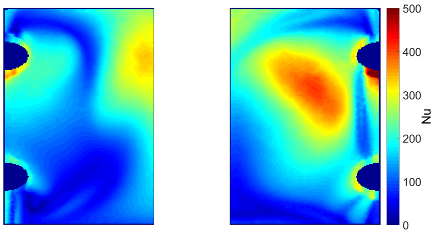

(a) Experimental (b) CFD

Figure 5.9: Nu map comparison - TP6 - Ro = 0.0088

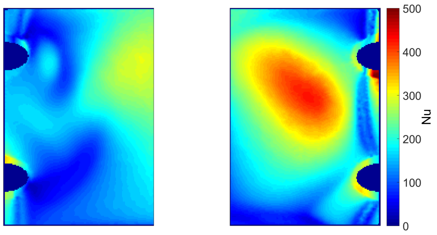

(a) Experimental (b) CFD

Figure 5.10: Nu map comparison - TP8 - Ro = 0.0138

spreading observed on the pressure surface, which is the opposite surface to which an enhancement would be expected under rotating conditions. This is because under rotating conditions there is a large change in flow structure in the feed channel with a shift of the core flow to the PS (figure 5.4) and therefore the impingement jet is effectively directed towards the suction side

The image originally presented cannot be made freely available via ORA because of copyright.

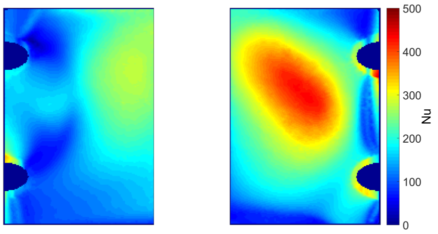

(a) Experimental (b) CFD

Figure 5.11: Nu map comparison - TP16 - Ro = 0.0167

The image originally presented cannot be made freely available via ORA because of copyright.

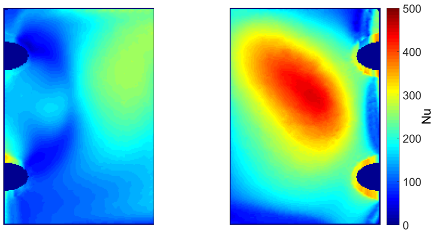

(a) Experimental (b) CFD

Figure 5.12: Nu map comparison - TP17 - Ro = 0.0187

of the target surface, enhancing heat transfer in this region. The increased spread of higher heat transfer on the pressure surface is also due to this change in inlet flow structure.

As for the stationary test point differences are found between the CFD simulations and experimental data. Again the CFD simulations show sharper peaks in heat transfer with the experimental results giving a much smoother distribution. The overall heat transfer levels are very similar on the pressure surface, however the suction surface levels appear to be overpredicted in the CFD. This is due to the overprediction of heat transfer directly under the impinging jet using this modelling strategy, which was also observed for the stationary test point.

5.2.4 Averaged Data

Figure 5.13 shows the overall target surface average experimental and CFD Nusselt number for different rotational speeds.

These averaged results over the pressure and suction surface show that there are some significant differences between the heat transfer levels predicted by the CFD simulations and those obtained from the RHTR.

On the suction surface the CFD consistently over-predicts the heat transfer levels, by approximately 15% for the test points at lower rotational speeds, with a much larger discrepancy

Figure 5.13: Overall averages with Rotation number

for the two test points with the highest rotation. The suction surface levels are predicted much more successfully with well matched results for all but the two test points at the highest rotational speeds.

It is expected that there is a problem with the experimental output for the test points at the highest rotation numbers. This is due to the sudden, unexpected drop in heat transfer on both surfaces, and the departure from the CFD successfully matching the experimental trends with rotation. Therefore the discrepancies between the CFD and experiment at these test points will be discounted.

5.3 Summary and Conclusions

CFD simulations using a common industrial RANS methodology have been undertaken on a leading edge impingement geometry under both stationary and rotating conditions. The flow structure and heat transfer distributions have been investigated with the heat transfer then compared to experimental data obtained from the RHTR.

The following conclusions have been drawn:

1. The flow structure in the impingement system is symmetrical under stationary conditions with rotation introducing a shift in flow towards the pressure surface of the feed channel.
2. This shift is the dominant effect of rotation on the impingement jet, directing it towards the suction surface of the leading edge passage.
3. There is a large increase in heat transfer on the suction surface under rotating conditions, due to the flow shift in the feed channel.
4. The CFD simulations over-predict the heat transfer on the suction surface, but by a consistent amount, and give good pressure surface predictions for most test points.

Although the CFD simulations miss some details in the experimental heat transfer distributions, they offer a good and consistent prediction of average heat transfer levels, and therefore this CFD methodology will be used in later chapters.

Chapter 6

Leading Edge Impingement - Static

In this chapter the design of an experimental setup used to obtain aerodynamic and heat transfer data for a turbine blade leading edge impingement system is detailed. Following this, results from the rig are presented and compared to computational predictions. The large scale perspex setup provides data under stationary conditions, unlike that from chapter 5, however provides full heat transfer distributions for a far larger region of a leading edge geometry which is derived directly from an HP turbine blade.

6.1 Experimental Design

The purpose of this experimental rig is to provide an assessment of aerodynamic and heat transfer properties of a leading edge impingement system. The aerodynamic data will consist of pressure measurements in both the feed and target passage, which will be used to obtain the discharge coefficients for the different impingement hole configurations under a range of conditions. The heat transfer data will be Nusselt number maps for the target surface of the impingement system.

6.1.1 Overall Rig Design

The experimental setup was required to provide the aerodynamic and experimental data for a leading edge impingement system under the following conditions:

- Engine representative jet and passage Reynolds number.

- Feed passage inlet and outlet flow.
- Film cooling outlets with engine realistic mass flow split.
- Multiple different impingement jet geometric configurations

The resulting overall rig layout designed in order to meet these is given in figure 6.1.

The rig is operated using a compressed air feed which is maintained at approximately 100 psi (7 bar). The single inlet pipe passes through a ball valve before being split into two separate lines, one each for the feed and leading edge passage, which can both be individually shut off using ball valves. The pipes then pass through similar series of an adjustable pressure regulator and choked venturi nozzle, downstream of which there is an offtake pipe with a burst disk. This is set to a pressure level and with a large enough pipe such that it will burst and exhaust the air before a pressure is reached that can damage the perspex test section. Upstream of the test section there are transition pieces and a heater mesh in order to heat the inlet flow for the transient liquid crystal method. Downstream of the test section, each of the feed and leading edge passage outlets pass through gate valves which will be used to control the outlet mass flow rates, which will be measured by the orifice plates before being exhausted to atmosphere. The film holes will exit directly to atmosphere from the test section.

For the tests that have been carried out in this chapter there will only be crossflow in the feed passage, and therefore the inlet and outlet of the leading edge passage remain blocked, but leading crossflow can be obtained in future experimental campaigns.

6.1.2 Mass Flow Control

Multiple mass flow rates must be controlled in order to obtain the required impingement jet Reynolds number and cross flow conditions. The inlet mass flow rates are controlled using a critical flow venturi nozzles, while the outlet flow rates are measured using orifice plate flow meters and adjusted using the gate valves upstream of them. The film hole flows exhaust to atmosphere with a representative mass flow split obtained through a choice of the film hole diameters.

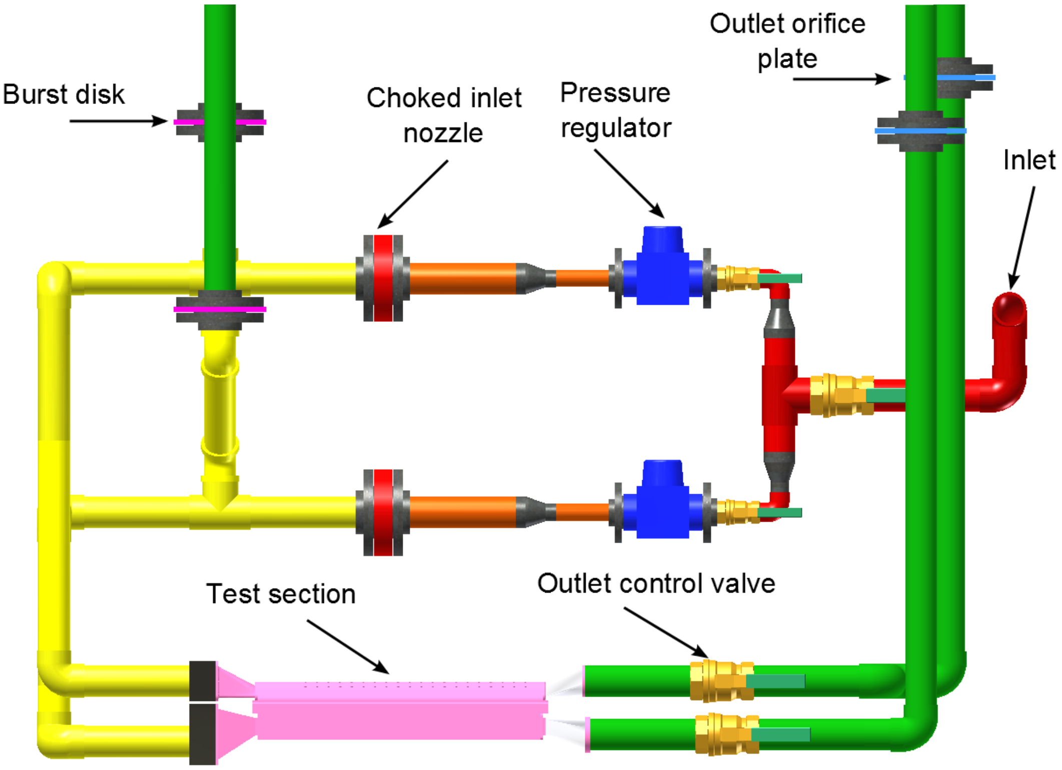

(a) Overall Rig

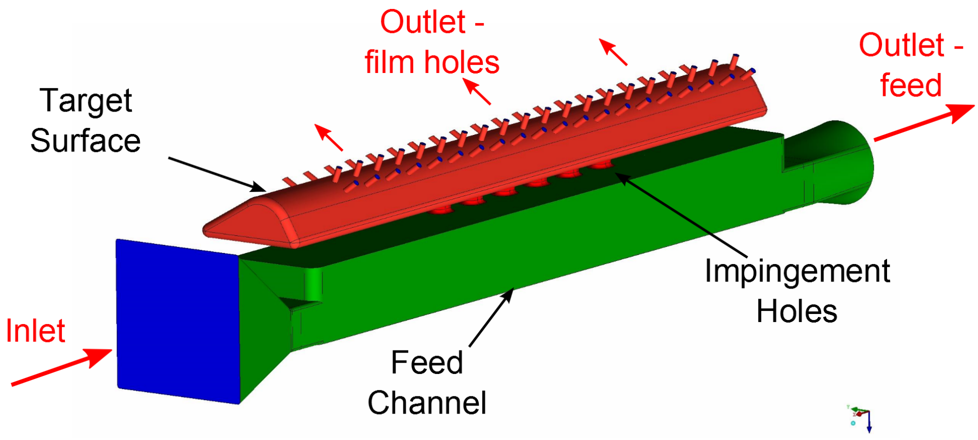

(b) Test Section

Figure 6.1: Schematic of experimental setup

Choked Venturi Nozzles

The choked nozzle offers good control of the inlet mass flow rate as it is determined only by the upstream stagnation temperature and pressure provided the critical conditions (guaranteed by a pressure ratio of approximately 2 or greater across the nozzle) are maintained. The ISO standard [106] gives details of the required nozzle specfications with the cylindrical throat type used for this rig. The mass flow rate is calculated using equation 6.1.

$$\dot{m} = \frac{C^* C_d A_{nt} p_0}{\sqrt{\frac{R}{M} T_0}} \tag{6.1}$$

The discharge coefficient, C_d, value for the nozzle is dependent on Reynolds number and therefore is calculated using an iterative procedure implemented in Matlab. The critical flow function, C^*, is obtained from tabular data contained within the standard [106].

The area of the nozzle throat is determined by the required mass flow rates and the available upstream pressure which ensures choked flow. The inlet nozzle throat diameter used was 6 mm for the lower Reynolds number tests, and 8 mm for the highest Reynolds number.

Orifice Plate Flow Meters

The outlet mass flow rates are measured using orifice plate flow meters, as described in the ISO standards [107, 108]. The measured mass flow rate is given by equation 6.2.

$$\dot{m} = \frac{C_d}{\sqrt{1-\beta^4}} \varepsilon \frac{\pi}{4} d^2 \sqrt{2 \Delta p \rho} \tag{6.2}$$

As with the choked nozzle the C_d value is dependent on Reynolds number, and therefore was calculated iteratively in Matlab. The orifice plates are situated within long straight lengths of pipe in order to comply with the standard. The pipe and orifice diameters were chosen at 50 mm and 35 mm respectively, giving a β of 0.7, in order for the full range of mass flow rates to be measured with an allowable pressure drop across the orifice plate.

6.1.3 Test Section Design

The test section was derived from a leading edge impingement design to be used in a Rolls-Royce demonstrator engine. The leading edge channel is a parameterised profile of the mid-

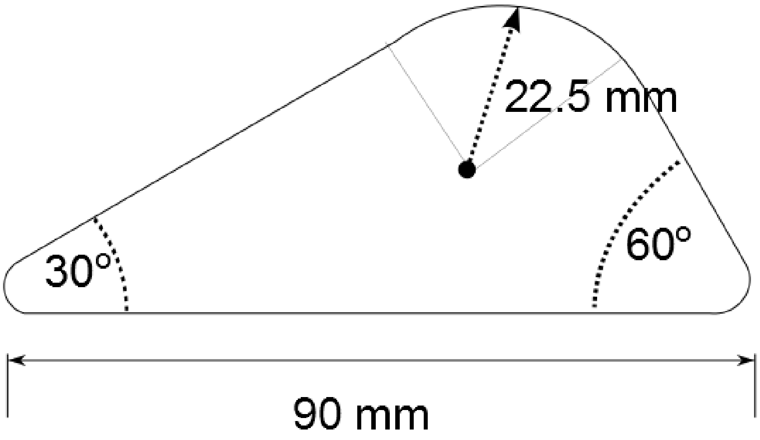

Figure 6.2: Leading edge channel geometry

Table 6.1: Geometric details - passages

	Feed	Leading Edge
D_H (mm)	55.88	36.09
A (mm^2)	3185	1582
L (mm)	500	500

height leading edge passage in the HP blade, shown in figure 6.2. The feed channel is a rectangular passage with area and aspect ratio to match the radial passage that feeds the leading edge impingement system in the blade, also at mid-height. Four rows of film cooling holes exit the leading edge passage, two rows of showerhead holes and two suction surface shoulder rows. Full geometric details are given for the passages in table 6.1 and for the film holes in table 6.2.

In the real engine case both the leading edge and feed passage have crossflow, with a portion of the mass flow both entering and leaving the passage through neither the film or impingement holes. The feed channel is typically the first pass of a radial serpentine passage, while the leading edge requires a flow throughout it's length to avoid film ingestion and to provide sufficient

Table 6.2: Geometric details - film cooling

	PS1	PS2	SS1	SS2	SS3
No. Rows	20	20	20	20	20
D (mm)	3.5	3.5	3.5	3.8	3.8
L (mm)	9.64	10.00	9.38	10.26	13.31
p (mm)	20	20	20	20	20

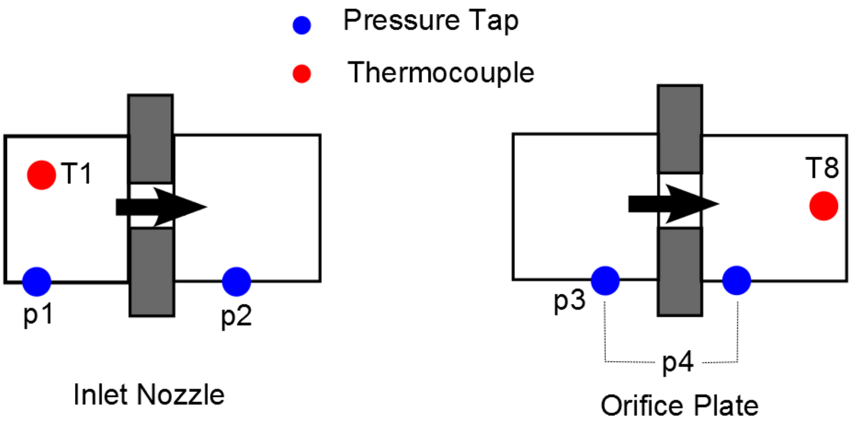

(a) Inlet nozzle and orifice plate

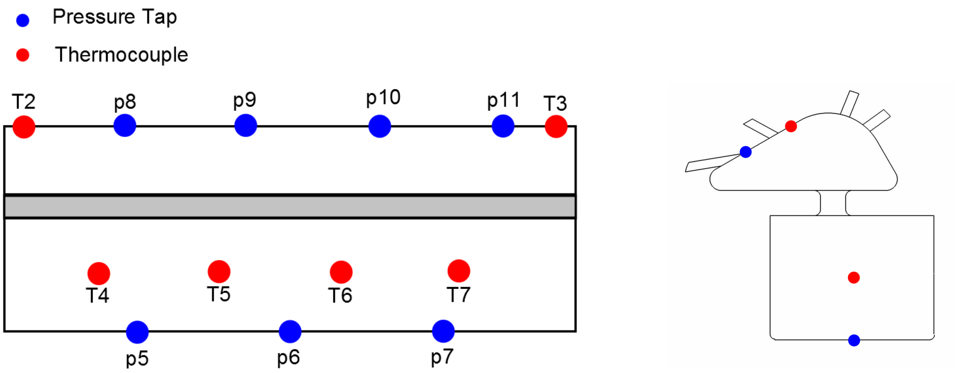

(b) Test section

Figure 6.3: Pressure tap and thermocouple locations

cooling in the blade root and tip regions. This is possible to achieve with this rig, however initially only conditions with crossflow in the feed passage will be considered.

The impingement plates are interchangeable in order to allow multiple different jet configurations to be tested. These will be described in greater detail subsequently in section 6.1.7.

6.1.4 Instrumentation

Instrumentation of the experimental setup consists of a number of pressure and thermocouple measurements, and a video camera for use in obtaining heat transfer measurements. An overall schematic of pressure tap and thermocouple locations is given in figure 6.3.

Pressure and thermocouple measurements were acquired using a NI cDAQ-9174 chassis with relevant modules [109]. Labview was used to record the data, and monitor mass flow rates, rig temperatures and pressures during the test runs. The final mass flow rates and Reynolds numbers were calculated using the full recorded data in Matlab [110].

Table 6.3: Pressure sensor details

Pressure sensor	Range	Locations
HXC001D6V	0-5 bar	Inlet nozzle - upstream
HXC001D6V	0-1 bar	Inlet nozzle - downstream
HCXM350D6V	0-350 mbar	All other locations

Pressure

Pressure measurements are obtained using a number of Sensortechnics pressure transducers [111] as detailed in table 6.3.

The larger range pressure sensors are required for the inlet due to the high supply pressure upstream of the choked nozzle. The 350 mbar range has been chosen for the other sensors in order to give good accuracy levels, whilst not reaching the range limits of the sensors, based on expected pressures given by preliminary CFD simulations. All sensors are connected to the pressure taps using Scanivalve tubing [112], and are recorded in Labview using an NI 9220 analog voltage reader [109]. These voltages are converted to pressure measurements via a linear scale calibration.

The pressure sensors were calibrated by applying a number of known differential pressures, that cover the full range of the sensor, across it's ports and recording the mean output voltage over 10 seconds. The set pressures were achieved using a Wika CPC4000 industrial pressure controller [113]. The offset value is recalculated before each test to zero the sensors.

The locations for the sensors have been chosen to meet the standard requirements for the choked nozzles and orifice plates, and for the calculation of the impingement hole discharge coefficients. The feed passage pressure taps are located on the centreline at the base of the passage with the leading edge taps located between the SS3 film locations. This is to obtain a pressure reading which is influenced minimally by local effects from the impingement jets. C_d values are calculated using these same locations for both experimental and computational setups.

Temperature

A number of thermocouples were required for mass flow measurement and the calculation of heat transfer coefficients. A thermocouple is required for each mass flow measurement device, and these were positioned in accordance with the relevant standards. Thermcouples were also positioned along the centreline of the feed passage to give a reference gas temperature for the HTC calculation, and on the surface of the leading edge passage in view of the video camera for calibration of the thermochromic liquid crystals. All temperature measurements were undertaken with K type thermocouples read into an NI 9213 thermocouple reader [109].

6.1.5 Heat Transfer Measurement

The heat transfer measurements were obtained using the transient liquid crystal method, as detailed in section 2.4.1. This method requires a step or ramp increase in gas temperature for the thermochromic crystals to be activated. A video camera is also required to record the colour changes which are then analysed to obtain heat transfer coefficients.

The heater mesh consists of a fine mesh connected by conductive busbars and clamped between electrically insulating material. A high current DC power supply [114] is used to power the mesh.

A Panasonic HC-X900 camcorder was used to to record the video in .avi format in 1080p at 25 fps through an AVerMedia HD capture card using VirtualDub software [115]. The video was then clipped around the relevant test time, and cropped to the region on which the heat transfer coefficients are calculated. The camera is positioned above the test section to give an unobstructed view of the leading edge target surface.

To calculate the Nusselt numbers the THTAC software was used [116]. This software has been developed in house at the Osney Heat Transfer Laboratory for the calculating heat transfer distributions for transient liquid crystal experiments, and has been validated extensively through use in [6, 83, 84, 100].

6.1.6 Commisioning

Mass Flow Verification

Before experimental results were obtained the means of mass flow measurement, the inlet venturi nozzle and outlet orifice plate, were verified. This was done by sealing the test section film holes with masking tape so that all mass flow entering the test section passed through the orifice

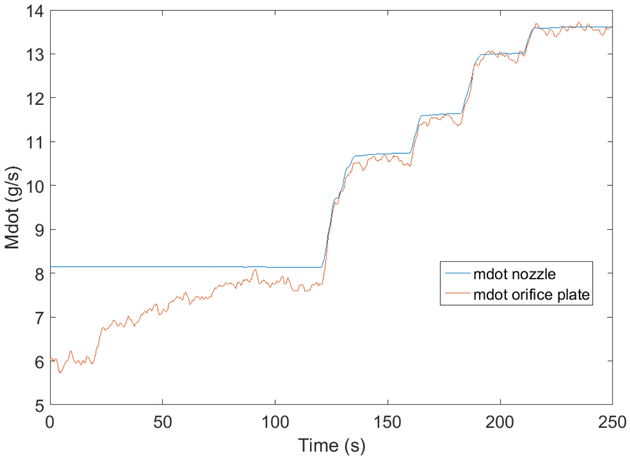

Figure 6.4: Mass flow measurement verification

plate. Figure 6.4 shows these two mass flow rates with increasing pressure upstream of the inlet nozzle.

Initially, before the inlet nozzle becomes choked, the inlet nozzle calculation as given by equation 6.1 is not correct. However as it becomes choked, with increased supply pressure, the two mass flow curves match very well. This indicates that both means of mass flow measurement have been implemented as detailed by the standard. They are therefore used for determining the mass flow rates for the experimental runs.

Liquid Crystal Calibration

The liquid crystal calibration is performed in-situ using a surface thermcouple bonded to the inner surface of the test section, upon which the liquid crystals are sprayed. The video camera is moved to an alternative mounting position in order to obtain a detailed view of the thermocouple bead. A test is then performed in which the area around the thermocouple is heated slowly, with the video and thermocouple data recorded. A still image from this test is given in figure 6.5 (a). The green light intensity from a selected area of pixels directly next to the thermocouple bead, and therefore at the same temperature as it, are then matched to the thermocouple temperatures to give a calibration curve of normalised green light intensity with temperature as shown in figure 6.5 (b). This calibration curve is then used to give the surface temperature information from which to calculate HTCs in the experimental runs.

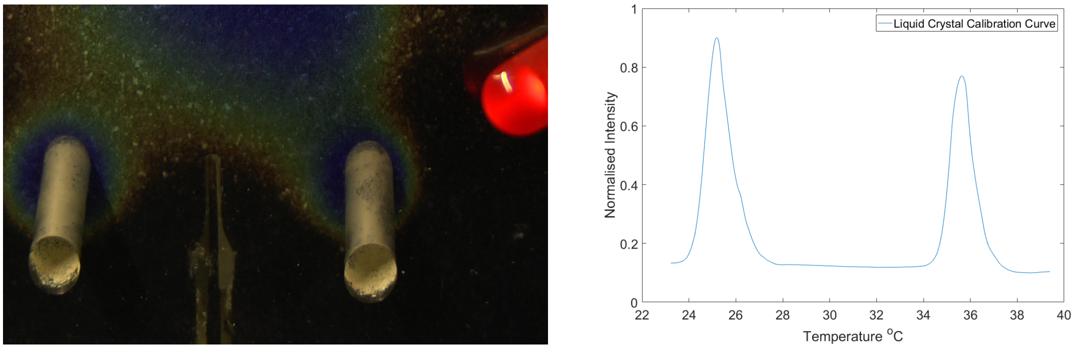

(a) Still from calibration video (b) Calibration curve

Figure 6.5: Liquid crystal calibration

Table 6.4: Impingement geometry details

Geom.	Jet No.	Hole Shape	Fillet	Arrangement
1	6	Racetrack	2.5 *mm*	Single line
2	6	Racetrack	2.5 *mm*	Staggered - 7.5 *mm*
3	6	Elliptical	2.5 *mm*	Staggered - 7.5 *mm*
4	6	Racetrack	2.5 *mm*	Staggered - 3.75 *mm*

6.1.7 Test Conditions

Multiple different impingement plate geometries have been tested at different Reynolds number and crossflow conditions, which are detailed in the following sections.

Impingement Geometries

Four different impingement geometries have been tested, with geometric details given in table 6.4 and holes details in table 6.5 and figure 6.6.

The overall plate configurations are either of a single row of holes, or in a staggered ar-

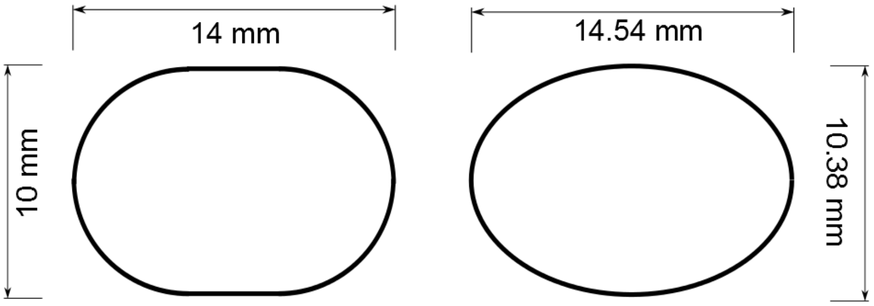

Figure 6.6: Impingement hole profiles - racetrack and elliptical

Table 6.5: Impingement geometry details

Geom.	Length	Width	D_h	Area
Racetrack	14 mm	10 mm	12.03 mm	118.54 mm^2
Elliptical	14.54 mm	10.38 mm	12.03 mm	118.54 mm^2

rangement. The staggered arrangement consists of two holes in a straight line, followed by four holes offset from this centreline in an alternating manner by distances specified in table 6.4. The baseline impingement hole is a racetrack shape, with the elliptical hole specified to have the same hydraulic diameter and cross-sectional area as the racetrack hole. The z/D_H for all geometries is 2.55, based on the centreline of the first impingement hole in each case.

The staggered and elliptical configurations are being tested as they can offer a reduction in web stresses in a turbine blade, however the use of them is only possible if heat transfer on the leading edge is not compromised.

Flow Conditions

Each impingement plate geometry will be tested under a range of jet Reynolds numbers from $13,000$ to $22,000$ to match the lower range expected for engine operation of a similar system.

6.2 Experimental Results

Two forms of experimental results will be presented. These are discharge coefficients for the impingement holes and Nusselt number distributions for the leading edge target surface.

6.2.1 Discharge Coefficients

Discharge coefficients are calculated based on the average jet mass flow rate and the pressure difference using equation 6.3. The C_d calculated gives the ratio between the actual mass flow through the impingement jet, and the theoretical maximum based on a simple incompressible flow calculation. The pressures used for this calculation are the mean feed and leading edge channel pressure readings from the pressure tap locations given in section 6.1.4.

$$C_d = \frac{\dot{m}_{jet}}{A_{jet}\sqrt{2\rho(p_{feed} - p_{LE})}} \tag{6.3}$$

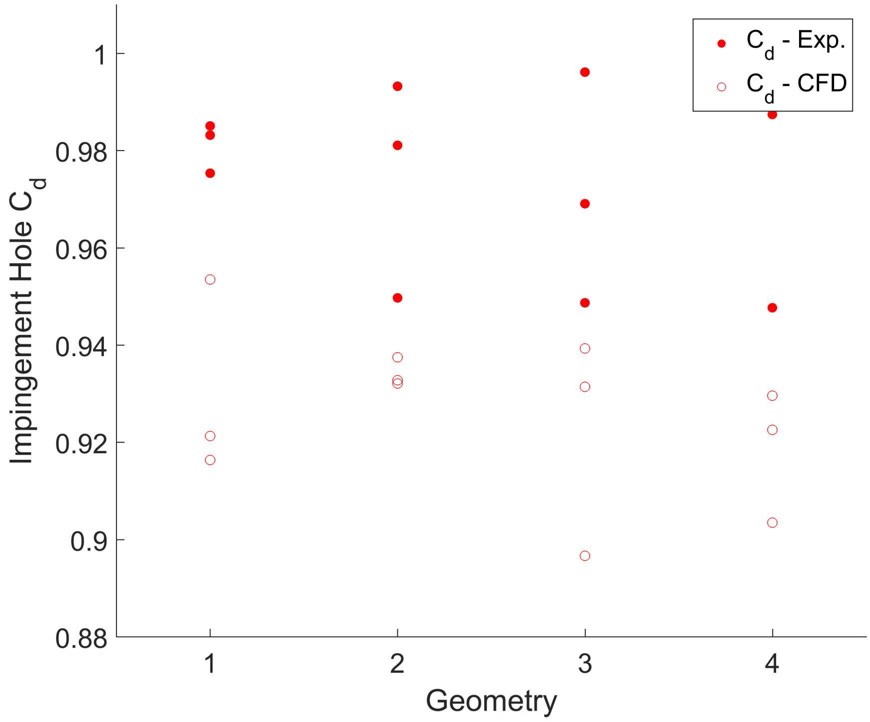

Figure 6.7: Cd values from experiment

Figure 6.7 gives the discharge coefficients calculated for the different impingement geometries from the experimental setup, and also from CFD simulations which are detailed in section 6.3.

The C_d values are seen to be very high, over 0.9, for all geometries and Reynolds numbers in both the experimental and CFD results. The values are very high due to the filleting of the impingement holes which allows the flow to easily pass through them and create the impingement jets. The discrepancies between the computational and experimental results are put down to the incorrect modelling of the flow separation through the hole.

6.2.2 Heat Transfer

Heat transfer results are presented in the form of Nusselt number maps. The THTAC software generates HTC maps for the selected surface, which have then been converted to Nusselt number based on jet hydraulic diameter and temperature dependent gas thermal conductivity. The driving gas temperature for the HTC calculation was chosen to be the first thermocouple in the feed passage, as this is in a region with very small temperature gradients, allowing for an easier comparison to CFD simulations. Areas where the film hole outlets obscured the view of the target surface have been masked out.

Figure 6.8 shows the Nusselt number maps for each of the four tested geometries for the middle jet Reynolds number of 17,500.

For the first geometry, the peaks of high heat transfer occur in a straight line under each impingement jet, with the third peak giving the highest Nusselt number. The fifth and sixth jets, furthest from the inlet in the feed passage, show significantly reduced levels of heat transfer as most flow has been used in the earlier jets, and consequently these jets have a lower Reynolds number. There are ridges of high heat transfer between the impingement jets that spread laterally across the leading edge passage. These occur as the flow recirculating from the impinging jets are funnelled across the leading edge geometry towards the SS2 and SS3 film holes, and are investigated further in section 6.3.2 where more detail of the internal flow structure can be visualised. High regions of heat transfer are also found at the entrance to the film holes as flow is accelerated into them, which has previously been observed in [104].

The second geometry shows very similar levels of overall heat transfer, however with the regions of high heat transfer shifted due to the staggered nature of the impingement hole configuration. The streaks of high heat transfer due to jet interaction are again seen, however are now angled due to the differing jet locations.

The heat transfer for the third impingement configuration is almost indiscernable from that for the second geometry, indicating that the change from racetrack to elliptical holes has very little impact on the heat transfer distribution. The fourth geometry gives a very similar pattern to the second, the only difference being the location of the staggered jet peaks, which are closer to the single line due to the reduced stagger.

Figures 6.9-6.12 show the Nusselt number maps for the different impingement geometries for the three Reynolds numbers tested.

For all geometries the overall heat transfer pattern is unchanged, with peaks under the jets and in regions of jet interaction, however with significantly increasing heat transfer with Reynolds numbers. This is expected due to the increased thermal capacity of the flow as the mass flow increases. This relationship is quantified below in section 6.3.3.

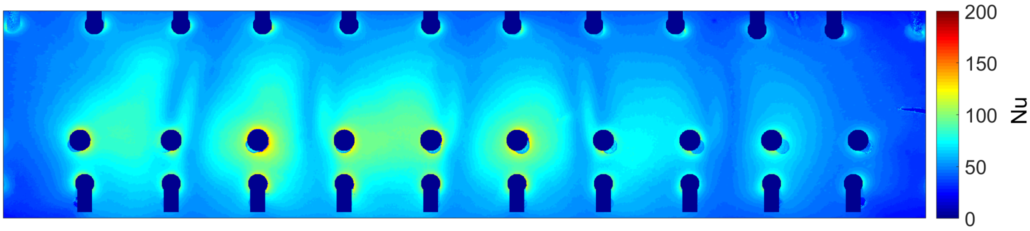

(a) Geometry 1 - single line, racetrack

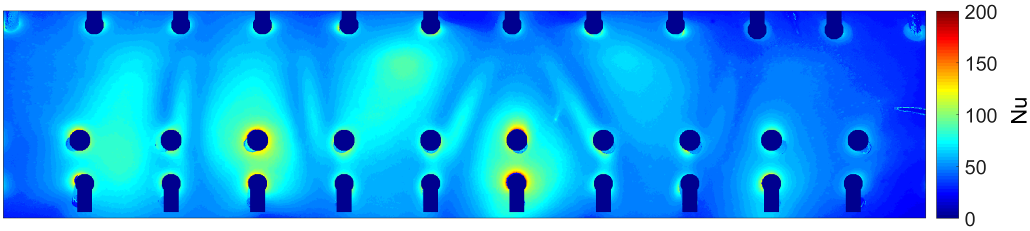

(b) Geometry 2 - staggered, racetrack

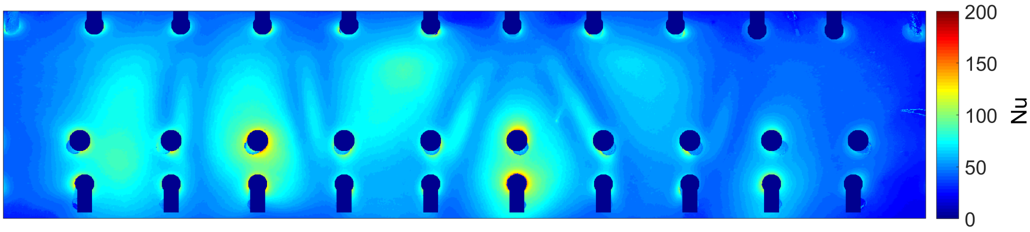

(c) Geometry 3 - staggered, elliptical

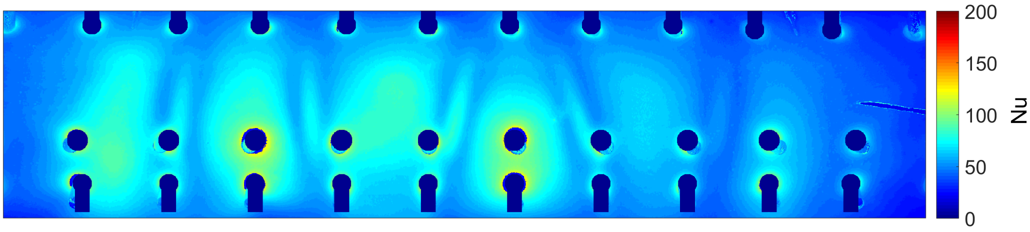

(d) Geometry 4 - reduced stagger, racetrack

Figure 6.8: Heat transfer - experimental - geometry comparison - Re = 17,500

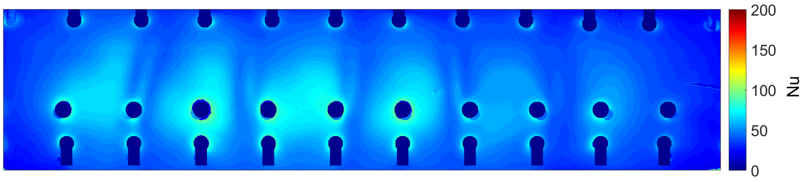

(a) Re = 13000

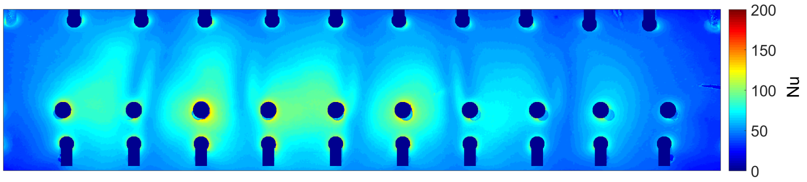

(b) Re = 17500

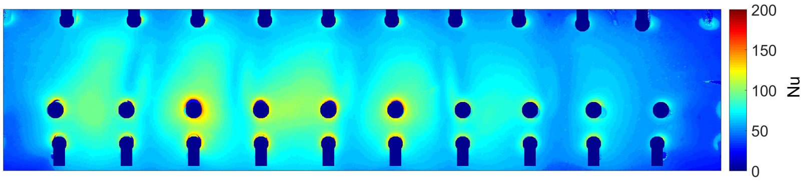

(c) Re = 22000

Figure 6.9: Heat transfer - experimental - Reynold numbers - geometry 1

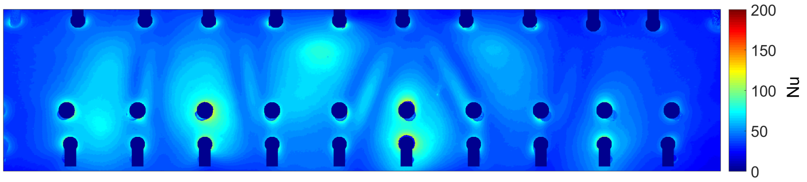

(a) Re = 13000

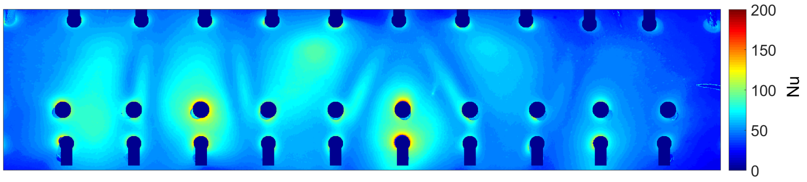

(b) Re = 17500

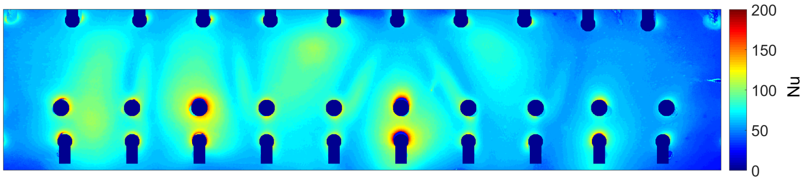

(c) Re = 22000

Figure 6.10: Heat transfer - experimental - Reynold numbers - geometry 2

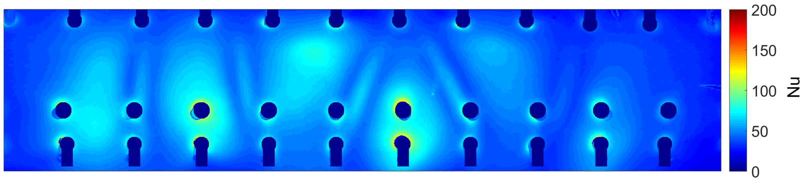

(a) Re = 13000

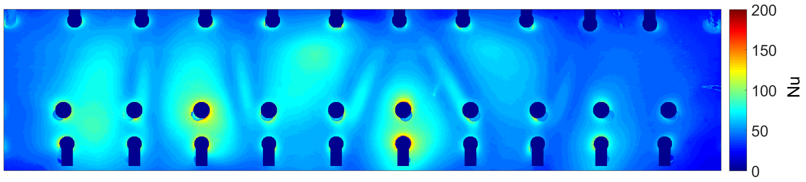

(b) Re = 17500

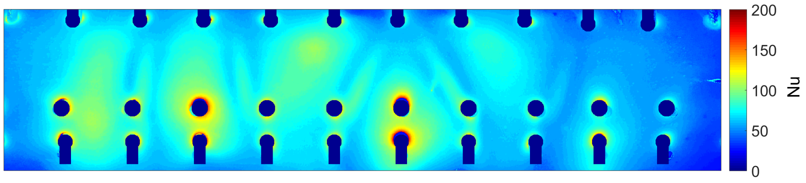

(c) Re = 22000

Figure 6.11: Heat transfer - experimental - Reynold numbers - geometry 3

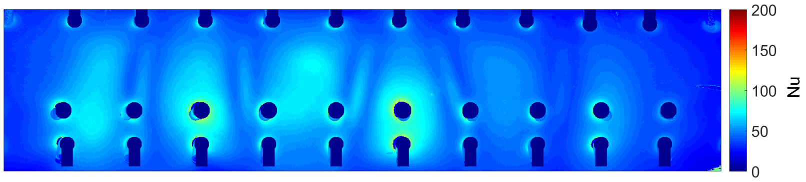

(a) Re = 13000

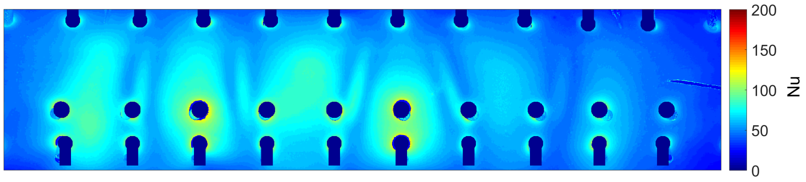

(b) Re = 17500

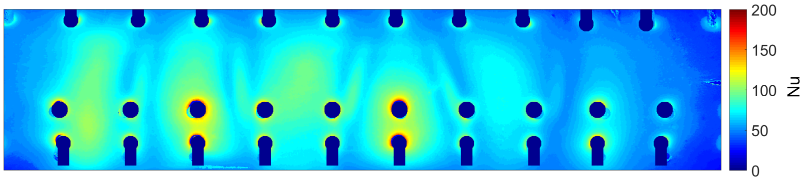

(c) Re = 22000

Figure 6.12: Heat transfer - experimental - Reynold numbers - geometry 4

Table 6.6: Uncertainty for experimental heat transfer results

	Measurement uncertainty	HTC uncertainty
Exp. starting temp.	0.2 ^oC	4.4 %
Gas temp. rise	1%	1.9 %
Thermal product	29 $Jm^2\sqrt{s}$	5.5 %
Crystal calibration temp.	0.25 ^oC	5.5 %
Video timing	0.04 s	1.9 %
Discretisation	-	1.2 %
Overall RSS	-	10.0 %

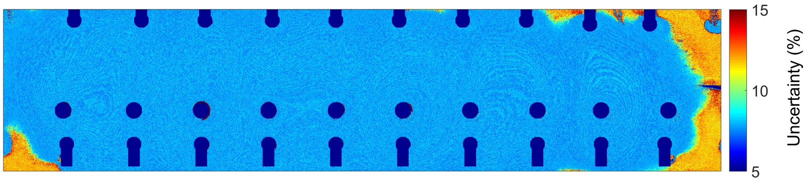

Figure 6.13: Experimental uncertainty distribution - geometry 1, Re = 17500

6.2.3 Experimental Uncertainty

Table 6.6 gives typical uncertainty values for the experimental setup and figure 6.13 shows the uncertainty map for the central Reynolds number case for geometry 1, from which the typical uncertainty values were also calculated.

It can be seen from these figures that the overall uncertainty level is approximately 10.0% with the greatest contribution from the uncertainty for the thermal product of perspex. The highest uncertainty values are seen away from the impinging jets where only the first crystal was activated during the test due to the lower HTC values.

6.3 Comparison with CFD

6.3.1 CFD Setup

The CFD simulations were undertaken using the same methodology as previously described in chapter 5. Meshing was undertaken in ICEM and Ansys Fluent was used as the solver with the

Table 6.7: Mesh details for impingement geometry

No. of Cells	11.6 million
No. of Prism Layers	15
Max y$^+$	2.157
Area-averaged y$^+$	0.269

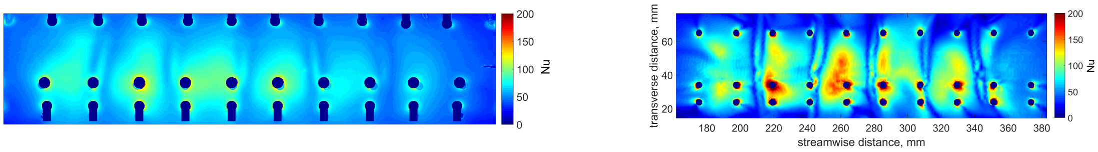

(a) Geom 1 - Exp. (b) Geom 1 - CFD

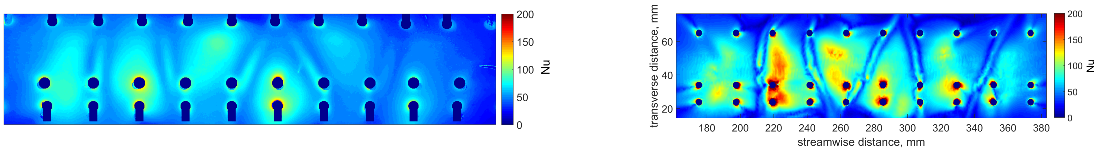

(c) Geom 2 - Exp. (d) Geom 2 - CFD

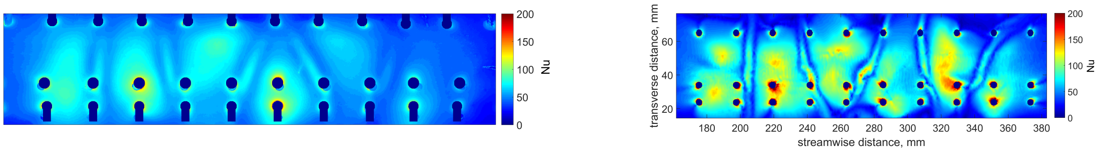

(e) Geom 3 - Exp. (f) Geom 3 - CFD

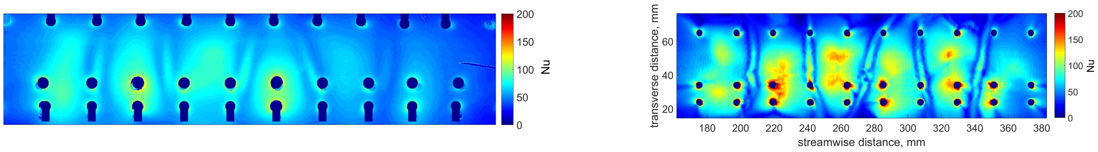

(g) Geom 4 - Exp. (h) Geom 4 - CFD

Figure 6.14: Heat transfer - experimental vs CFD - Re = 17500

k-ω SST turbulence model. Table 6.7 gives the details for the mesh for the baseline geometry and operating condition.

6.3.2 Heat Transfer - Distributions

Figure 6.15 shows a comparison between the experimental and CFD results for all geometries at the middle Reynolds number of 17500. The overall heat transfer distribution is reasonably well predicted, however there are some differences between the simulations and experimental results.

The location of the peaks of high heat transfer under the impinging jets are predicted well

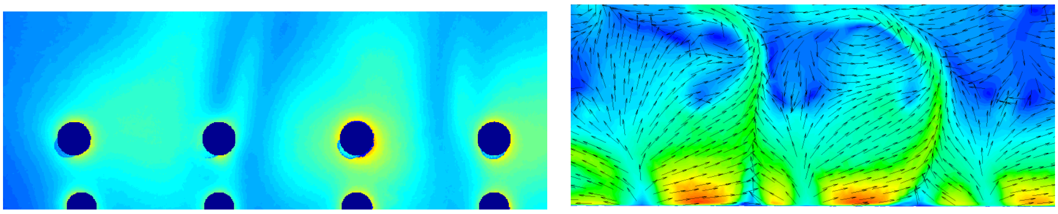

(a) Experimental Nusselt number (b) CFD near-wall velocity contour for same region

Figure 6.15: Heat transfer - detailed view of high heat transfer region with CFD velocity contour

for all geometries, as are the regions of high heat transfer at the entrance to the film holes and between the jets. However, the CFD simulations predicts significantly higher peak values and more clearly defined peaks with levels falling away to lower levels away from the jets. The experimental results show less pronounced peaks which spread further across the target surface. This is the same as found in Chapter 5 of this thesis, and also in other studies such as [51].

Figure 6.15 (a) shows a small region of the experimental Nusselt number maps for geometry 1 at a Reynolds number of 17500, in order to highlight the region of high heat transfer streaks between the impingement jets, with (b) showing a velocity contour with overlayed vectors for a near wall plane for the same region. It can be seen from this that the thin high heat transfer regions results from a high velocity wall jet, that occurs between the impingement jets as the recirculating flow is directed across the leading edge surface. The thin developing boundary layer of the this jet results in a high heat transfer level. These high velocity regions occurs as a combination of the passage shape, that funnels flow in this direction, and also due to the presence of film holes that bleed flow from this passage a distance away from where the jets impinge.

6.3.3 Heat Transfer - Averages

The Nusselt number maps presented previously have been averaged and plotted below to illustrate the overall heat transfer with geometry, figure 6.16, and with Reynolds number, figure 6.17.

It can be clearly seen that the impingement hole configuration has little effect on heat transfer. For both the experimental and CFD results the overall heat transfer levels are similar for all geometries for a given Reynolds number. This is an important result for thermal engineers who may used the staggered configuration, or elliptical jets, in order to reduce stress concerns,

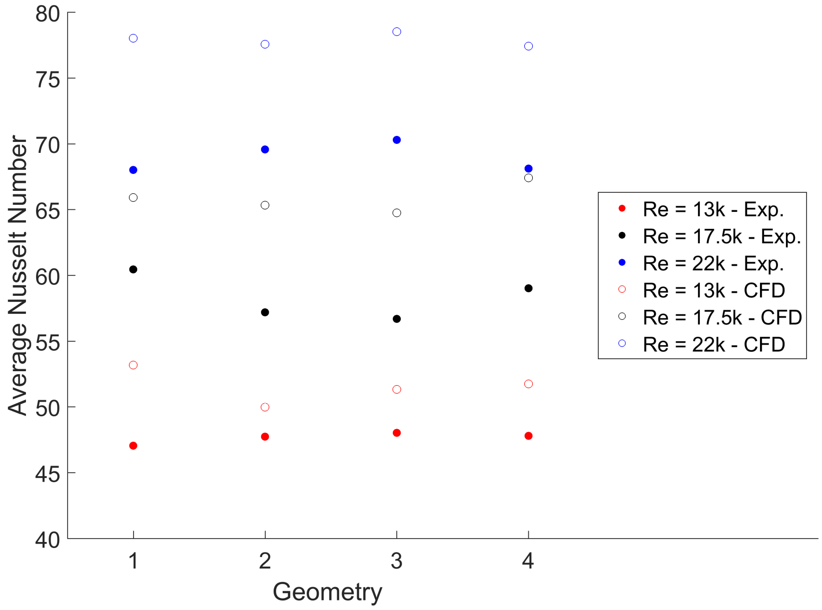

Figure 6.16: Heat transfer averages - comparison between experiment and CFD simulations - geometry

which can be done without reducing the leading edge heat transfer.

The CFD consistently overpredicts the heat transfer for this system by approximately 10 % across all geometries and Reynolds numbers.

A power fit of the form $a * Re^b$ has been produced for the experimental data, given in equation 6.4 and illustrated on figure 6.17. The other correlation shown on figure 6.17 is that for the most similar geometry found in [52], and shows good agreement with the experimental data, albeit with a slightly different relationship with Reynolds number. The experimental data is also in line with other relationships for impingement systems found in the literature such as [51,67]. The levels produced from these other correlations are around 8% higher that those found in a similar leading edge system in [51], with this differences put down to the lower z/D_H, and asymmetric leading edge passage shape found in this work. The Reynolds exponent of approximately 0.71 is similar to that of many previous impingement correlations, for example those presented in [52, 55, 102, 117]. The overall Nusselt number levels do show some difference to these previous studies due to varying driving gas temperature definitions and the asymmetric nature of the leading edge passage in this study.

$$Nu = 0.05738 Re^{0.7093} \tag{6.4}$$

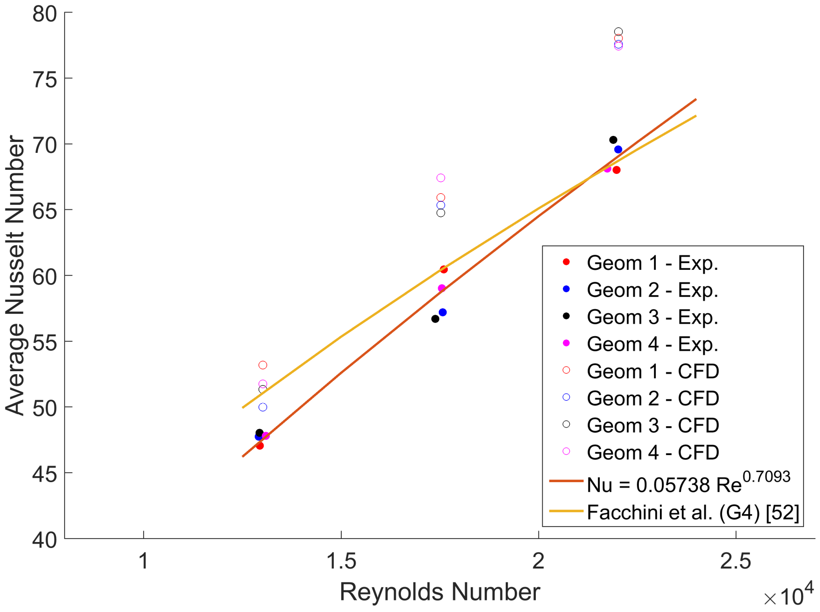

Figure 6.17: Heat transfer averages - comparison between experiment and CFD simulations - Re

6.4 Summary and Conclusions

A new experimental rig for a leading edge impingement system has been designed and constructed, and a series of heat transfer tests have been completed. Four different impingement configurations have been tested for an engine-representative turbine blade leading edge geometry with film cooling flows. The heat transfer distributions and levels have been compared to RANS CFD simulations.

The following conclusions have been drawn.

- The experimental heat transfer distributions produced show the typical patterns expected of such a system, with peaks of high heat transfer under each impinging jet.
- Additional regions of high heat transfer are also seen where flow accelerates into the film cooling holes, and between the jets where recirculating, high velocity flow is funnelled across the leading edge surface towards the suction surface film cooling holes.
- The effect of altering the impingement configurations on heat transfer is very small, which allows the rearrangement of jets to such configurations to reduce web stresses in a turbine blade.
- An increase in jet Reynolds number gives an increased surface Nusselt number in line

with previous studies.

- CFD simulations reasonably predict the overall heat transfer distribution, with a consistent overprediction in levels of approximately 10%.

Chapter 7

Leading Edge Impingement - Mechanical

The current industry practice for blade design initially involves modelling and experimental techniques to determine the heat transfer levels obtained by a particular cooling system. These levels are then passed onto a separate team which applies them to a full blade stress model to determine if a particular blade design has adequate life [118]. This process is very time consuming and expensive due to the multiple full analyses that must be undertaken, with each change in cooling design requiring a full re-analysis.

The method proposed in this section involves isolating a single cooling system within a blade, and running a combined cooling then stress analysis within the same software environment. It has the capability for faster analysis and optimisation of individual cooling components which can then be recombined back into a full blade design for confirmation that the final overall design meets the required specification. It also allows for analysis of individual aspects of a cooling system design in terms of metal temperature and stress distribution.

Both the new method and existing techniques rely on imported thermal boundary conditions in the stress modelling. These are supplied by CFD simulations or experimental results, such as those previously detailed in chapter 5.

7.1 Overview of Method

The method comprises of the following stages:

1. Isolate the cooling feature as a section of geometry which is to be analysed

2. Run a conjugate CFD simulation for the selected geometry
   (a) Create mesh
   (b) Run simulation using engine conditions
   (c) Export metal temperature for mechanical analysis
3. Run a mechanical analysis using results from the CFD solution
   (a) Mesh metal domain
   (b) Import metal temperature from conjugate CFD
   (c) Run mechanical analysis
4. Analyse results to see if the required specification is met and if the cooling system can be improved.
5. Alter geometry or boundary conditions and iterate as required
6. Recombine features into full cooling configuration for turbine blade

All of these stages are completed within the Ansys workbench environment which allows for simple implementation combining the CFD and mechanical simulations.

7.2 Methodology - CFD

The first stage in this method is to conduct a conjugate CFD simulation of the specified domain at engine representative conditions. This simulation was undertaken using common industrial RANS methodology with boundary conditions specified from existing knowledge of the operation of a typical turbine blade cooling system.

7.2.1 Geometry and Meshing

The geometry used in these simulations was a leading edge impingement system designed to fit within a typical mid-section turbine blade profile, illustrated in figure 7.1. The leading edge passage was shaped accordingly and a rectangular cross section with rounded corners was used for the feed passage. Multiple rows of film holes were included in the geometry, three on the

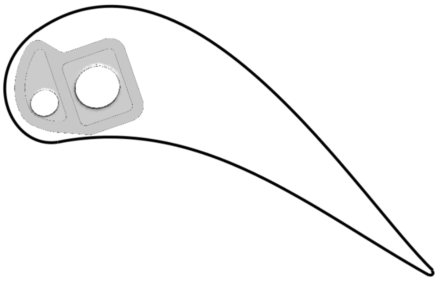

Figure 7.1: CFD geometry and location within representative blade

Table 7.1: Geometric details - passage

	Feed	Leading Edge	Jet
$D_H\ (mm)$	5.77	3.80	1.203
$A\ (mm^2)$	31.61	16.63	1.185
$L\ (mm)$	55	55	1
Re (In / Out)	182190 / 74200	55000 / 43550	54510

suction surface and two on the pressure surface. The suction surface films and one pressure surface film are fed from the leading edge passage with the remaining pressure surface film fed from the feed channel. Details of the geometry are given in table 7.1, with film cooling details given in table 7.2.

The blade metal was created using a 1 mm thick wall to surround the cooling passages. A 5 mm thick tip was added at the top of the passages for the full profile except for two dust holes with diameters of 4 mm and 2.5 mm for the feed and leading edge passages respectively. This geometry is shown in figure 7.2 (a) and (b), with the dust holes visible in (c). The properties of the Rene N5 nickel based alloy [119] are given in table 7.3. The material used in these simulations is a Rolls-Royce nickel alloy with similar properties to this.

The meshing for the CFD was undertaken in ICEM 14.0 with an example mesh given in

Table 7.2: Geometric details - film cooling

	PS1	PS2	SS1	SS2	SS3
No. Rows	20	20	20	20	20
$D\ (mm)$	0.35	0.35	0.35	0.38	0.38
$L\ (mm)$	0.964	1.000	0.938	1.026	1.331

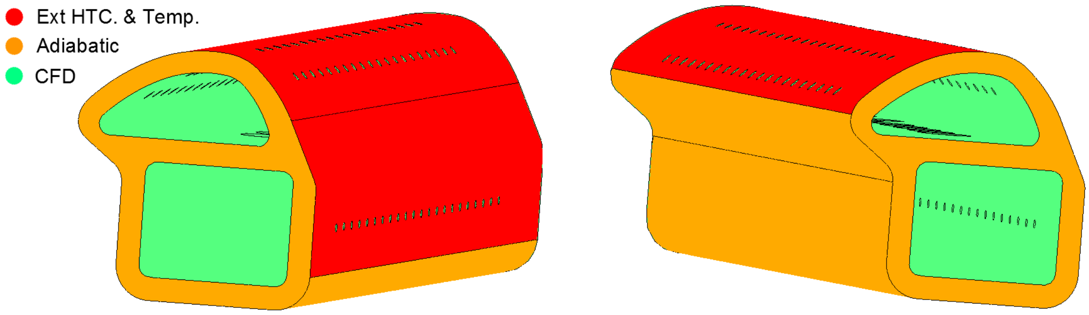

(a) Conjugate CFD B.C. (b) Conjugate CFD B.C.

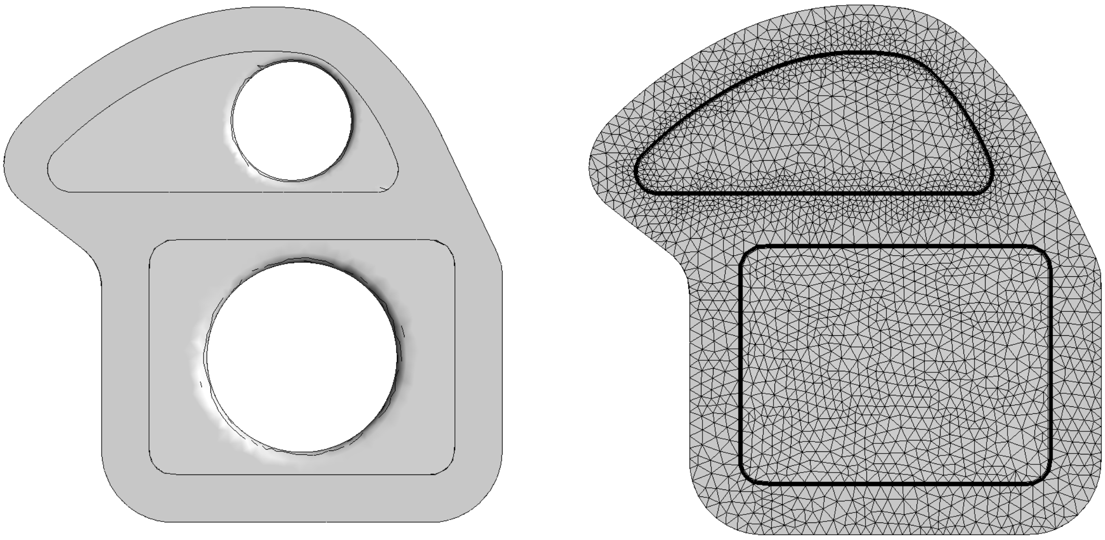

(c) Dust hole location and sizing (d) Conjugate CFD meshing

Figure 7.2: CFD geometry, boundary conditions and meshing

Table 7.3: Thermal and mechanical blade material properties

Material	Rene N5
ρ	8600
E	106000
G	108000
ν	0.401

figure 7.2 (d). An unstructured tetrahedral mesh with 12 prism layers to capture the boundary layer was used for the fluid domain while the solid was meshed with an unstructured tetrahedral mesh. The meshing parameters were based on previous simulations run in chapter 5. The fluid mesh consisted of 12.7 million cells with an area-averaged $y^+ < 1.5$ and a maximum $y^+ < 8$. The solid mesh contained 6.3 million cells.

7.2.2 Simulation Setup

The simulation setup was similar to previous impingement calculations, with some changes due to the conjugate nature of these simulations.

Fluent 14.0 was used for all CFD simulations. A stepped solution procedure was followed with the complexity of the calculations built up gradually, as for the simulations in previous chapters. The working fluid was air, modelled as an ideal gas with temperature dependent specific heat, viscosity and thermal conductivity. The SIMPLE pressure-based solver was utilised with second order discretisation for energy, momentum and turbulence properties. The k-ω SST turbulence model was used for these calculations due to its satisfactory performance for rotating impingement systems shown in chapter 5. Pressure outlets and mass flow inlets were specified to match engine design conditions as given in table 7.1. The pressure outlet conditions were variable for each row of film holes and the radial location of each hole, based on the expected external pressure distribution obtained from an in-house simulation of the blade passage.

The heat transfer boundary conditions consisted of specified engine-representative HTC and free stream temperature values on the leading edge external metal with an adiabatic condition on the external metal that would be internal to the blade, if the entire blade was modelled. A similar approach to this has been validated in [120] These conditions are shown in figure 7.2 (a-b) with orange indicating an adiabatic boundary, red the hot free stream boundary and green

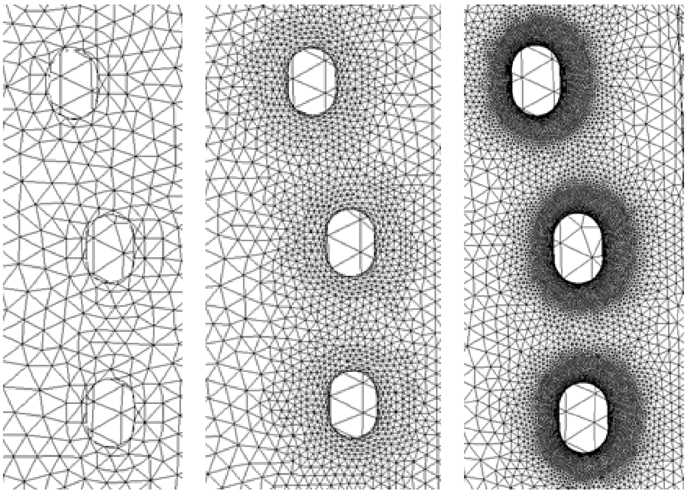

(a) Coarse (b) Mid (c) Fine

Figure 7.3: Mesh independence study

the coupled solid-fluid boundaries. The external HTC value used was just over 4000 $W/(m^2K)$ with a free stream temperature of approximately 1800 K.

The primary simulation result is the blade metal temperature to be imported into the mechanical analysis and therefore internal heat transfer coefficients were not analysed for this case.

7.3 Methodology - Mechanical

The mechanical analysis was conducted in the Ansys Mechanical software package accessed from Ansys Workbench. The solid domain is imported and meshed using the inbuilt mesher. A tetrahedral mesh was used with refinement around the impingement and film holes. A mesh independence study was conducted to determine the level of refinement required around the impingement holes.

7.3.1 Mesh Independence Study

A mesh independence study was carried out to ensure sufficient resolution present around the impingement holes, where the highest stress concentrations and gradients are likely to be found, with a suitable level of refinement applied to all simulations based on the outcome of this study.

Three different refinement levels were tested, given in figure 7.3, with the corresponding stress distributions shown in figure 7.4.

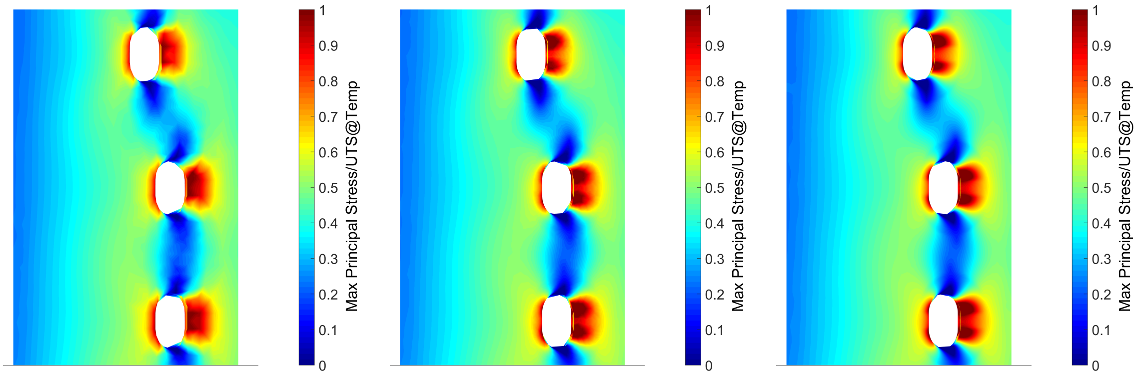

(a) Coarse (b) Mid (c) Fine

Figure 7.4: Stress in impingement holes - mesh independence study

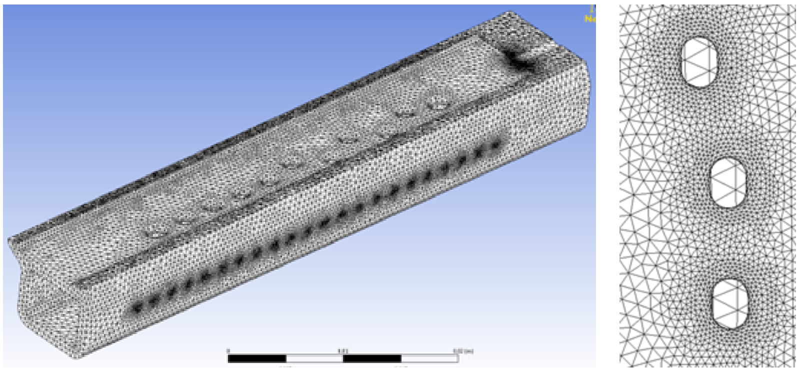

(a) Mesh for mechanical simulations (b) Refinement

Figure 7.5: Final mechanical meshing

It is clear from the stress distributions that the coarse mesh does not provide enough resolution around the impingement holes. However the mid and fine meshes both produce very similar results, and therefore the mid level of refinement around the impingement holes is used for all calculations. A final example mesh and refinement is given in figure 7.5.

7.3.2 Analysis

The metal temperature from the CFD simulation was imported into the Ansys Mechanical software and mapped onto the solid domain using the imported load tool. A rotation was applied to simulate that experienced in an engine, with the blade anchored at a fixed radial displacement, that matched the engine dimensions, on the root surface of the geometry. This boundary condition causes a region with very high stresses near the root of the blade, however this does not affect the area of interest in the central section of the metal. It also closely simulates the actual boundary condition found in the engine, with the fir tree anchoring the blade root to the disk.

The analysis is then run using the standard setup with post-processing then conducted within the Ansys Mechanical software. The initial post-processing consists of producing stress contours around the central three impingement holes, as these are where the simplified passage cross section is most similar to that of the real blade, in order to validate the method. The different stresses in the working co-ordinate system and the principal stresses were plotted to ensure complete validation of the method and to identify any discrepancies.

7.4 Validation of Method

7.4.1 CFD - Film Cooling Pressure Ratios

There are two stages to the validation of this methodology, the first of which is to validate the CFD simulations. Due to the CFD being run at engine conditions no experimental data is available for direct validation, however some level of validation is possible against in-house software predictions that have proven to be reliable in real engine cases.

Film cooling is key to ensuring a low enough blade metal temperature, and can used as a validation case for the aerodynamics within the CFD. The internal cooling system must be able to maintain the required pressure ratios across each of the film cooling rows. Figure 7.6 shows the total-to-static pressure ratio across each row of films in the CFD simulation (shown as dots) compared to the average value from the mid-section film holes from an in-house software prediction (horizontal lines) [121].

It can be seen from figure 7.6 that the pressure ratios predicted by the CFD, across the central blade section where the comparison is valid, are very close to those expected from the in-house software predictions which have been proven reliable for similar configurations. Heat transfer predictions will be undertaken by comparing metal temperature predictions in the following section.

7.4.2 Metal Temperatures

The mechanical validation has all been conducted against in-house Rolls-Royce software which itself has been extensively validated for real engine cases.

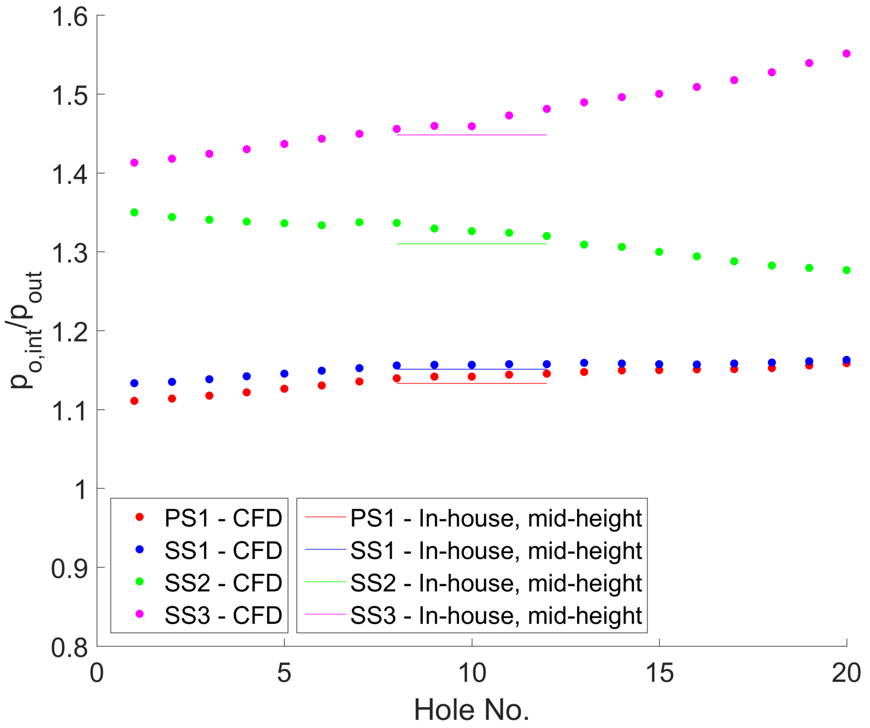

Figure 7.6: Pressure ratios across film holes - internal total to external static pressures

Initial validation compared the metal temperature predictions from the conjugate CFD simulations against those from the in-house Rolls-Royce software [122], figure 7.7. The validation has to take place against other FEA simulations due to the lack of stress distribution data available at engine conditions.

The metal temperature distribution found from the conjugate CFD follows the expected trends. The outer surface of the blade is found to be much hotter than the inner, due to the imposed boundary conditions on these surfaces. On the leading edge of the blade the lowest

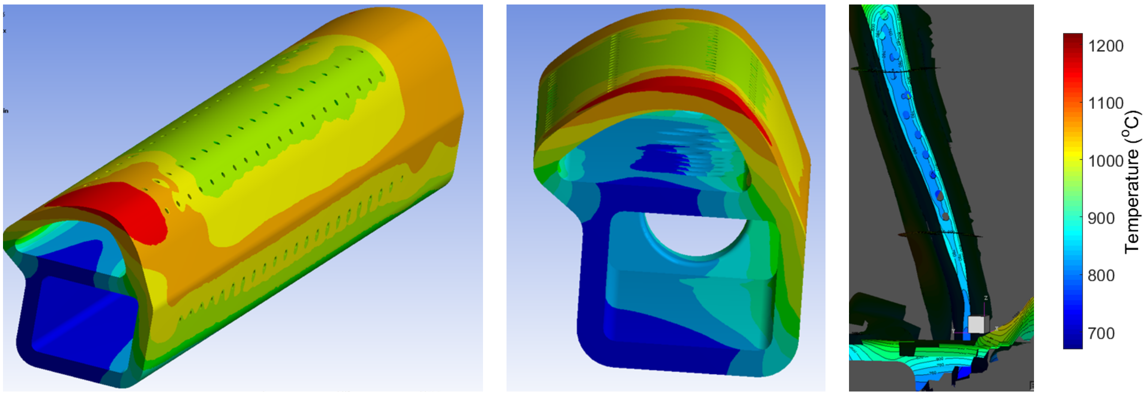

(a) Conjugate CFD prediction - 1

(b) Conjugate CFD prediction - 2

(c) In-house prediction

Figure 7.7: Blade metal temperature

temperatures are found under the impingement jets, indicating that effective cooling is taking place. Very high temperatures are found at the root and tip of the blade where no impingement or film cooling is present. However when considering the stress levels within the mid-height section of the web, as this study intends, these are not found to be significant.

The web temperature levels and distribution are seen to be very similar to the in-house software predictions with the coolest temperatures of around 700^{o}C found just towards the suction surface side of the impingement holes in the web.

The similarity between these indicates that the temperature distribution predicted by the conjugate CFD is sufficiently accurate to use to predict stress levels within the blade.

7.4.3 Principal Stresses

Figure 7.8 compares the maximum, mid and minimum principle stresses predicted by the new method to those calculated by the in-house stress analysis software [122]. The contours are shown on the same scale for the web surface around the three central impingement holes, as viewed from the leading edge of the blade.

The maximum principal stress levels are very close for the two different methods with only minor differences in the distribution. The same pattern of peak stress down the sides of the holes and the lowest stresses at the radial ends of the holes are followed in both cases, however are angled slightly in the in-house results. This is as the simulation was performed on a blade with a twisted, three-dimensional profile, which introduces stress components which are not present on the analysis of the constant cross-section geometry.

This is again evident on the mid and minimum principal stress plots where a clear gradient is observed across the web, which is not predicted by the new method. However the overall stress levels are similar for these components, confirming the correct boundary conditions have been used.

7.4.4 Directional Stresses

Figure 7.9 illustrates the axial, radial and tangential components of stress from both analyses.

It can be seen that the levels of stress are similar for all components however with a different distribution in the axial and tangential directions. These are created by the difference

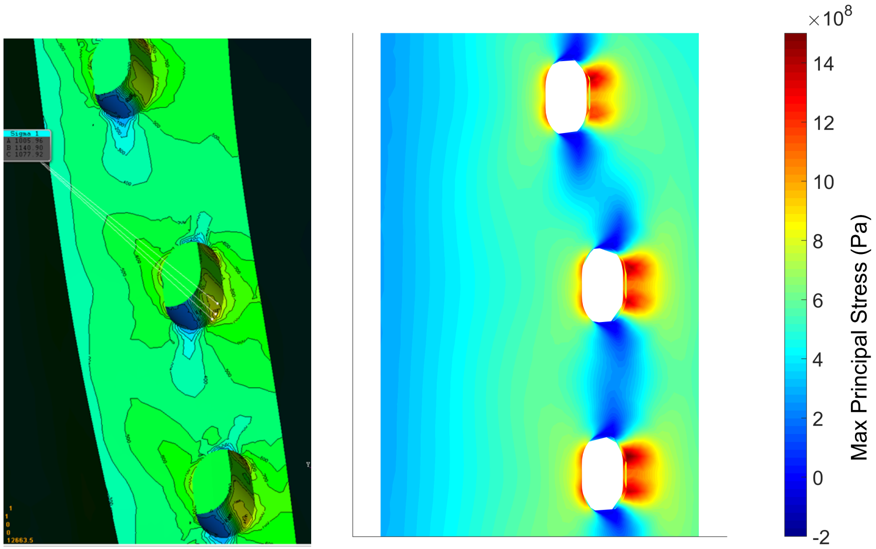

(a) Max - in-house (b) Max

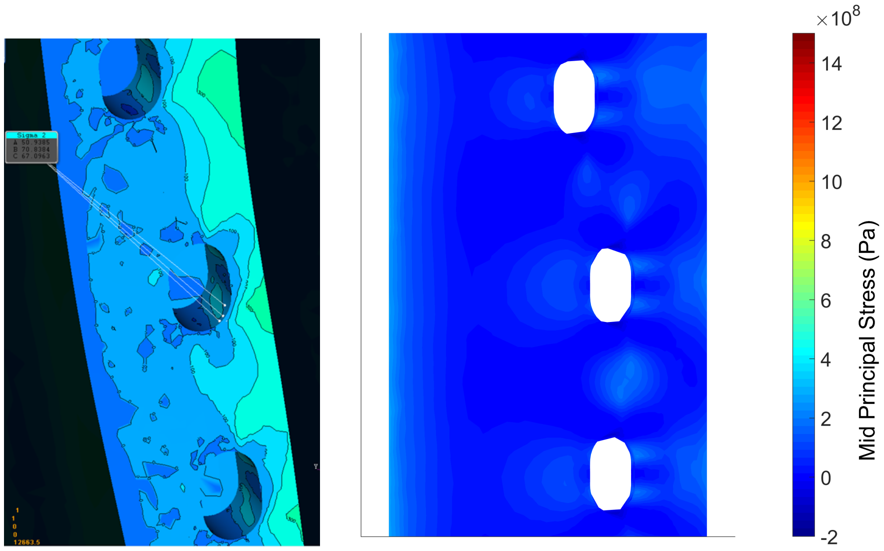

(c) Mid - in-house (d) Mid

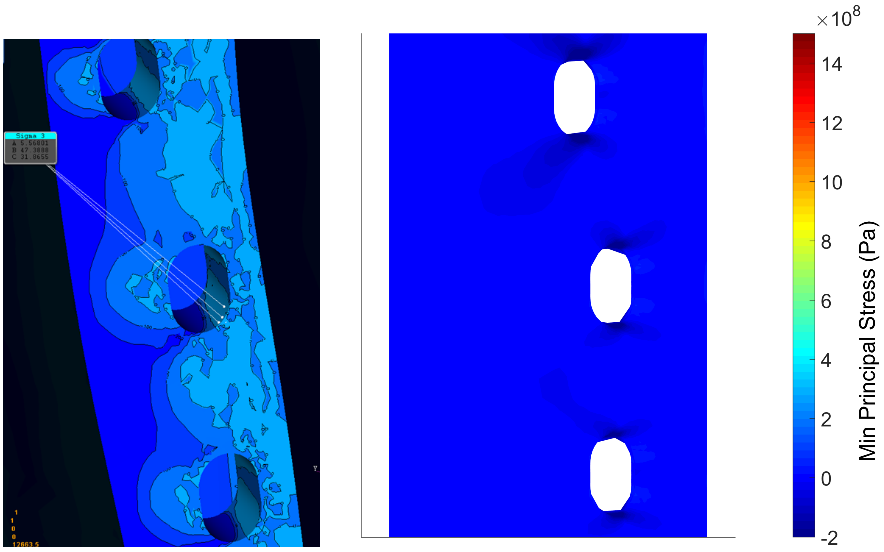

(e) Min - in-house (f) Min

Figure 7.8: Mid height max, mid and min principal stresses

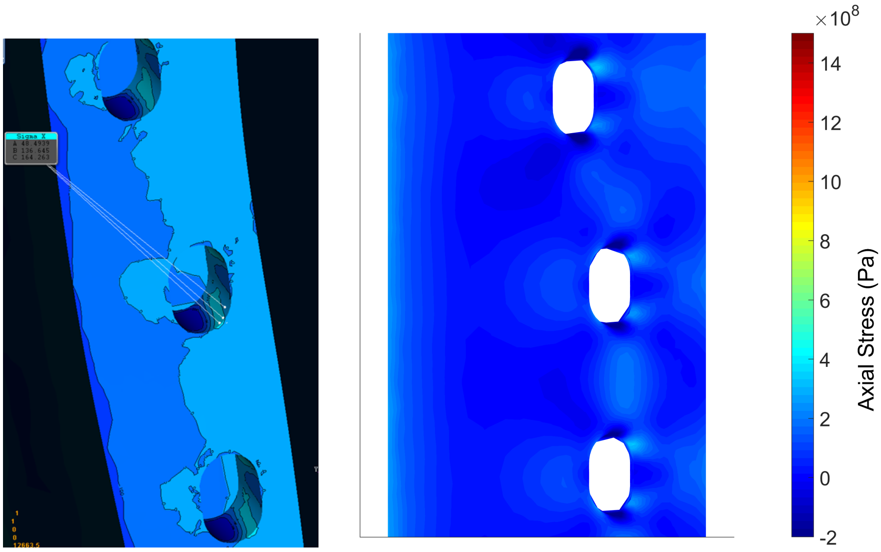

(a) Axial - in-house (b) Axial

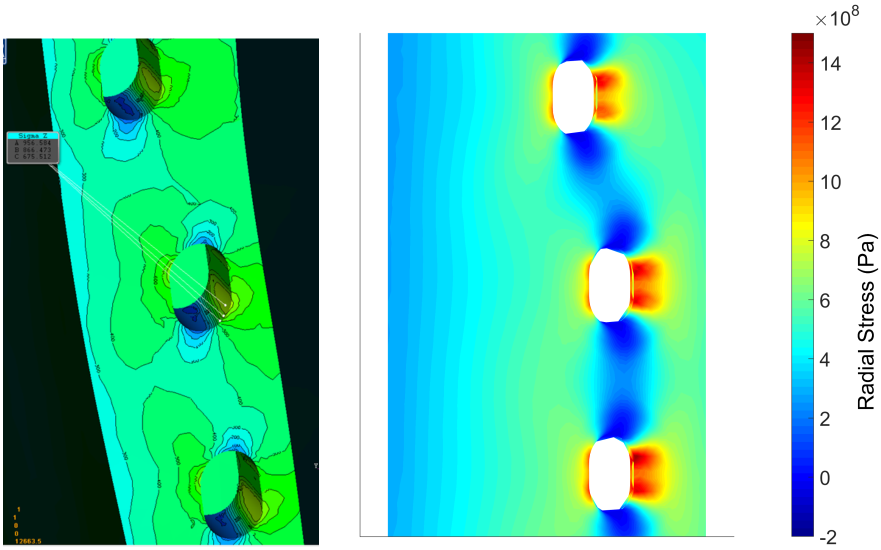

(c) Radial - in-house (d) Radial

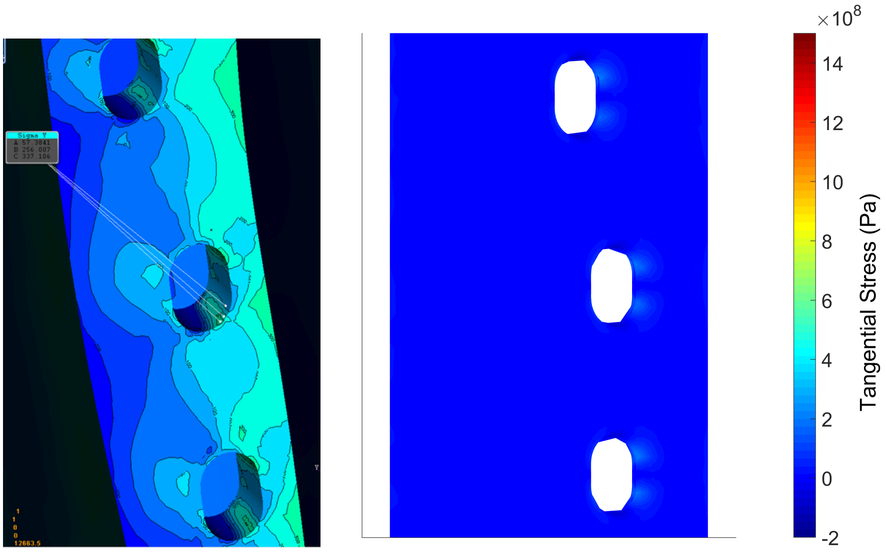

(e) Tangential - In-house (f) Tangential

Figure 7.9: Mid height axial, radial and tangential stresses

between the geometries used for the analyses. The radial stress distribution, however, is very well matched with only slight differences introduced due to the blade lean. It is also clear that the radial stress is the most dominant, contributing greatly to the maximum principal stress.

Therefore as blade life depends primarily on the maximum principal stress, which is seen to be well matched, the differences in stress distribution introduced by considering a prismatic cross section geometry, rather than a full three-dimensional geometry, are not considered to be significant. This is especially true when examining the relative performance of multiple designs, rather than the absolute stress levels of a single cooling system inside a complete blade.

7.4.5 Stress Assessment Criteria

Following the validation of the method, the latter was then used in order to develop understanding of the causes of high stress levels and concentrations within a leading edge impingement system and investigate methods of reducing the effect of these on blade life. The criterion used to assess the relative mechanical performance of the different variations is given by equation 7.1.

$$Stress\ criterion = \frac{Max.\ prin.\ stress}{UTS\ @\ T_{local\ metal}} \tag{7.1}$$

Stress contours will be presented in this form for the remainder of this paper. This criterion is used as blade life is heavily dependent on the maximum principal stress however the material properties vary greatly with temperature, figure 7.10, and this variation must be taken into account in order assess the stress field of the different systems. As for the material properties in table 7.3 the data given is for the Rene N5 nickel based alloy [119], which displays similar dependence of UTS on temperature. This is also the criterion used by Rolls-Royce design teams when assessing the relative life performance of different configurations.

7.5 Metal Temperature - Initial Investigation

In this section the effect of the temperature profile in the metal on the mechanical performance of the blade are investigated. The same baseline geometry, with filleted impingement holes, was used for the results presented below.

The FEA software allows for manually generated temperature profiles to be interpolated

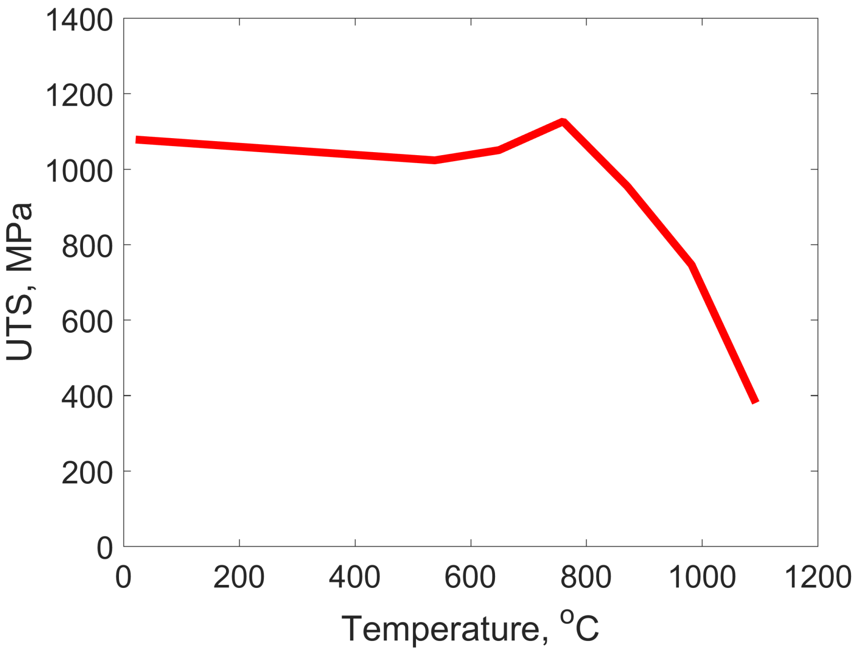

Figure 7.10: UTS of blade material with temperature

onto the geometry, and a stress analysis conducted. This enables the effects of individual features of the temperature profiles, such as gradients and bulk temperatures, on the stress distribution to be evaluated. Initially the full temperature distribution from the conjugate CFD simulation was compared to an isothermal blade, and to a 2D mid-section profile.

7.5.1 Temperature Profile vs Isothermal

The first test was conducted to show the importance of the temperature distribution on the mechanical performance of the blade. This compared the results of the full conjugate simulation against one where the metal was set to be isothermal at 950^{o}C. This is a representative temperature for the metal, and is well away from the peak UTS, as seen in figure 7.10. The comparison of the full temperature distribution against the isothermal analysis is given in figure 7.11.

It is observed that with the full temperature distribution the stress levels are far higher than in the isothermal case. This is due to the expansion of the hot outer metal relative to the cool web, which places large stresses on this web, and due to the temperature gradient across the web itself. It is clear that the metal temperature has a large influence on the stress levels, and therefore the features that cause this were then investigated in order to improve the thermal management of the blade.

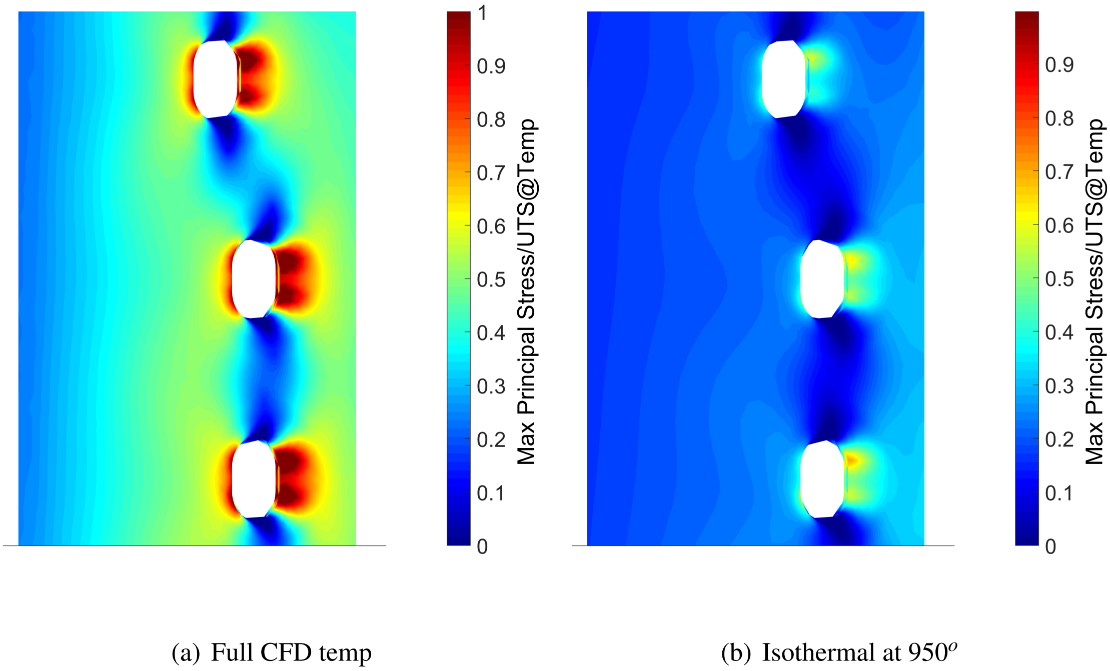

(a) Full CFD temp (b) Isothermal at 950^o

Figure 7.11: Stress - full CFD distribution against isothermal at a representative temperature

7.5.2 Two-dimensional Blade Temperature Profile

Until this point full three-dimensional temperature profiles have been used, however when imposing a metal temperature in order to analyse the effect of the distribution it is easier to isolate particular effects if a two-dimensional profile is used. Figure 7.12 shows the stress distribution for a metal temperature of the full 3D profile against the 2D profile from the mid-section of the metal, applied to the entire domain.

The stress distribution is very similar for both of these cases, indicating that radial temperature changes in the metal have a negligible effect on the stress around the impingement holes. Therefore two-dimensional temperature profiles will be used to investigate the impacts of the temperature profile on the stress distribution and therefore blade life. This is because a change in the two-dimensional temperature profile will directly translate to the three-dimensional distribution and is much more easily manipulated than a full three-dimensional distribution.

7.6 Results - Geometric

In this section different impingement geometries have been tested in order to assess the extent to which different features affect the mechanical performance of an impingement system. The

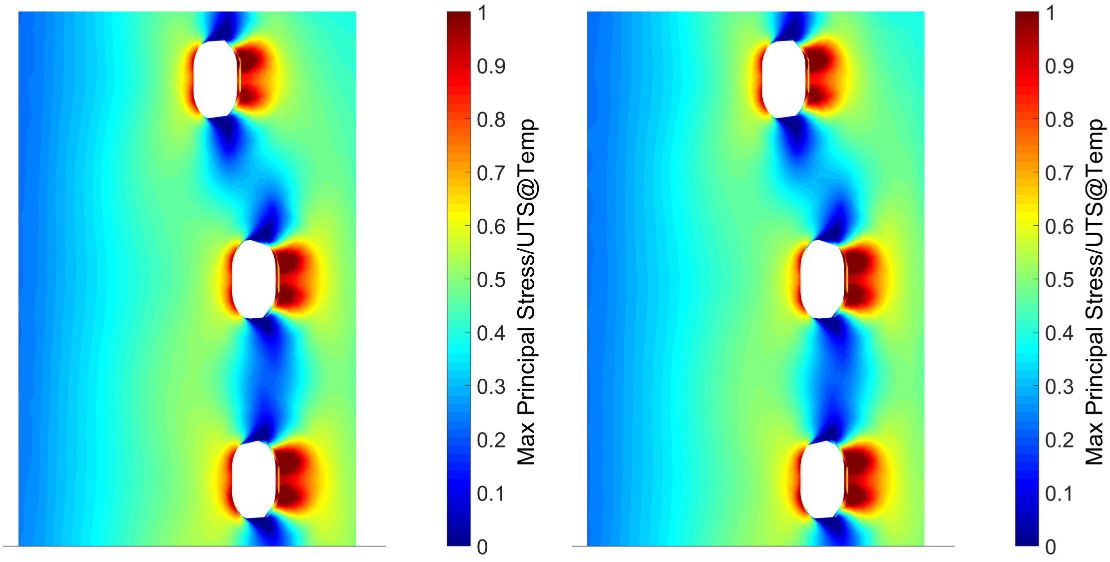

(a) Full CFD temperature (b) 2D profile from CFD

Figure 7.12: Use of 2D temperature profile

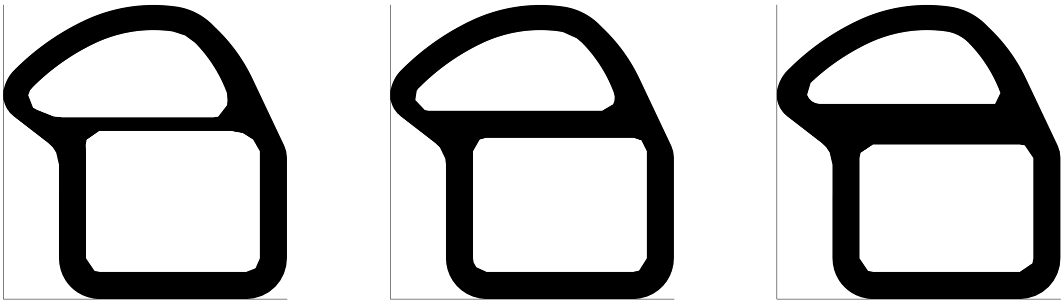

(a) 0.5 mm (b) 1.0 mm (c) 1.5 mm

Figure 7.13: Variation of web thickness - slice through mid-height of geometry

simulations were conducted with the 2D profile gained from the baseline CFD applied to each geometry. This is to quantify the effects of changing the geometry with a representative temperature distribution, whilst isolating these from changes to the metal temperature which may be caused by altering the geometry.

7.6.1 Web Thickness

Initially the web thickness was varied from 1 mm, to 0.5 mm and 1.5 mm, illustrated in figure 7.13.

It can be seen clearly from this figure that the changes in web thickness are very large,

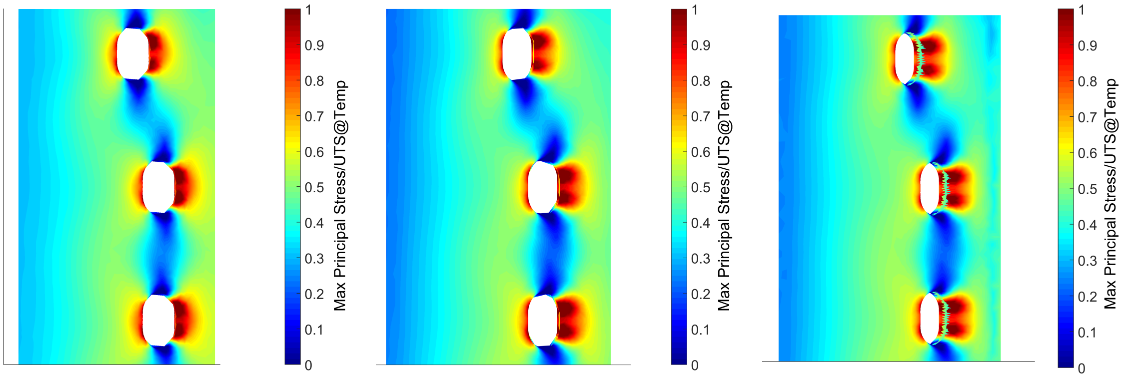

(a) Stress - 0.5 mm (b) Stress - 1.0 mm (c) Stress - 1.5 mm

Figure 7.14: Variation of web thickness - stress

and therefore any effect from changing the web thickness should be visible. The 1.5 mm web geometry maintains a 0.5 mm fillet radius while the fillet radius on the impingement holes is reduced to 0.25 mm on the 0.5 mm web geometry.

Figure 7.14 gives the maximum principal stress/UTS@temp contours for each web thickness.

Despite the very large changes in web thickness very little change in stress levels are observed. The double peak of stress on the side of the impingement hole is less clear in the narrow web thickness geometry, due to the change in fillet on the impingement holes, and is slightly more pronounced on the 1.5 mm web. However there is very little change in the peak values, indicating that altering the web thickness is not likely to yield a significant improvement in the mechanical performance of an impingement system.

7.6.2 Impingement Hole Fillet

Another key aspect of the impingement geometry is the degree to which the impingement holes are filleted. The fillet is present due to limitations in the manufacturing process and therefore a comparison between a filleted and sharp-edged geometry was made. The full radius fillet is defined such that the fillet radius is half the hole length, in this case 0.5 mm. The stress distributions resulting from this are given in figure 7.15.

The effect the fillet has on the stress distribution is seen to be small, with peak stresses very similar in the two different cases. There are some areas with reduced stresses in the filleted case. Due to these relatively small differences it is assumed that there is no significant effect

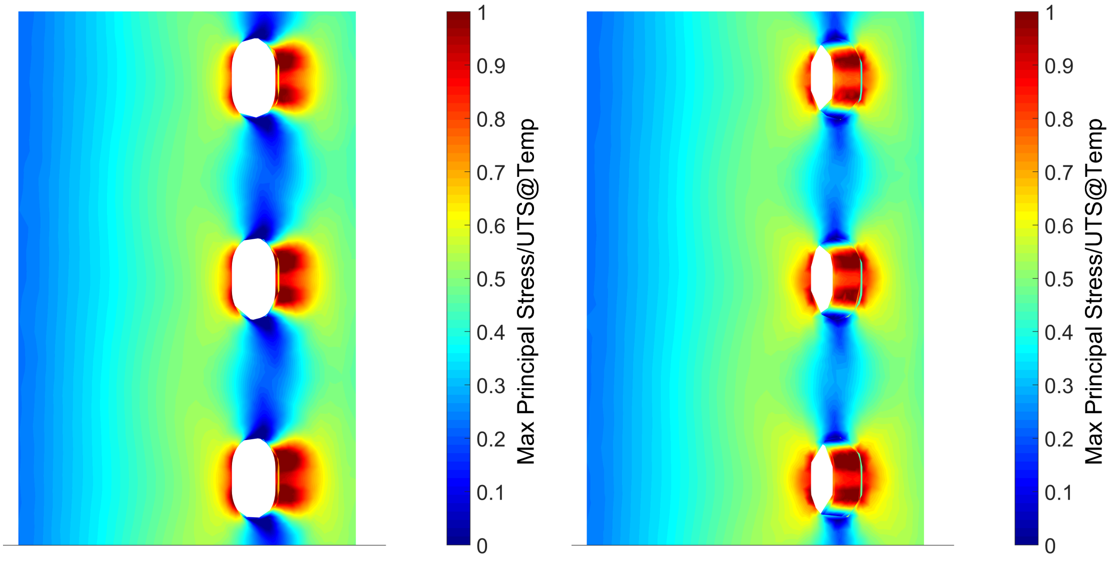

(a) Full radius fillet (b) No fillet

Figure 7.15: Variation of fillet on impingement holes

in having filleted impingement holes and any small changes observed are seen to improve the stress distribution. This is useful for blade design where it is not possible to tightly control the fillet radius within the manufacturing process.

7.6.3 Impingement Hole Geometry

Following this the impingement hole geometry was altered, within a constant 1 mm thick web. In all of these geometries non-filleted impingement holes were used due to the different fillet radius definition that would be required for angled holes. The hole configurations tested were with the impingement holes angled radially outward at 45^o, axially towards the suction surface at 30^o and a combined radially and axially angled geometry, figure 7.16. The stress results from the different geometries are given in figure 7.17, with detailed views of the in-hole stresses in figure 7.18.

As with previous changes in the geometry there are only small changes in the stress distribution found with the angled impingement jets. The peak stress levels are very similar with only small changes of the distribution within the impingement hole itself, which are more evident in the radially angled holes. These show a small gradient in peak stress levels throught the hole itself, in opposing directions for the radially inner and outer peaks.

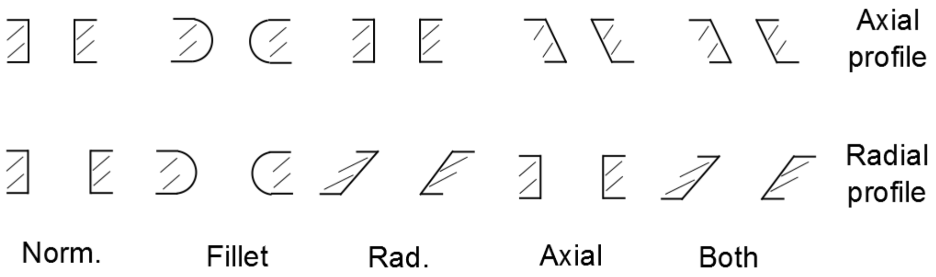

Figure 7.16: Radial and axial impingement hole profiles

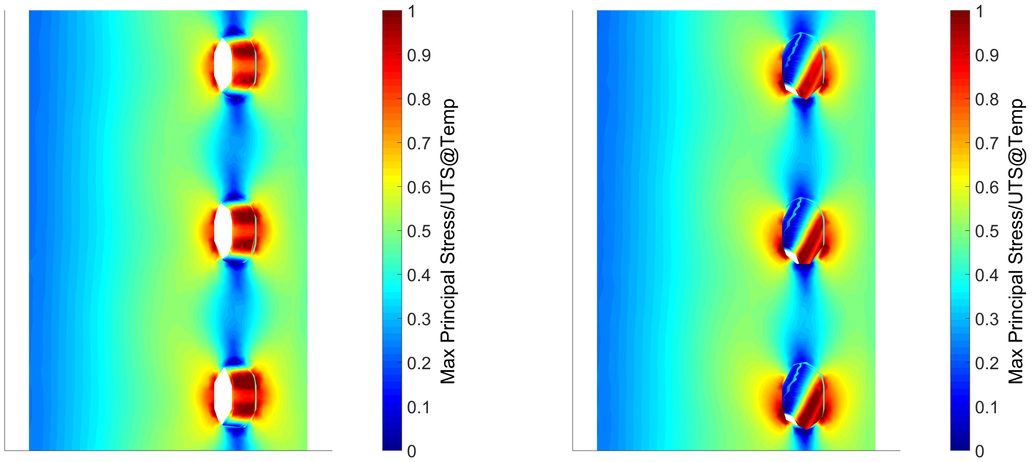

(a) Normal, no fillet

(b) Radially angled - 45^o

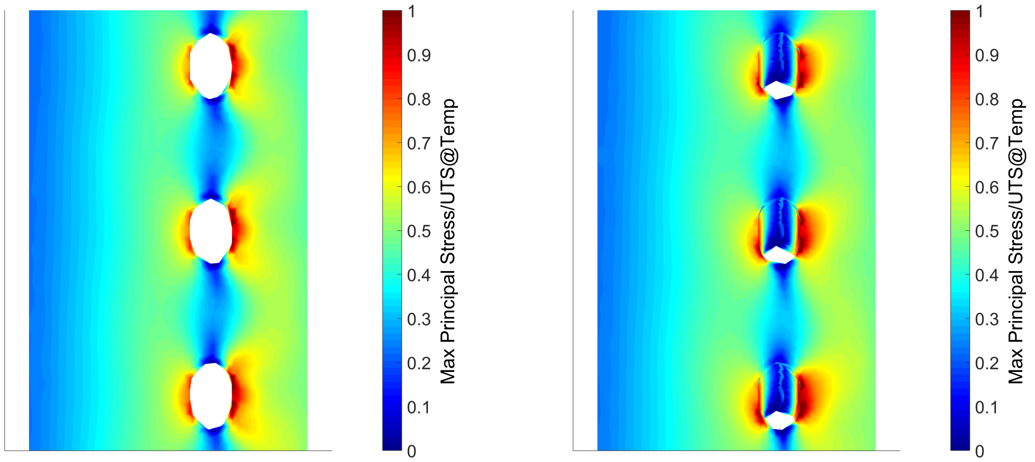

(c) Axially angled - 30^o

(d) Axially and radially angled

Figure 7.17: Variation of hole shape (different viewing angles in order to see internal surface of impingement hole)

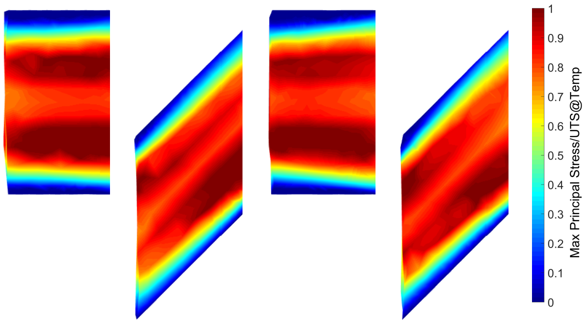

(a) Norm. (b) Rad. (c) Axial (d) Both

Figure 7.18: Variation of hole shape - side view of central hole

It has been found that altering the impingement geometry, while applying a fixed temperature profile, has little effect on the stress criterion on which blade life is heavily dependent. This is both in terms of absolute levels and distribution. Therefore different metal temperature profiles will be investigated to quantify their effect on the stress levels with the aim of reducing these. The temperature profiles then can be obtained through careful design of the impingement system, which is possible as it has been shown that the alterations in geometry have little direct effect on stress levels.

7.7 Results - Temperature Profile

7.7.1 Baseline Blade Temperature Profile

In order to examine the relative stress levels with different metal temperatures, an approximate temperature profile for the blade was developed. This was done in order to allow easy variation of the blade metal temperature against a representative baseline case. The profile consisted of a two-dimensional polynomial profile around the leading edge and feed passage and a one-dimensional profile across the web. The one dimensional profile was modelled as both a 1st and 2nd order polynomial between the minimum and maximum temperatures to determine the effects of the gradient across the web. The profiles are shown in figure 7.19.

It is observed in figure 7.20 that the first order approximate profile gives significantly different stress results, as would be expected, however the second order profile stress analysis is very similar to that using the 2D profile from the CFD. This indicates that the second order approximate 2D profile can be used as a baseline from which adjustments can be made. The effect of

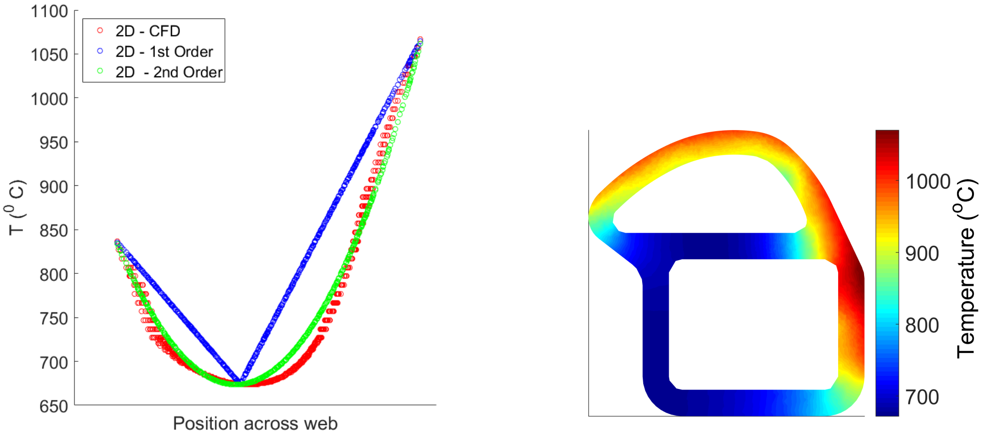

(a) Temperature profiles (b) CFD

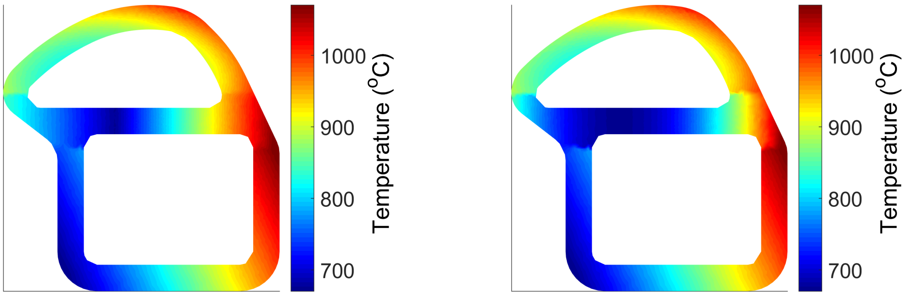

(c) 1st order profile (d) 2nd order profile

Figure 7.19: Illustration of different temperature profiles

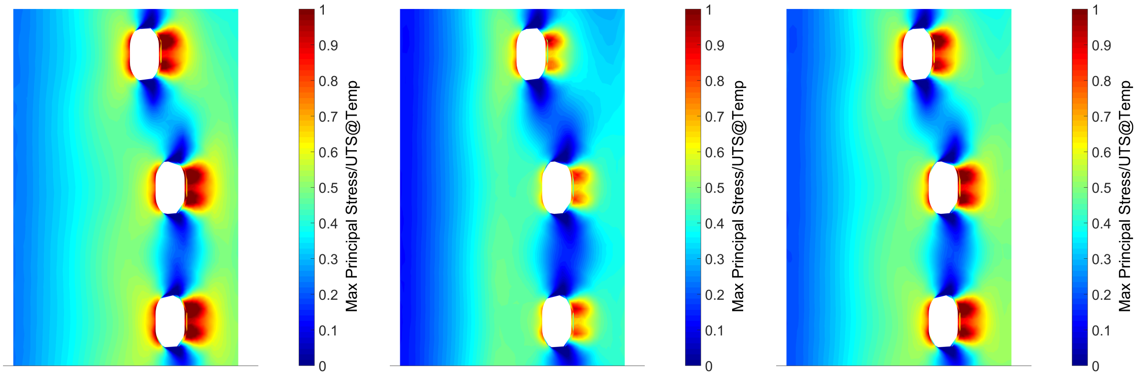

(a) 2D CFD (b) 1st order (c) 2nd order

Figure 7.20: Variations of max principal stress/UTS@temp for different temperature profiles

these can then be easily assessed in order to find the optimum blade temperature distribution.

7.7.2 Variation of Temperature Profile

Two main aspects of the temperature profile were investigated. These are the temperature gradient across the web, and the bulk temperature difference between the outer blade ‘shell’ and the web itself. The temperature profiles are illustrated in figure 7.21 with the corresponding stress distributions given in figure 7.22.

Figure 7.21 (a), (b) and (c) show the bulk temperature profiles. In these cases the web temperature has been fixed at constant temperatures of 700^{o}C, 750^{o}C and 800^{o}C respectively. Figure 7.21 (d) shows the temperature distribution across the web for the simulations where the minimum temperature in the web has been increased by 25^{o}C and 50^{o}C, whilst maintaining the same temperatures at either end of the web.

In both cases the outer metal temperature distribution remains that of the approximate temperature distribution created previously.

The stress distributions for each of these temperature profiles are given in figure 7.22 for those with a bulk web temperature while in figure 7.23 are those with a representative profile, however with an adjusted minimum temperature.

The effect of changing the bulk web temperature on the web stress distribution is very clear. With increasing web temperature the stresses are reduced significantly over the range investigated. The distribution remains similar to that found using the conjugate CFD metal temperatures, with some small changes across the web as would be expected. The stress levels around

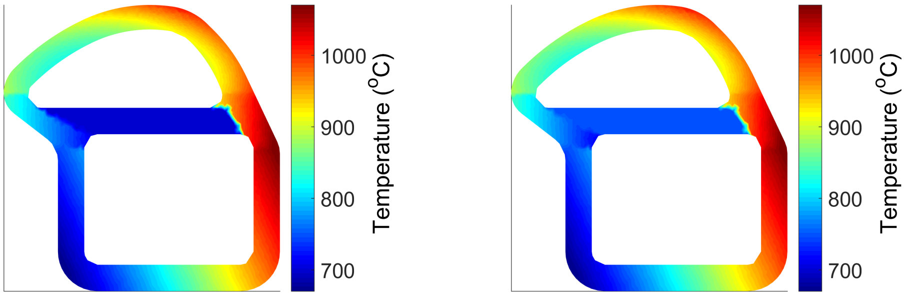

(a) Web @ 700^{o}C (b) Web @ 750^{o}C

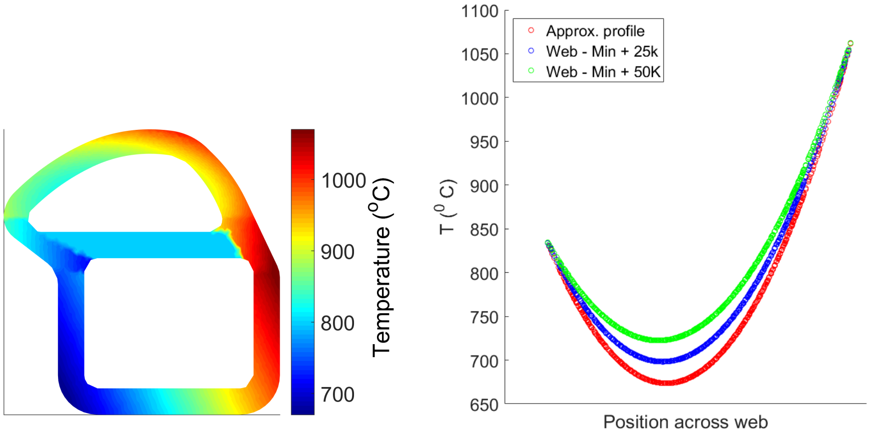

(c) Web @ 800^{o}C (d) Temperature across web

Figure 7.21: Blade metal temperature profiles

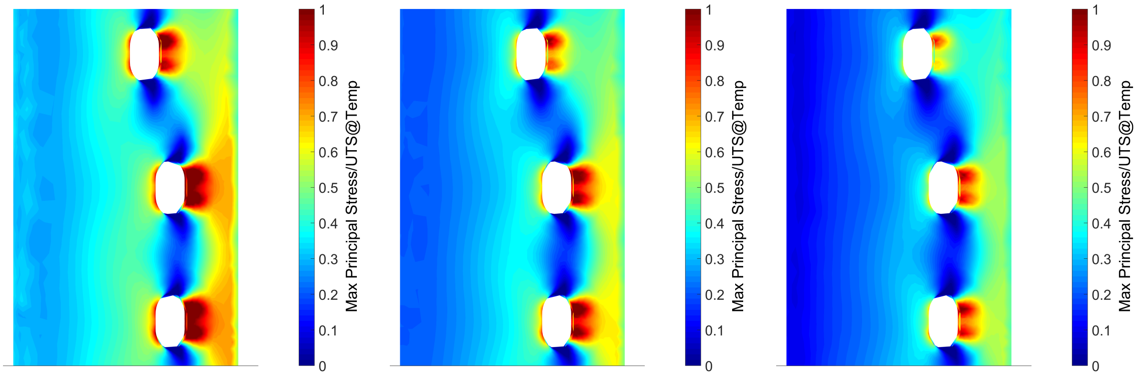

(a) Web @ 700^{o}C (b) Web @ 750^{o}C (c) Web @ 800^{o}C

Figure 7.22: Stress distributions with different blade metal temperature profiles - bulk web temperatures

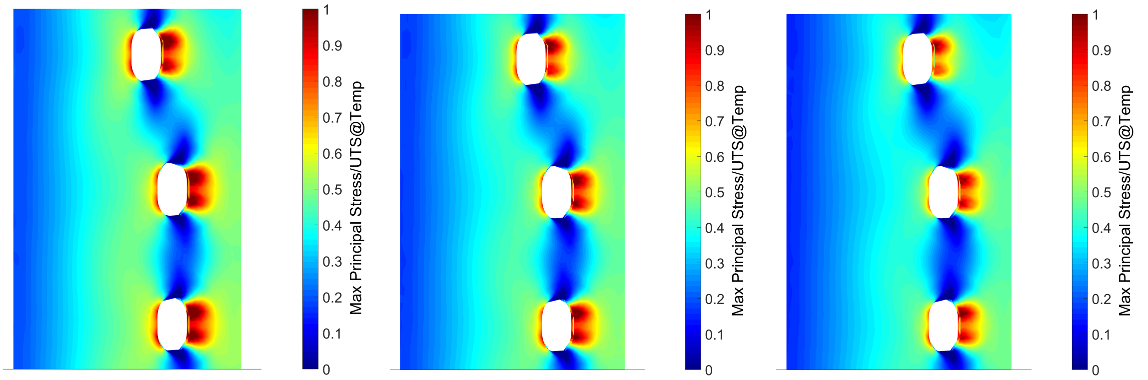

(a) Approx. temp profile (b) Min + 25^{o}C (c) Min + 50^{o}C

Figure 7.23: Stress distributions with different blade metal temperature profiles - adjusted minimum web temperature

the impingement hole indicate a constant temperature 750^{o}C web gives stress levels equivalent to those found using the conjugate CFD temperature distribution.

The effect of raising the minimum web temperature, whilst maintaining the same temperature at its edges, is less pronounced, yet still clear. With an increase in the minimum web temperature stress levels around the impingement holes and on the web are reduced.

This investigation shows that there is significant potential in reducing web stresses in impingement systems by increasing the temperature of the web. The flow of the cool air through the impingement holes cools the web and therefore impingement designs should consider both the cooling within the holes in the web, which should be minimised, and the cooling on the target surface, which should be maximised.

7.8 Summary and Conclusions

A new methodology utilising the Ansys Workbench, Fluent and Mechanical software has been developed and applied to a leading edge impingement cooling system in a gas turbine blade. This method combines full conjugate CFD of an isolated section of the blade with a stress analysis to allow the relative perfomance of different impingement configurations to be assessed. Temperature profiles are also imported directly into the mechanical simulation, enabling changes to the geometry and temperature profile to be tested without the need to run a full conjugate CFD simulation. The application of this method has led to the following conclusions.

1. Due to the strong dependence of the maximum principal stress on the radial stress, a constant cross section geometry can be used to examine the relative stress distributions in different cooling designs.
2. Significant changes in the web metal thickness have very little effect on the stress distribution in the web or around the impingement holes, and therefore changes to obtain the ideal heat transfer and temperature characteristics will not adversely affect stress levels.
3. Variations in impingement hole geometry and the presence of a fillet on the holes also have little effect on the stress distribution, also allowing for changes to the geometry to improve the heat transfer properties of the system.
4. The metal temperature distribution through a transverse section of the geometry greatly influences the stress distribution, whilst the radial temperature distribution has very little effect on stress levels.
5. Higher web temperatures, relative to the external wall temperatures, can significantly reduce stress levels around the impingement holes.

In future this methodology could be applied to different internal cooling geometries to assess them both, in terms of cooling and stress requirements. The tool could also be used to find an optimal temperature distribution, which the cooling configuration can then aim to achieve.

Chapter 8

Study of Sensitivity of Stress Field to HTC Distribution

In this chapter the sensitivity of the metal temperature and stress distributions in a leading-edge impingement system to variation in heat transfer levels on different surfaces is investigated. The focus of this work was to investigate the convective parameters responsible for the temperature field. In addition, an elastic FEA stress analysis was included to calculate the resulting stress field which, in turn, is responsible for blade life.

The stress distributions are calculated using the same process as in chapter 7, however the temperature distributions are obtained from an FEA simulation with imposed heat transfer conditions on all surfaces, rather than from a conjugate CFD solution. This significantly reduces the time taken for each simulation and also allows for the effect of altering HTC levels on different surfaces to be directly modelled.

The intent was that this study could be used to directly improve the cooling performance of a blade design through the variation of HTCs in different regions, either by geometric or convective changes, and to also assess the effect of uncertainty in the HTC levels used in the modelling process on the temperature and blade life.

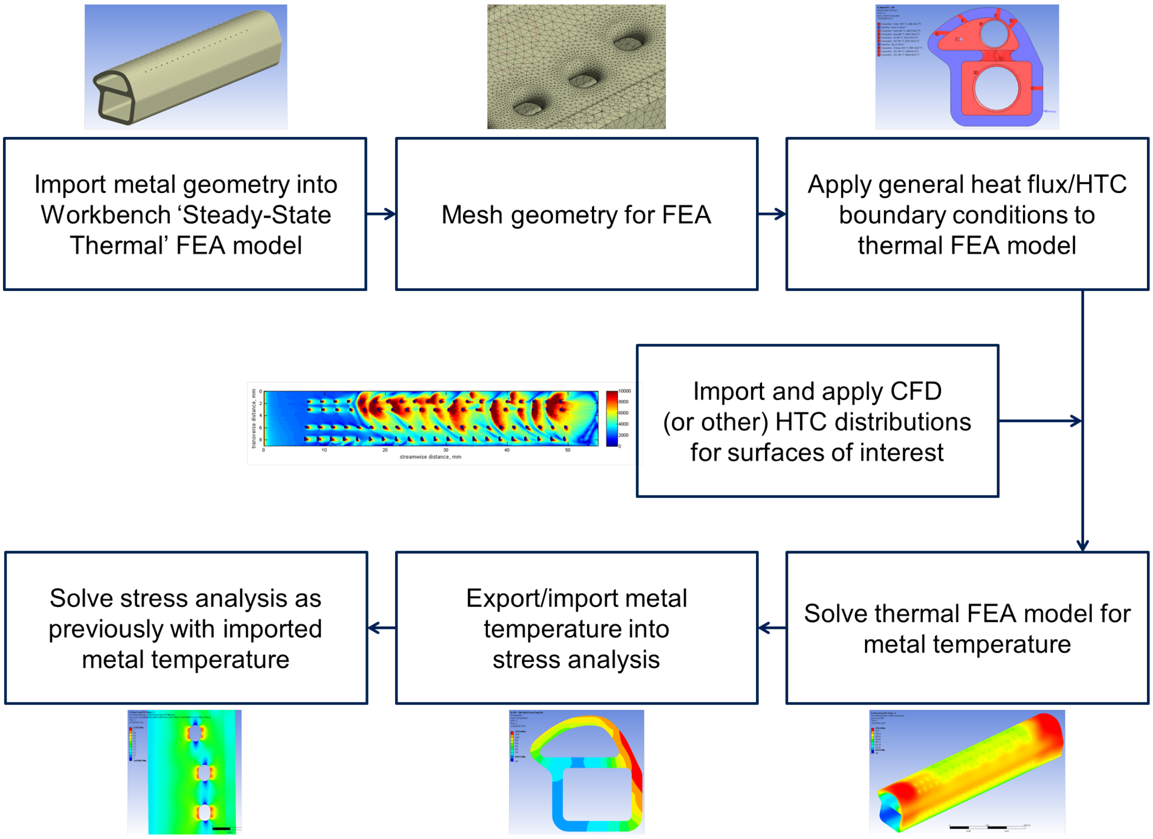

Figure 8.1: Method outline flow chart

8.1 Method

8.1.1 Outline

The method involves a number of stages which are illustrated in figure 8.1.

1. Initially the required geometry is produced using CAD software and imported into Ansys Workbench. A 'Steady-State Thermal' FEA model is then created using this geometry.

2. Following this the geometry is meshed using the in-built Ansys Mechanical meshing software. For this particular leading edge geometry, the same as that used in chapter 7, a global element size was set, with refinement on the film and impingement hole surfaces.

3. Once meshing has been completed thermal boundary conditions are applied to the model. These can be specified in a number of ways. In this case heat flux and HTC with driving gas temperature conditions were used on internal and external surfaces. The boundary conditions can either be specified directly as specific values on each surface or using an imported distribution. For the leading edge internal surface a full distribution from a conjugate CFD simulation was imported and mapped to the relevant surfaces.

4. The thermal model is then solved using the Ansys Mechanical FEA software to give a full, three-dimensional metal temperature distribution. The material properties were set to be representative of a modern turbine blade.

5. The full temperature distribution is then analysed, and also exported for use in a stress analysis.

6. A stress analysis is performed using the same methodology as in chapter 7 using the imported temperature distribution.

8.1.2 Thermal Simulation Details

The finite element simulation requires many different thermal boundary conditions which in this case are taken from a combination of correlations and other simulations. Figure 8.2 (a) illustrates the different regions to which thermal boundary conditions were applied.

The external surfaces were modelled identically to the conjugate CFD in chapter 7, with a uniform HTC of just over 4000 $W/(m^2K)$ and a free stream temperature of approximately 1800 K applied over the leading edge. The remaining external surfaces were modelled as adiabatic, as in a real blade case these would be internal to the blade and therefore can be reasonably approximated as adiabatic.

The internal surfaces were modelled using a constant representative coolant gas temperature for simplicity, and the earlier conjugate CFD analysis has shown there is relatively insignificant temperature change (less than 3^oC) throughout the passage length. The HTCs on the internal surfaces were calculated using the Dittus-Boelter correlation to achieve representative levels for each passage, apart from the leading edge internal surface where a distribution was imported from a conjugate CFD solution. This was done in order to remain representative of a real system as under the impinging jets there are large spatial variations in HTC. The resulting heat flux distribution is given in figure 8.2 (b).

Details of heat transfer coefficients applied to each internal surface are given in table 8.1. These were all calculated using the Dittus-Boelter correlation based on the Reynolds number and hydraulic diameter of the relevant feature.

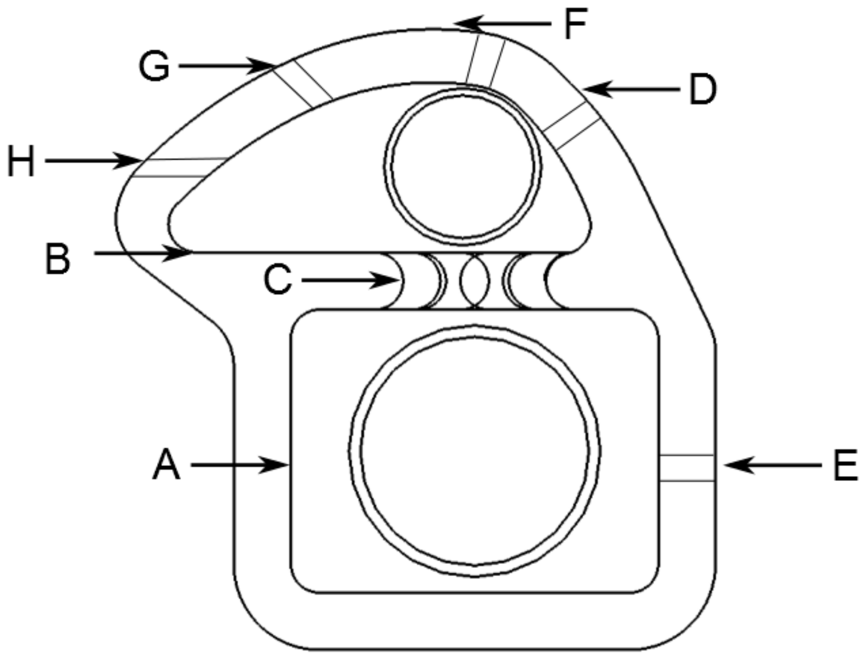

(a) HTC regions

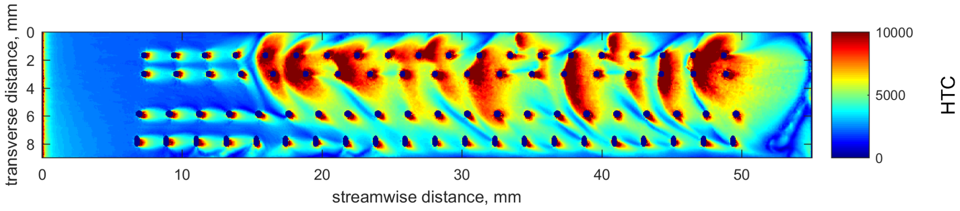

(b) LE internal HTC distribution

Figure 8.2: HTC regions and LE internal HTC distribution

Table 8.1: HTC details

Label in 8.2		Re No.	D_H (mm)	Nu No.	HTC
A	Feed	128195	5.77	244.6	2440.5
B	LE	49275	3.80	113.8	1879.5
C	Jet	54510	1.203	123.4	6439.5
D	PS1	19980	0.38	55.3	9133.2
E	PS2	21180	0.35	57.9	10382.3
F	SS1	21550	0.38	58.7	9694.8
G	SS2	22845	0.35	61.6	11045.8
H	SS3	18332	0.35	51.6	9252.6

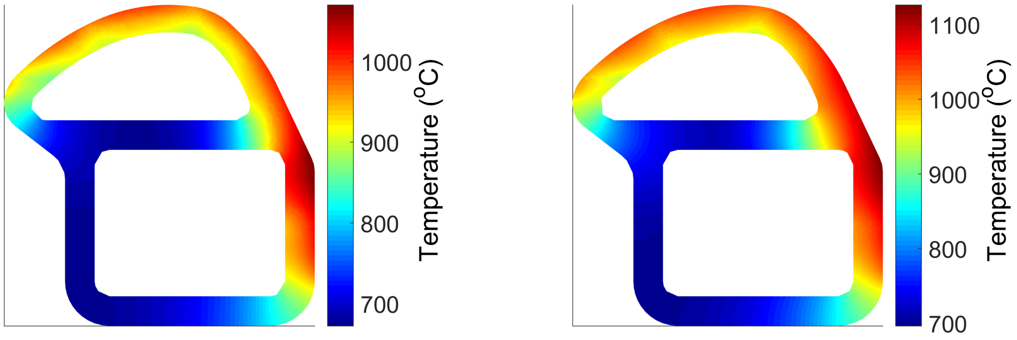

(a) Conjugate CFD (b) Thermal FEA

Figure 8.3: Conjugate CFD vs thermal FEA - metal temperature comparison

8.2 Comparison of New Method with Conjugate CFD

The results obtained using the FEA thermal simulation are compared below to those obtained using a full conjugate CFD solution, in order to verify that the salient features in the temperature and stress distributions are accurately represented.

8.2.1 Temperature Distribution

Figure 8.3 compares the metal temperature distribution from the conjugate CFD to that obtained by the new method as described above.

The general trends in distribution are seen to be similar in both cases with high temperatures around the right hand section of the blade, and considerably lower temperatures in comparison to this under the impingement jets. The lowest temperatures are also found in the web, due to the in-hole cooling effect of the impingement system, and in the feed wall where the adiabatic boundary condition is found. However the conjugate CFD shows consistently lower temperatures than the new method. This is due to the underestimated heat pickup caused by using the Dittus-Boelter correlations. The correlation does not take into account local features, such as separation and reattachment regions, which can significantly raise the heat transfer levels.

However, the temperature distribution from the FEA model is close to the conjugate CFD, and maintains the key features of the distribution, such that it may be used as a baseline from which relative changes due to HTC adjustments can be assessed.

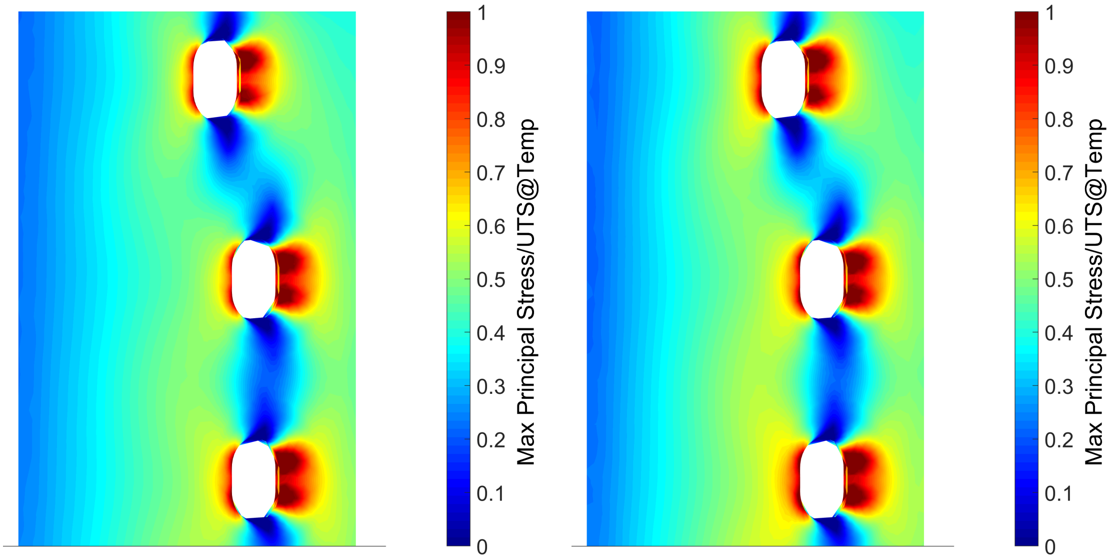

(a) Conjugate CFD

(b) Thermal FEA

Figure 8.4: Conjugate CFD vs thermal FEA - stress comparison

8.2.2 Stress Distribution

Figure 8.4 compares the stress distribution from the conjugate CFD to that obtained by the new method. As before, this is displayed in the form of maximum principle stress/UTS at temperature contours.

The distributions are seen to be very similar for these two simulations. The stress concentrations around the impingement holes are of similar shape and magnitude while web stress levels further from the holes also seen to be very well matched.

This confirms that the FEA thermal model with applied HTCs is representative of the fully resolved conjugate simulation, and therefore can be used as a baseline from which to assess the effect of HTC alterations in different regions.

8.3 HTC Adjustments - Temperature

Following the establishment of the method, HTC levels were systematically varied on the different surfaces in order to assess the sensitivity of both metal temperature and stress levels to changes in HTCs. HTCs were varied on the leading edge, web and in-hole areas by ± 20 % as illustrated in figure 8.5. This level of change was chosen as it is likely to be achievable by im-

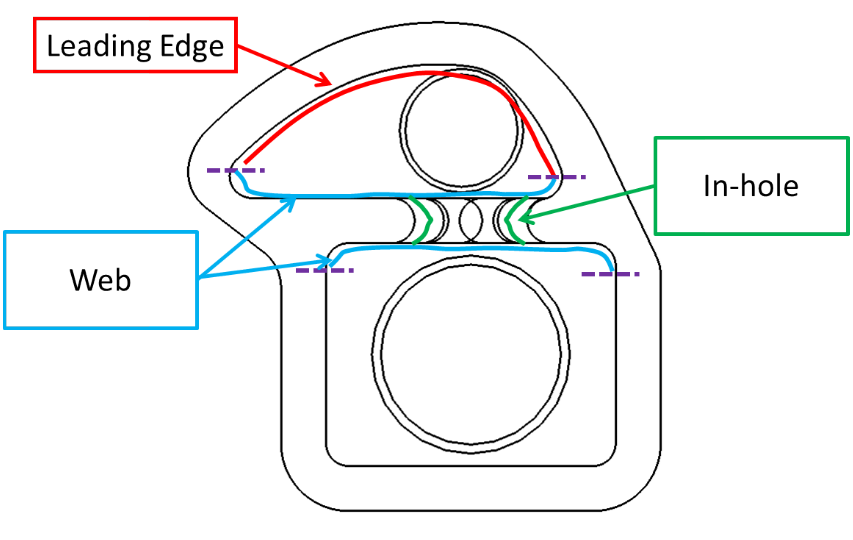

Figure 8.5: HTC adjustment regions

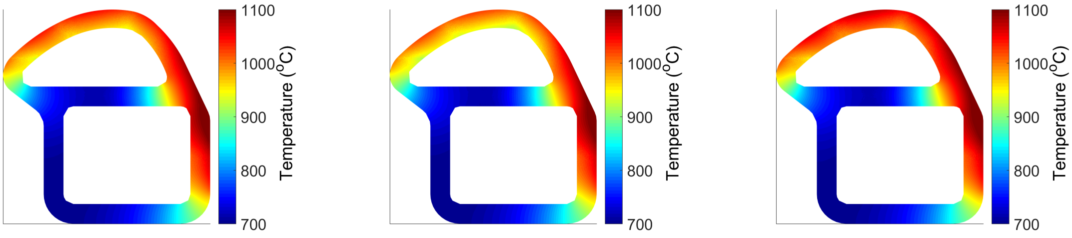

(a) Initial (b) LE HTC +20% (c) LE HTC -20%

Figure 8.6: LE internal HTC +/- 20% - metal temperature

provements in cooling technology whilst remaining realistic. It was judged to be large enough to cause identifiable changes in both temperature and stress distributions if these are reasonably dependent on the HTC levels in the areas which are investigated.

Leading Edge

The temperature distributions for the leading edge internal HTC alterations are given in figure 8.6.

It is clear that the alteration of the leading edge heat transfer levels has a very large influence on the metal temperature in this region. An increased HTC greatly reduces the temperature while it is increased for a reduction in HTC levels. Other regions of the leading edge model remain unaffected by this change with no differences in temperature observed other than in the leading edge region. This indicates that the leading edge HTC can be altered to obtain a more desirable temperature without impacting the temperature distribution in other regions.

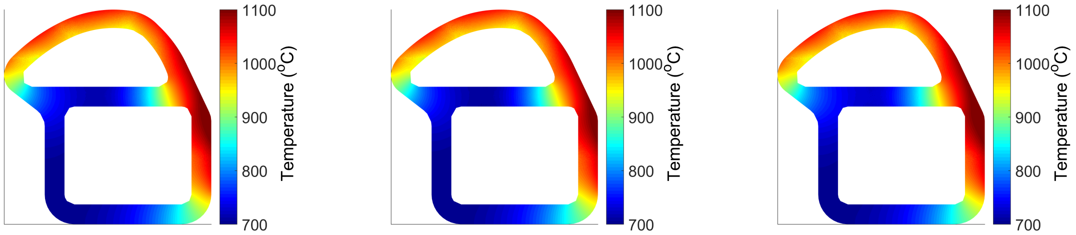

(a) Initial (b) Web HTC +20% (c) Web HTC -20%

Figure 8.7: Web HTC +/- 20% - metal temperature

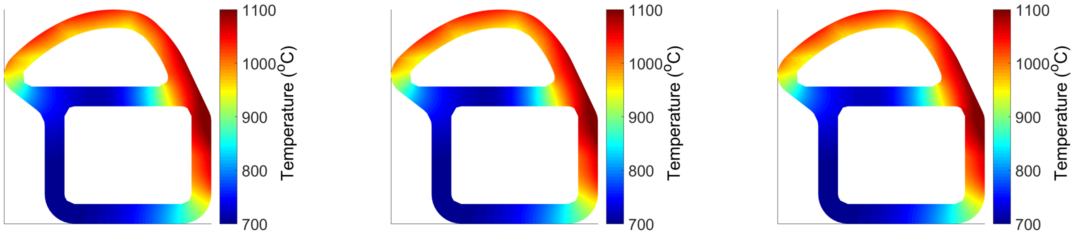

(a) Initial (b) In-hole HTC +20% (c) In-hole HTC -20%

Figure 8.8: In-hole HTC +/- 20% - metal temperature

Web

Temperature distributions from the simulations with the web HTC altered are given in figure 8.7.

The changes in temperature for this case are less prominent than those on the leading edge due to the lower heat fluxes involved, however clear changes are observed. These changes are also in regions of higher stress so are still likely to impact on the stress/UTS@temp levels, and therefore blade life. As would be expected the higher HTC levels result in a cooler web with a lower HTC giving a hotter web. However as seen in chapter 7 a hotter web is likely to be desirable to reduce stress and increase blade life.

In-hole

Figure 8.8 gives the temperature distribution with an alteration of the in-hole HTC levels.

The in-hole HTCs are very high, and therefore a significant change in temperature might be expected to occur from this perturbation. However due to the small surface area over which the coolant acts very little change in temperature distribution is observed in comparison to those resulting from other heat transfer alterations. A small change in web temperature is found, but significantly less than those from the same proportionate changes in HTC on the web.

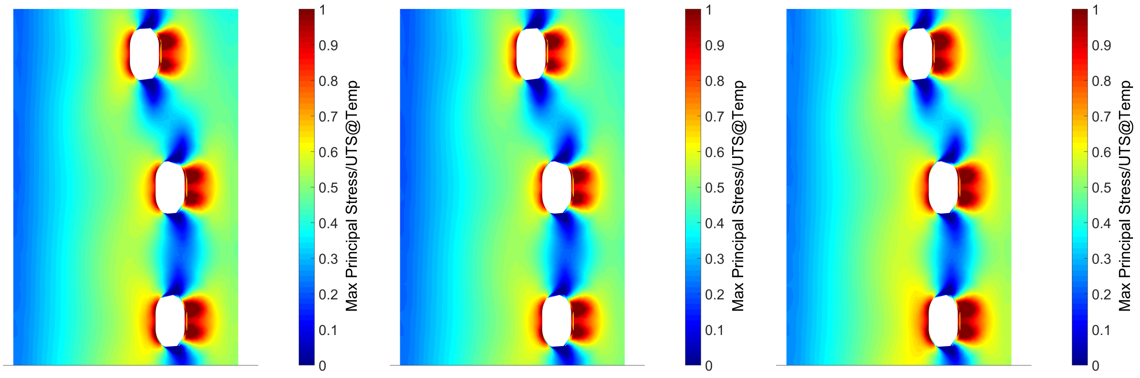

(a) Initial (b) LE HTC +20% (c) LE HTC -20%

Figure 8.9: LE internal HTC +/- 20% - stress distribution

In summary it is found that alterations to the leading edge and web heat transfer coefficients result in significant changes in temperature distribution, whilst the in-hole HTC alterations do not. This result guided the subsequent research away from the in-hole convective HTC. This is significant as the author was aware of forced geometric changes to the hole geometry which would affect this HTC distribution. The changes in temperature distribution are large enough that changes in the stress distribution would be expected, see section 8.4 below. The changes in temperature distribution are isolated in the region in which the HTC is altered.

8.4 HTC Adjustments - Stress

Leading Edge

The stress distributions from simulations that use the temperature distributions resulting from the leading edge HTC adjustments are shown in figure 8.9.

This figure indicates that there is not a large change in the web stress distribution for these cases. It would be expected for there to be lower stress levels in the case with higher LE HTCs as the lower leading edge temperatures would lead to less differential expansion between the web and outer shell. The opposite would be expected for the case with lower LE HTC levels.

This is observed to some degree, with stress levels around the impingement holes seen to be slightly lower for the raised HTC case, however the changes appear to be fairly small.

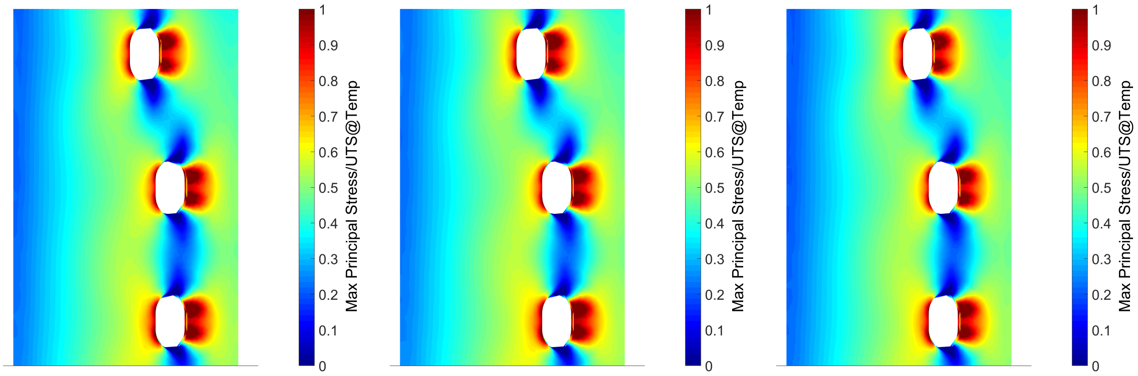

(a) Initial (b) Web HTC +20% (c) Web HTC -20%

Figure 8.10: Web HTC +/- 20% - stress distribution

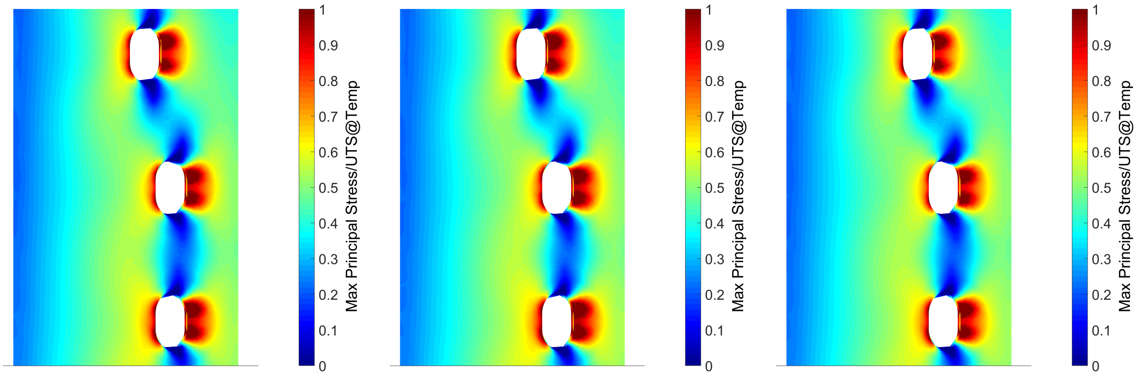

(a) Initial (b) In-hole HTC +20% (c) In-hole HTC -20%

Figure 8.11: In-hole HTC +/- 20% - stress distribution

Web

Figure 8.10 gives the stress distribution with altered web HTCs.

This case only shows very small changes in stress levels for the given alterations. The increased web HTC exhibits slightly higher stress levels, as the colder web results in greater relative expansion of the outer shell to the web. The reverse effect is seen when the web temperature is increased with a decreased HTC level.

In-hole

The stress distributions for adjusted in-hole HTC levels are shown in figure 8.11.

There are no visible differences in these stress distributions. This is expected due to the lack of any significant temperature changes resulting from the in-hole HTC adjustments.

A number of interesting points can be drawn from this section.

- It is observed that a 20% change in HTC levels can have a significant impact on metal temperature levels. Alterations in the leading edge HTC have the greatest effect, however in-hole levels have a very limited impact due to the small surface area.
- The changes in metal temperature are seen to be isolated in the region in which the HTC is altered, with no indirect effect in other regions of the metal.
- Stress levels are seen to be reduced by either increasing the leading edge HTC, or decreasing the web HTC as this reduces the temperature difference between the web and shell and consequently the relative expansion of the shell compared to the web.

8.5 Combined HTC Adjustments

Following the assessment of individual HTC adjustments a simulation was run to obtain a further reduction in stress levels through the combination of multiple adjustments. Due to the isolation of the effects of each HTC adjustment on the metal temperature it is likely that HTC adjustments in multiple regions can be successfully combined.

The combined simulation was run using an increased HTC on the leading edge and a decreased HTC on the web, both were changed by $+20\%$ and -20% respectively.

A change of $+20\%$ in HTC would be achieved in practice by increasing the flow by approximately 25 %. This could be implemented by changing the distribution of cooling flow around the blade to reduce the stress in life limiting zones, in this case the leading edge.

8.5.1 Temperature Distribution

The temperature distribution with the combined HTC adjustments is compared to the initial distribution in figure 8.12.

There are significant differences in the temperature distribution in the areas where expected from the HTC alterations. The leading edge is significantly cooler while the web temperature has increased over the initial simulation. This gives a small bulk temperature difference between the web and shell, and hence lower stresses in the web would be expected.

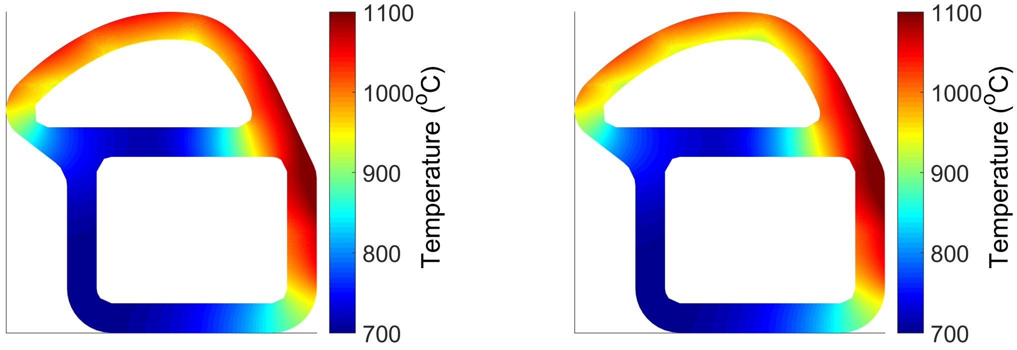

(a) Initial (b) Combined HTC Adjustments

Figure 8.12: Combined HTC adjustments comparison - metal temperature

8.5.2 Stress Distribution

Figure 8.13 gives the stress distribution comparisons for the combined simulation.

There is a clear improvement with the HTC alterations with significantly lower stresses around the impingement holes and across the web, resulting from the reduced temperature difference between the web and shell.

8.6 Cold Coolant

A potential development in future engines is to improve blade life through the use of cooled coolant air. In this system coolant air is passed through a heat exchanger in order to reduce its temperature before being used to cool the HP turbine blade, resulting in a significantly colder coolant temperature and the potential to extract more heat from the blade [123]. To simulate the approximate effect this may have on blade life the initial HTC levels were used with a coolant temperature reduced by 100 K at the inlet to see if stress levels were likely to decrease.

8.6.1 Temperature Distribution

Figure 8.14 shows the metal temperature distribution for the initial and cold coolant simulations.

The temperature distribution is much as would be predicted. With a uniform decrease in the temperature of both coolant streams the distribution remains very similar, however is significantly colder throughout, at approximately 100 K below the initial simulation.

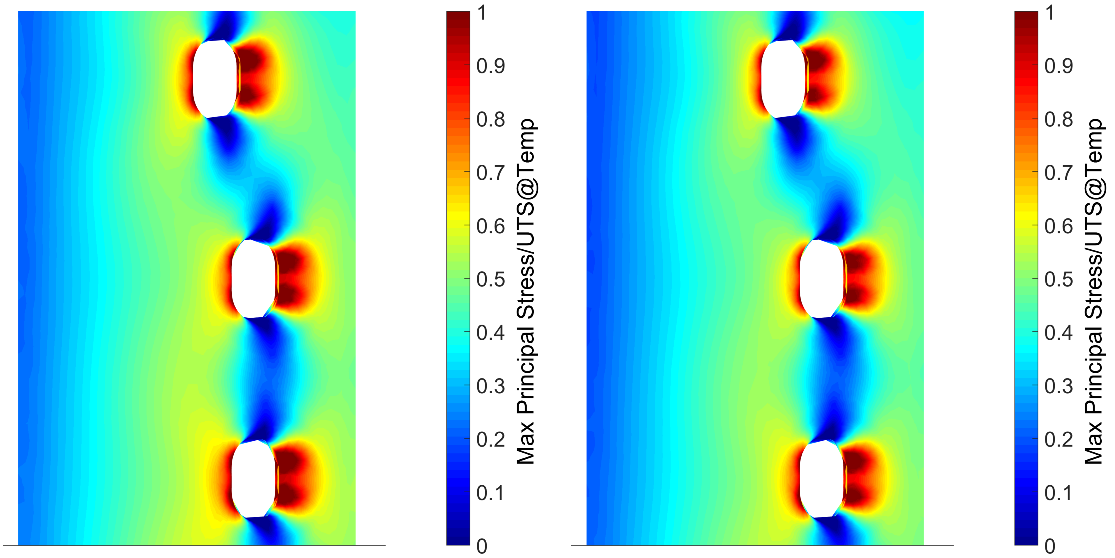

(a) Initial (b) Combined HTC Adjustments

Figure 8.13: Combined HTC adjustments comparison - stress distribution

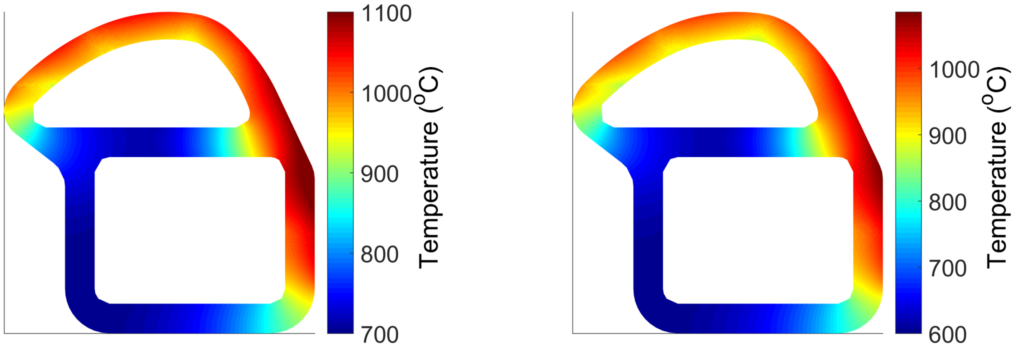

(a) Initial (b) Cold Coolant

Figure 8.14: Cold coolant comparison - metal temperature

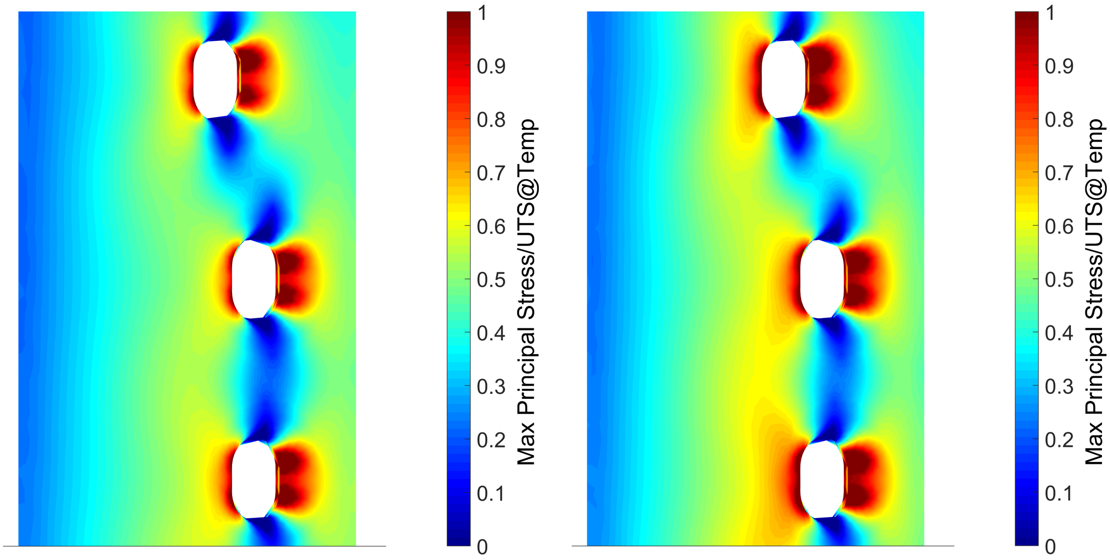

(a) Initial

(b) Cold Coolant

Figure 8.15: Cold coolant comparison - stress distribution

8.6.2 Stress Distribution

The stress distribution comparison for the cold coolant simulation is given in figure 8.15

With the reduced metal temperatures the stress levels have significantly increased. Both the stress concentrations around the impingement holes and the web stresses are higher. This is found as a larger temperature difference between the shell and web is created, combined with a colder web that reduces the UTS value for this region slightly, resulting in higher levels of the stress metric used.

8.7 Average Stress

Stress contours present the full distribution over the surface of a component, however in cases with only small changes in distribution these are often not clearly visualised. Therefore quasi-volume-averaged stress levels for each case, in the web region around the central impingement hole, are shown in figure 8.16.

The figure shows an intial average value for the Max Principal Stress/UTS@Temperature to be approximately 0.344. The trends observed in the stress contours are found in the averaged data with the LE having the most impact on the stress levels, followed by the web HTC with the

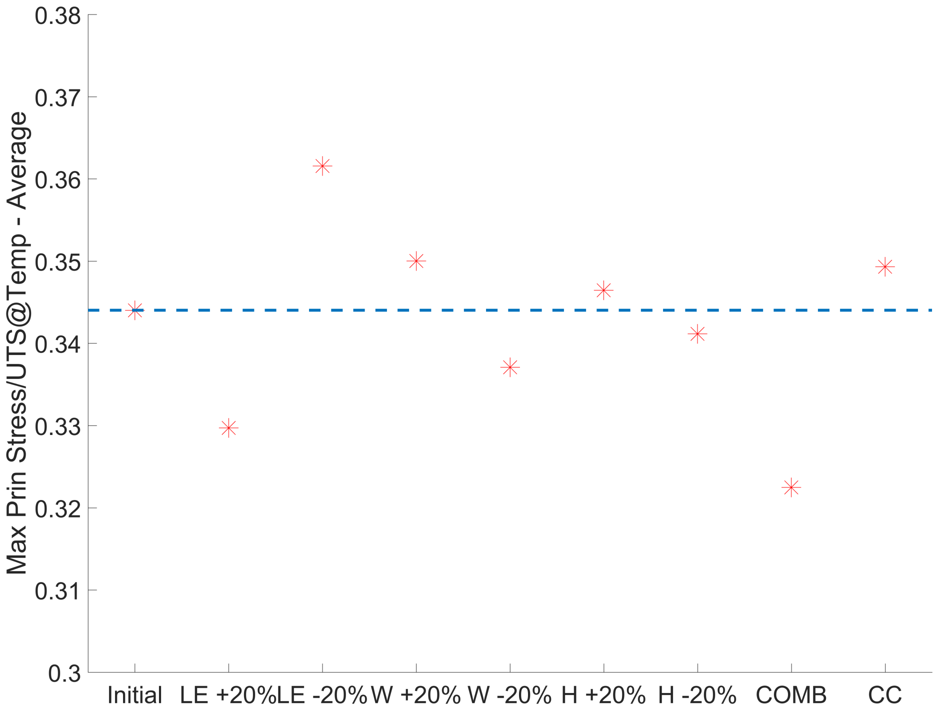

Figure 8.16: 3d average of max principal stress/UTS@temp

in-hole levels having a minimal effect. It is also confirmed that the combination of increased LE and reduced web HTC adjustments produces the lowest stress levels, a 6% improvement over the initial simulation. The cold coolant simulation shows a modest rise in stress levels.

8.8 Summary and Conclusions

Thermal FEA simulations have been run in order to determine the effect of the HTC levels within different regions of a leading edge impingement system on the metal temperature and stress distribution. HTC levels were adjusted on the web, leading edge and inside the impingement holes, and the following conclusions were drawn.

1. The internal leading edge HTC was found to have the largest effect with the web HTC also having a significant effect, while the in-hole HTC was far less important due to the small area over which it acts.

2. The stress levels found in the web and around the impingement holes were found to decrease with an increase in the internal LE HTC, and a reduction in the web HTC.

3. Simulations run with a cold coolant feed showed that, despite the significantly reduced metal temperature, the stress levels increased a little with the other parameters unchanged.
4. A significant reduction in average stress levels of 6% could be achieved in this case with a combined 20% increase in LE HTC and reduction in web HTC.

This work has therefore been successful in showing the relative importance of different HTC levels in terms of stress reduction in a leading edge impingement system, and how significant stress reductions can be obtained with achievable adjustments in HTC levels in different regions of the geometry.

Chapter 9

Thermal Matching - Methodology and Results

Thermal matching is a key stage of the gas turbine engine development process, particularly for the high pressure turbine blade [118]. Following the design process, a set of development engines are constructed and put through a series of evaluation tests, one of which is the thermal paint test. This test involves coating the turbine components with temperature sensitive paints, which give surface temperature contours for the test piece under the specified running conditions. This distribution is then compared to that which has been predicted by the thermal model for the given test condition to assess the accuracy of the thermal model.

In the ideal case, these distributions would match and no further action would be required. However, invariably the distributions contain significant differences due to the inevitable uncertainties in model parameters and boundary conditions encountered when modelling a complex turbine cooling system. Therefore the thermal model of the blade must be altered in order to match the ‘correct’ distribution measured at the blade surface by the thermal paint test, in order to give accurate blade life predictions obtained from an analysis that uses the full distribution of temperatures through the blade.

The current methodology involves an experienced cooling engineer manually adjusting different parameters within the cooling model in order to obtain a satisfactory match. These parameters are usually either the HTC levels in the internal cooling passages, film effectiveness levels or the upstream temperature distribution known as the traverse. The existing approach has a number of drawbacks. These include:

- It is very time consuming to manually make adjustments, and a thermal match can take 4-6 months to complete
- There is no evidence that the optimum parameters have been selected
- The use of individual judgements instead of a standardised procedure is likely to give a different solution dependent on the process variables as decided by the individual engineer
- A very experienced cooling engineer is required to undertake the task

This illustrates that there is significant scope for the improvement of the thermal paint matching in terms of ease of use, time and repeatability. The research hypothesis for the present work was that improvements could be obtained by applying machine learning techniques, as detailed in section 2.6.

Two improved methods will be demonstrated in this chapter, a theoretically simple process and one using Gaussian process regression. These are validated in a number of test cases before being applied to a leading edge impingement system to demonstrate their capability for full blade thermal matching.

9.1 Methodology

The new process by which the thermal matching is undertaken is illustrated in figure 9.1. Each step is explained in greater detail below for the initial test cases, those of most importance being steps 2, 4 and 6.

1. The required geometry is imported into an FEA thermal model, in this case an Ansys Workbench Steady-State Thermal model. Here it is meshed to a resolution fine enough for reasonable detail within the metal, similar to that used in chapter 7. The initial thermal boundary conditions are also defined at this stage.
2. Simulations are then run at multiple parameter points in order to obtain the training data for the model. The parameters used for the thermal matching will usually be factors by which the HTCs on various surfaces are multiplied. The training simulations run depend on the method of fitting to be used and must be carefully chosen in order to provide data of sufficient quality to the model.

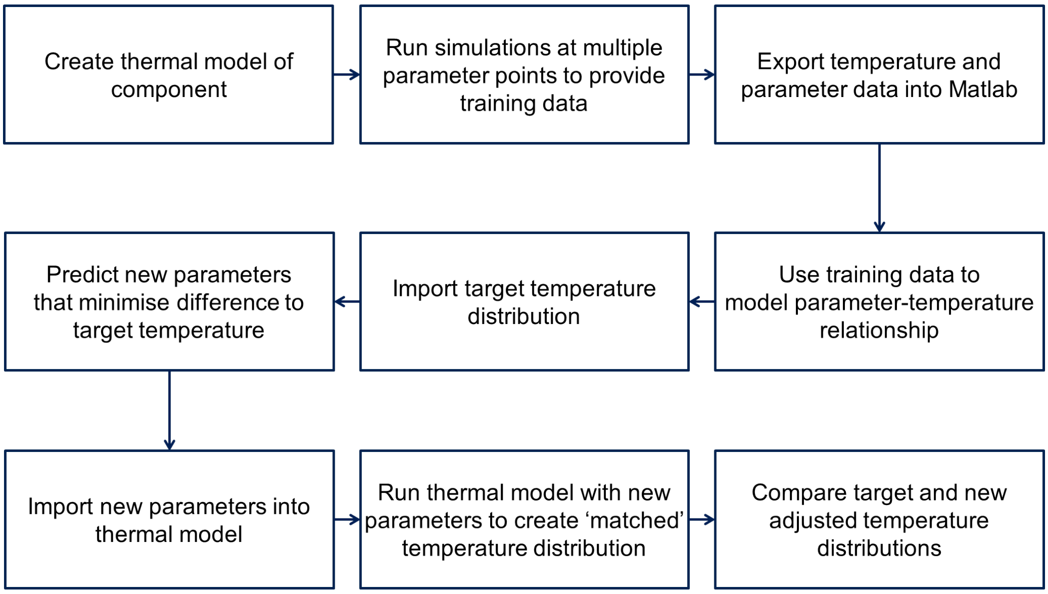

Figure 9.1: Flow diagram of new thermal matching procedure

3. The training data, consisting of the full metal temperature distribution and the HTC multipliers, is then exported into Matlab for the model fitting.

4. A model is then created to represent the temperature-HTC relationship using the training data. Multiple methods can be used for this step, with those selected in this case described in further detail below.

5. A target temperature distribution, which usually corresponds to the thermal paint data, is then imported into Matlab in order for the initial model to be fitted.

6. New multipliers are then predicted from the model to hit the target distribution. The process by which this is done varies for each model, and will be detailed below.

7. New HTC distributions are then calculated from the predicted HTC factors and imported into the FEA solver.

8. The thermal model is then run with the new HTC levels in order to obtain the adjusted temperature distribution.

9. Finally the temperature distribution calculated from the adjusted HTC levels is compared to the target distribution in order to check that a satisfactory match has been obtained.

Two different modelling and prediction methods have been applied to the thermal matching problem. The first involves a simplified Taylor series method, while the second employs

Gaussian process regression.

9.1.1 Linear Method

This first method assumes a linear relationship between the difference in temperature between a simulation and a baseline condition, and the change in HTC at this point.

Firstly, a baseline simulation is run (subscript 0 in equation 9.1) with the initial HTC values. The Δh values referred to in this section are normalised multipliers of the initial values. The form of the relationship between the temperature at each node and the HTC factor is represented by that given in equation 9.1.

$$T = T_0 + \frac{\partial T_1}{\partial h_1}\Delta h_1 + \frac{\partial T_2}{\partial h_2}\Delta h_2 + \frac{\partial T_3}{\partial h_3}\Delta h_3 + ... + \frac{\partial T_m}{\partial h_m}\Delta h_m \tag{9.1}$$

The gradient terms can then be estimated through the careful choice of further simulations. To obtain each term the HTC parameters are varied separately and in turn, and the gradient terms calculated as shown in equation 9.2

$$\frac{\partial T_1}{\partial h_1} = \frac{T - T_0}{\Delta h_1} \tag{9.2}$$

In practice two simulations are run for each parameter, one with increased HTC and one with a decreased value, to implement a central difference approximation to the first order partial derivative. This is to improve the accuracy of the discretisation and leads to equation 9.3 which is used to obtain each gradient term.

$$\frac{\partial T}{\partial h} = \frac{1}{2}\left(\frac{T_h - T_0}{\Delta h_h} + \frac{T_l - T_0}{\Delta h_l}\right) \tag{9.3}$$

Having obtained the gradient terms these can then be used to get a prediction of the required HTC adjustment to reach a given target temperature. This involves solving the matrix equation given in 9.4, where n is the number of nodes and m the number of HTC parameters.

$$\begin{bmatrix} T_{t,1} - T_0 \\ \vdots \\ T_{t,n} - T_0 \end{bmatrix} = \begin{bmatrix} \frac{\partial T_1}{\partial h_1} & \cdots & \frac{\partial T_1}{\partial h_m} \\ \vdots & \ddots & \vdots \\ \frac{\partial T_n}{\partial h_1} & \cdots & \frac{\partial T_n}{\partial h_m} \end{bmatrix} \times \begin{bmatrix} \Delta h_{t,1} \\ \vdots \\ \Delta h_{t,m} \end{bmatrix} \tag{9.4}$$

If a subset of nodes is selected such that $m = n$, the number of nodes is equal to the number of parameters, the matrix of gradients becomes square, and therefore invertible, leading to equation 9.5.

$$\begin{bmatrix} \Delta h_{t,1} \\ \vdots \\ \Delta h_{t,n} \end{bmatrix} = \begin{bmatrix} T_{t,1} - T_0 \\ \vdots \\ T_{t,n} - T_0 \end{bmatrix} \times \begin{bmatrix} \frac{\partial T_1}{\partial h_1} & \cdots & \frac{\partial T_1}{\partial h_n} \\ \vdots & \ddots & \vdots \\ \frac{\partial T_n}{\partial h_1} & \cdots & \frac{\partial T_n}{\partial h_n} \end{bmatrix}^{-1} \tag{9.5}$$

Therefore a prediction of each HTC adjustment is obtained from a small number of nodes. This is problematic as an individual subset of few nodes is unlikely to give a representative value for the overall metal temperature.

In order to overcome this problem, multiple subsets of different nodes can be run and then the predicted HTC adjustments averaged to give values to be used in the final temperature matching procedure. There is, however, still difficulty in selecting a subset of relevant nodes for each calculation and in the determination of how many different node subsets should be run in order to provide reproducible, representable adjustments. This will be further investigated within the validation process.

9.1.2 Gaussian Process Regression

Theory

Gaussian process regression (GPR) models are probabilistic models that use training data in order to give predictions for a new input. This process involves modelling the outputs, y, as a function of the input parameters, x, in the form given by equation 9.6, where $h(x)$ and β comprise a set of basis functions, and $f(x)$ is a Gaussian process with zero mean and covariance function $k(x,x')$.

$$y = h(x)^T \beta + f(x) \qquad\qquad f(x) \sim GP(0, k(x,x')) \tag{9.6}$$

The basis function is an explicit function of the parameters at a given point, and is usually a simple polynomial, while the covariance function gives the relationship between the required parameter point and the training data points away from the basis function. The covariance

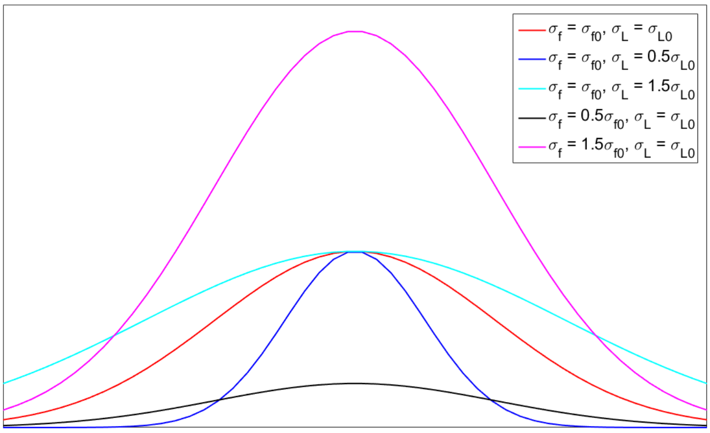

Figure 9.2: Squared exponential covariance function - for different values of σ_f and σ_l

function has zero mean and varies around the basis function value obtained from the parameters. The model must be fitted to the data in order to determine the model parameters. These are the basis function coefficients, covariance function coefficients and the noise level in the data.

The covariance function can be of many forms, such as the squared exponential form given in equation 9.7. It must be smooth, where a similar response is predicted given two close input and training parameter points. The length scale parameter within the covariance function may be the same for all predictors, or different, with values predicted from the training data.

$$k(x_i, x_j|\theta) = \sigma_f^2 exp\left[-\frac{1}{2}\frac{(x_i - x_j)^T(x_i - x_j)}{\sigma_l^2}\right] \tag{9.7}$$

The shape of the squared exponential covariance function and how it varies with the alteration of the σ_f and σ_l parameters is illustrated for representative values in figure 9.2. σ_f defines the peak value, while σ_l determines the rate of decay away from the peak.

Prediction from Model

After the model parameters have been fitted the model can be used to predict a response given a new parameter point using equation 9.8.

$$P(y|f, X) \sim N(y|H\beta + f, \sigma^2 I) \tag{9.8}$$

The prediction at any given point is represented by a normal distribution with variance estimated from the noise of the training data, σ^2. The mean, or exact predicted value with

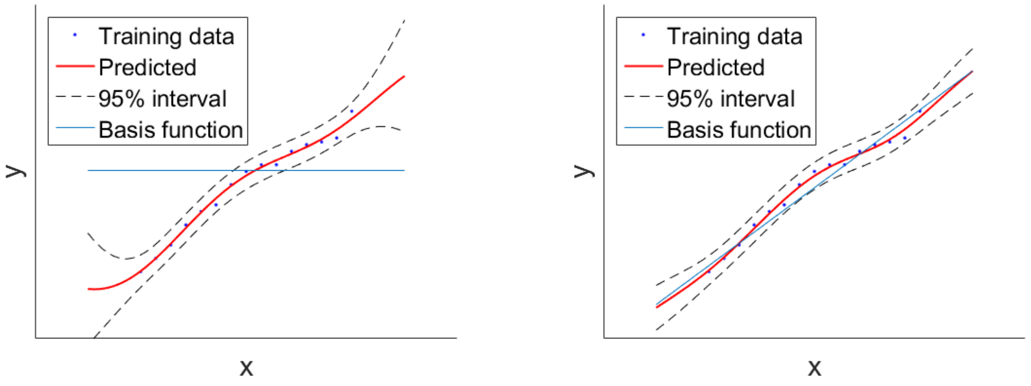

(a) Constant basis function (b) Linear basis function

Figure 9.3: One-dimensional GPR model example

no noise, is given by the sum of the basis function and all covariance functions evaluated at a specific parameter point.

One Dimensional Illustration

This section briefly illustrates the Gaussian process regression process for a one-dimensional example with manually created data. Figure 9.3 shows the training data, basis functions, predicted model and 99% confidence intervals for constant and linear basis function based models.

It is seen that the models with both basis functions fit the data well. The basis function effectively shifts the model to a first approximation, with the covariance functions modelling the variation away from this basis function.

Figure 9.4 illustrates the process by which the covariance functions are used to model the data. Initially a covariance function is evaluated for each data point (a). These are then individually weighted in order to fit the training data, as shown in (b). In order to create the model these covariance functions are then summed at each data point in order to give the difference between the basis function and required value (c).

Training Data

In order to create the model training data must be obtained. This is done by running multiple simulations using different values of the input parameters and storing the output. In this case the training data are the values of temperature evaluated for the thermal model with specific values of the HTC multiplication factors. In the equivalent of a one dimensional model this would

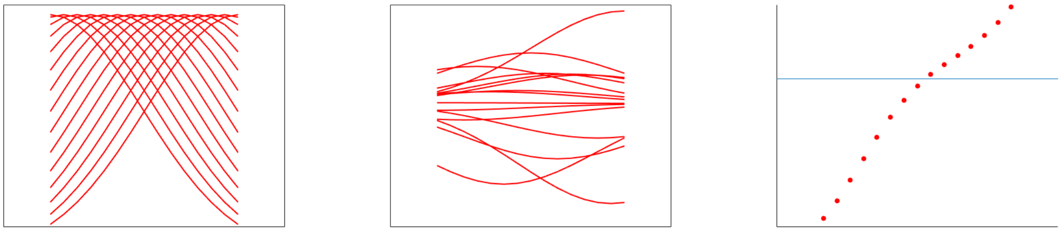

(a) Covariance functions (b) Weighted (c) Summed

Figure 9.4: One-dimensional GPR model example - covariance function fitting (constant basis function)

correspond to the temperature at one location. More generally the temperature is evaluated at multiple points.

The training data points are obtained using a central composite design, which is illustrated in figure 9.5 for a three parameter characterisation. The initial data point is given by the red point, with the 14 blue dots giving the adjusted training data points.

Implementation

The GPR methodology is implemented in Matlab using new functions that are contained in the statistics and machine learning toolbox [110].

Initially a model is created using the training data. The ***fitrgp*** function from the toolbox uses the input parameter and response training data, and returns a *RegressionGP* model. This model contains the estimated basis function coefficients, noise variance and kernel parameters which have been fitted using a maximum marginal log likelihood method [96, 110]. Within ***fitgrp*** the basis function and kernel, or covariance, functions can also be specified along with initial fitting parameters.

The *RegressionGP* model can then be used to predict a response given new inputs (values of x) using the ***predict*** function. This function simply returns the predicted response, in this case temperature from the new HTC multipliers, and can also report estimates of the confidence intervals for the response.

The ***fmincon*** function finds the minimum value of a constrained, multi-variable non-linear function and is used to find the optimum HTC multipliers in order to fit the target data.

In the case of thermal matching, the above functions are applied on a node-by-node basis. The temperature data and HTC multipliers are used to create a model for each node individu-

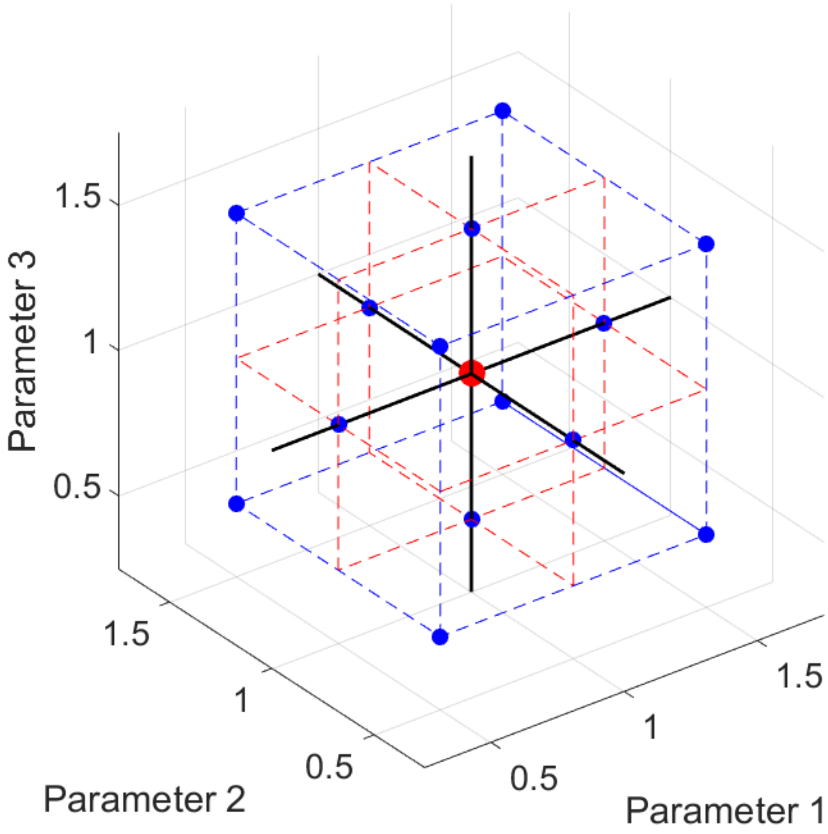

Figure 9.5: Training data points for 3 HTC parameters

ally. The ***fmincon*** function is then used to find the HTCs which minimize the mean-squared-difference between the target and predicted temperature, obtained using the ***predict*** function. Minimum and maximum individual and combined constraints are used within the fitting process in order to guarantee a predicted adjustment that is reasonably close to the original model and physically realistic. This also ensures the prediction remains within, or close to, the training data range which reduces modelling errors.

For a large finite element model mesh size the minimisation can be applied on a subset of nodes in order to improve solution time. These nodes can be selected randomly, but ideally should have reasonably even spacing to most accurately represent the overall model.

9.2 Validation

The methods were then validated using two separate cases, a simple test block and a leading edge impingement model. The validation was performed with the HTC multipliers being the unknowns required to achieve a match, x in equation 9.6, and the obtained temperature distribution, corresponding to y in equation 9.6.

9.2.1 Cuboidal Block Test Case

The first validation was undertaken using a very simple geometry and thermal boundary conditions, illustrated in figure 9.6. The setup consists of a cuboidal block with different thermal boundary conditions applied to its six surfaces. The ends of the block are adiabatic with a constant heat flux of $250kW/m^2$ set to the upper surface of the block. The other three surfaces, the base and sides, are set to an initial HTC value of $500W/m^2K$. These are the surfaces where the HTC will be varied to create the training and target data.

The validation was conducted using the two methods, linear and GPR, as detailed previously. The models were created entirely independently of the target data, with only the temperature outputs at a subset of 1000 nodes used to predict the adjusted HTC levels after the models had been created.

Table 9.1 gives the HTC levels applied to the block in order to obtain the target temperature distributions. Five validation runs were conducted with each HTC enhanced in turn, a common

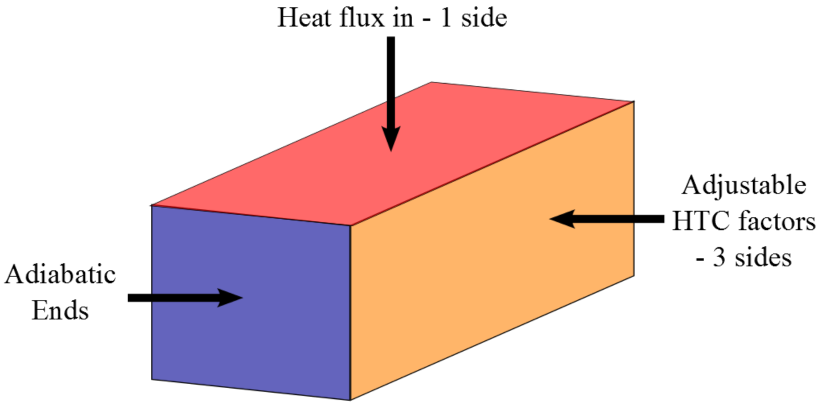

Figure 9.6: Test block validation simulation setup

Table 9.1: HTC factor details - test block

Target Sim. No.	HTC Factor 1	HTC Factor 2	HTC Factor 3
1	1.25	1	1
2	1	1.25	1
3	1	1	1.25
4	0.75	0.75	0.75
5	1.25	1.25	1.25

mode decrease and a common mode increase in HTC. The HTC adjustments predicted for each case compared to those applied to create the target distribution are shown in figure 9.7.

The first three simulations, where a single HTC adjustment is made, are very well matched by both methods. These are the simplest cases and therefore a good method would be expected to be well matched under these conditions. Where multiple HTC adjustments are made in simulations 4 and 5 some significant differences are observed.

Where there is a common mode reduction, simulation 4, the GPR method shows very close matching to the target HTC adjustment (within 8%) with the simple method being reasonably close to the predicted values (within 16%). However where there is a common mode increase in HTC in simulation 5 some very large differences are observed. The simple method is reasonably well matched however the GPR method gives very different HTC adjustments with much higher values for all surfaces. This appears initially to be a large error however due to the highly coupled relationship between the surfaces in this configuration it is possible that an *'alternative minimum'* was found in the optimisation process, and that the temperature distribution found by applying these HTC adjustments will give a good match. This is investigated in the following

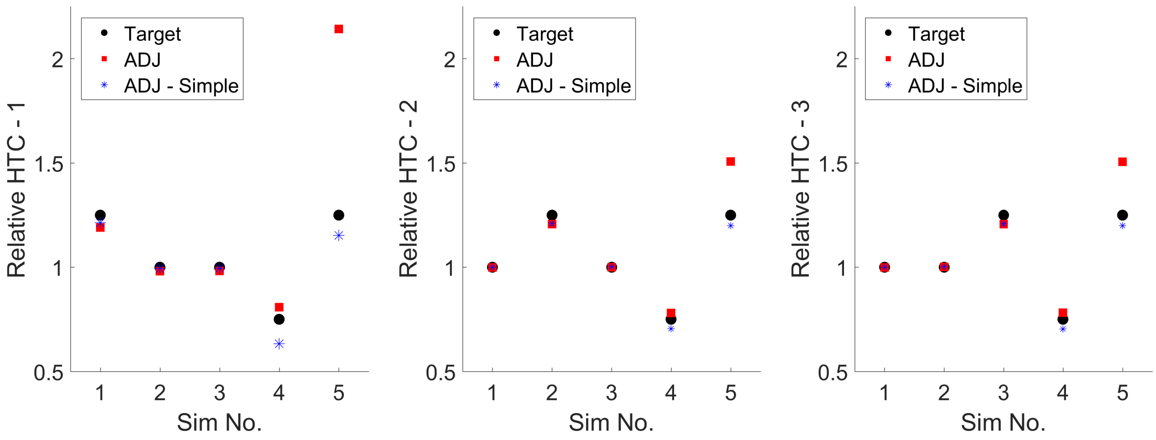

Figure 9.7: Test block validation - HTC results

section.

Figure 9.8 shows the mean temperature differences between the initial (unadjusted), linear and GPR methods and the target distribution.

As expected, given the very similar HTC adjustments, the temperature distributions for the first three simulations are very close to the target. For the common mode decrease in HTC, the GPR method performs significantly better than the simple method, however both are much improved over the initial distribution. The common mode increase results do show that an *'alternative minimum'* was found by the GPR method. Despite the very different HTC adjustments the temperature distribution shows a similar difference to the target as the method did for the fourth validation simulation. It also gives a similar level of matching to the simple method in this case.

This validation case indicates that both methods work reasonably well and consistently provide significant improvements over an unmatched distribution. However it does highlight the need for methods to be validated in order to ensure that the true, representative adjustments are found. This should be less of an issue in a real engine geometry, as is tested in chapter 10, due to the reduced coupling between the local temperature and the HTC multiplying factors in different regions.

The same validation process will now be applied to an engine representative leading edge impingement system to ensure the methods are robust for this more complex cooling configuration.

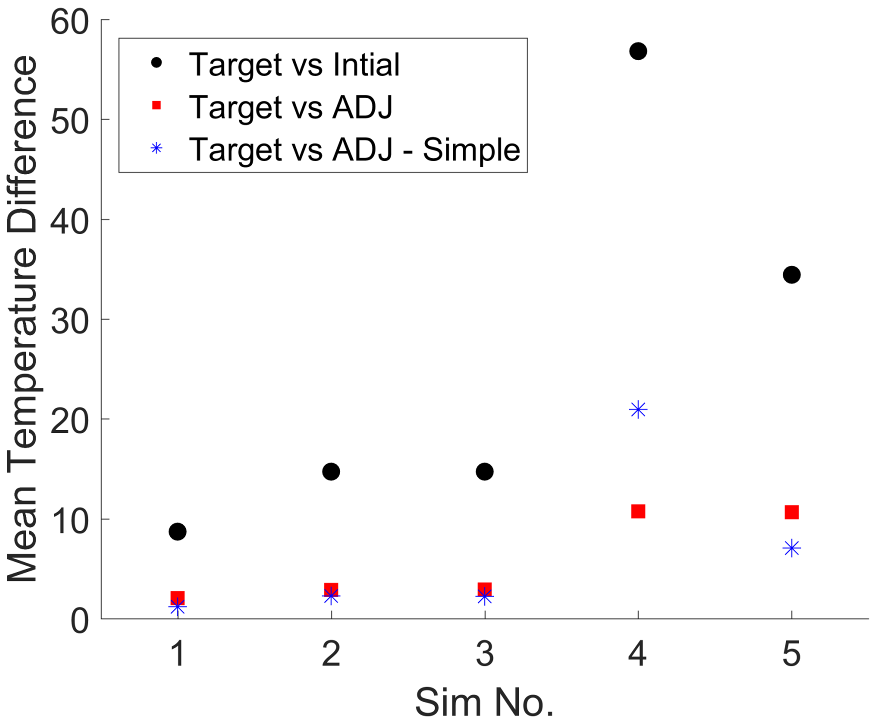

Figure 9.8: Test block validation - temperature results

Table 9.2: HTC factor details - leading edge impingement

Target Sim. No.	LE Factor	Web Factor	Feed Factor
1	1.25	1	1
2	1	1.25	1
3	1	1	1.25
4	0.75	0.75	0.75
5	1.25	1.25	1.25

9.2.2 Leading Edge Impingement Test Case

Figure 9.9 shows the different regions where HTC adjustments were made. These are classified as the leading edge, web and coolant feed regions. The initial leading edge HTCs were taken from a conjugate CFD solution, while those on other surfaces were calculated using the Dittus-Boelter correlation based on each individual passage Reynolds number. The upper and lower web surfaces therefore both have different initial HTC values, due to the different Reynolds number and passage dimensions, but in this case are subject to the same HTC adjustment factor.

As for the previous validation both methods will be applied using target temperature distributions generated with known HTC adjustments, which are given in table 9.2.

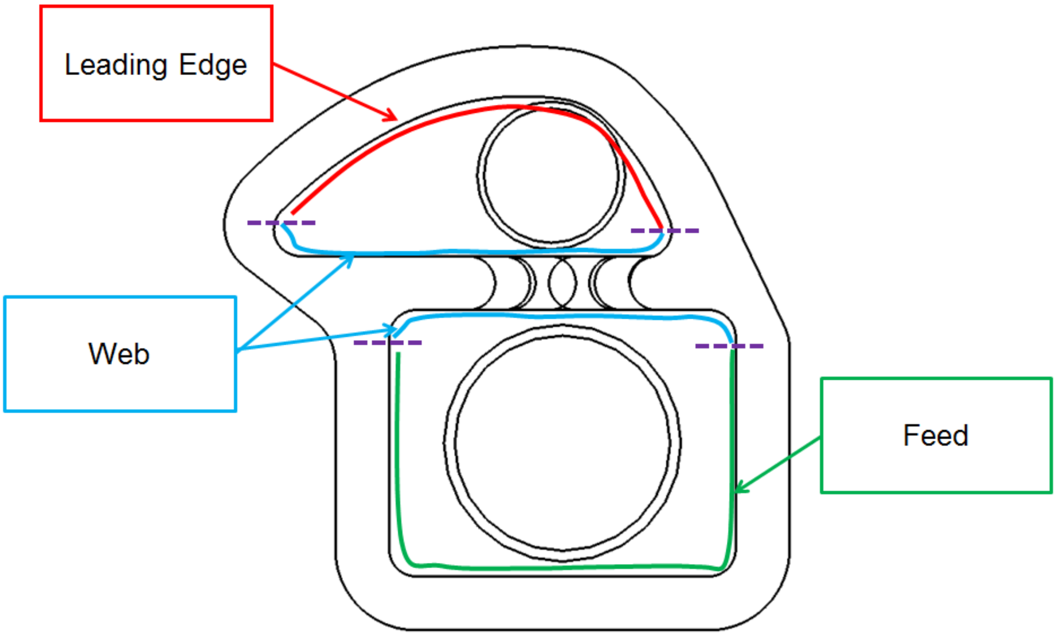

Figure 9.9: Leading edge impingement validation setup

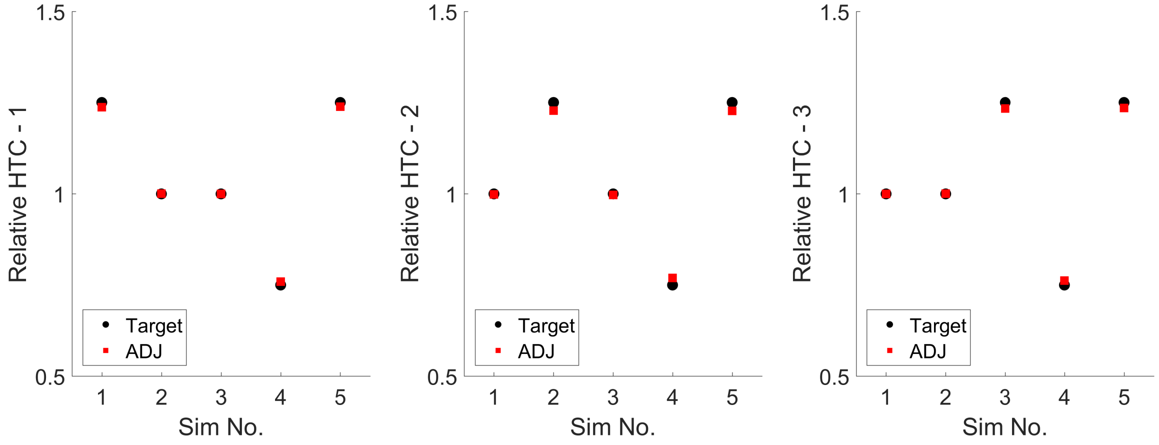

Figure 9.10: Leading edge validation - HTC results

Figure 9.10 gives the predicted HTC adjustments obtained using the GPR method compared with the target values. The predicted multipliers are very close (within 2%) to their targets with a consistent small underprediction in the change from the initial values. Unlike the previous validation, the method does not find any *'alternative minimums'* for the validation cases. This is due to the greater independence between the HTC adjustments, resulting from the nature of the geometry and regions chosen. Therefore in terms of HTC adjustments this validation is very successful, and likely will also be in terms of the temperature distribution.

The mean temperature differences between the initial and adjusted, and target distributions for the validation simulations are given in figure 9.11. It is clear that, as expected from the very good match of HTC factor levels, the adjusted temperature distribution is extremely close to the

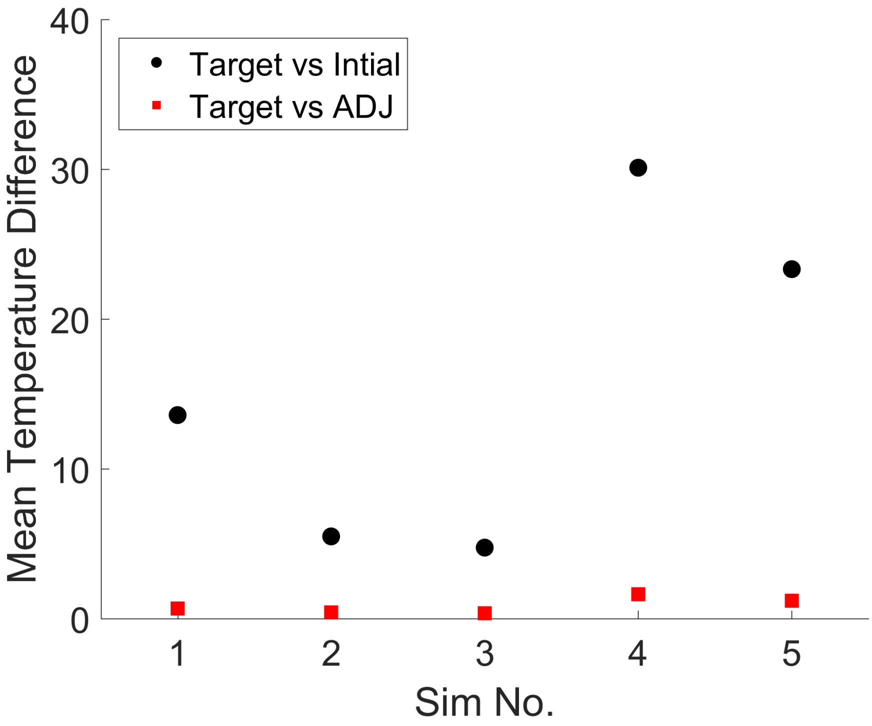

Figure 9.11: Leading edge validation - temperature results

target distribution for all cases, despite a significantly different starting temperature difference. This indicates that this method should provide good quality, reliable predictions for leading edge impingement, and similar cooling systems.

Following this validation the GPR method will now be applied to a thermal matching that is very close to the *'real'* situation to show its capability to undertake the temperature matching accurately, much faster and more reliably than the current manual methods.

Problems with Linear Method

When applied to the leading edge model, significant problems were encountered using the simple method for HTC adjustment prediction. The primary reason for this is that only a very small subset of nodes, equal to the number of parameters that are to be varied, must be used for each set of predictions. In this validation case with three adjustable HTC regions, three nodes are used. When the nodes have relatively similar temperature variations with HTC parameter changes, as in the test block case, this method can produce good results as each node will give similar HTC factor predictions. However for the leading edge impingement geometry different nodes have very different relationships, and therefore gradient terms, with the different input parameters. This leads to huge variations in some HTC predictions with very physically unrealistic values. Some of these problems could potentially be resolved by careful node selection, using node combinations which have similar temperature-HTC relationships. However, it is the aim for a thermal matching procedure to be used on any blade geometry, and therefore this means that this simple method is not satisfactory. It is clear from this that any method must globally optimise the HTC factor predictions, rather than use averaged or otherwise combined local optimums which may not be representative of the overall best solution.

9.3 Results

Following the above validation the Gaussian process regression method was used to perform a temperature matching for a situation very close to the thermal paint test, where it could ultimately be used most effectively.

The target distribution was set to be the full metal temperature distribution obtained from a conjugate CFD solution. The initial temperature distribution was obtained in a steady-state thermal FEA solution using HTC levels calculated from the passage Reynolds number and a leading edge internal HTC distribution from CFD, which are detailed in chapter 8. These are illustrated in figure 9.12 (a) and (b).

There are two different adjusted simulations shown in this figure. (c) is an initial attempt using three HTC factors on the leading edge, upper and lower web, while (d) uses new HTC adjustment regions of the leading edge, web and feed as shown in figure 9.9. Although the initial setup could match the leading edge region well, the web and feed regions could not be matched as there was no adjustable factor local to this region, therefore the regions were changed leading to (d) in order to address this.

The GPR method is able to chose the best factor to be applied to a datum solution, but the approach is dependent on the choice of sensible, physically reasonable, factors. This example has shown that the aerothermal engineer using the method must exercise judgement as to which zones should be assigned independent factors.

The adjusted simulations both show a significantly improved match over the initial distribution, which over estimate the temperature by a large amount in most regions. The adjusted simulations significantly increased the HTCs in all of the adjustable regions.

The leading edge region is well matched by the adjusted simulations both in terms of the

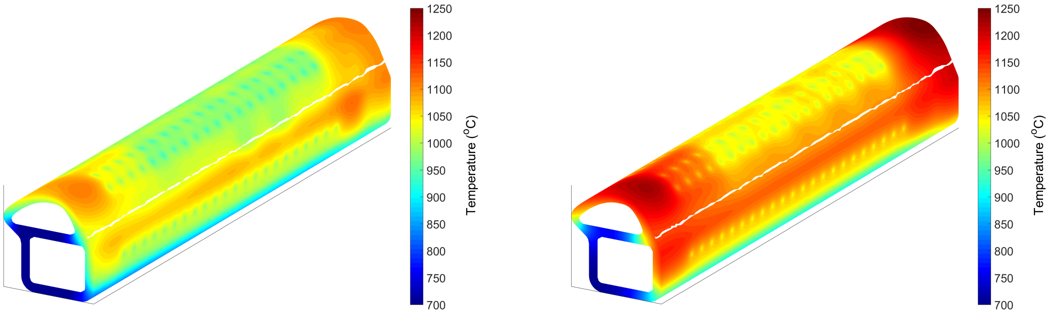

(a) Target (b) Initial

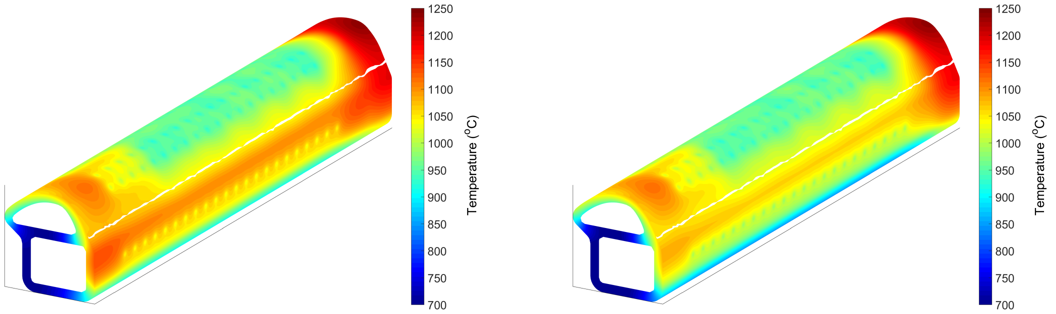

(c) Adjusted (d) Adjusted - new regions

Figure 9.12: Leading edge matching - temperature - full

temperature levels and distribution, showing clearly the cooler metal at the location of the impingement jets as well as significantly higher temperatures in the uncooled areas. In the web and feed area the first adjusted simulation (c) is slightly closer to the target distribution however still shows significant differences. The web is colder than the initial case, however still much above the target with the feed and outer surface away from the leading edge showing higher temperatures than the target. This is due to the lack of HTC adjustability in this lower section of the geometry, which is rectified with the new regions of HTC adjustment, figure 9.12 (d). This figure shows a similar good match in the leading edge region whilst it also obtains a closer distribution across the web, feed and other sections of the geometry, due to the increased HTCs in the feed region, enabling increased cooling of this section to more closely reflect the target distribution. This highlights the need to select the correct HTC regions to adjust in order for all features of the target distribution to be accurately represented in the matching process. This can be helped by using an increased number of adjustable parameters, however it must be balanced against the increased computational cost that is introduced. Of course, as the computational power available to the aerothermal engineer increases with time, it will inevitably be possible

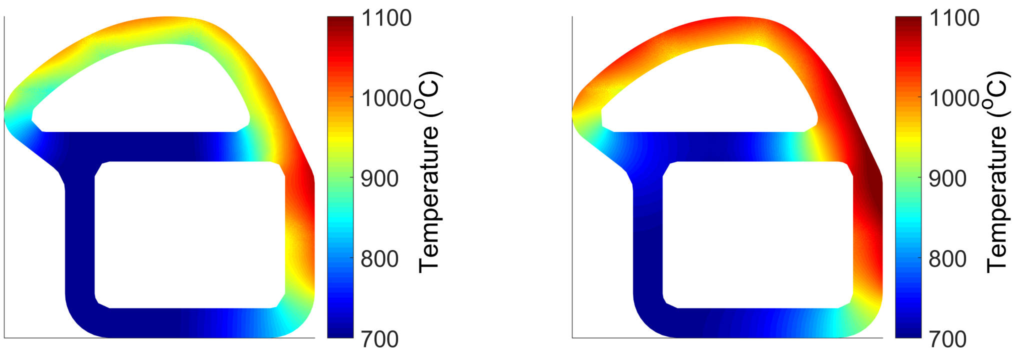

(a) Target (b) Initial

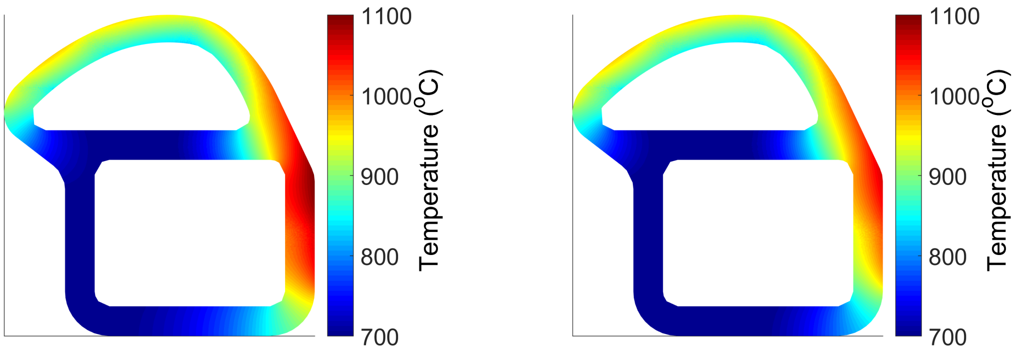

(c) Adjusted (d) Adjusted - new regions

Figure 9.13: Leading edge matching - temperature - mid height cross section

to increase the number of factors used and therefore reduce the judgement required.

A mid-section slice of the temperature distribution discussed above is given in figure 9.13, in order to compare the internal distribution in the most critical area of the matching process.

This comparison illustrates very clearly the improvements made through the use of the new regions for HTC adjustments. The initial distribution is very far from the target and therefore large HTC adjustments are required. For the first adjusted case (c) the leading edge is seen to be well matched in terms of temperature levels. The web and lower regions are far closer to target than the initial simulation however still show significant differences to the target due to the lack of adjustability in these regions. The second adjusted simulation with the new regions, figure 9.13 (d), is a very close match to the target temperature. All of the outer metal shell has a very similar temperature level and distribution with only a marginally lower peak value in the adjusted distribution on the outer edge near to the web. The web has a slightly different temperature distribution, however similar levels, due to a single HTC value being used across the web rather than a full distribution. A full distribution could be applied and then adjusted on these surfaces which would rectify this discrepancy.

In general, with the new regions used for HTC adjustment, the temperature matching using the GPR method is extremely successful, providing a very good temperature match in a standardised and much faster process.

9.4 Further Validation

Up to this point all thermal matches using the GPR method have been obtained using the default settings for the ***'fitgrp'*** and ***'fmincon'*** Matlab functions. However, there is significant scope for adjusting the modelling process in order to improve its accuracy for particular cases. The sensitivity of the procedure to the following parameters is tested in this section.

- Number of nodes used for the minimisation process
- Basis function of GPR model
- Kernel (covariance) function of GPR model

The effect of these parameters will initially be investigated using the same methodology as the previous validation for the LE impingement geometry, where the target temperature distribution is created using known HTC factors.

9.4.1 Number of nodes

The number of nodes which are used to predict the new HTC adjustments have a large influence on the quality of the prediction, with more nodes likely to give improved results. However an increased number of nodes comes at a very large computational cost, as more GPR models have to be created and then used within the target-prediction minimisation. Therefore a compromise must be reached between a number of nodes that is large enough for the models to give a good representation of the full metal whilst being small enough for a reasonable solution time. For this chapter the nodes selected are an evenly spaced, random subset of all imported training data mesh nodes, obtained using the Matlab ***'rand'*** function.

Figure 9.14 gives the HTC adjustments for the different LE validation cases using 10, 100, 1000 and 5000 nodes for the modelling and minimisation.

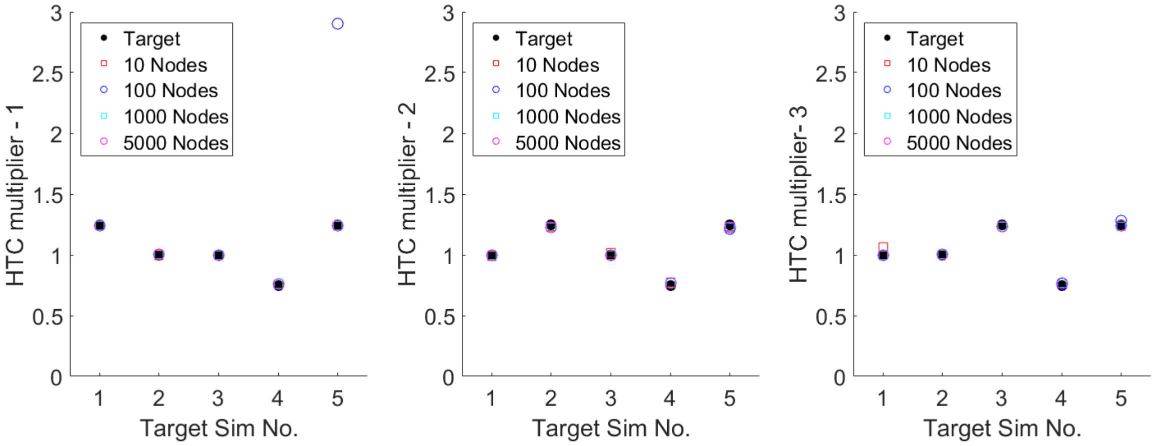

Figure 9.14: Leading edge validation - node number

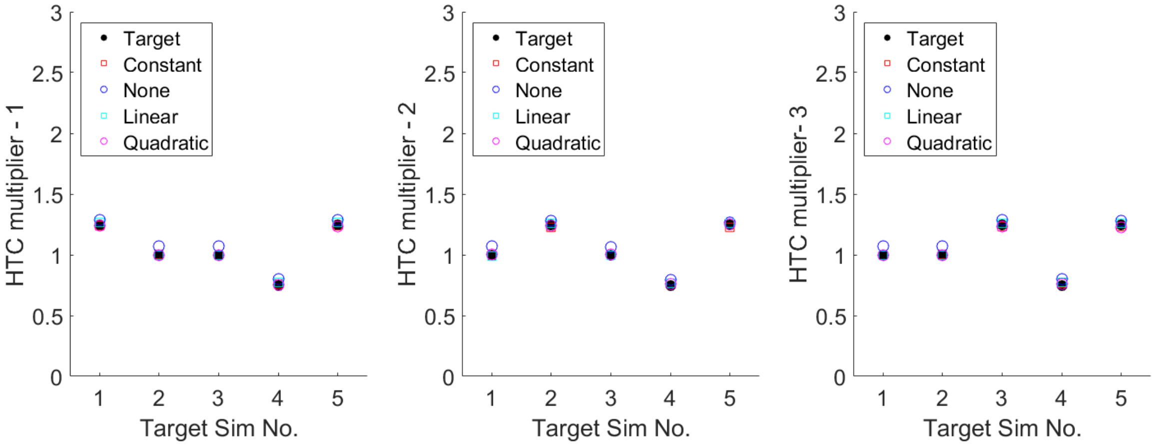

Figure 9.15: Leading edge validation - basis function

It is clear from this that the 10 node simulation gives significantly different HTC predictions to the other simulations. The 1000 and 5000 node simulations show no discernable difference from each other, with very small differences between these and the 100 node predictions. It therefore appears that 1000 randomly chosen nodes should provide enough data points for the modelling and minimisation processes to be accurate in this validation case.

9.4.2 Basis Function

Following the node number test, the form of the basis function used for the GPR modelling was investigated. All predictions are now undertaken with 1000 nodes for the model creation and minimisation. Four different basis functions were investigated - constant, zero, linear and quadratic. The results from the validation cases run with these different basis functions are shown in figure 9.15.

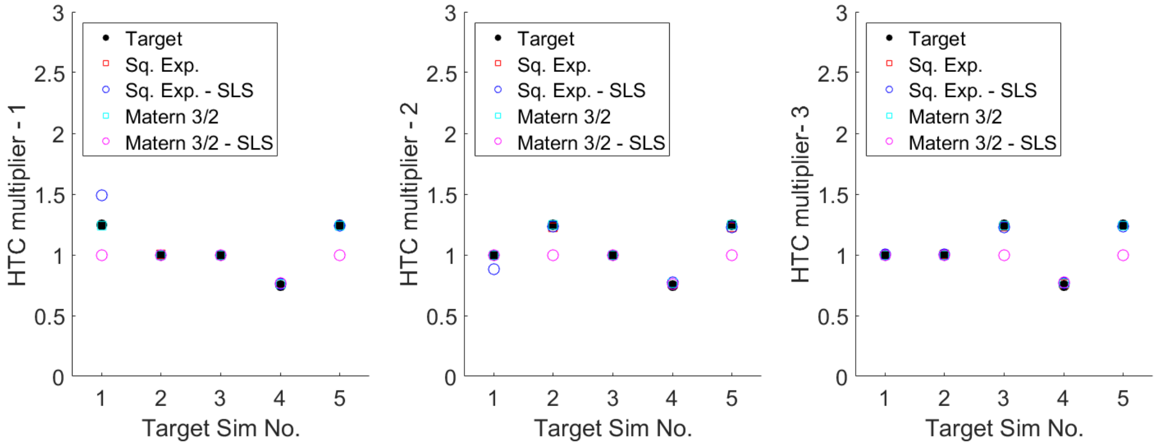

Figure 9.16: Leading edge validation - kernel function

There is far less variation from the target HTC values with different basis functions. All of the simulations with constant, linear and quadratic basis functions give very good predictions. However the predictions obtained using no basis function are consistently poor and therefore a non-zero basis function should be used in future. The model with zero basis function would not be expected to perform well, as the temperature data has not been normalised and therefore the GPR process is unable to model the large offset that is required.

9.4.3 Kernel (covariance) Function

Multiple different kernel, or covariance functions were then tested, all using a constant basis function for the GPR process.

Two different kernel functions were tested, the squared exponential and Matern 3/2 functions, equations 9.9 and 9.10 respectively. Two variations of the model were tested with each, one using a sinlge length scale for the predictors, and one using separate length scales for the predictors. An explanation of the use of these kernel functions can be found in [96].

$$k(x_i,x_j|\theta) = \sigma_f^2 exp\left[-\frac{1}{2}\frac{(x_i-x_j)^T(x_i-x_j)}{\sigma_l^2}\right] \tag{9.9}$$

$$k(x_i,x_j|\theta) = \sigma_f^2\left(1+\frac{\sqrt{3}r}{\sigma_l}\right)exp\left(-\frac{\sqrt{3}r}{\sigma_l}\right), \qquad r=\sqrt{(x_i-x_j)^T(x_i-x_j)} \tag{9.10}$$

Figure 9.16 gives the predictions when the kernel function is varied for the validation cases.

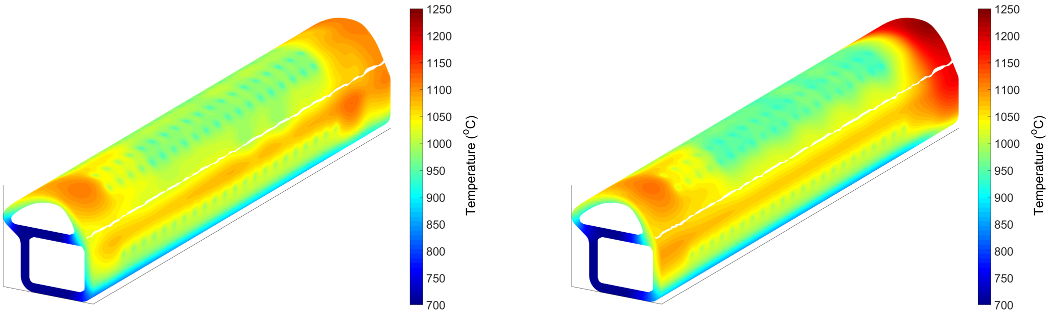

(a) Target (b) Adjusted

Figure 9.17: Leading edge matching - temperature - surface input - full

From this validation it appears that either of these two covariance functions can be used, however only in the form using a single length scale for all predictors. This is due to very large errors in the predicted HTC values when using a separate length scale for each of the predictors.

9.5 Further Results

In an real engine thermal paint test a full three-dimensional target distribution is not available, only an outer surface temperature distribution. Therefore the method must be validated with only surface target temperature used as an input.

9.5.1 Surface Target Distribution

The leading edge model and target distribution from the previous section will now be used to predict HTC adjustments where only the surface distribution is used for the target inputs.

Figures 9.17 and 9.18 give the outer and mid-section metal temperature comparison between the target and adjusted distributions.

The temperature distribution is very well matched, as it was with the the full three dimensional target input, in both the surface and mid-chord slice.

Both of these figures show clearly that the GPR based prediction method works well with just a hot surface temperature distribution.

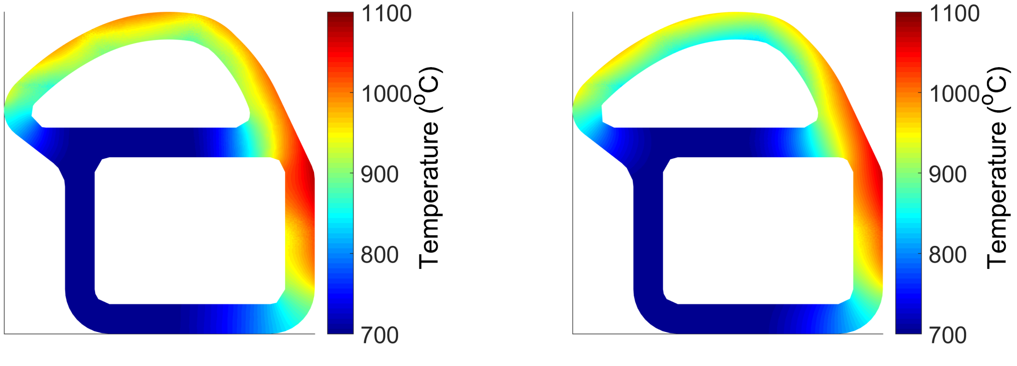

(a) Target (b) Adjusted

Figure 9.18: Leading edge matching - temperature - surface input - mid height cross section

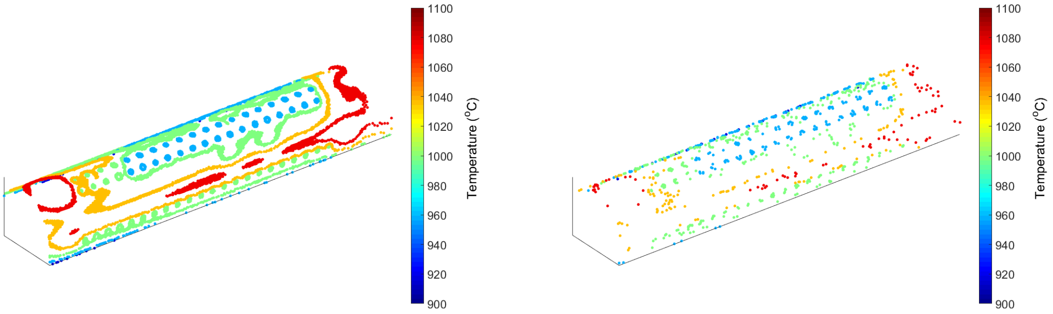

(a) All (b) Selected

Figure 9.19: Leading edge matching - contour band input points

9.5.2 Surface Contours Target Distribution

The real thermal paint test does not produce a fully resolved surface temperature distribution but a series of contour bands at approximately 40^0C intervals. In order to simulate this, a number of temperatures spaced by 40 K were chosen, and surface target points within 2 K of them were selected, and set to the central value of the contour band. All of the points selected are shown in figure 9.19 (a), with the nodes used for the HTC adjustment calculation given in (b), a subset of (a).

The resulting temperature distribution comparisons from using these contour band target inputs are given in figures 9.20 and 9.21.

The use of these contour band inputs is clearly not problematic for this method as again a very good temperature match is obtained throughout the geometry.

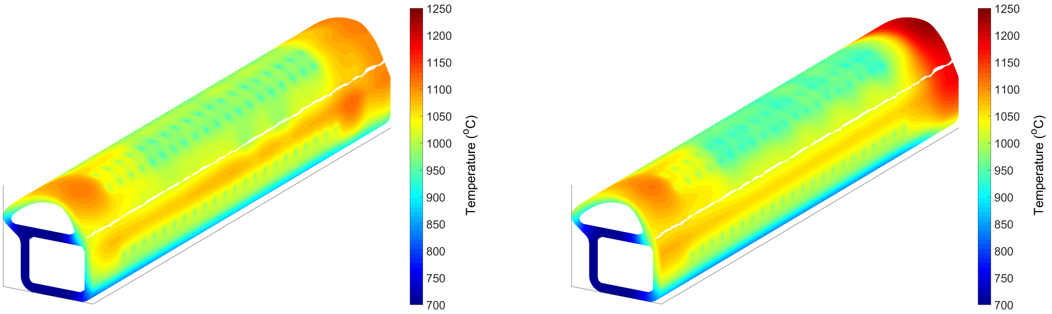

(a) Target (b) Adjusted

Figure 9.20: Leading edge matching - temperature - contour band input - full

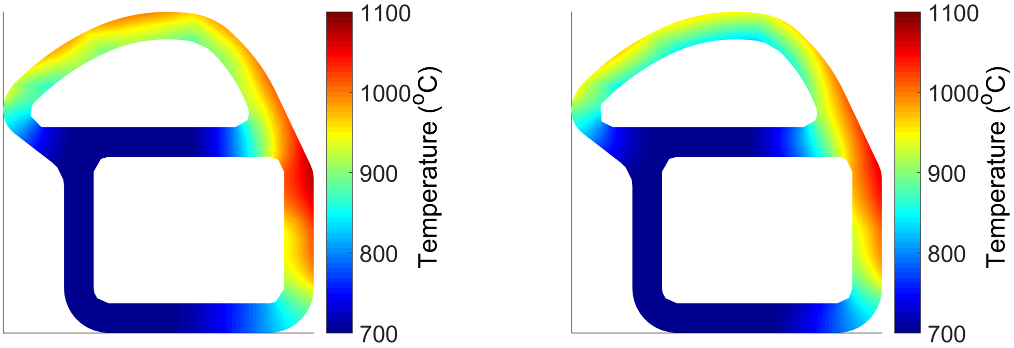

(a) Target (b) Adjusted

Figure 9.21: Leading edge matching - temperature - contour band input - mid height cross section

9.6 Summary and Conclusions

The thermal matching process is a key stage in the engine design process, however it is currently completed using a time-consuming, non-standardised procedure. Two new methods, a linear method and one using Gaussian process regression (GPR) models have been investigated. These have been validated for both a simple block and a representative LE geometry with a very close match obtained between the adjusted and target distributions. The GPR model was then applied to a full target distribution obtained from a conjugate CFD model. The following conclusions have been found.

1. The new methods detailed and implemented in the chapter have been demonstrated to offer reliable temperature matches using adjusted HTC values on selected internal surfaces.
2. The linear method was found to be adequate for a very simple configuration, but not for a more realistic geometry.
3. The GPR-based method provides consistently good predictions for both a block and leading edge geometry. It was then successfully applied to a realistic case similar to that required in a thermal paint match test.
4. The GPR method was proven to give very good thermal matches with full three-dimensional, surface and contour band inputs for this leading edge cooling configuration.

The new modelling and prediction method therefore offers a faster, more reliable alternative to the existing manual methods for thermal matching and therefore will be implemented and tested using thermal paint test data and a thermal model from a real engine blade in the following chapter.

Chapter 10

Thermal Matching - Real Blades

The new automated thermal matching method based on Gaussian process regression modelling was introduced and validated for a leading edge impingement geometry in Chapter 9. In order to make this approach applicable to the turbine component thermal matching process used in engine development the full blade temperature must be matched, rather than a small section of the blade. The model must also include effects of heat transfer changes on the coolant temperature in other sections of the blade through the use of a more complex thermal model. In this Chapter a thermal match is initially undertaken for an IP blade, with an increasing number of adjustable parameters, before a match on an HP blade is conducted.

10.1 IP Blade - Modelling Procedure

The modelling procedure differs slightly to that used on the leading edge impingement model, however the matching procedure is undertaken using identical methodology. Full details are given in the following section.

10.1.1 Blade Geometry and Cooling Configuration

The first blade for which the thermal matching methodology will be tested on is the IP blade from a Rolls-Royce engine. Both a non-matched and matched thermal model were made available, which allows for multiple stages of validation of the methodology.

The geometry is a shrouded IP blade with internal and film cooling systems fed from the blade root. The main cooling features of the blade are as follows:

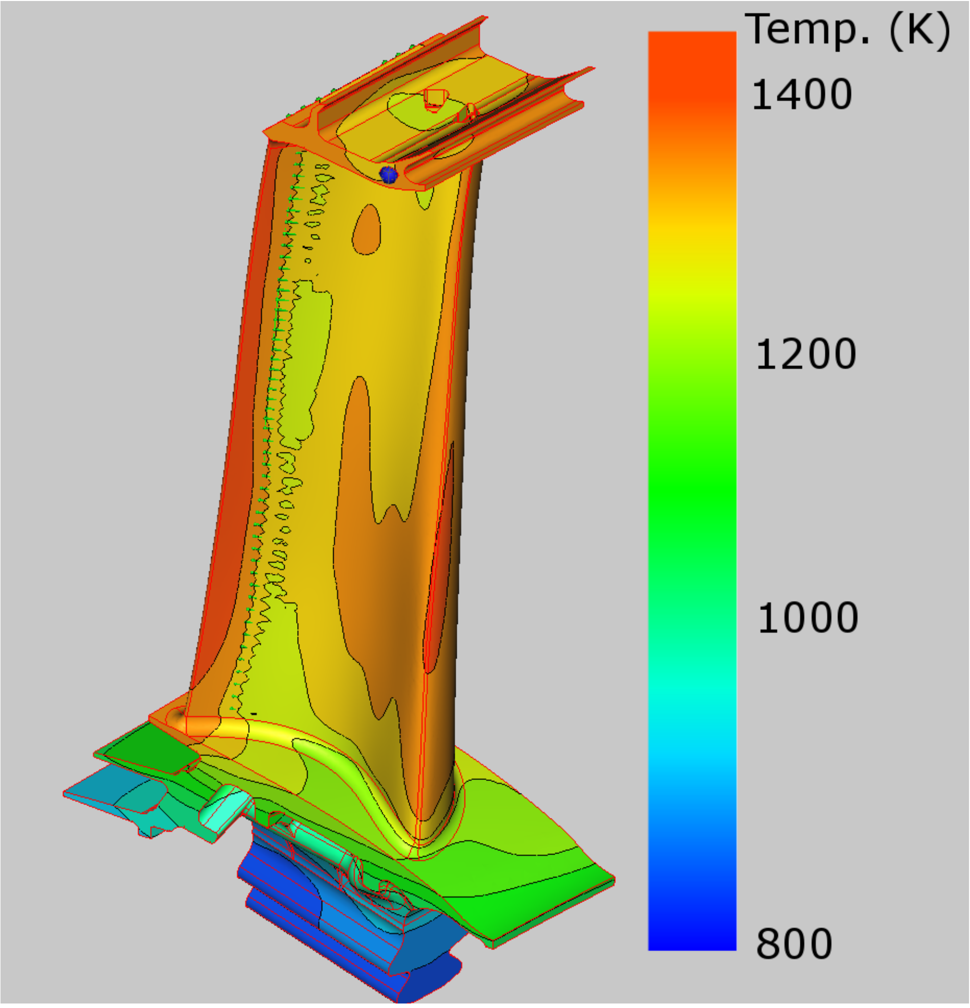

Figure 10.1: Blade geometry with surface temperature contours

- A triple pass ribbed cooling passage fed from the trailing edge pass.
- A single row of film holes on the pressure surface, near to the trailing edge, fed from the first pass of the serpentine passage.
- A large number of shroud cooling passages.

Figure 10.1 shows the geometry and figure 10.2 cooling configuration of the IP blade.

10.1.2 Modelling Setup

The cooling model that is to be matched is significantly more complex than that in Chapter 9 for which the method has been developed. In the previous case, HTCs were applied to a steady-state thermal FEA model, whereas in this case the in-house RR software, SC03, along with the JB56 plugin, is used.

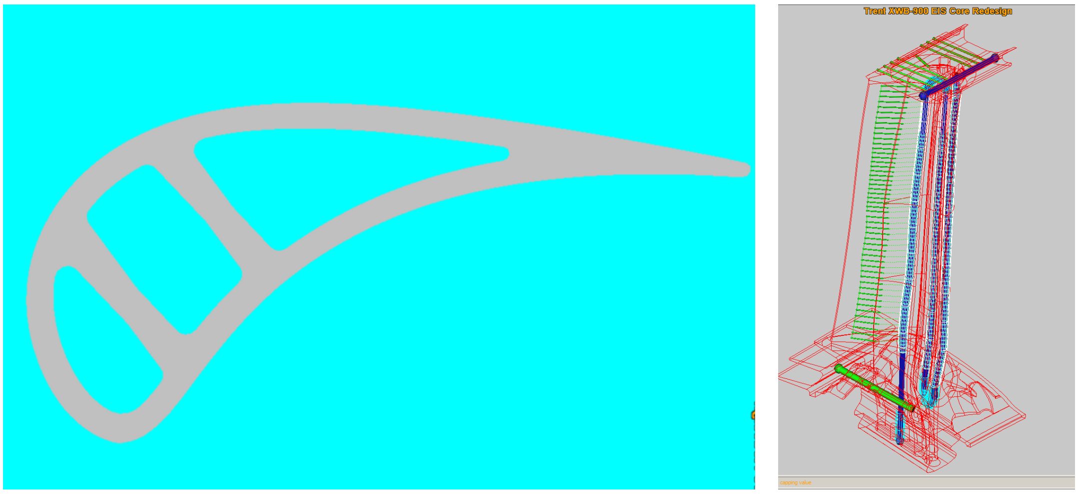

(a) Internal cooling passage cross section (b) JB56 cooling configuration diagram

Figure 10.2: Cooling configuration of the IP blade

The baseline model is that created of the blade and cooling configuration with no additional factors or data applied to it. This is matched to a target model which was manually matched to the thermal paint test for this blade.

Software

SC03 is an FEA solver with plugins incorporated into the model. For example, the JB56 module incorporates a flow net solver that was used in this research. JB56 is a low order fluid solver that reads in temperature and geometric data and then exports heat transfer coefficient distributions to the FEA solver.

The models can handle internal and external cooling of a variety of types, including radial passage, impingement and film classes of cooling. The HTC data that the code outputs is, by default, based on empirical correlations, however the latter can be altered to include additional factors or other imported data such as those from CFD solutions.

Unlike the modelling in Chapter 9, however, there is an iterative loop that adjusts the gas temperature based on the heat pickup through the metal. This therefore increases the complexity of the solution and it was not clear that the GPR based method would be successful. As the training data is be generated with this included, the metal temperatures passed to the model, and therefore the model itself, will be implicitly included within the model.

Factors that can be altered in order to match the thermal model include internal and external HTCs, film effectiveness levels and gas temperatures. In the following section internal HTCs

Table 10.1: Simulation no. for training data - CCD design

No. of Params.	3	4	5	6	7
Total Sim No.	15	25	43	77	143

will be used as they provide adjustable coverage over the entire blade, and internal cooling is also the main form of cooling for this blade, as only a single row of PS film holes are present. Gas temperature levels are not adjusted as they are strongly coupled with upstream and downstream blade rows, and this model was matched in isolation from these.

Generation of Training Data

The training data is generated using the CCD design, with a varying number of parameters. Initially three parameters were selected, as previously used in Chapter 9, however this number was increased in order to add greater fidelity to the matching procedure.

The software used in this chapter is fully scriptable, and therefore obtaining the training data with an increased number of parameters was feasible. The number of training data simulations required to occupy the CCD design with different parameter numbers are given in table 10.1.

For these simulations HTC factors were used as the adjustable parameters, and therefore multiplier levels of 0.5, 1 and 1.5 were used as in previous cases.

10.2 IP Blade - Results

Multiple matches have been undertaken in order to get improved knowledge of which adjustable parameters are capable of achieving the best thermal match the the target distribution. Initially three parameters were used, with an increased number for the later tests.

10.2.1 Match 1 - Three Parameters

The three parameters that were chosen for the initial match were as follows:

- Internal HTC factor
- External HTC factor
- Shroud HTC factor

Table 10.2: HTC factors - match 1

Internal HTC	External HTC	Shroud HTC
0.845	1.573	0.922

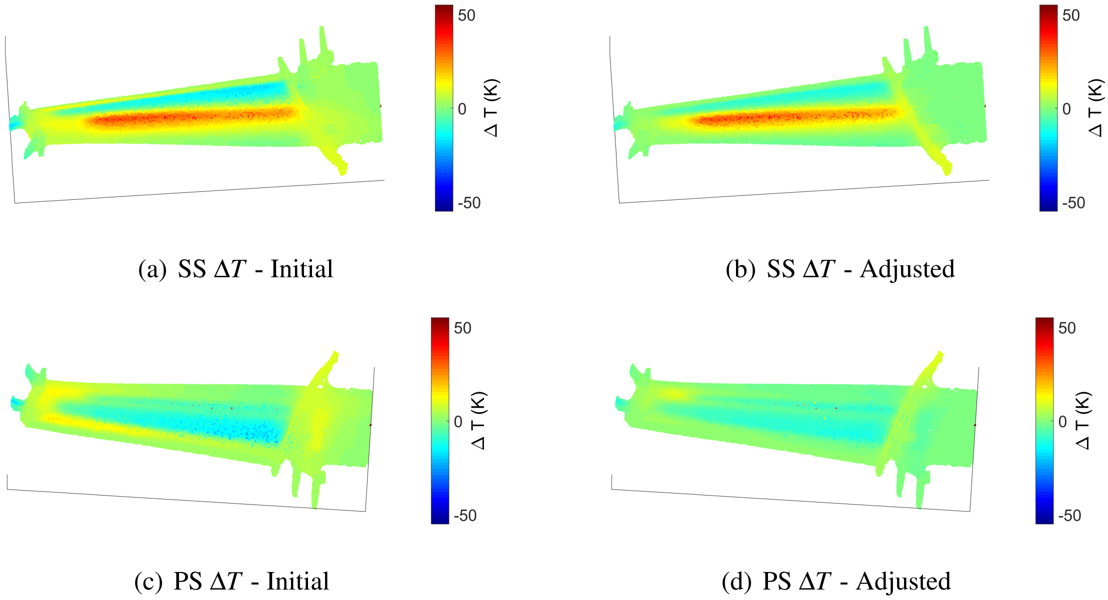

(a) SS ΔT - Initial

(b) SS ΔT - Adjusted

(c) PS ΔT - Initial

(d) PS ΔT - Adjusted

Figure 10.3: Initial and matched temperature differences for IP blade - three parameters

These were chosen following discussions with a cooling engineer in order to provide a full coverage of the blade area. The adjustments predicted by the GPR method in order to obtain a match with these parameters are given in table 10.2. These factors are within a reasonable range of the adjustments typically used to achieve a thermal match for a blade.

The difference between the initial and target, and adjusted and target temperatures are illustrated in figure 10.3. A positive value indicates the adjusted temperature is higher than the target temperature with a negative value indicating an underestimated temperature.

The initial difference in temperatures is seen to be very large in places, both above and below the target distribution, and it is evident that the model required significant matching in order to give an appropriate temperature distribution.

The first match shows an improved match, however there are still some significant differences between the adjusted and target distributions. The pressure surface levels are much closer to the target, as are the shroud temperatures, and the colder region on the suction surface. However the significantly hotter streak across the suction surface is still present. This is due to the use of uniform internal and external factors applied to the HTCs. The results show that where there are some areas either side of the target distribution, the current parameters are unable to

Table 10.3: HTC factors - match 2

Pass 1 (TE)	Pass 2 SS	Pass 2 PS	Pass 3 (LE)
0.838	1.630	0.797	1.024

reflect the requirement for different HTC factors, and therefore cannot provide a close match to the target in these regions. Therefore a matching strategy with a greater spatial resolution in the blade region is required. This approach was tested in the second matching process.

10.2.2 Match 2 - Four Parameters

Following the lack of spatial resolution using the three parameters in the previous section, the four parameters chosen for the second match were:

- Pass 1 HTC (trailing edge pass of internal cooling passage)
- Pass 2 SS HTC
- Pass 2 PS HTC
- Pass 3 HTC (leading edge pass of internal cooling passage)

These four locations were chosen as they should provide increased spatial fidelity across the surfaces of the blade in order to match the target, with the relatively small increased cost of two additional parameters. The shroud HTC factor was removed for this set of simulations in order to reduce the time taken to generate the training data whilst assessing the internal cooling parameters required.

The adjustment factors required to match the target distribution as calculated using the GPR method are given in table 10.3. The temperature differences between the target and matched distributions with these four parameters are shown in figure 10.4.

It is immediately clear that these parameters offer a much better match than the first test. The temperature differences across the blade are much reduced in almost all places, generally between $-10K$ to $+15K$ of the target. The maximum differences have been much reduced. The shroud area does have a slightly poorer match than in the previous case due to the lack of any adjustment in this region. A final case including this shroud adjustment was therefore implemented.

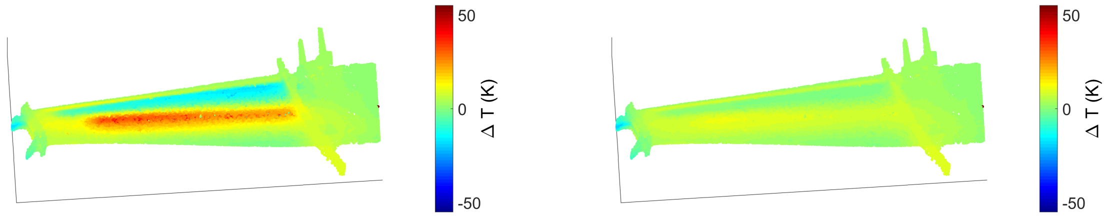

(a) SS ΔT - Initial (b) SS ΔT - Adjusted

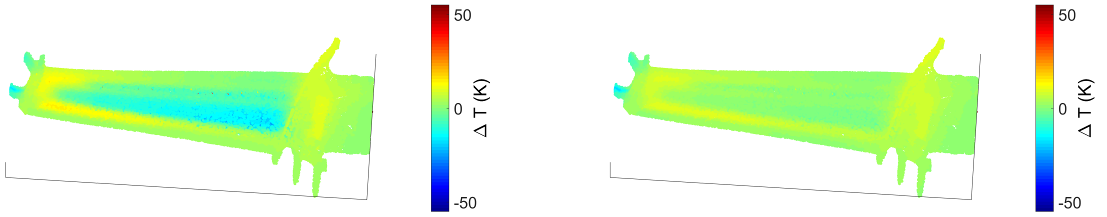

(c) PS ΔT - Initial (d) PS ΔT - Adjusted

Figure 10.4: Initial and matched temperature differences for IP blade - four parameters

Table 10.4: HTC factors - match 3

Pass 1 (TE)	Pass 2 SS	Pass 2 PS	Pass 3 (LE)	Shroud
0.796	1.691	0.701	1.055	0.832

10.2.3 Match 3 - Five Parameters

The final match used the following parameters, based on the best combination of the previous two cases:

- Pass 1 HTC (trailing edge pass of internal cooling passage)
- Pass 2 SS HTC
- Pass 2 PS HTC
- Pass 3 HTC (leading edge pass of internal cooling passage)
- Shroud HTC factor

These should provide adjustment in all regions of the blade, and enough local resolution to match the distribution well. The required levels of adjustment for each of these multipliers are given in table 10.4, with the corresponding temperature difference plots in figure 10.5.

This figure shows that, with five parameters, the thermal match is very good. The levels are within $10K$ of the target across the entire blade, and in most regions are significantly closer. This

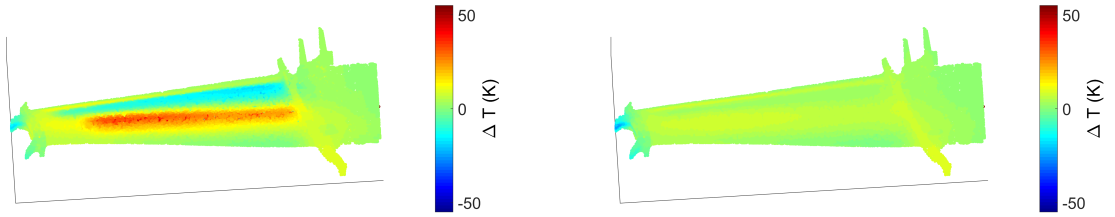

(a) SS ΔT - Initial (b) SS ΔT - Adjusted

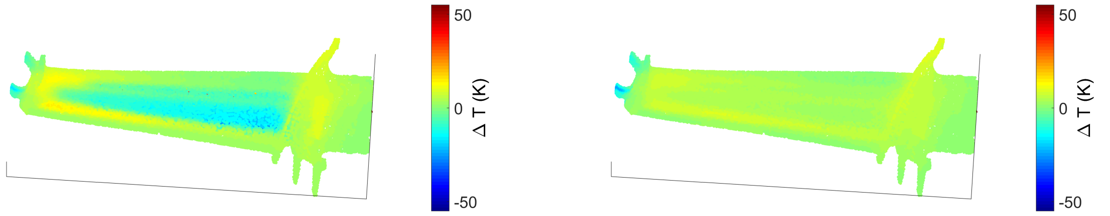

(c) PS ΔT - Initial (d) PS ΔT - Adjusted

Figure 10.5: Initial and matched temperature differences for IP blade - five parameters

constitutes a very good thermal match as is well within the accuracy measurement of a thermal paint test. The only region above this are the shroud fins, which behave in a significantly different manner to the rest of the model and therefore will not be picked up by the current parameter selection.

Further details of this final thermal match are given in figure 10.6. The pressure and suction surfaces both show maximum temperatures differences less than $10K$ which constitutes a very good thermal match. The shroud is matched within $2K$ with the exception of the shroud fins, which are known to require very extreme factors in order to be matched, and therefore would not be expected to be well matched using this methodology. The mid-span plot shows the region of the blade furthest from the target temperature is the suction surface in the central passage, however with a maximum difference of approximately $6K$ this is still very well matched.

10.2.4 Comparison of Matched Models

This section shows how each level of model compared to the target distribution using a number of metrics. These are the nodal mean absolute temperature difference, the maximum and minimum temperature differences and the percentage of nodes whose match was improved when the model was adjusted. This data is given in table 10.5.

It is seen that with each successive iteration of the model and parameter alteration the thermal match is improved by all of these metrics, the exception being the min ΔT. This is not

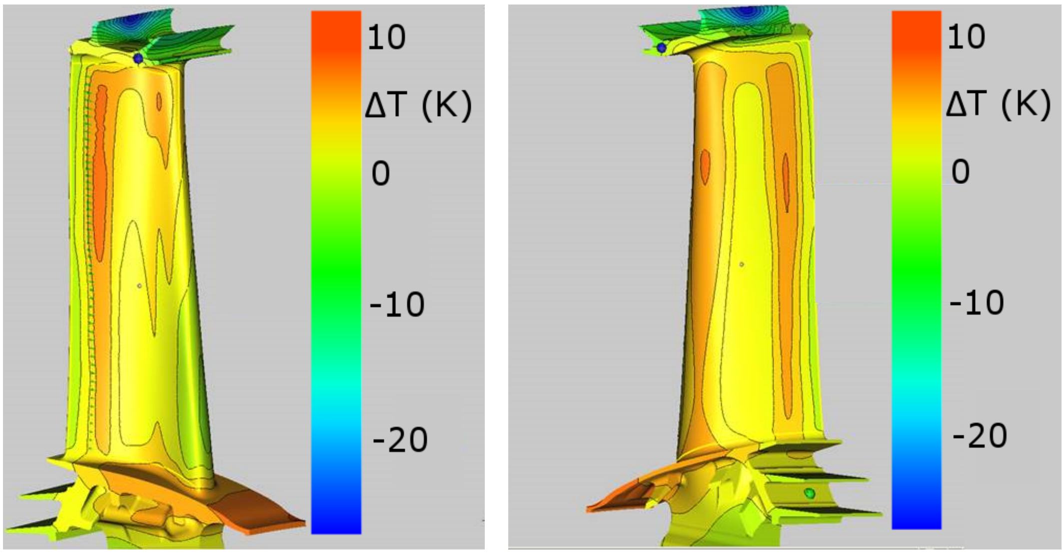

(a) PS (b) SS

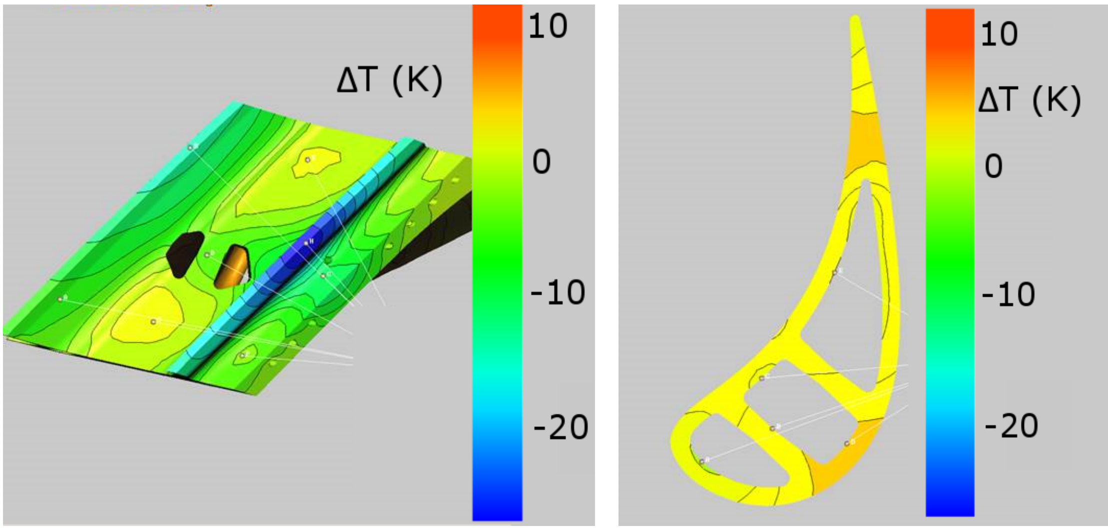

(c) Shroud (d) Mid Span

Figure 10.6: Matched temperature differences for IP blade - five parameters - detailed views

Table 10.5: Match comparison - temperature differences

Match No.	nodal mean $\|\Delta T\|$	max ΔT	min ΔT	node % improved
Initial	7.50	48.74	-31.66	-
1	4.34	51.01	-16.77	84.64
2	4.16	12.09	-20.26	85.57
3	3.78	10.22	-25.21	86.98

representative of the true match, however, as for the 2nd and 3rd matches this location was on the rear shroud fin which was not able to be effectively modified by the selected parameters. As this constitutes a very small and relatively unimportant section of the blade, it will be discounted. In this case it is clear that the five parameter test gives the best match. The match obtained by this is well within the required accuracy of the thermal distribution and was obtained much faster than possible with the existing manual methods.

The previous sections show that the new methodology can provide good quality solutions for thermal matching in a real blade using internal HTCs as parameters. In a thermal matching process multiple parameters other than the internal HTCs can also be altered, including the RTDF (Radial Temperature Distribution Factor) and the trip location for the SS or PS boundary layer. The feasibility of this method for these other parameters is assessed in the following sections.

10.2.5 Match 4 - RTDF

The RTDF is a zero-mean profile applied to the mean inlet gas temperature for the component being modelled to represent the radial variation in the temperature profile within the engine. This can have a large effect on the radial variation of metal temperature within the component, and is often very challenging to model accurately.

For the purposes of this thermal matching the RTDF profile was modelled using a zero-mean quadratic with a normalised position co-ordinate from 0 to 1, which allows two parameters to be in equation 10.1.

$$rtdf = a(x-0.5)^2 + b(x-0.5) + c \qquad a = -12c, \quad b \ \ indeterminate. \tag{10.1}$$

The actual RTDF applied to this blade was represented using a quadratic, equation 10.1, with the resulting temperature distribution as the target. The training data consisted of nine training simulations that covered the required parameter range. The profiles for these training simulations are given in figure 10.7.

The matching procedure was then run as described above to establish the best RTDF parameters. The target and predicted parameter values are given in table 10.6, with the resulting

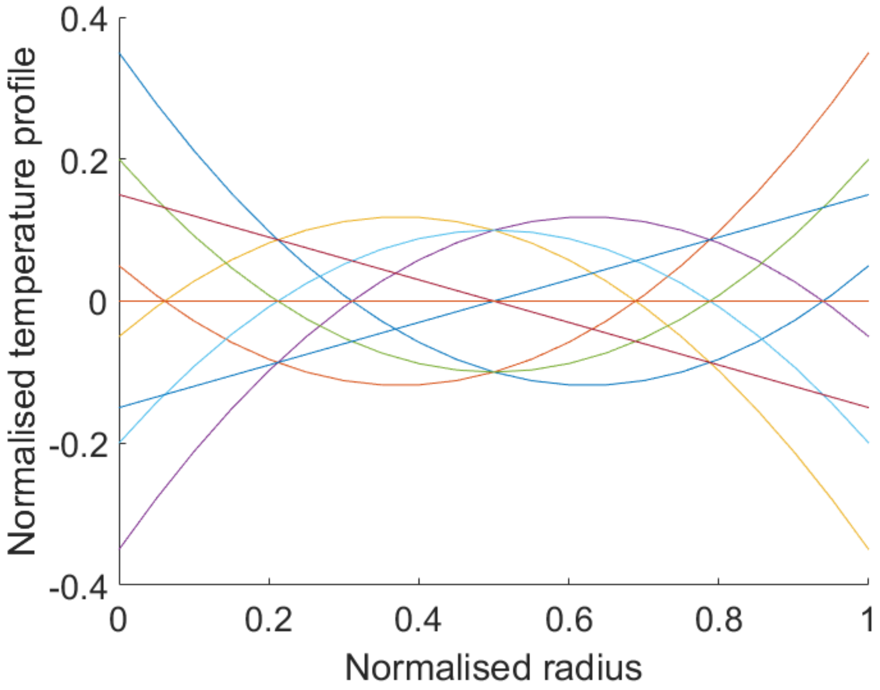

Figure 10.7: RTDF training simulation profiles

Table 10.6: Target and predicted RTDF parameters

	Parameter 1	Parameter 2
Target	0.0537	-0.05
Predicted	0.0540	-0.0507

profiles given in figure 10.8.

It is clear from this result that, in isolation, the RTDF can be matched extremely well using the new automated method using training data that adequately covers the possible extent of the profile.

10.2.6 Match 5 - SS Trip Location

In the SC03/JB56 modelling procedure the external surface HTC distributions are characterised using a normalised one-dimensional distribution in the streamwise direction. An example of a typical profile is given in figure 10.9.

The peak HTC is found at the leading edge, with levels decreasing significantly until the transition point. At this location the HTC rises sharply, it is approximately doubled, before decreasing again with streamwise distance before settling to a value around 70% of the maximum value. The exact location of this transition is very hard to predict in practice, and due to the

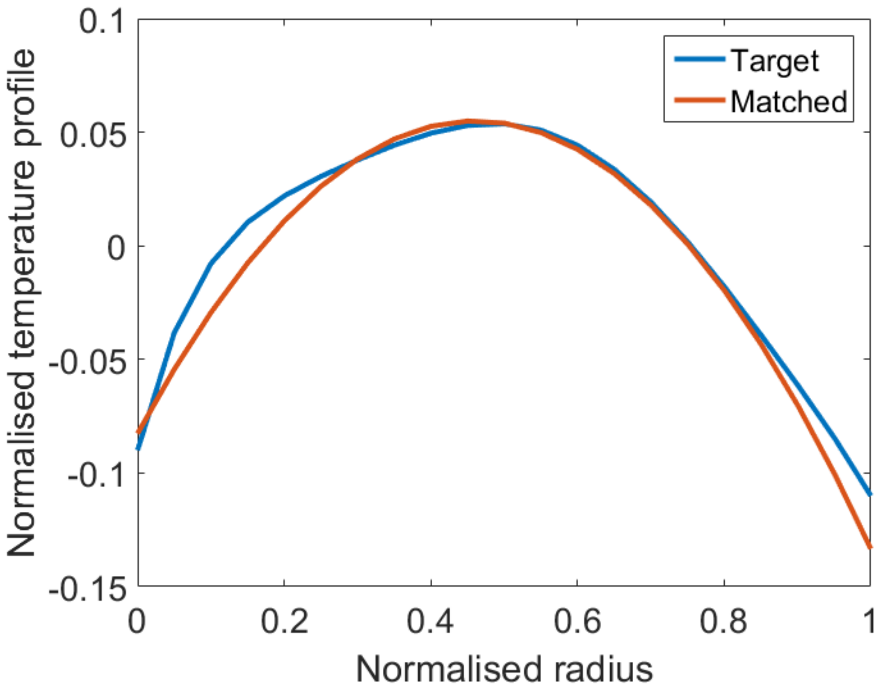

Figure 10.8: RTDF target and predicted profiles

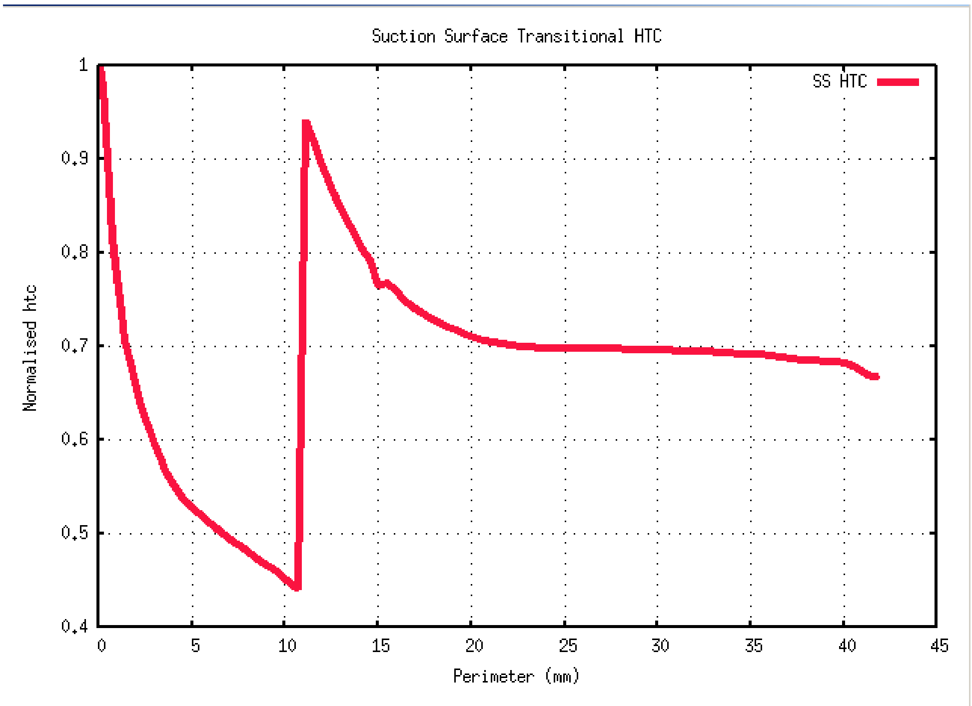

Figure 10.9: Example SS external HTC profile

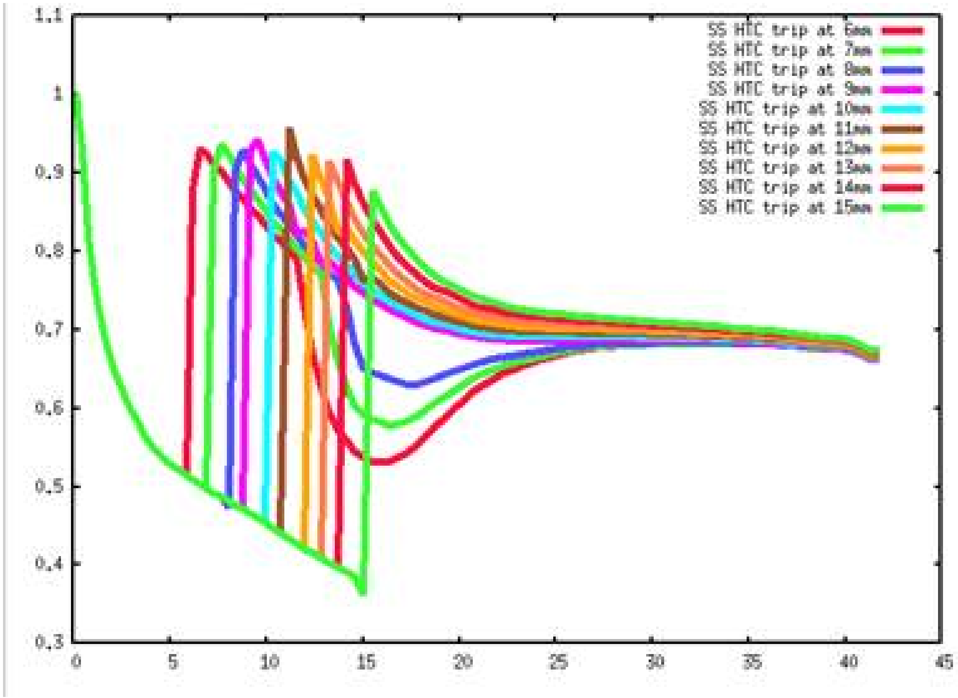

Figure 10.10: SS external HTC training profiles

Table 10.7: Target and predicted SS transition locations

Target	All training simulations	Limited training simulations
11 mm	10.983 mm	10.903 mm

sharp rise in HTC at this location it can have large effects on the metal temperature distribution. It is therefore often used as an adjustable parameter in the thermal matching process.

In this match the training data will consist of a number of simulations, each with a different trip location. The range of these was chosen to be 6-15 mm, as the typical trip location for this particular blade was expected to be 10-11 mm. The target simulation will have a defined trip location. The HTC profiles for the training are given in figure 10.10.

Two separate matches were tested, both with a target trip location of 11 mm. The first match used all of the training simulations, whilst the second used only the central, minimum and maximum trip locations. The predicted locations are given in table 10.7.

As for the RTDF profile, the method is clearly successful in accurately matching the trip location in isolation, both with a large, and small, number of training simulations.

Table 10.8: Target and predicted RTDF and SS transition parameters

	Trip Location (mm)	RTDF parameters	
Target	10	0.0537	-0.05
Predicted	9.73	0.0535	-0.0481

10.2.7 Match 6 - Combined RTDF and SS Trip Location

Following the matches of the RTDF and SS trip location in isolation, the method was tested on the same geometry for a combination of these. There were three parameters to match, the trip location and two for the RTDF quadratic. The target and predicted parameters are given in table 10.8.

These results show that the method is clearly capable of predicting these parameters where both the transition location and RTDF are adjustable. This method has therefore been proven to be reliable for thermal matching using internal cooling, external cooling and the upstream traverse as adjustable parameters.

The method is now be applied to a thermal match using an HP blade where the cooling configurations are significantly more complex, with an increased difficulty in obtaining a match implying the greatest potential benefit of the automated method introduced by the author.

10.3 HP Blade - Modelling Procedure

Following the success of the Gaussian process regression based method on an IP blade, the methodology was applied to an HP blade. An HP blade contains a much more complex cooling configuration than an IP blade and therefore provides a more demanding test case for the method. The HP blade is subject to the highest heat loads in the engine and the use of cooling air leads to significant reduction in turbine efficiency, which increases with coolant flow. A typical engine development project requires a thermal paint test and if performed manually the matching process can take hundreds of hours. Therefore this is an area where the gains provided by the new method can be most pronounced.

10.3.1 Blade Geometry and Cooling Configuration

The HP blade analysed in the section below is that from a demonstrator engine, and was chosen due to the availability of a good quality set of thermal paint test data. The cooling configuration of the blade is complex, containing varied internal cooling passages, film cooling and trailing edge ejection.

The main cooling features of the blade are as follows:

- Multiple ribbed internal cooling passages
- Trailing edge cooling slots
- 'Tip flag' passage to feed trailing edge slots near blade tip (a radial passage located towards the trailing edge of the blade that only supplies the trailing edge slots near to the tip, and no film cooling or other slots)
- Multiple film cooling rows on both pressure and suction surfaces

10.3.2 Modelling Setup and Generation of Training Data

There are two main differences between this HP blade thermal match and the IP blade tests described above. These are the increased complexity of the cooling design and the use of real thermal paint data.

The inclusion of more cooling features in this blade design led to an investigation using eight parameters to attempt to achieve an accurate thermal match on different sections of the blade. Due to the different behaviour of each feature the parameters each required a different range of adjustment for the training data. The parameters chosen and the range over which the training data was generated are given in table 10.9.

The parameters chosen were based on engineering experience of the operation of an HP blade and previous parameters that have been used in successful thermal matches. The ranges chosen are typical of the adjustments that might be expected, and will be shown to be acceptable in a following section.

In this case real thermal paint data was used, as mentioned above. The data available consists of a number of discrete contour bands, an example of which is illustrated in figure 10.11.

Table 10.9: HP blade parameters and training data range

Parameter	Min.	Max.
SS trip location	2	4
PS trip location	1	3
Internal SS HTC	0.25	1
Internal PS HTC	1	2
Internal sidewall HTC	0.5	1.5
3D recovery temperature	0.95	1.05
SS film effectiveness	0.8	1.2
PS film effectiveness	0.8	1.2

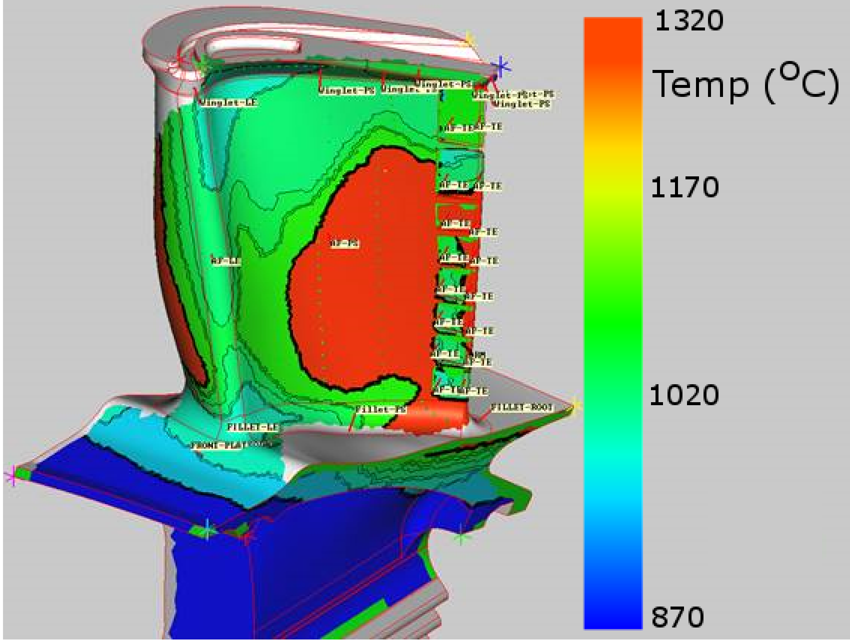

Figure 10.11: Example of thermal paint contours on HP blade geometry from the PS before contour extraction

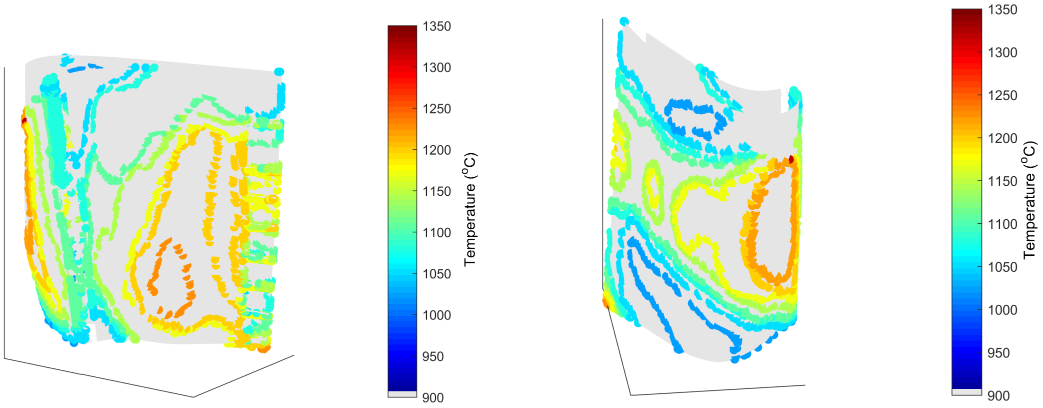

(a) PS view (b) SS view

Figure 10.12: Extracted thermal paint target locations

The information from the thermal paint occurs on the contour lines themselves, corresponding to the colour change temperatures of the thermal paints. Along these contours the surface metal temperature has reached the activation point of a particular thermal paint, and therefore was operating at this temperature in the tests. These locations were therefore extracted and used as the target temperature distribution, figure 10.12.

10.3.3 New difficulties for HP blade

A number of new challenges were encountered when processing the HP blade thermal data to obtain a thermal match. These were related to the parameter choice and generation of training data.

In order for the method to obtain a reliable match, with an accurate model of the parameter-temperature relationship in the required region, the temperature range obtained from the training simulations should bound the target temperatures. This can be difficult to ensure before running the training simulations due to the unknown response of the surface temperature to changes in model parameters.

The initial set of parameters used for the training simulations for this blade were not suitable, as can be seen in figure 10.13. This figure shows the target temperatures in red and training simulation temperatures in blue for the target nodes in increasing temperature order. For a large proportion of the nodes it is clear that the target temperatures are outside the temperature range covered by the training temperatures.

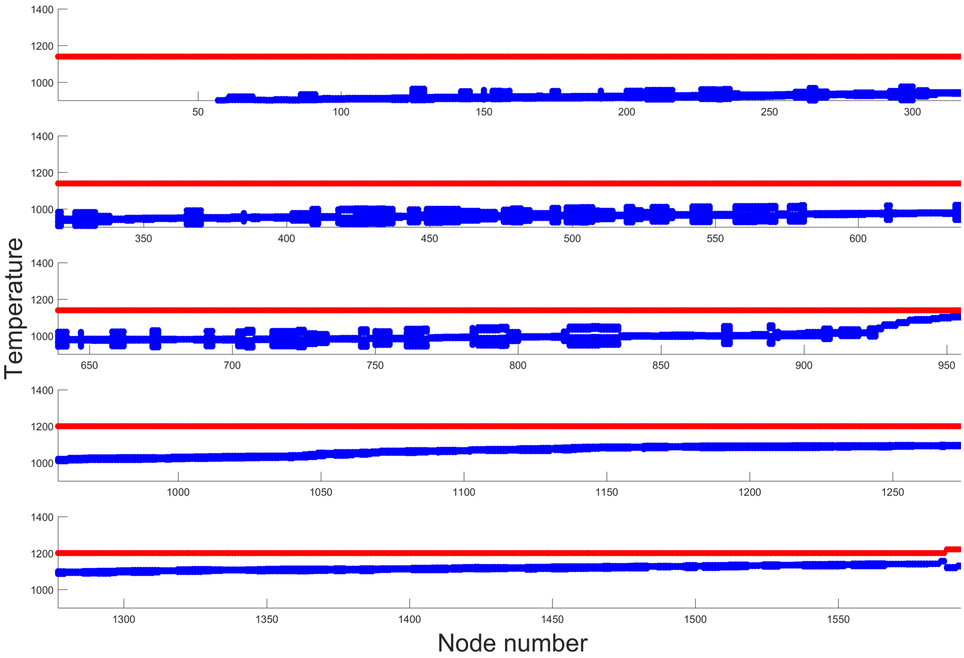

Figure 10.13: Illustration of training and target data mismatch

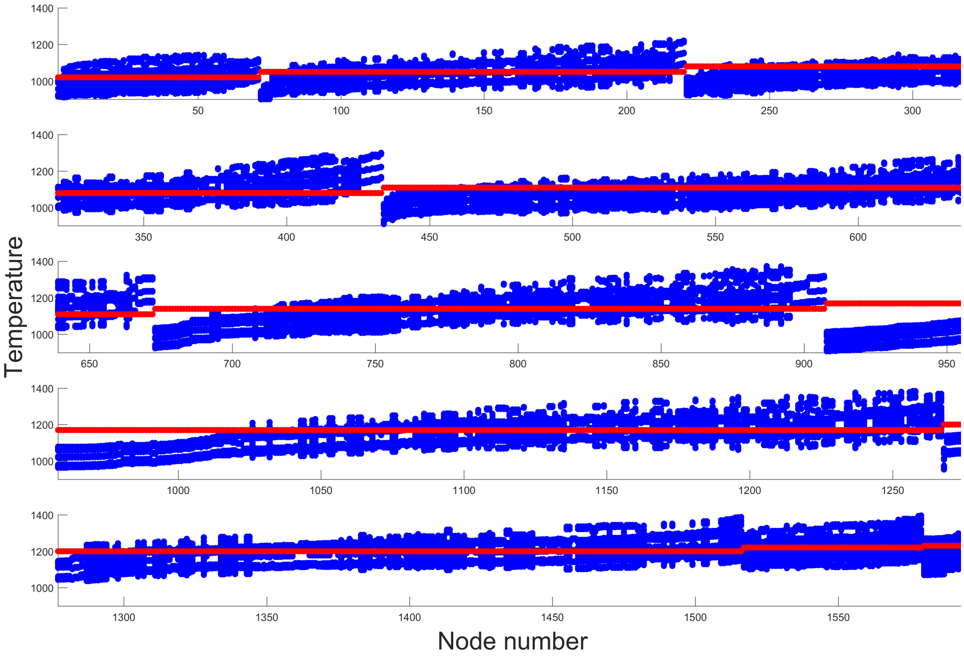

Figure 10.14: Illustration of training and target data for actual match

Table 10.10: Adjusted HP blade parameters

Parameter	Adjusted value
SS Trip Location	1.5409
PS Trip Location	0.8732
Internal SS HTC	1.4078
Internal PS HTC	3.8424
Internal Sidewall HTC	0.7338
3D Recovery Temp	1.0343
SS Film Effectiveness	0.7000
PS Film Effectiveness	1.1890

Figure 10.14 shows the same plot for the actual match undertaken. This plot shows that for most target nodes the new training simulations have a broad enough range for a thermal match to be obtainable within the limits of the training parameters. There are still some nodes for which this is not the case however this is not unexpected due to the relatively small number of parameters that can be adjusted to implement a match.

The figures also highlight the importance of the initial model being reasonably close to the target simulation. If this is not the case, very large parameter variations would be required, which can either reduce the quality of the match or result in the requirement for additional training simulations. It is also important that the target temperatures are within the training range, to ensure that a match is possible, before the matching process is run, to avoid erroneous results.

10.4 HP Blade - Results

The HP blade introduced in the previous section was matched to the target distribution given in figure 10.12. The method was run as before, but for this match all of the target nodes were used due to the increased number of parameters. Also, due to the variety of parameters used, different length scales (σ_l in equation 9.2) were used for each parameter within the squared exponential covariance function.

Table 10.10 gives the parameters obtained in order to match the target temperature distributions.

The parameters for the matched model are generally in line, or close to those in the training data. However there are some outside the training range, as many of the parameters act in combination on similar regions of the blade, and there were some target nodes which were outside the range of training data, such as nodes 920-1000 in figure 10.14.

Figure 10.15 shows the target, initial and matched temperature distributions for the PS, with figure 10.16 giving the same plots for the SS.

The initial, unadjusted temperatures are reasonably close to the target contours, but do show some significant differences. For example, the trailing edge of the initial distribution shows significantly more variation than the target temperature, and shows slightly cooler surface temperatures away from the trailing edge.

The matched temperature distribution has a generally higher temperature, leading to a better match on the PS, particularly towards the leading edge of the blade. The overall distribution is still more discretised than the paint data, as the selected block parameters cannot alter the distribution continuously. The trailing edge lands are not well matched. The match has been improved at the base of the blade, however the tip is less well matched than before adjustment. This is due to the presence of a specific ‘tip-flag’ passage which feeds the trailing edge slot directly near to the tip. This is not modelled well by the FEA/low-order cooling software, and a specific parameter was not set aside to adjust this. Therefore with the parameters chosen it is not possible to match this region due to conflicts against other regions. This would be rectifiable in future thermal matching exercises if this cooling feature is present, by assigning a specific enhancement factor to enable its value to be adjusted.

The SS initial and matched distributions show similar features, and also issues, as the PS distributions although are in general closer to the target. The initial distribution is too hot across the surface however shows very similar spatial features to the target.

The matched distribution is very close in all areas except for the trailing edge tip region, due to the lack of a parameter dedicated to the tip flag passage. The hot region on the leading edge section and the colder region downstream show an improved match relative to the initial model, with the trailing edge region largely unchanged.

Figure 10.17 shows the difference between the target, initial and adjusted temperature distributions. These plots illustrate the conclusions previously reached, with the adjusted distribution

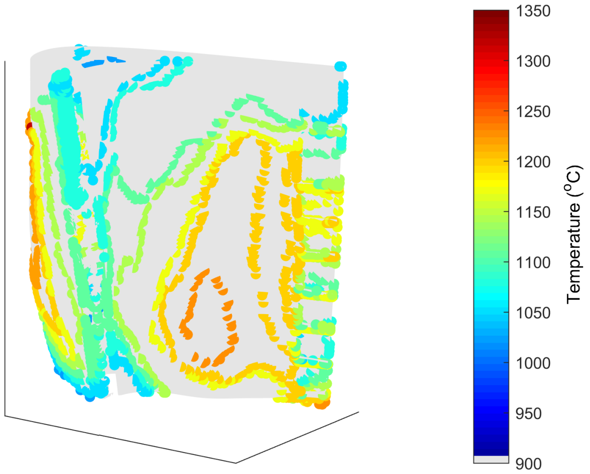

(a) Target

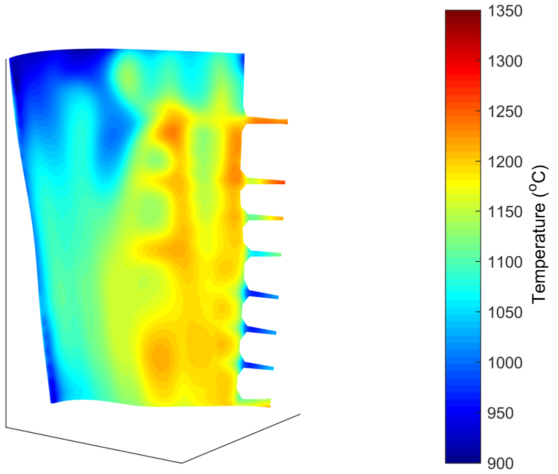

(b) Initial

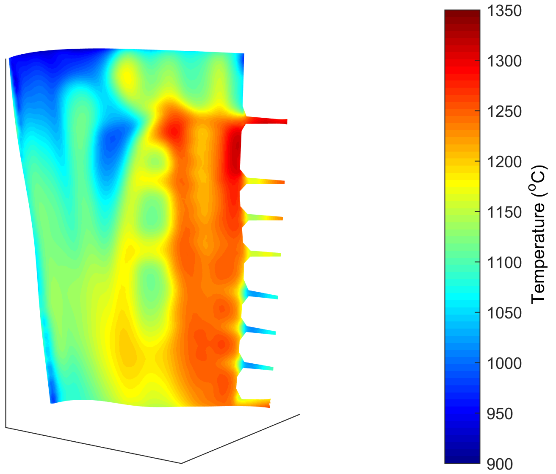

(c) Adjusted

Figure 10.15: HP blade temperature distributions - PS

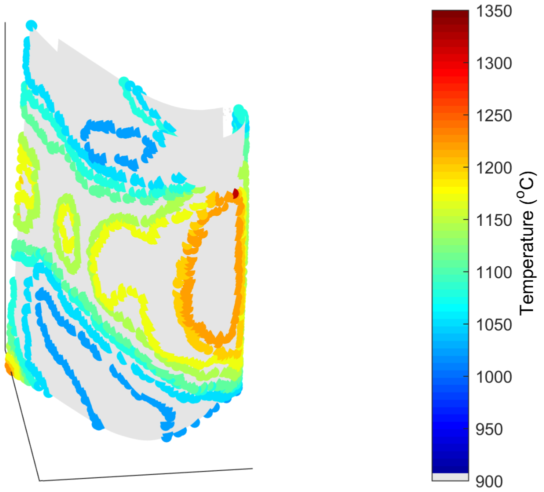

(a) Target

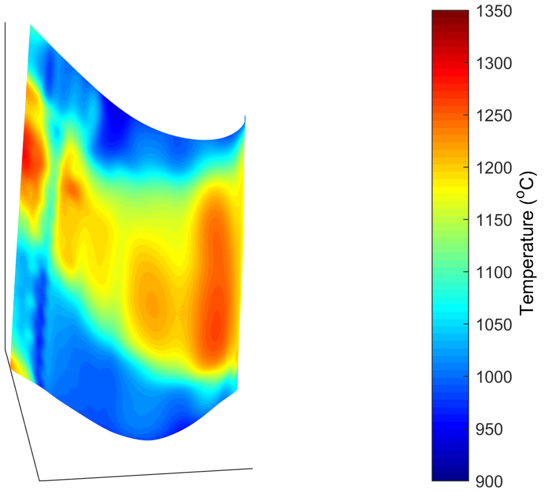

(b) Initial

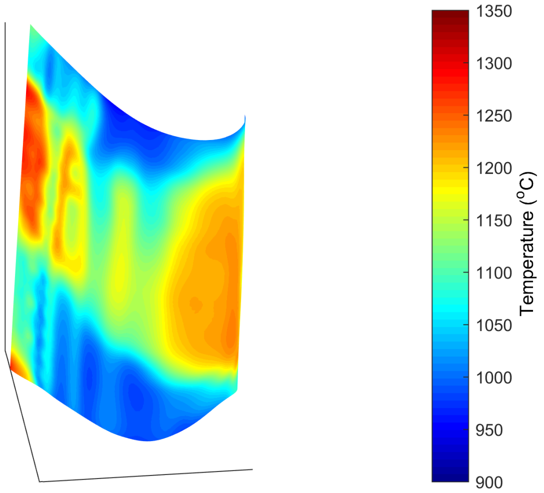

(c) Adjusted

Figure 10.16: HP blade temperature distributions - SS

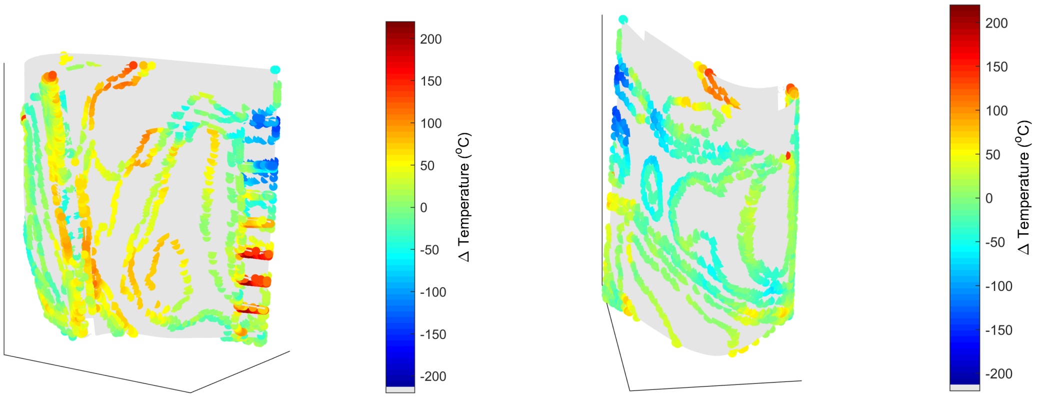

(a) Target minus initial - PS (b) Target minus initial - SS

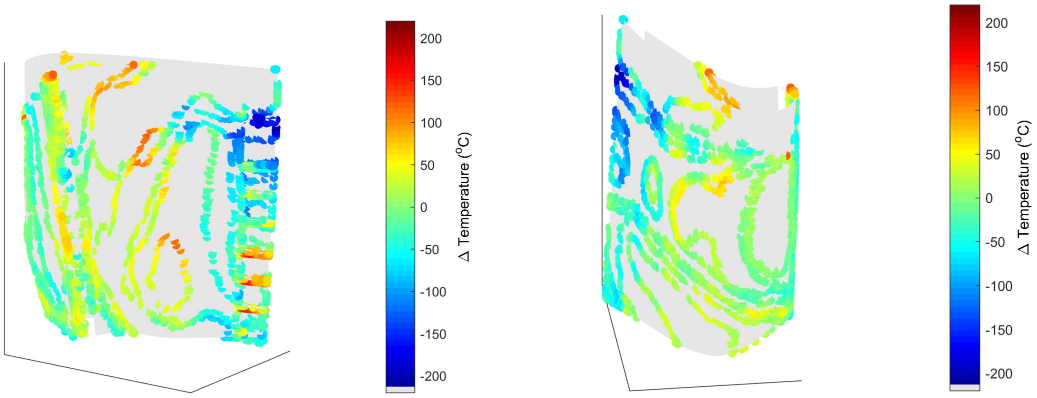

(c) Target minus adjusted - PS (d) Target minus adjusted - SS

Figure 10.17: Difference to target temperature distributions

Table 10.11: Temperature values for initial and adjusted simulations

	nodal mean $\|\Delta T\|$	max ΔT	min ΔT
Initial	45.01	208.83	-149.00
Adjusted	39.14	154.30	-214.73

showing an improved match, largely within the thermal paint error, across the entire blade surface excluding the trailing edge. Near the blade root the match has been improved to within 50^{o}C of the target from over 100^{o}C too cold, however the lack of adjustment on the tip flag passage results in a poor match towards the tip, which can easily be rectified for future blades and results from a very specific feature which is not usually present.

Table 10.11 gives the mean, maximum and minimum difference between the target, and initial and adjusted distributions. The values show an improvement in mean temperature difference by 13%, however still large maximum differences of over 200^{o}C. These are heavily influenced by the poorly matched trailing edge region that has been explained above. Without this region, in which a good match cannot be expected with the choice of parameters made, these values would be much improved.

Figure 10.18 shows the difference between the target, initial and adjusted temperature distributions for four blade height locations. These plots are those used to assess the thermal match internally within Rolls-Royce, the green boxes giving the thermal paint data with error bars and the blue lines the temperature extracted from the model. These show a match that would be considered very good with the model temperature within or close to the thermal paint data for around 80% of spanwise distance. The modelled temperature is very close to the thermal paint in the first three plots, with almost all areas overlaying the thermal paints. The tip-most plot shows more deviation from the paint data, particularly in the trailing edge region, due to the tip flag passage modelling as has been detailed previously.

In this section the new technique for automated thermal matching has been successfully applied to an HP blade. Actual thermal paint data was used for the target temperature distribution, and a good match was obtained for most of the blade. The exception being a small region on the trailing edge near to the blade tip due to a poorly modelled cooling feature, specific to this blade geometry, which can be easily rectified in future matches by defining a single parameter to this passage.

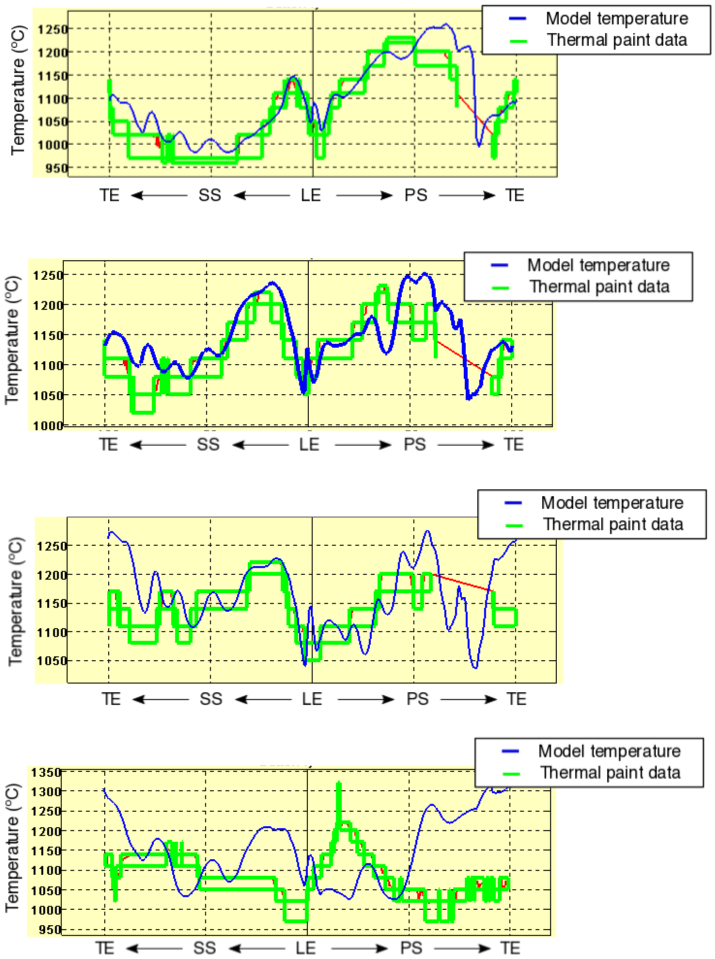

Figure 10.18: RR matching plots at increasing blade heights

10.5 New Approach for Sparse Thermal Paint Data

The output of a thermal paint test is localised to discrete lines which correspond to the change points between the calibration bands of the paints used. These lines indicate the temperature reached at the locations on the line during the test. In otherwords, the temperature data is localised to specific lines. Depending on the paints used, or the particular temperature distribution, there can be large areas of the surface of the blade for which there is no temperature information.

This section introduces a method for obtaining full surface temperature distributions from the thermal paint contours using a Gaussian process regression model, with covariance functions based on a physical interpretation of blade thermal characteristics.

10.5.1 Method Outline

The method applied uses Gaussian process regression to model spatially distributed data from a selected set of sample locations corresponding to the phase change paint transition temperatures. The overall method has been introduced previously in this chapter, the extension being the improvement of the thermal paint data using a custom covariance function to give a full spatial distribution.

For such sparse data it is difficult to automatically obtain the correct covariance functions, as the overall length scales relevant to the distribution may not be contained within the sample points themselves. A new custom covariance function, based upon the squared exponential function, has been introduced by the author. This is given in equation 10.2 for two separate length scale components.

$$k_{custom}(x_i, x_j|\theta) = \sigma_{f1}^2 exp\left[-\frac{1}{2}\sum_{m=1}^{d}\frac{(x_{im}-x_{jm})^2}{\sigma_{l1m}^2}\right] + \sigma_{f2}^2 exp\left[-\frac{1}{2}\sum_{m=1}^{d}\frac{(x_{im}-x_{jm})^2}{\sigma_{l2m}^2}\right] \quad (10.2)$$

In this covariance function the decay of importance away from a point in parameter space is given by the squared exponential function, however there are two separate components of these. The two components each have relative weighting given by σ_{f1}^2 and σ_{f2}^2, and different length scales for each direction. The task is then to find the σ_f and σ_l values for these components, and the number of components required, for the physical problem.

These are found by assuming that the thermal solution for the FEA model of the blade will have the same characteristics as the blade itself. The covariance parameters are found by applying a fast Fourier transform to the mean temperature profile of the FEA solution in each direction, in this case the height and streamwise co-ordinates, h and s.

The transformed spectrum in the 'spatial frequency' domain is then analysed for peaks. Each peak occurs at a given spatial frequency, which has a corresponding length scale which can then be used in the previously presented covariance function, σ_l. The relative magnitude of each of the peaks is then determined and applied to the multiplier for each component, σ_f.

These parameters are fixed in the covariance function, which is subsequently fitted to the input contour in order to obtain the basis function value and overall weighting to fit the actual data. This then gives a complete GPR model from which a full surface distribution can be found.

This modelling procedure offers significant advantages in that all of the thermal paint data is used, and the modelling of the surface between contour lines has a physical basis from the same system.

Figure 10.19 illustrates the key stages of obtaining the full surface distribution, and compares the new method with that using a standard covariance function for a particular case.

The first plot, (a), gives the temperature distribution and its value averaged in the spanwise direction, minus the mean value, is shown in (b). The fast Fourier transform with normalised signal power is given in (c), where it can be see there are two significant peaks for this distribution, in this direction, specifically at 1 and 5. The input contour, the locations for which thermal paint test data is available and the distribution predicted using the standard squared exponential covariance function are shown in (d) and (e). Finally the distribution predicted by the new method is shown in (f).

It is clear from this that the new method provides a significantly improved prediction of the full temperature distribution using only the contour values and inferred parameters as inputs, both of which can be done for a real thermal paint test.

Figure 10.20 shows the full temperature distribution, contour inputs and full predictions of surface temperatures using the new method for another two cases. The first case, figure 10.20

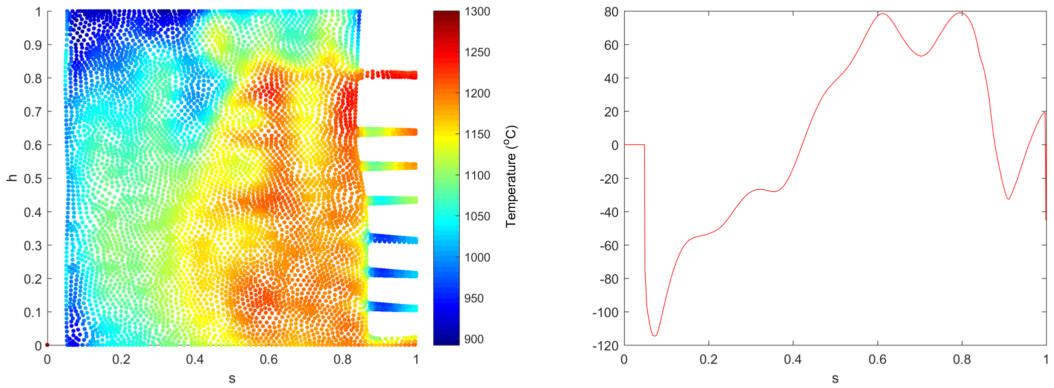

(a) Imported temperature (b) Average temperature with s *(mean subtracted)*

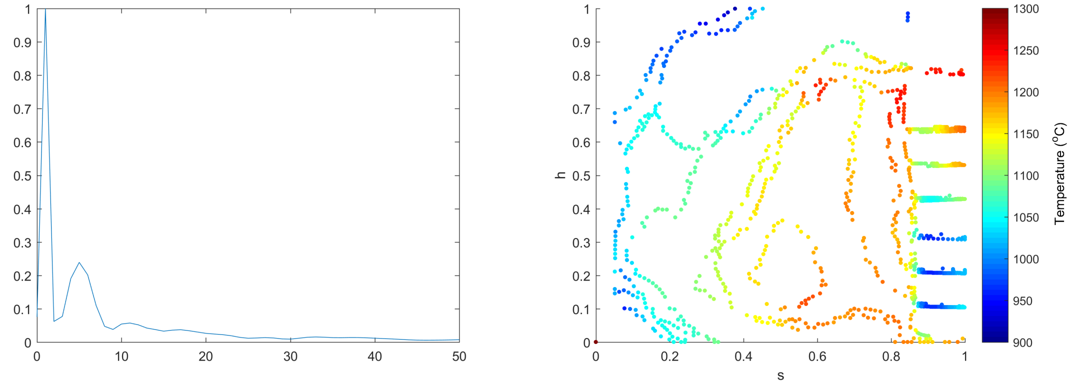

(c) Normalised FFT of average temperature (d) Input contour

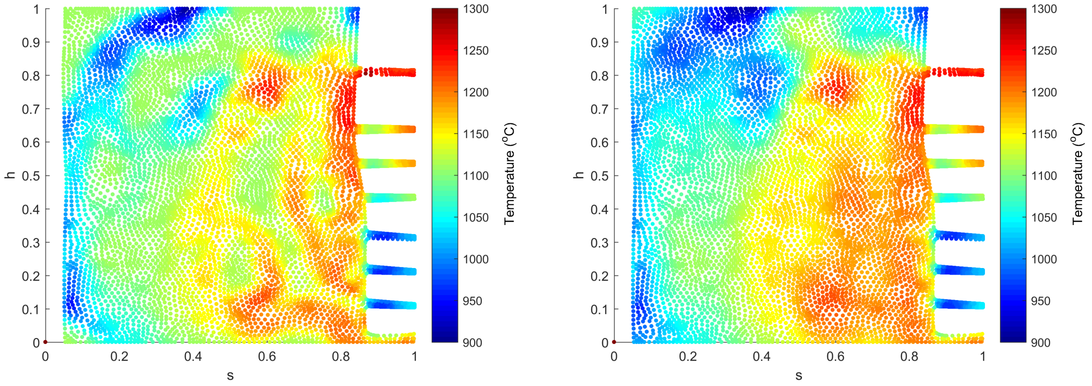

(e) Modelled temperature - standard covariance function (f) Modelled temperature - new custom covariance function

Figure 10.19: Series of figure showing new thermal paint data technique

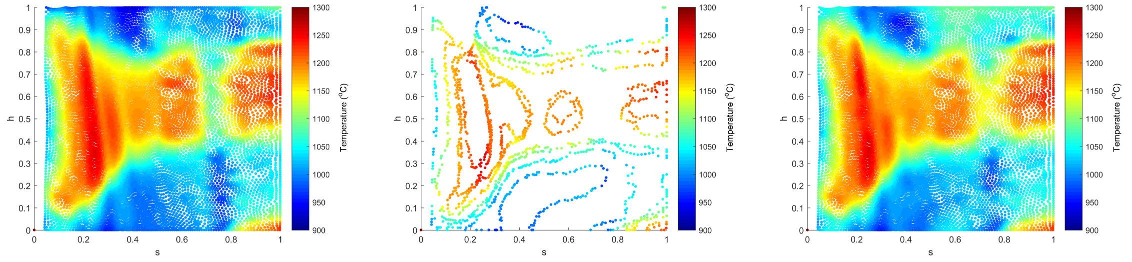

(a) Imported temperature - SS (b) Input contour - SS (c) Modelled temperature - SS

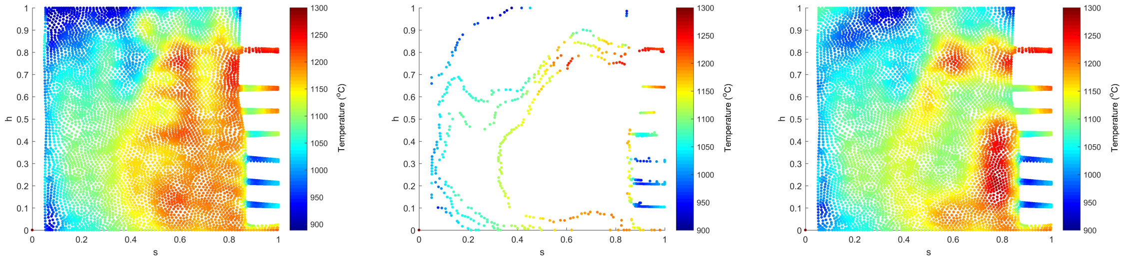

(d) Imported temperature - PS (e) Input contour - PS (f) Modelled temperature - PS

Figure 10.20: Further examples of new technique

(a)-(c), again shows a very good match with the actual distribution, while the second (d)-(f) is largely correct however with some details not picked up resulting from the large areas where no thermal paint data is available.

Figure 10.21 gives the full surface temperature distribution for three separate cases using actual thermal paint test data. For each of these cases there is no full distribution to validate against, as this is actual engine test data, however each surface distribution shows temperatures and distributions that would likely be expected given the input data.

In this section a new method has been developed by the author capable of producing a full surface temperature distribution from the thermal paint contour bands. Although the contour bands themselves should still be used as the target temperature in the automated matching procedure, the full distributions obtained allow for improved assessment of the matches obtained.

10.5.2 Match using modelled target distribution

Figure 10.22 compares the modelled target temperature distribution to the initial and matched distributions for the HP blade PS surface, with figure 10.23 giving the same comparison for the SS.

These figures reinforce the conclusions gained from this match previously, however are easier to observe. The PS surface of the blade is reasonably well matched with the exception

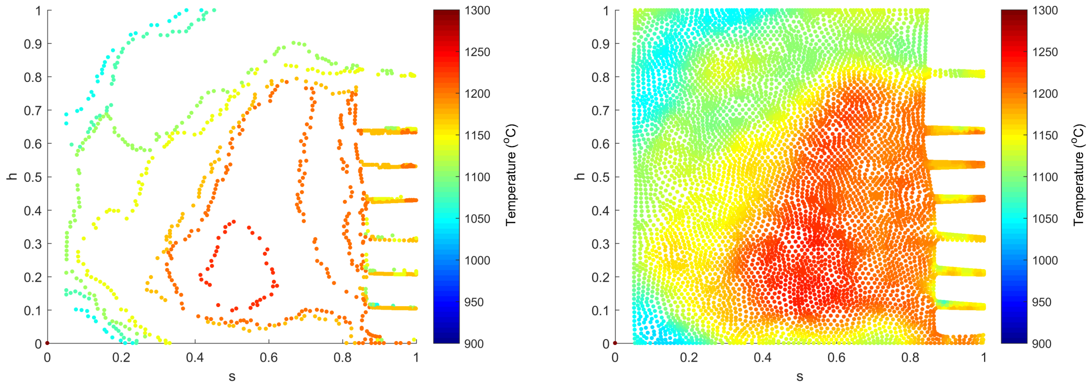

(a) Imported contour (b) Modelled temperature distribution

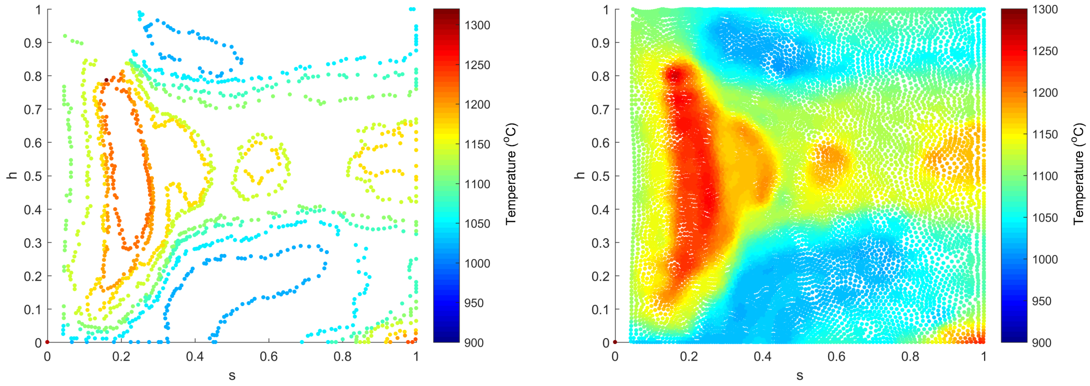

(c) Imported contour (d) Modelled temperature distribution

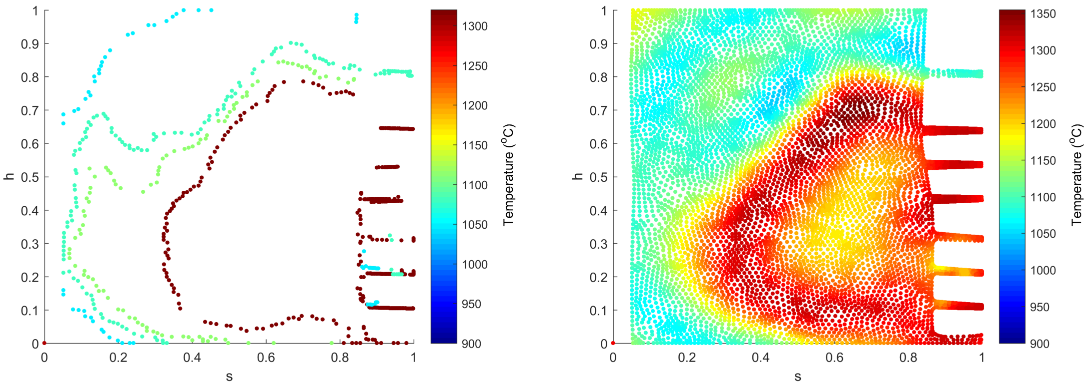

(e) Imported contour (f) Modelled temperature distribution

Figure 10.21: Method applied to actual thermal paint contours

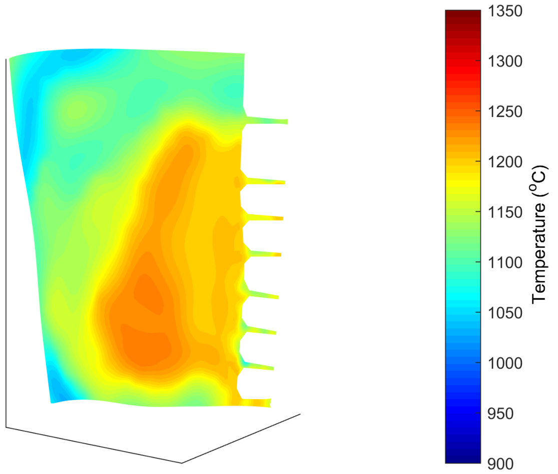

(a) Target - modelled

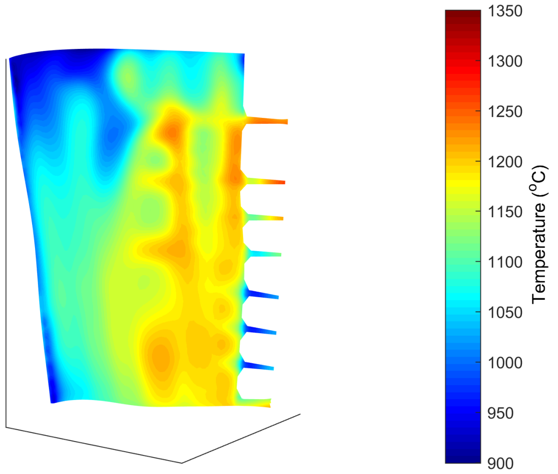

(b) Initial

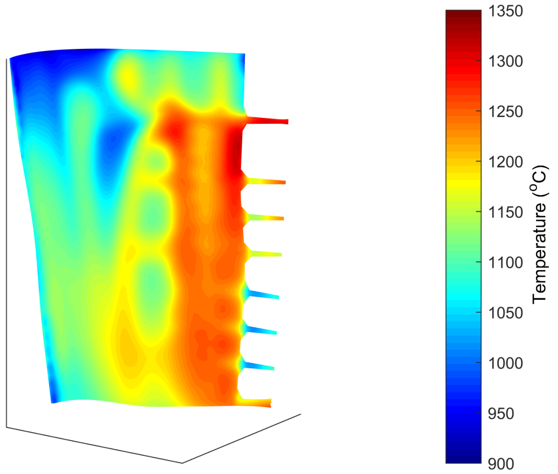

(c) Adjusted

Figure 10.22: HP blade temperature distributions - PS

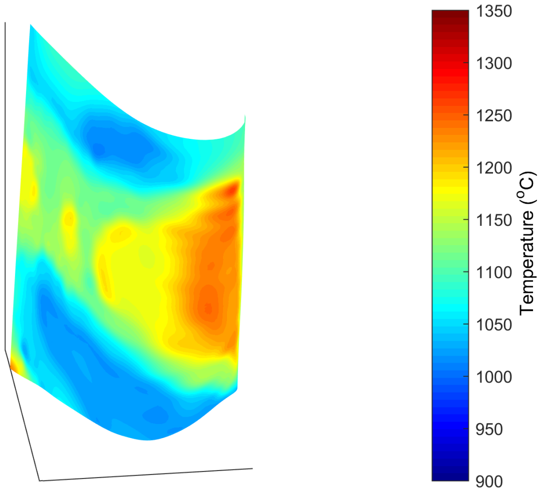

(a) Target - modelled

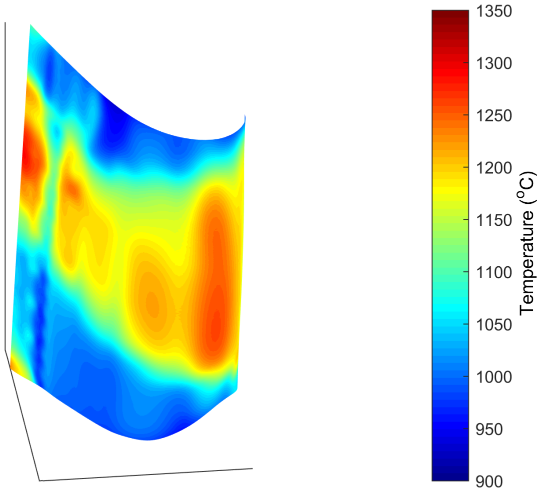

(b) Initial

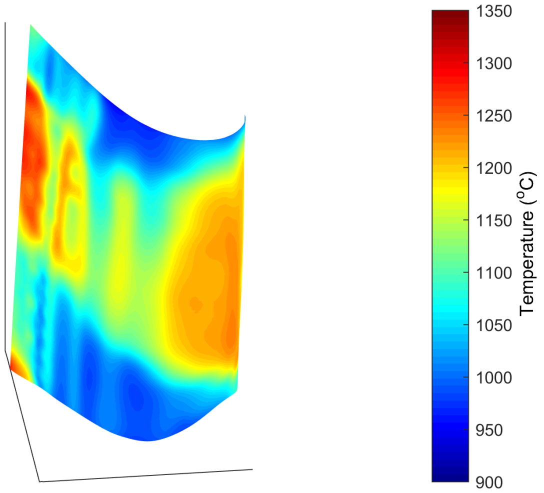

(c) Adjusted

Figure 10.23: HP blade temperature distributions - SS

of the trailing edge near to the tip, due to the poor modelling of the ‘tip flag’ passage. The SS match is much improved relative to the initial distribution, particularly in the leading edge region, while the trailing edge regions shows similar difficulties in the modelling to the PS.

10.6 Summary and Conclusions

The GPR based method for obtaining a thermal match that was implemented and tested for a leading edge impingement design in chapter 9 has been tested on a full blade geometry. The initial blade used was an IP blade, with the target temperature a distribution matched to the real engine thermal paint test. This provides a very high level of validation for a full blade cooling configuration under engine conditions. Multiple parameter selections were used, each providing an improved thermal match. The final match using five parameters was easily within thermal paint accuracy limits and was obtained significantly faster than it is possible to do using existing manual methods.

The method was then tested on an HP blade using real thermal paint test data, rather than a matched model. A larger number of parameters was required due to the increased complexity of the cooling system, however a good match was obtained for most of the blade surface. There were some areas where the match was less good, however this was due to a geometric feature particular to this blade, and would easily be rectified in future cases.

Following this a method using GPR with a modified, physically based covariance function was presented. It was shown to be reasonably well validated against know distributions, and can give additional insight into the blade surface temperature distribution using the contours obtained from a thermal paint test.

The following conclusions have been drawn:

- The GPR based method can successfully give a thermal match for a full blade under engine conditions significantly faster than previously possible.
- The correct choice of parameters must be made in order to match the full temperature distribution due to local effects such as those induced by rotation.
- The method is able to provide reliable matches for blades, even with very complex cooling systems such as in an HP blade.

- The GPR method has been fully validated and therefore should be used for future blade thermal paint tests as it provides reliable, consistent and very fast thermal matches.
- Full surface distributions of metal temperature can be modelled using a GPR technique based on a physical model created using the thermal paint data.

This work has therefore been very successful as it greatly improves the thermal matching procedure used for gas turbine blades, a process which is essential for all future jet engine designs.

Chapter 11

Summary and Conclusions

11.1 Summary

A number of aspects of internal cooling for HP turbine blades have been investigated. These include the heat transfer properties of radial passages and leading edge impingement systems, the mechanical performance of a leading edge impingement system and a new methodology for turbine blade thermal matching.

Radial Passages

The effect of rotation on the heat transfer in radial passages was investigated. Commonly used industrial RANS CFD simulations were compared to experimental data obtained from the RHTR, and their ability to predict heat transfer levels under stationary and rotating conditions was analysed. Key features identified in the initial work were then investigated. Different inlet velocity profiles were imposed at the start of the passage under stationary and rotating conditions, with the effect on the heat transfer distribution analysed. Simulations were also run with no rib-reversal between passes with some significant differences found in the flow structure and heat transfer in the second and third passes.

Leading Edge Impingement - Rotating

The influence of rotation and the predictive ability of RANS CFD methodologies was investigated for a leading edge impingement design. This was a single line design with confined jets due to the availability of data from the RHTR. Rotation was found to affect the design in the opposite way than expected due to changes in flow structure in the feed plenum. The CFD was found to offer good predictions for this geometry, with some overprediction in Nusselt number levels, however the correct trends with rotation were found.

Leading Edge Impingement - Static

A static experiment was conducted for a leading edge impingement design directly derived from a demonstrator engine. Multiple different impingement configurations were tested. The geometries each had similar average heat transfer levels, which were in line with previous studies, with some variation in distributions between configurations. RANS CFD simulations predicted the distributions and trends with Reynolds number well, however overpredicted levels consistently by around 10%.

Leading Edge Impingement - Mechanical

The research was extended to investigate the impact of variation in heat transfer results on the mechanical performance of a turbine cooling system. A method was developed to isolate an individual cooling system from a blade, analyse the stress distribution and improve the mechanical performance through manipulation of the cooling system. Temperature profiles, both from conjugate CFD simulations and manually generated, were applied to an impingement geometry to find desirable features in a metal temperature distribution, with geometric changes also considered.

Leading Edge Impingement - HTC Sensitivity

The effect of changes in HTC levels on the surfaces of a leading edge impingement system were investigated. Heat transfer enhancements and reductions were applied to key surfaces in turn and the changes in temperature and stress levels and distribution were noted. Significant alterations in stress levels were found from only a 20% change in HTC levels. Desirable individual changes were then combined to determine whether the changes in stress levels were maintained when multiple HTC alterations were combined.

Thermal Matching - Leading Edge

Automated methods were developed for the thermal matching problem which is a key stage in the design process for a gas turbine engine. Two methods, a simple and a Gaussian process regression based model were introduced. These are both used to give a prediction of HTC factors that are required in order for the temperature distribution to be matched. These methods were extensively validated with the GPR based methodology proving robust and accurate. This method was subsequently applied to a leading edge impingement geometry where it was used successfully to match a target temperature distribution.

Thermal Matching - Full IP Blade

The Gaussian process regression based method was then applied to a full IP blade cooling system and validated using real thermal paint results. Multiple parameter sets were used in order to provide an understanding of the modelling setup for full blade thermal matching procedures. Successful matches of the target distribution were obtained and the requirements for the chosen parameters were assessed.

Thermal Matching - Full HP Blade

The new thermal matching technique was applied to a full HP blade with actual thermal paint data used as the target distribution. An increased number of parameters were required due to the additional complexity of the cooling system. A successful match was obtained with the exception of a small region of the blade due to a specific cooling feature, which is easily rectifiable for future matches.

Thermal Matching - Thermal Paint Data Improvement

The Gaussian process regression technique was then used with a physically based, custom covariance function to obtain a modelled full surface temperature distribution from the thermal paint contour bands. This was validated for a number of different surfaces, and can provide additional information on the actual operation of the blade, and the quality of thermal matches.

11.2 Conclusions

The aims of this thesis have all been met, with the RANS CFD evaluated for rotating radial passages and leading edge impingement systems in Chapters 3-5, and Chapter 6 providing new detailed experimental heat transfer distributions for a leading edge impingement configuration. Chapters 7 and 8 give a new mechanical method applied to a leading edge impingement system, with suggestions for improving the stress distribution. Finally, Chapters 9-10 introduce and validate a new automated method for thermal matching based on Gaussian process regression, for a leading edge impingement system and real engine turbine blades.

The main conclusions that have been drawn from this work are given below.

- **Radial Passage Rotational Effects** - In a serpentine passage the heat transfer distribution in a pass is heavily influenced by the upstream conditions, this being either the inlet geometry or previous passes.

- **Radial Passage CFD** - RANS CFD is not capable of reliably predicting the complex inlet flows caused by the upstream geometry in this case, however it produces better predictions in the third pass where this has less influence.

- **Radial Passage Inlet Effects** - Modelling the upstream flows correctly is vital to produce good heat transfer predictions. These must also be taken into account for real engine design.

- **Radial Passage Rib Reversal Effects** - The relative direction in ribs between passes in serpentine passages has a significant influence on flow and heat transfer, with non-reversed ribs giving improved heat transfer performance in later passes.

- **LE Impingement Rotational Effects** - In impingement systems where the jet-target surface distance is relatively low, rotation has the greatest effect in the feed passage, with little jet deflection in the target passage. Therefore rotation enhances heat transfer on the suction surface of the target passage as the jets are directed towards this surface due to the feed flow being biased towards the opposing side of the channel.

- **LE Impingement Static Experiment** - The heat transfer properties of the engine-derived leading edge impingement system are very similar for multiple different hole configurations, which allows for the optimum layout for stress considerations to be used.

- **LE Impingement CFD** - RANS CFD offers good predictions of the heat transfer distribution and trends with Rotation and Reynolds number, however overpredicts average levels by 10%.
- **Mechanical Method Validation** - It was shown that a mechanical analysis of an individual cooling system which has been isolated from a blade can be used to determine improvements in the stress distribution, and therefore life, of that system.
- **LE Mechanical Geometric** - The solid geometry of a leading edge impingement system was found to have little impact on the stress levels within the life-limiting web section of the geometry.
- **LE Mechanical Temperature Profile** - The temperature profile through the blade cross section is the main driver behind the stress distribution, with a large difference between the shell and web temperatures causing the highest web stress levels.
- **HTC Sensitivity** - An adjustment in HTC values on carefully chosen surfaces within a LE impingement system can significantly alter the stress levels in a blade, with a 6 % reduction in web stress demonstrated using 20 % HTC alterations.
- **Thermal Matching Method** - A method based on Gaussian process regression has been implemented to automate the process of thermal matching for turbine blades. It performed significantly better than a baseline linear method for engine representative geometries.
- **Thermal Matching Validation** - This method has been extensively demonstrated and evaluated on a leading edge impingement system, and has been found to reliably produce very good thermal matches to a specified target distribution.
- **Thermal Matching Real Blade** - The thermal match procedure has been applied to real engine blades, where it successfully produced thermal matches to a high accuracy far faster and using a more standardised procedure than existing methods.

- **Thermal Paint Data Improvement** - A new method based on Gaussian process regression with a physical basis has been implemented to offer full surface temperature distributions which can improve analysis of paint tested blades, and thermal matching of models to these.

11.3 Suggestions for Future Work

11.3.1 Radial Passages

The RHTR produces very valuable heat transfer results for engine realistic geometries under engine representative conditions, however only for a relatively short length of the passage. This makes comprehensive validation of the heat transfer predictions from CFD for some regions, such as the the inlet effects and bends, challenging. Therefore the experimental test section could be modified to improve the camera view of the passages to provide results for a larger region.

RANS CFD simulations were used for this work, however were found to provide inadequate predictions for the radial passages under rotating conditions with the complex inlet effects. Therefore higher cost CFD methodologies, such as LES, could be tested against the same experimental data to see if improved predictions are produced, and if any improvements justify the increase in computational cost.

11.3.2 Leading Edge Impingement

The mechanical methodology was applied and validated for a leading edge impingement system for this work. The method could be applied and tested for other cooling systems in different sections of the blade, to ensure similar methods can be used for them and that the correct boundary conditions are applied in future cases.

The static experimental results presented provided detailed heat transfer measurements for the characterisation of such a system, and for validation of CFD simulations. In a real engine case, crossflow may be present in both the leading edge and feed passages, and a future experimental campaign could investigate the effects of these relative to the presented heat transfer distribution and levels, and to ensure conclusions drawn on the accuracy of RANS CFD simulations hold for this more complex case. Higher cost CFD methods may also be tested against this high resolution data to test if any improvement in accuracy over RANS CFD is present for real engine geometries and conditions.

11.3.3 Thermal Matching

The current thermal matching methodology has been undertaken using a low order thermal model to match to the thermal paint data, as is currently done in industry. With increasing levels of computational power, conjugate CFD simulations may be used in part to replace these low order thermal models, and therefore the methodology may be adapted for use with conjugate CFD. This may be done either using a surrogate thermal model on which the CFD solution is imposed, or to apply the method directly to the conjugate CFD through the alteration of boundary conditions.

The method for providing a full surface temperature distribution currently uses a relatively simple covariance function. The complexity and physical basis of this may be improved further to give increased accuracy for the distributions produced. The method may also be tested and validated for use in a wider variety of scenarios where only sparse data is available in the gas turbine engine.

Bibliography

[1] ACARE 2020 targets, http://www.cleansky.eu/content/homepage/aviation-environment, 2016.

[2] Rolls Royce. *The Jet Engine*. John Wiley & Sons, 2015.

[3] MJ Holland and TF Thake. Rotor blade cooling in high pressure turbines. *Journal of aircraft*, 17(6):412–418, 1980.

[4] JC Han. Recent studies in turbine blade cooling. *International Journal of Rotating Machinery*, 10(6):443–457, 2004.

[5] JC Han. Fundamental gas turbine heat transfer. *Journal of thermal science and engineering applications*, 5(2):021007, 2013.

[6] JC Ryley. *Turbine blade mid-chord internal cooling*. PhD thesis, University of Oxford, 2014.

[7] R Davenport. The benefits of a rotating rig for research into advanced turbine cooling systems. In *RTO AVT Symposium on Design Principles and Methods for Aircraft Gas Turbine Engines*, 1998.

[8] JC Han and LM Wright. Enhanced internal cooling of turbine blades and vanes, http://www.netl.doe.gov. 2014.

[9] JH Wagner, BV Johnson, and FC Kopper. Heat transfer in rotating serpentine passages with smooth walls. *Journal of Turbomachinery*, 113(3):321–330, 1991.

[10] JH Wagner, BV Johnson, RA Graziani, and FC Yeh. Heat transfer in rotating serpentine passages with trips normal to the flow. In *ASME 1991 International Gas Turbine and Aeroengine Congress and Exposition*. American Society of Mechanical Engineers, 1991.

[11] BV Johnson, JH Wagner, GD Steuber, and FC Yeh. Heat transfer in rotating serpentine passages with trips skewed to the flow. In *ASME 1992 International Gas Turbine and Aeroengine Congress and Exposition*. American Society of Mechanical Engineers, 1992.

[12] L Al-Hadhrami and JC Han. Effect of rotation on heat transfer in two-pass square channels with five different orientations of 45 degree angled rib turbulators. *International Journal of Heat and Mass Transfer*, 46(4):653–669, 2003.

[13] LM Wright, WL Fu, and JC Han. Influence of entrance geometry on heat transfer in rotating rectangular cooling channels (AR= 4:1) with angled ribs. *Journal of heat transfer*, 127(4):378–387, 2005.

[14] M Huh, J Lei, YH Liu, and JC Han. High rotation number effects on heat transfer in a rectangular (AR= 2:1) two-pass channel. *Journal of Turbomachinery*, 133(2):021001, 2011.

[15] YH Liu, M Huh, JC Han, and S Chopra. Heat transfer in a two-pass rectangular channel (ar= 1: 4) under high rotation numbers. *Journal of Heat Transfer*, 130(8):081701, 2008.

[16] J Lei, SJ Li, JC Han, L Zhang, and HK Moon. Heat transfer in rotating multipass rectangular ribbed channel with and without a turning vane. *Journal of Heat Transfer*, 135(4):041903, 2013.

[17] A Rallabandi, J Lei, JC Han, S Azad, and CP Lee. Heat transfer measurements in rotating blade–shape serpentine coolant passage with ribbed walls at high Reynolds numbers. *Journal of Turbomachinery*, 136(9):091004, 2014.

[18] I Mayo, GL Gori, A Lahalle, and T Arts. Aerothermal characterization of a rotating ribbed channel at engine representative conditions—part I: High-resolution particle image velocimetry measurements. *Journal of Turbomachinery*, 138(10):101008, 2016.

[19] I Mayo, A Lahalle, GL Gori, and T Arts. Aerothermal characterization of a rotating ribbed channel at engine representative conditions—part II: Detailed liquid crystal thermography measurements. *Journal of Turbomachinery*, 138(10):101009, 2016.

[20] K Saha and S Acharya. Effect of entrance geometry and rotation on heat transfer in a narrow (AR= 1: 4) rectangular internal cooling channel4) rectangular internal cooling channel. In *ASME Turbo Expo 2014: Turbine Technical Conference and Exposition*. American Society of Mechanical Engineers, 2014.

[21] M Schüler, HM Dreher, SO Neumann, B Weigand, and M Elfert. Numerical predictions of the effect of rotation on fluid flow and heat transfer in an engine-similar two-pass internal cooling channel with smooth and ribbed walls. *Journal of Turbomachinery*, 134(2):021021, 2012.

[22] G Su, HC Chen, JC Han, and JD Heidmann. Computation of flow and heat transfer in rotating two-pass rectangular channels (AR= 1:1, 1:2, and 1:4) with smooth walls by a Reynolds stress turbulence model. *International Journal of Heat and Mass Transfer*, 47(26):5665–5683, 2004.

[23] G Su, HC Chen, JC Han, and JD Heidmann. Computation of flow and heat transfer in two-pass rotating rectangular channels (AR= 1:1, AR= 1:2, AR= 1:4) with 45-deg. angled ribs by Reynolds stress turbulence model. In *ASME Turbo Expo 2004: Power for Land, Sea, and Air*, pages 603–612. American Society of Mechanical Engineers, 2004.

[24] AP Rallabandi, H Yang, and JC Han. Heat transfer and pressure drop correlations for square channels with 45 deg ribs at high Reynolds numbers. *Journal of Heat Transfer*, 131(7):071703, 2009.

[25] AP Rallabandi, N Alkhamis, and JC Han. Heat transfer and pressure drop measurements for a square channel with 45 deg round-edged ribs at high Reynolds numbers. *Journal of Turbomachinery*, 133(3):031019, 2011.

[26] JS Park, JC Han, Y Huang, S Ou, and RJ Boyle. Heat transfer performance comparisons of five different rectangular channels with parallel angled ribs. *International Journal of Heat and Mass Transfer*, 35(11):2891–2903, 1992.

[27] CLP Tsang. *High blockage turbulators in gas turbine cooling passage*. PhD thesis, University of Oxford, 2002.

[28] M Huh, YH Liu, JC Han, and S Chopra. Effect of rib spacing on heat transfer in a two-pass rectangular channel (AR= 1:4) with a sharp entrance at high rotation numbers. In *ASME Turbo Expo 2008: Power for Land, Sea, and Air*, pages 287–300. American Society of Mechanical Engineers, 2008.

[29] YH Liu, LM Wright, WL Fu, and JC Han. Rib spacing effect on heat transfer and pressure loss in a rotating two-pass rectangular channel (ar= 1: 2) with 45-degree angled ribs. In *ASME Turbo Expo 2006: Power for Land, Sea, and Air*, pages 363–373. American Society of Mechanical Engineers, 2006.

[30] JC Han and JS Park. Developing heat transfer in rectangular channels with rib turbulators. *International Journal of Heat and Mass Transfer*, 31(1):183–195, 1988.

[31] LM Wright, WL Fu, and JC Han. Thermal performance of angled, v-shaped, and w-shaped rib turbulators in rotating rectangular cooling channels (AR= 4:1). In *ASME Turbo Expo 2004: Power for Land, Sea, and Air*, pages 885–894. American Society of Mechanical Engineers, 2004.

[32] JA Lamont, SV Ekkad, and MA Alvin. Effect of rotation on detailed heat transfer distribution for various rib geometries in developing channel flow. *Journal of Heat Transfer*, 136(1):011901, 2014.

[33] J Lamont, S Ramesh, SV Ekkad, A Tolpadi, C Kaminski, and S Salamah. Heat transfer enhancement in narrow diverging channels. *Journal of Turbomachinery*, 135(4):041017, 2013.

[34] SV Ekkad, D Kontrovitz, H Nasir, G Pamula, and S Acharya. Effect of rib turbulators in the first pass on heat transfer distributions in a two-pass channel connected by two rows of holes. In *ASME Turbo Expo 2001: Power for Land, Sea, and Air*. American Society of Mechanical Engineers, 2001.

[35] G Pamula, SV Ekkad, and S Acharya. Influence of crossflow-induced swirl and impingement on heat transfer in a two-pass channel connected by two rows of holes. *Journal of turbomachinery*, 123(2):281–287, 2001.

[36] SV Ekkad, G Pamula, and S Acharya. Influence of crossflow-induced swirl and impingement on heat transfer in an internal coolant passage of a turbine airfoil. *Journal of heat transfer*, 122(3):587–597, 2000.

[37] A Pramanick and SV Ekkad. Effect of rotation on flow and temperature distributions in a two-pass channel connected by two rows of holes. In *ASME Turbo Expo 2002: Power for Land, Sea, and Air*, pages 543–550. American Society of Mechanical Engineers, 2002.

[38] L Yang, K Tyagi, SV Ekkad, and J Ren. Influence of rotation on heat transfer in a two-pass channel with impingement under high Reynolds number. In *ASME Turbo Expo 2015: Turbine Technical Conference and Exposition*. American Society of Mechanical Engineers, 2015.

[39] J Sundberg. Heat transfer correlations for gas turbine cooling. 2006.

[40] N Zuckerman and N Lior. Jet impingement heat transfer: physics, correlations, and numerical modelling. *Advances in heat transfer*, 39(06):565–631, 2006.

[41] TS O'Donovan and DB Murray. Jet impingement heat transfer–part I: Mean and root-mean-square heat transfer and velocity distributions. *International Journal of Heat and Mass Transfer*, 50(17):3291–3301, 2007.

[42] TS O'Donovan and DB Murray. Jet impingement heat transfer–part II: A temporal investigation of heat transfer and local fluid velocities. *International Journal of Heat and Mass Transfer*, 50(17):3302–3314, 2007.

[43] C Son, DRH Gillespie, PT Ireland, and GM Dailey. Heat transfer characteristics of an impingement plate used in a turbine vane cooling system. In *ASME Turbo Expo 2001: Power for Land, Sea, and Air*. American Society of Mechanical Engineers, 2001.

[44] JA Lamont and SV Ekkad. Effect of rotation on jet impingement heat transfer for various jet configurations. In *ASME 2012 Heat Transfer Summer Conference collocated with the ASME 2012 Fluids Engineering Division Summer Meeting and the ASME 2012 10th International Conference on Nanochannels, Microchannels, and Minichannels*, pages 717–726. American Society of Mechanical Engineers, 2012.

[45] WV Harmon, CA Elston, and LM Wright. Experimental investigation of leading edge impingement under high rotation numbers with racetrack shaped jets. In *ASME Turbo Expo 2014: Turbine Technical Conference and Exposition*. American Society of Mechanical Engineers, 2014.

[46] JA Lamont and SV Ekkad. Effects of rotation on jet impingement channel heat transfer. In *ASME 2011 Turbo Expo: Turbine Technical Conference and Exposition*, pages 1269–1278. American Society of Mechanical Engineers, 2011.

[47] JA Parsons and JC Han. Rotation effect on jet impingement heat transfer in smooth rectangular channels with heated target walls and radially outward cross flow. *International Journal of Heat and Mass Transfer*, 41(13):2059–2071, 1998.

[48] EL Martin, LM Wright, and DC Crites. Computational investigation of jet impingement on turbine blade leading edge cooling with engine-like temperatures. In *ASME Turbo Expo 2012: Turbine Technical Conference and Exposition*, pages 311–322. American Society of Mechanical Engineers, 2012.

[49] EL Martin, LM Wright, and DC Crites. Impingement heat transfer enhancement on a cylindrical, leading edge model with varying jet temperatures. *Journal of Turbomachinery*, 135(3):031021, 2013.

[50] L Andrei, C Carcasci, R Da Soghe, B Facchini, F Maiuolo, L Tarchi, and S Zecchi. Heat transfer measurements in a leading edge geometry with racetrack holes and film cooling extraction. *Journal of Turbomachinery*, 135(3):031020, 2013.

[51] B Facchini, F Maiuolo, L Tarchi, and N Ohlendorf. Experimental investigation on the heat transfer of a leading edge cooling system: effects of jet-to-jet spacing and showerhead extraction. In *ASME Turbo Expo 2013: Turbine Technical Conference and Exposition*, pages V03AT12A026–V03AT12A026. American Society of Mechanical Engineers, 2013.

[52] B Facchini, F Maiuolo, and L Tarchi. D2.4 report on UNIFI experiments. Technical report, ERICKA, 2013.

[53] S Schulz, A Schindler, and J von Wolfersdorf. An experimental and numerical investigation on the effects of aerothermal mixing in a confined oblique jet impingement configuration. *Journal of Turbomachinery*, 138(4):041007, 2016.

[54] F Hoefler, S Schueren, J von Wolfersdorf, and S Naik. Heat transfer in a confined oblique jet impingement configuration. In *ASME Turbo Expo 2009: Power for Land, Sea, and Air*, pages 311–321. American Society of Mechanical Engineers, 2009.

[55] Y Huang, SV Ekkad, and JC Han. Detailed heat transfer distributions under an array of orthogonal impinging jets. *Journal of Thermophysics and Heat Transfer*, 12(1):73–79, 1998.

[56] SV Ekkad, Y Huang, and JC Han. Impingement heat transfer on a target plate with film cooling holes. *Journal of Thermophysics and Heat transfer*, 13(4):522–528, 1999.

[57] J Lee, Z Ren, J Haegele, G Potts, JS Jin, P Ligrani, MD Fox, and HK Moon. Effects of jet-to-target plate distance and reynolds number on jet array impingement heat transfer. *Journal of Turbomachinery*, 136(5):051013, 2014.

[58] Y Xing and B Weigand. Optimum jet-to-plate spacing of inline impingement heat transfer for different crossflow schemes. *Journal of Heat Transfer*, 135(7):072201, 2013.

[59] RT Hebert, SV Ekkad, L Gao, and RS Bunker. Impingement heat transfer, part II: effect of streamwise pressure gradient. *Journal of thermophysics and heat transfer*, 19(1):66–71, 2005.

[60] JA Lamont, SV Ekkad, and MA Alvin. Effects of rotation on heat transfer for a single row jet impingement array with crossflow. *Journal of Heat Transfer*, 134(8):082202, 2012.

[61] MB Ibrahim, BJ Kochuparambil, SV Ekkad, and TW Simon. CFD for jet impingement heat transfer with single jets and arrays. In *ASME Turbo Expo 2005: Power for Land, Sea, and Air*, pages 359–373. American Society of Mechanical Engineers, 2005.

[62] A Terzis, G Wagner, and P Ott. Hole staggering effect on the cooling performance of narrow impingement channels. *ASME, GT2012-68323, TurboExpo*, pages 11–15, 2012.

[63] JC Bailey and RS Bunker. Local heat transfer and flow distributions for impinging jet arrays of dense and sparse extent. In *ASME Turbo Expo 2002: Power for Land, Sea, and Air*, pages 855–864. American Society of Mechanical Engineers, 2002.

[64] L Gao, SV Ekkad, and RS Bunker. Impingement heat transfer part I: Linearly stretched arrays of holes. *Journal of thermophysics and heat transfer*, 19(1):57–65, 2005.

[65] CN Jordan, LM Wright, and DC Crites. Impingement heat transfer on a cylindrical, concave surface with varying jet geometries. In *ASME Turbo Expo 2012: Turbine Technical Conference and Exposition*, pages 335–346. American Society of Mechanical Engineers, 2012.

[66] WV Harmon, LM Wright, DC Crites, MC Morris, and A Riahi. Combined effects of jet plate thickness and fillet radius on leading edge jet impingement with round and racetrack shaped jets. In *ASME Turbo Expo 2015: Turbine Technical Conference and Exposition*. American Society of Mechanical Engineers, 2015.

[67] B Facchini, F Maiuolo, L Tarchi, and N Ohlendorf. Experimental investigation on the heat transfer in a turbine airfoil leading edge region: Effects of the wedge angle and jet impingemnt geometries. In *10th European Conference on Turbomachinery, Fluid Dynamics and Thermodynamics*, 2013.

[68] SV Ekkad, Y Huang, and JC Han. Impingement heat transfer measurements under an array of inclined jets. *Journal of thermophysics and heat transfer*, 14(2):286–288, 2000.

[69] ME Taslim, L Setayeshgar, and SD Spring. An experimental evaluation of advanced leading edge impingement cooling concepts. *Journal of Turbomachinery*, 123(1):147–153, 2001.

[70] R Brakmann, L Chen, B Weigand, and M Crawford. Experimental and numerical heat transfer investigation of an impinging jet array on a target plate roughened by cubic micro pin fins. In *ASME Turbo Expo 2015: Turbine Technical Conference and Exposition*. American Society of Mechanical Engineers, 2015.

[71] ME Taslim, Y Pan, and SD Spring. An experimental study of impingement on roughened airfoil leading-edge walls with film holes. In *ASME Turbo Expo 2001: Power for Land, Sea, and Air*. American Society of Mechanical Engineers, 2001.

[72] ME Taslim, K Bakhtari, and H Liu. Experimental and numerical investigation of impingement on a rib-roughened leading-edge wall. In *ASME Turbo Expo 2003, collocated with the 2003 International Joint Power Generation Conference*, pages 31–41. American Society of Mechanical Engineers, 2003.

[73] F Hoefler, S Schueren, J von Wolfersdorf, and S Naik. Heat transfer characteristics of an oblique jet impingement configuration in a passage with ribbed surfaces. *Journal of Turbomachinery*, 134(3):031022, 2012.

[74] AC Chambers, DRH Gillespie, PT Ireland, and R Kingston. Enhancement of impingement cooling in a high cross flow channel using shaped impingement cooling holes. *Journal of Turbomachinery*, 132(2):021001, 2010.

[75] ME Taslim and A Khanicheh. Experimental and numerical study of impingement on an airfoil leading edge with and without showerhead and gill film holes. *Journal of turbomachinery*, 128(2):310–320, 2006.

[76] ME Taslim and D Bethka. Experimental and numerical impingement heat transfer in an airfoil leading-edge cooling channel with cross-flow. *Journal of Turbomachinery*, 131(1):011021, 2009.

[77] K Elebiary and ME Taslim. Experimental/numerical crossover jet impingement in an airfoil leading-edge cooling channel. *Journal of Turbomachinery*, 135(1):011037, 2013.

[78] B Rosic. Viscous flow and turbulence, lecture notes. 2015.

[79] PR Spalart and SR Allmaras. A one equation turbulence model for aerodinamic flows. *AIAA journal*, 94, 1992.

[80] BE Launder and DB Spalding. The numerical computation of turbulent flows. *Computer methods in applied mechanics and engineering*, 3(2):269–289, 1974.

[81] DC Wilcox. Formulation of the k-ω turbulence model revisited. *AIAA journal*, 46(11):2823–2838, 2008.

[82] FR Menter. Two-equation eddy-viscosity turbulence models for engineering applications. *AIAA journal*, 32(8):1598–1605, 1994.

[83] M McGilvray, CO Pineiro, T Axe, JC Ryley, and DRH Gillespie. Comparison of stationary internal cooling passage numerical simulations to experimental data. In *10th European Tubomachinery Conference, Lappeenranta, Finland*, 2013.

[84] M McGilvray, DRH Gillespie, and JC Ryley. Investigation of wrapping ribs onto smooth walls for mid-chord internal cooling passages. In *ASME Turbo Expo 2014: Turbine Technical Conference and Exposition*. American Society of Mechanical Engineers, 2014.

[85] D Jackson, PT Ireland, and B Cheong. Combined experimental and CFD study of a HP blade multi-pass cooling system. In *ASME Turbo Expo 2009: Power for Land, Sea, and Air*, pages 851–862. American Society of Mechanical Engineers, 2009.

[86] PT Ireland and TV Jones. Liquid crystal measurements of heat transfer and surface shear stress. *Measurement Science and Technology*, 11(7):969, 2000.

[87] SV Ekkad and JC Han. A transient liquid crystal thermography technique for gas turbine heat transfer measurements. *Measurement Science and Technology*, 11(7):957, 2000.

[88] DRH Gillespie and M McGilvray. Transient liquid crystal heat transfer experiments. Technical report, University of Oxford, 2015.

[89] JC Ryley, M McGilvray, and DRH Gillespie. Calculation of heat transfer coefficient distribution on 3d geometries from transient liquid crystal experiments. In *ASME Turbo Expo 2014: Turbine Technical Conference and Exposition*. American Society of Mechanical Engineers, 2014.

[90] DRH Gillespie, Z Wang, and PT Ireland. Heating element. *British Patent Application PCT/GB96/2017*, 1995.

[91] DB Helmer. Modified transient infrared methodology for leading edge impingement measurements. In *ASME Turbo Expo 2014: Turbine Technical Conference and Exposition*. American Society of Mechanical Engineers, 2014.

[92] DB Helmer and F Hoefler. Steady IR methodology for leading edge impingement measurements. In *ASME Turbo Expo 2015: Turbine Technical Conference and Exposition*. American Society of Mechanical Engineers, 2015.

[93] PP Benham, RJ Crawford, and CG Armstrong. *Mechanics of engineering materials*. Pearson Prentice Hall, Longman Group, 1996.

[94] AM Howatson, PG Lund, and JD Todd. *Engineering Tables and Data*. 2008.

[95] TM Mitchell. *Machine Learning*. Mcgraw-Hill, 1997.

[96] CE Rasmussen. Gaussian processes for machine learning. 2006.

[97] E Romero. D3.7 - Report of results of rotating heat transfer tests - radial cooling geometries. Technical report, ERICKA, 2014.

[98] Z Wang, PT Ireland, and ST Kohler. Gas temperature measurement in internal cooling passages. In *ASME 1996 International Gas Turbine and Aeroengine Congress and Exhibition*. American Society of Mechanical Engineers, 1996.

[99] Z Wang, PT Ireland, ST Kohler, and JW Chew. Heat transfer measurements to a gas turbine cooling passage with inclined ribs. *Journal of turbomachinery*, 120(1):63–69, 1998.

[100] JC Ryley, M McGilvray, and DRH Gillespie. Stationary internal cooling passage experiments for an engine realistic configuration. In *10th European Conference on Turbomachinery, Fluid Dynamics and Thermodynamics*, 2013.

[101] C Tsang, DRH Gillespie, and PT Ireland. Flow measurements inside a large scale model of a turbine component internal cooling passage. In *Proceedings of the 6th European Conference on Turbomachinery, Fluid Dynamics and Thermodynamics*, 2005.

[102] E Romero, L Tarchi, and R Bauer. D2.5 - Report of results of rotating heat transfer tests - impingement cooling geometries. Technical report, ERICKA, 2014.

[103] S Zecchi and N Ohlendorf. D2.1 - CAD design for RHR impingement flow model. Technical report, ERICKA, 2010.

[104] DRH Gillespie. *Intricate internal cooling systems for gas turbine blading.* PhD thesis, University of Oxford, 1998.

[105] DRH Gillespie, Z Wang, PT Ireland, and ST Kohler. Full surface local heat transfer coefficient measurements in a model of an integrally cast impingement cooling geometry. In *ASME 1996 International Gas Turbine and Aeroengine Congress and Exhibition*. American Society of Mechanical Engineers, 1996.

[106] BS EN ISO. 9300:2005. *Measurement of gas flow by means of critical flow Venturi nozzles*.

[107] BS EN ISO. 5167-1:2003. *Measurement of fluid flow by means of pressure differential devices inserted in circular cross-section conduits running full - Part 1*.

[108] BS EN ISO. 5167-2:2003. *Measurement of fluid flow by means of pressure differential devices inserted in circular-cross section conduits running full - Part 2*.

[109] National Instruments DAQ, http://www.ni.com/data-acquisition, 2016.

[110] MATLAB The MathWorks, http://uk.mathworks.com, 2016.

[111] First Sensor http://www.first-sensor.com/en/.

[112] Scanivalve http://www.scanivalve.com/.

[113] WIKA CPC4000 Industrial Pressure Controller, http://www.wika.co.uk, 2016.

[114] Magna-Power http://www.magna-power.com.

[115] VirtualDub http://virtualdub.org.

[116] DRH Gillespie, M McGilvray, and B Tang. THTAC: Transient Heat Transfer Analysis Code. Technical report, University of Oxford, 2016.

[117] RE Chupp, HE Helms, and McFadden PW. Evaluation of internal heat transfer coefficients for impingement cooled turbine airfoils. *Journal of Aircraft*, 6(3):203–208, 1969.

[118] S Friedrichs. Turbine heat transfer, part 1 - introduction and overview. In *Cambridge Turbomachinery Course*, pages 219–254, 2012.

[119] High-temperature high-strength nickel based alloys. Technical report, Nickel Development Institute, 1995.

[120] N Moritz, K Kusterer, D Bohn, T Sugimoto, R Tanaka, and T Taniguchi. Conjugate calculation of a film-cooled blade for improvement of the leading edge cooling configuration. *Propulsion and Power Research*, 2(1):1–9, 2013.

[121] J Telisinghe. Leading edge design spreadsheet, private communication, 2014.

[122] J Telisinghe. External boundary conditions and stress distributions, private communication, 2014.

[123] TH Wong. A study of the impact of cooled cooling air at future large engine operating conditions and potential solutions. Technical report, University of Oxford and Rolls Royce, 2010.